Lipid Humification by Soil Clays

by
ADRIAN RICHARD ADAMS

Dissertation presented for the
degree of DOCTOR OF PHILOSOPHY
in the Faculty of AgriSciences at
Stellenbosch University

Supervisor: Dr C.E. Clarke
Co-supervisor: Dr A.G. Hardie

April 2019

The financial assistance of the National Research Foundation (NRF) towards this research is hereby acknowledged. Opinions expressed and conclusions arrived at, are those of the author and are not necessarily to be attributed to the NRF.

Declaration

By submitting this dissertation electronically, I declare that the entirety of the work contained therein is my own, original work, that I am the sole author thereof (save to the extent explicitly otherwise stated), that reproduction and publication thereof by Stellenbosch University will not infringe any third party rights and that I have not previously in its entirety or in part submitted it for obtaining any qualification.

Date: April 2019

"You are young yet, my friend," replied my host,
"but the time will arrive when you will learn
to judge for yourself of what is going on in the world,
without trusting to the gossip of others."

"Believe nothing you hear,
and only one half that you see."

—Edgar Allan Poe

"The system of Doctor Tarr and Professor Fether"
(Graham's Magazine, vol. XXVIII, no. 5, November 1845)

Abstract

Lipid Humification by Soil Clays

A.R. Adams

Department of Soil Science
Stellenbosch University
Private Bag X1, Matieland 7602, South Africa

Dissertation: Ph.D. (Soil Science)
April 2019

We studied three aspects of the natural polymerisation (humification) of lipids by soil clays—namely, the products formed, reaction mechanism and kinetics—at environmental temperatures (*c.* 20–50°C). Various clays were reacted with oleic acid (our chosen model lipid). The Mn-oxide birnessite was the most reactive toward oleic acid, polymerising it into *quasi*-solid polyesters.

A probing of the birnessite-oleic acid reaction mechanism revealed that the formation of a surface exchange complex between oleic acid carboxyl groups and birnessite surface sites ($\equiv Mn^{3+}/\equiv Mn^{4+}$) is a crucial first step of the reaction. Subsequent chelation and one-electron reduction of Mn^{3+} to Mn^{2+} forms radical oleic acid species which couple and thereby polymerise.

Kinetic studies revealed that the birnessite-oleic acid reaction was near-linearly dependent on birnessite mass-loading (rate order ~ 0.75) but virtually independent of birnessite surface pH (rate order ~ 0.2). A determined activation energy (E_a) for the reaction of 12.8 ± 4.2 kJ mol^{-1} revealed that it is energetically more spontaneous than the usual autoxidation pathways.

These findings broaden our understanding of the role soil clays play in lipid humification in soils.

Keywords: humification, lipids, soil minerals, polyesters, complexation, RGB colour analysis

Uittreksel

Lipied Humifikasie deur Grond Kleie

"Lipid Humification by Soil Clays"

A.R. Adams

Departement Grondkunde
Stellenbosch Universiteit
Privaatsak X1, Matieland 7602, Suid-Afrika

Proefskrif: Ph.D. (Grondkunde)
April 2019

Ons het drie aspekte van die natuurlike polimerisasie (humifikasie) van lipiede deur grond kleie bestudeer—naamlik, die produkte gevorm, reaksie meganisme en kinetika—teen omgewings-temperature (ong. 20–50°C). Verskeie kleie is met oleïen suur (ons gekose model lipied) gereageer. Die Mn-oksied birnessiet was die mees reaktief teenoor oleïen suur, deur dit te polimeriseer na kwasi-soliede poliësters.

'n Ondersoek na die birnessiet-oleïen suur reaksie meganisme toon dat die formasie van 'n oppervlaks-uitruilingskompleks tussen oleïen suur karboksiel groepe en birnessiet oppervlaks-liggings ($\equiv Mn^{3+}/\equiv Mn^{4+}$) 'n noodsaaklike eerste stap van die reaksie is. Gevolglike chelasie en een-elektron reduksie van Mn^{3+} na Mn^{2+} form radikaal oleïen suur spesies wat koppel en daardeur polimeriseer.

Kinetika studies toon dat die birnessiet-oleïen suur reaksie naby-liniêr afhanklik is op birnessiet massa-lading (tempo orde ~ 0.75) maar so te sê onafhanklik is van birnessiet oppervlaks-pH (tempo orde ~ 0.2). 'n Bepaalde aktiverings-energie (E_a) vir dié reaksie van 12.8 ± 4.2 kJ mol^{-1} toon dat dit energiek meer spontaan is as die gewone outoksidasie roetes.

Hierdie bevindings verbreed ons begrip van die rol wat grond kleie in lipied humifikasie in gronde speel.

Sleutelwoorde: humifikasie, lipiede, grond-minerale, poliësters, kompleksering, RGB kleur analiese

Acknowledgements

I would like to thank my supervisors Doctor Cathy Clarke and Doctor Ailsa Hardie for their support, encouragement, persistence and patience throughout this study. Tackling a new scientific endeavour is never easy and knowing that I was not walking this path alone helped immensely. Their contributions are immeasurable.

A debt of gratitude is also due to the Department of Soil Science, my home from home for over six years—to all my colleagues, staff members and friends during this time—it was a truly engaging, enlightening and fun period. I am eternally grateful for the amazing opportunity to teach and mentor undergraduate soil science students, especially during their rock and mineral identification practicals. Words could never fully express how much of a rewarding experience that was for me, and how much I grew personally from it. Similar holds true for our annual faculty open days, the opportunity to engage with the public and "*sell*" our "*product*" was a lot of fun.

On the university campus, I would like to thank various departments, individuals and entities for all their contributions to this study, be it analytical services, consumables or just general great advice and friendship. These include the Departments of Chemistry (Dr Paul Verhoeven, Prof. Len Barbour, Mr Wesley Feldmann, Dr Leigh Loots and Mrs Peta Steyn), Process Engineering (Mrs Hanlie Botha), Plant Pathology (Mrs Anria Pretorius and Mrs Tammy Jensen), Physics (Prof. Paul Papka), Botany and Zoology (Dr Aleysia Kleinert and Prof. Alex Valentine), Earth Sciences (Prof. Alakendra Roychoudhury) as well as the Central Analytic Facility (CAF; Mr Lucky Mokwena, Dr Marietjie Stander, Mr Malcolm Taylor, Dr Jaco Brand, Mrs Riana Rossouw, Mrs Charney Anderson Small and Mr Herschel Achilles). I would also like to thank the university for financial support.

Outside the university I wish to thank the Inkaba yeAfrica programme and National Research Foundation (NRF) for generous financial support and scholarships. Further thanks go to Dr Remy Butcher and Mr Zakhelumuzi Khumalo for XRD analyses at the particle accelerator wing of iThemba Labs near Cape Town.

Last, but certainly not least, I would like to thank my loving and tirelessly dedicated parents and Creator, for the years and years of endless support and love—for always standing by me no matter what it is I embark on—I truly could never ever have asked for more.

Contents

List of Figures

List of Tables

Terminology and Nomenclature

Constants

$\mathscr{F}$	Faraday's constant, 96,485 C mol^{-1}	
g_n	Gravitational acceleration, 9.81 m s^{-2}	
R	Universal gas constant, 8.314 J K^{-1} mol^{-1}	

Variables

E_a	Activation energy	[kJ mol^{-1}]
E	Oxidation-reduction potential	[V]
$E°$	Standard oxidation-reduction potential ($25°C, P_{H_2} = 1$ bar)	[V]
T	Temperature	[°C or K]

Abbreviations and acronyms

ATR-FTIR	Attenuated total reflectance—Fourier-transform infrared
BET	Brunauer-Emmett-Teller
CEC	Cation exchange capacity (in $cmol_c$ kg^{-1})
CI	Chemical ionisation
DSC	Differential scanning calorimetry
EDTA	Ethylenediaminetetraacetate
EI	Electron impact
EPR	Electron paramagnetic resonance
ESI	Electrospray ionisation
FAME	Fatty acid methyl ester
FFA	Free fatty acid
GC-FID	Gas chromatography—flame ionisation detection
GC-MS	Gas chromatography—mass spectrometry
HAT	Hydrogen atom transfer
HPLC	High performance liquid chromatography
ICP-OES	Inductively-coupled plasma—optical emission spectroscopy
IUPAC	International Union of Pure and Applied Chemistry
NMR	Nuclear magnetic resonance
QSAR	Quantitative structure-activity relationship
RGB	Red, green, blue
ROS	Reactive oxygen species

RP-HPLC	Reversed-phase HPLC
SOM	Soil organic matter
TGA	Thermogravimetric analysis
TOC	Total organic carbon
TOF	Time-of-flight
UV-VIS	Ultraviolet-visible
XAS	X-ray absorption spectroscopy
XRD	X-ray diffraction

CHAPTER 1

Introduction

The clay fraction of soils (<2 μm size particles) contains several mineral phases that are responsible for the abiotic catalysis and/or mediation of a vast array of reactions in soils (Huang and Hardie, 2012). The dominant mineral phases present in the clay fraction include aluminosilicate clay minerals, quartz (SiO_2) and several oxides and hydroxides (collectively known as *oxyhydroxides* or *sesquioxides*) of aluminium (Al), iron (Fe) and manganese (Mn).

One of the major soil reactions that are influenced by the minerals present in the clay fraction is the natural polymerisation of *biomolecules* into dark, high molecular weight (often >3 kDa)[1] *humic substances*—a process known as *humification*. Biomolecules are the residues that result from the decomposition of complex organic substances such as lignin, cellulose, proteins, waxes and complex lipids into simpler substances by various biogeochemical processes. Common biomolecules include simple sugars, amino acids, polyphenols, phospholipids and simpler lipids (*e.g.* glycerides and free fatty acids).

The humic substances formed from humification are much more recalcitrant than their biomolecule precursors and comprise a significant portion of soil organic matter (SOM), a major component of the terrestrial carbon sink.

[1] kDa = kilo-Dalton, or 1,000 Dalton (a unit of molecular weight—*e.g.* ^{12}C has a mass of 12 Da).

Stable SOM of this sink serves to partially mitigate the increase in size of the atmospheric carbon pool—a phenomenon linked to increasing global temperatures and climate change (Arrhenius, 1896; Callendar, 1938; Anderson *et al.*, 2016).

1.1 Rationale behind this study

Some of the most recalcitrant humic substances are those derived from lipids (Lorenz and Lal, 2010). However, very little is known about the humification pathways of lipids in soils. Whilst lipid transformation reactions such as high temperature (>100°C) lipid peroxidation and polymerisation are well-known to the food, health and material sciences, it is currently unknown how lipids are transformed to high-molecular weight substances in the soil environment, at soil-relevant temperatures (*c.* 20–50°C).

The minerals present in the soil clay fraction are known to catalyse the humification of sugars and amino acids *via* the Maillard reaction as well as polyphenols *via* the polyphenol pathway (Huang and Hardie, 2009, 2012; Hardie *et al.*, 2010). They also catalyse the integrated Maillard-polyphenol pathway Hardie *et al.*, 2010). These minerals are therefore highly suitable candidates for the catalysis and/or mediation of lipid humification reactions in soils. However, whilst the humification of lipids by soil clays is likely, it has neither been studied nor proven before. This study therefore undertook to investigate possible reactions that occur between lipids and minerals found within the soil clay fraction.

1.2 Aims and objectives

Three key questions arise when considering the possible reaction that may occur between lipids and soil clays, and those are (a) *what* products form from such a reaction or interaction, (b) *how* do these products form (or *how* does this reaction occur), and (c) how *fast* does this reaction occur? These questions constituted the three aims of the study:

(a) identifying the products formed from the reaction between lipids and soil clays at soil-relevant temperatures;

(b) elucidating the reaction mechanism of this reaction—*i.e.* how the reaction occurs; and

(c) determining the kinetics of the reaction—which factors or variables affect the rate of the reaction.

1.3 Format of this dissertation

As this dissertation progresses through the aims and objectives, the general progression towards more detailed information and more complex analysis (outlined in Fig. 1.1) occurs. Initially, the study starts out by screening several clays for their reactivity toward a model lipid, namely oleic acid. Simple visual information and spectroscopic techniques are used to screen which clays are the most reactive toward this lipid. The most reactive case(s) is (are) then focused upon, with more detailed information gathered using more advanced analytical techniques. In general, the sample preparation involved, and analytical procedures followed, become more complex as the study progresses, so that is why it makes more sense to select the most demonstrative or conclusive cases as the study progresses. Once the more detailed data is collected, this additional detail can be used to enrich the more rapid methods (downward data enrichment), by backwards-calibration for example.

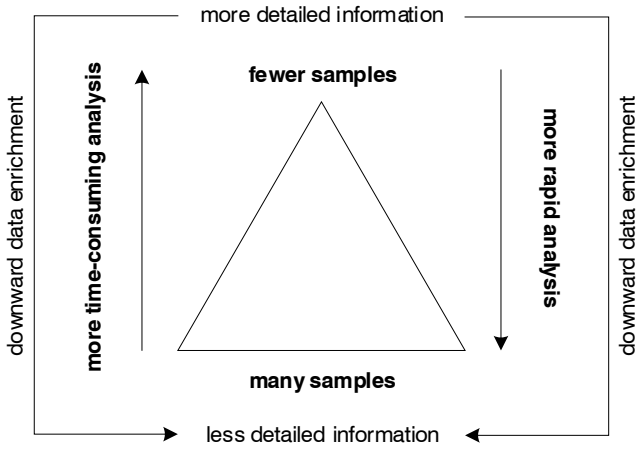

Fig. 1.1 The progression from less-detailed and more rapidly acquired data to more-detailed and less rapidly acquired data that occurs throughout this study.

There are seven chapters in this dissertation. After this first introductory chapter, the following chapter—*Chapter 2*—is a literature review providing a general brief background on global carbon pools and fluxes, more detailed background on lipid chemistry and their reactions, and ending with background knowledge on the properties of the minerals in the soil clay fraction.

Chapter 3 deals with aim (a) and is a screening chapter to investigate which minerals are most reactive toward lipids, and which lipid-derived products form from the reaction between lipids and minerals. In this chapter, attenuated total reflectance—Fourier-transform infrared (ATR-FTIR) spectroscopy and

X-ray diffraction (XRD) analysis are employed to perform an initial screening of the products formed from the reaction as well as the extent of the reaction for each mineral and lipid combination.

Chapter 4 deals with aim (b) by probing further into the identities of the products formed from the lipid-mineral reaction, and thereby inferring a reaction mechanism for the lipid-clay reaction. Techniques employed include ultraviolet-visible (UV-VIS) spectroscopy, electron paramagnetic resonance (EPR) spectroscopy, more XRD analysis, thermogravimetric analysis (TGA), differential scanning colorimetry (DSC), mass spectrometry (MS) and gas-chromatography—mass spectrometry (GC-MS).

Chapter 5 deals with the kinetics (aim (c)) of the most reactive case from chapters 3 and 4, by employing a colour component red, green and blue (RGB) analysis to monitor the lipid-mineral reaction over time. Various factors potentially influencing the reaction rate are investigated, including mineral mass-loading (initial clay-to-lipid ratio), pH of the mineral surface, and temperature. The chapter ends with RGB values being correlated with various measurable parameters about the reaction to investigate whether it reveals any further information about the reaction other than only colour change over time.

Chapter 6 delves into the potential environmental significance of the findings of chapters 3–5, looking at the general implications the findings may hold for lipid humification reactions in soils and influences on other soil reactions.

The dissertation ends off with *Chapter 7*, a chapter detailing the general conclusions and potential future work that has arisen from the questions generated by this study.

Several appendices also provide supplemental material, which includes a discussion on the basics of kinetics—general rate expressions, reaction rate variables and reaction orders (*Appendix A*); XRD and ATR-FTIR data obtained during the characterisation of the clays used in this study (*Appendices B* and *C*, respectively); calibration of the UV-VIS spectrophotometric method employed to quantify Mn^{3+} concentration (*Appendix D*) and the visual results obtained from a baseline/control experiment (*Appendix E*) which investigated the autoxidation of natural oils (olive oil and raw linseed oil), the lipid used in this study (oleic acid) and a related lipid (linoleic acid), under the reaction conditions employed in chapter 3.

CHAPTER 2

Literature Review

2.1 Global carbon pools and fluxes

Carbon is arguably the most important element on planet earth. It is the building block of all living things, including us. In its various chemical forms, it controls numerous processes on earth that are essential for sustaining life and

maintaining ecological balance. This global control is exercised *via* several carbon pools (see Fig. 2.1 below) whose constituents are found disseminated around the planet in a ubiquitous fashion.

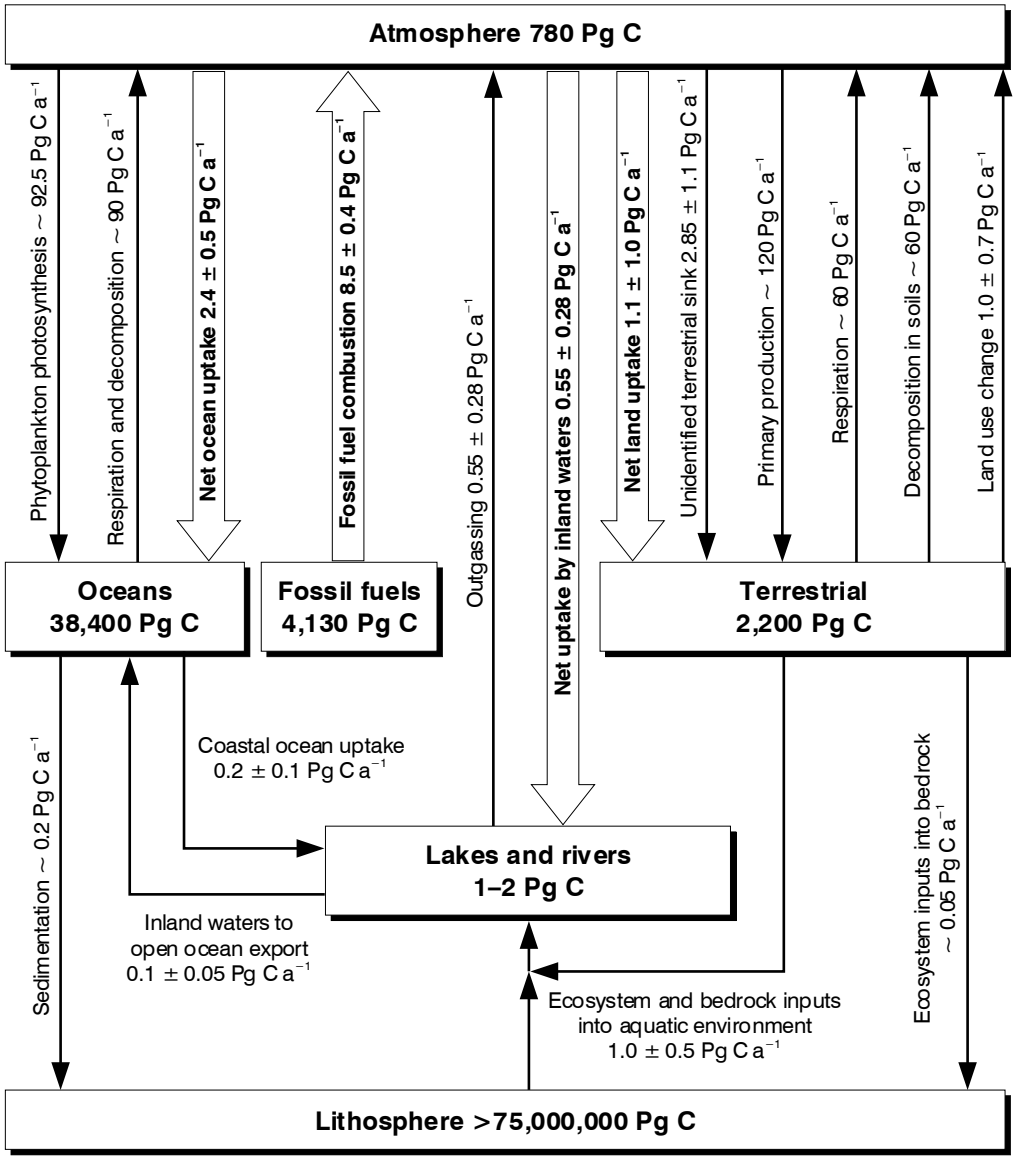

Fig. 2.1 The global carbon pools (boxes) in petagrams carbon (Pg C) as well as the fluxes (arrows) between them in petagrams carbon per annum (Pg C a^{-1}). 1 Pg = 10^{15}g (or one billion metric tonnes). Data from Falkowski *et al.* (2000), Lal (2008), Battin *et al.* (2009), Scholes *et al.* (2009) and Regnier *et al.* (2013).

Upon the senescence of living organisms, the carbon contained within them is transformed into various other forms, including gaseous carbon, soil organic carbon (SOC), dissolved organic carbon (DOC) found in water, and lithified

forms of organic carbon (*e.g.* coal, oil and natural gas), in several processes that can take place over a period ranging from a few hours or days to millions of years. Organic carbon can also be transformed into *inorganic* carbon (*e.g.* carbonates) which can be found in sedimentary rocks, soils and dissolved in water.

In its gaseous forms, carbon is also found in the atmosphere. Here, the most prevailing forms of gaseous carbon such as carbon dioxide (CO_2) and methane (CH_4), together with water vapour, exercise a large effect on the temperature of the earth's surface, by trapping infrared radiation (heat) in the atmosphere. As a result, these gases have often been termed "*greenhouse gases*" and their heating effect the "*greenhouse effect*" (Fourier, 1827).

The nature of these various carbon pools is very dynamic, with constant *fluxes* (inflows and outflows) occurring among the pools. The integration or nexus of these pools and fluxes is what is known as the *carbon cycle*. The sizes and examples of these pools and fluxes, and how they form the carbon cycle, are illustrated in Fig. 2.1.

Pools that capture carbon are known as carbon "*sinks*" whilst those that release carbon are known as "*sources*" (Bullock, 2005). In the global carbon sinks illustrated in Fig. 2.1 (*e.g.* land, ocean, lakes and rivers), carbon is most notably sequestered *via* photosynthetic processes, removing atmospheric carbon dioxide (CO_2) by transforming it, along with water (H_2O) into carbohydrates (CH_2O) and oxygen (O_2) (Catling *et al.*, 2001; Falkowski, 2003; Redfield, 1934; Redfield *et al.*, 1963):

$$CO_2(g) + H_2O(\ell) + \text{light} + \text{chlorophyll } a \rightarrow CH_2O(s) + O_2(g) \tag{2.1a}$$

$$\begin{aligned} 106CO_2(g) + 122H_2O(\ell) + 16NO_3^-(aq) + HPO_4^{2-}(aq) + 18H^+(aq) \\ + \text{light} + \text{chlorophyll } a \rightarrow (CH_2O)_{106}(NH_3)_{16}H_3PO_4(s) \\ + 138O_2(g) \end{aligned} \tag{2.1b}$$

Aerobic respiration is the reverse of the reactions in equations 2.1*a* and *b*, releasing energy, nutrients and CO_2 back into the atmosphere. Anaerobic respiration (without oxygen, *e.g.* "*methanogenesis*") also occurs, transforming CH_2O into CH_4 and CO_2 which is released into the atmosphere (Catling *et al.*, 2001; Jain *et al.*, 2012):

$$2CH_2O(s) \rightarrow CH_4(g) + CO_2(g) \tag{2.2}$$

One of the greatest inputs of carbon into the atmosphere is the anthropogenic burning of fossil fuels, for example the hydrocarbon *iso*-octane which is found in gasoline (Hershey *et al.*, 1936):

$$2C_8H_{18}(\ell) + 25O_2(g) \rightarrow 16CO_2(g) + 18H_2O(\ell) \tag{2.3}$$

In recent decades, the atmospheric carbon pool has received significant attention due to its increasing size and consequent intensifying greenhouse ef-

fect, which leads to increasing earth surface temperatures. The links between increasing atmospheric CO_2 concentrations, increasing temperatures, and possible human influence thereupon, were first noted by scientists such as Svante Arrhenius in 1896 and later Guy Callendar in 1938. Today, there are numerous models that indicate increasing temperatures are a response to increasing emissions of greenhouse gases such as CO_2, even when all of the complexities of the climate system are considered (Anderson *et al.*, 2016).

The atmospheric carbon pool is increasing in size by approximately 4.2 billion metric tonnes of carbon each year (Fig. 2.1). This is offset by net uptakes of carbon, from the atmosphere, by the oceans, inland aquatic environments, and terrestrial ecosystems (plants and soil). Whilst the uptakes by the oceans and inland aquatic ecosystems are fairly well constrained, the uptake by the terrestrial ecosystems, by contrast, is not so well determined (for instance, when comparing the size of the error in each flux). As can be observed from Fig. 2.1, the sizes of the fluxes between the terrestrial pool and the atmospheric pool, are very approximate and not well constrained at all (*i.e.* they are reported with the approximate symbol (∼) preceding them). In many cases, when calculating the carbon budget (which always has to balance completely) using the carbon cycle, the terrestrial uptake is often simply determined by back-calculation, using the net uptake of carbon from the atmosphere (fossil fuel burning minus net atmospheric accumulation) and subtracting the oceanic and inland aquatic uptakes. The balance of the sequestered carbon, should, in theory then, be that amount which the terrestrial pool (including soil) is sequestering. Once the land-use change (such as deforestation) is factored in, the size of this sequestration flux is determined to be about 2.2–2.9 billion tonnes of carbon per year (Lal, 2008; Scholes *et al.*, 2009; Aufdenkampe *et al.*, 2011; Regnier *et al.*, 2013). Given that its constituents are not determined, this flux is simply termed the "*unidentified terrestrial sink*" (Lal, 2008).

Although this simple determination of the size of the terrestrial sink flux is handy, there are several issues which have arisen with such a simplification, chief among which is that this flux appears to be changing all the time (and hence the apparent capacity of the terrestrial ecosystem and soil to sequester carbon), with seemingly each new study conducted on carbon budgeting. The capacity of the terrestrial pool to sequester carbon (and mitigate the increasing size of the atmospheric carbon pool, which directly controls global climate), the changes occurring to this capacity, and the effects of anthropogenic activities on carbon sink capacity, can only be determined and constrained properly if the various carbon fluxes associated with it are constrained more narrowly with smaller error and variability.

The monitoring and accurate determination of the terrestrial pool's capacity to sequester carbon, and the tracking of anthropogenically-induced changes (Scholes *et al.*, 2009) is becoming increasingly important, since, it has been suggested by some studies (*e.g.* Canadell *et al.*, 2007) that the capacity of both the

ocean and terrestrial pool to sequester carbon appears to be steadily decreasing, at a more rapid rate than carbon budgeting models have previously predicted. Upon deeper consideration of this statement, one realises just how important it becomes to understand the dynamics and inner workings of this terrestrial carbon pool, given that most human activity and manipulation of the environment occurs in this carbon pool, even though significant activity does occur in the oceanic pool. What this means is, given the vast size and nature of the oceanic pool, if any atmospheric pool stabilisation and changing of capacity is to be induced in any carbon sink, it would most likely be *via* the terrestrial carbon pool—the one where most of our anthropogenic activity occurs, the one which is rapidly changing in capacity, and the one which is still yet to be fully and accurately determined in terms of its sequestration capacity—and *how* and *why* this capacity is changing.

As mentioned before, to acquire a more accurate picture of the size and dynamics of the carbon flux linked to the terrestrial carbon sink, one must better understand and further determine, define and constrain the inner workings of this sink. An important link that occurs within this carbon sink is the one between living organisms and the soil, especially between plants and soils. Once any living organism ceases to live, its carbon is not lost but transferred and transformed into another form. In this case, when plants die their carbon-rich litter and exudates are transferred onto and into the soil, where it is either (a) completely degraded into gaseous carbon (*e.g.* CO_2), water, nutrients and energy (Montgomery *et al.*, 2000) or (b) partially degraded and the products of decomposition transformed and synthesized into *soil organic matter* (SOM).

2.2 Humic substances

Soil organic matter consists of various forms, typically resulting from the different degrees of decomposition and natural processing which the once-living material (detritus) has undergone, as well as how resistant this detritus is to degradation. Leaf and stem material found in and on top of topsoil for example is material that is no longer living, but still recognisable in terms of its original living form and texture. However, located slightly deeper within the soil (pedologically speaking the "*O*" or *organic* horizon) is another, amorphous, dark brown to black material which also forms part of the soil's organic matter fraction. These dark substances are known as *humic substances* (Kumada, 1965; Aiken *et al.*, 1985; Oades, 1989; Hardie *et al.*, 2007, 2009*a*; Zhang *et al.*, 2015).

Humic substances are organic substances that are derived from the more recognisable plant material through a complex series of chemical reactions known as *humification* (Kumada, 1965). Aiken *et al.* (1985) described humic substances as naturally occurring, biogenic, heterogeneous, yellow to black in colour, having high molecular weight, and being refractory. Oades (1989) classified

humic substances into three different types, namely:

(1) *Humin*—that fraction of humic substances which is completely insoluble in either acid or base (all pH values);

(2) *Humic acid*—that fraction which is soluble in water with pH greater than 2 (soluble in base but not acid); and

(3) *Fulvic acid*—that fraction which is soluble at all pH values (acid and base soluble).

Molecular weights range from a few thousand Da for fulvic acids to several million Da for humin. Fulvic acids are highest in oxygen content, acidity and ion-exchange capacity, whilst humin is lowest in all three these attributes (Oades, 1989).

2.3 Humification

Humification, in very general and rudimentary terms, can be thought of as the browning of organic substances in soils (Kumada, 1965; Hardie *et al.*, 2009*a*; see Fig. 2.2). It is a very complex and poorly understood process, which can include any number of chemical transformations of the original organic detritus. Humification includes processes such as the polymerisation and oxidation of simple biomolecules (*e.g.* sugars, amino acids, polyphenols, lipids) into dark, low and high molecular weight substances, as well as the depolymerisation and chemical lysis of complex biomolecules (*e.g.* lignin) into simpler molecules that can undergo repolymerisation with other biomolecules into dark, low and high molecular weight humic substances (Hardie *et al.*, 2009*a*). The latter case is the most noticeable where recognisable forms of organic detritus are transformed into unrecognisable, amorphous, dark humic substances. The process of humification can be mediated by any number of natural processes, including *biotic* (the action of bacteria, fungi, soil microfauna, and their associated enzymes) and *abiotic* processes (*via* the chemical and often catalytic capacity of soil minerals) (Bollag *et al.*, 1998).

Organic detritus typically contains a large variety of carbon-rich substances that vary in their degree of resistance to degradation and/or humification, and will therefore humify or brown to different degrees, and the humic substances formed will have varying degrees of resistance to degradation themselves. In general, humic substances are *more resistant* to degradation than the substances that they were derived from. Organic material that is relatively easy to degrade and/or humify is known as *labile*, whilst substances which are relatively more difficult to degrade and/or humify are known as *recalcitrant* (Plaster, 2014).

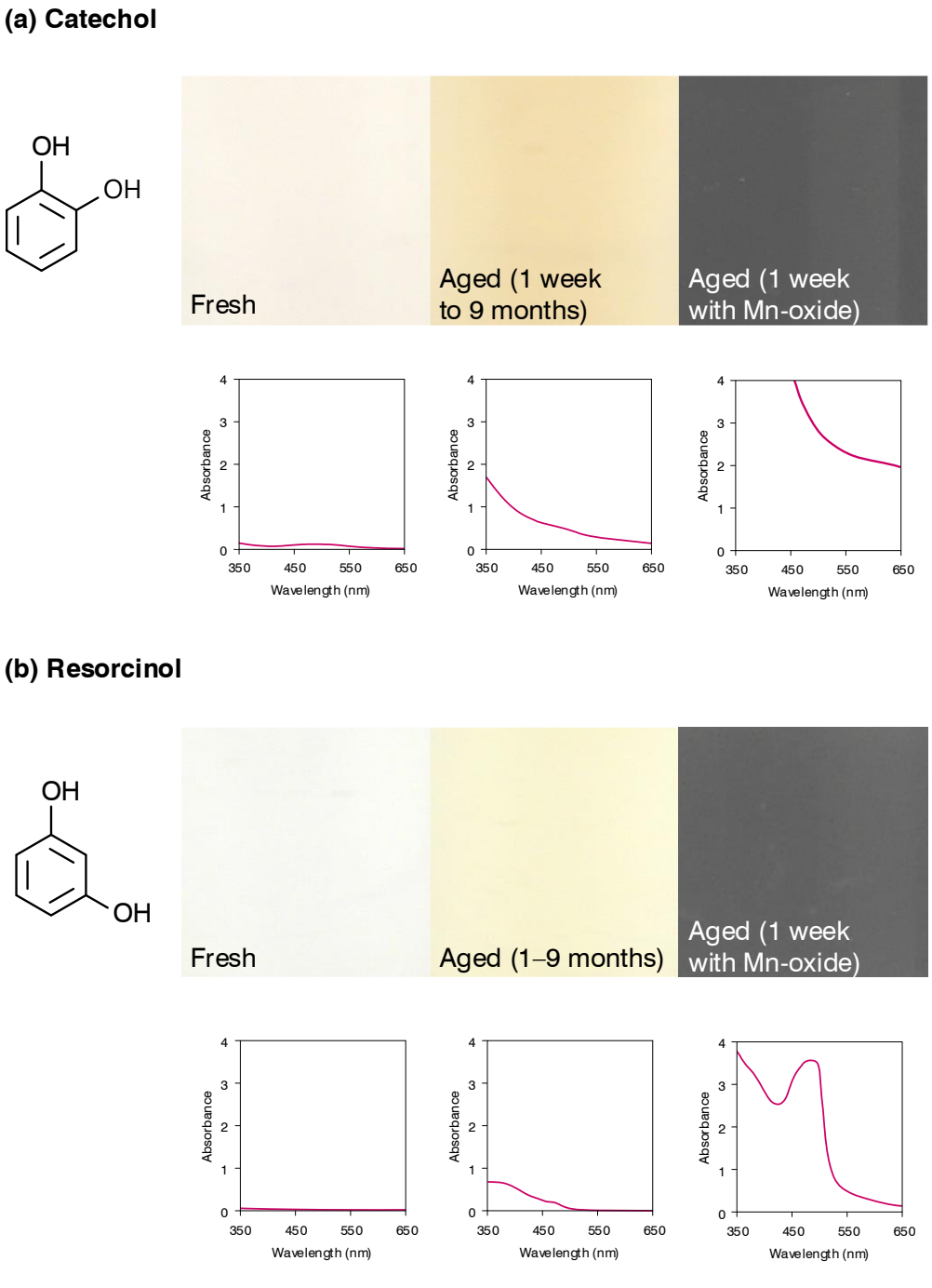

Fig. 2.2 A visual illustration of the humification (or browning/darkening) of polyphenols, namely (a) catechol and (b) resorcinol. Visual spectra are added below each photograph to demonstrate the increasing absorbance of light with increased darkening.

When organic detritus begins to decompose, it can release both labile and recalcitrant compounds into the soil. Examples of labile substances are organic compounds such as sugars, amino acids, starches, proteins, polyphenols, organic acids (Lorenz and Lal, 2010; Plaster, 2014) and relatively easily degradable humic substances.

More recalcitrant substances include lipids, waxes, lignin (Lorenz and Lal, 2010; Thevenot *et al.*, 2010; Plaster, 2014; Datta *et al.*, 2017; Romero-Olivares *et al.*, 2017) and humic substances that are resistant to degradation. In terms of the terrestrial carbon sink, and the fluxes between this sink and the atmosphere, the labile SOM is most reactive and is thus referred to as the *active fraction* (Parton *et al.*, 1987; Zou *et al.*, 2005). The recalcitrant SOM, in contrast, is least reactive and is referred to as the *passive fraction* (Parton *et al.*, 1987). The active fraction usually only remains intact for a few months to a few years (Parton *et al.*, 1987) whereas the passive fraction can remain intact for several centuries or even millennia (Parton *et al.*, 1987; Schmidt *et al.*, 2011).

Historically, there has been an assumption that the chemical structure alone of humic substances determines their intrinsic lability or recalcitrance, and hence their stability, decomposition rates and age in soils (Kleber *et al.*, 2011; Schmidt *et al.*, 2011). Humic substances with lignin-like structures for example do not necessarily make up the most recalcitrant and oldest fraction of SOM, and Schmidt *et al.* (2011) argued that stability is more likely influenced by environmental and biological controls, rather than intrinsic chemical structures. These controls can include numerous factors such as elevated atmospheric CO_2, warming, nitrogen deposition and droughts (Min *et al.*, 2015). This begins to reshape the definition of which humic substances should be considered as part of the active fraction, the fraction which drives the flux of CO_2 between the soil and the atmosphere (Zou *et al.*, 2005).

2.3.1 Mineral-catalysed humification

Whilst humification can often be thought of as a purely biological or biochemical process, several studies (*e.g.* Wang and Li, 1977; Wang *et al.*, 1978; Shindo and Huang, 1982; Wang *et al.*, 1983*a*, 1983*b*; Wang and Huang, 1986, 1987, 1989, 1992, 1994; Fukushima *et al.*, 2009; Hardie *et al.*, 2009*a*, 2009*b*; Hardie *et al.*, 2010) have shown over the years that soil minerals have the capacity to mediate and often catalyse humification reactions. Three major humification pathways are outlined in Fig. 2.3. These are the Maillard reaction, polyphenol pathway and lipid peroxidation pathway.

The French scientist Louis Maillard, after whom the Maillard reaction is named, was the first individual to describe the browning reaction which occurs between reducing sugars and amino acids (Maillard, 1912). The reaction is commonly observed whilst cooking and is the reaction responsible for the browning of various foods and the aromas associated with it. It is often termed *non-enzymatic browning* because it is not catalysed by enzyme activity (Vaclavik and Christian, 2008; Rongsirikul and Hongsprabhas, 2016), but rather by heat (Vaclavik and Christian, 2008; Martins *et al.*, 2000).

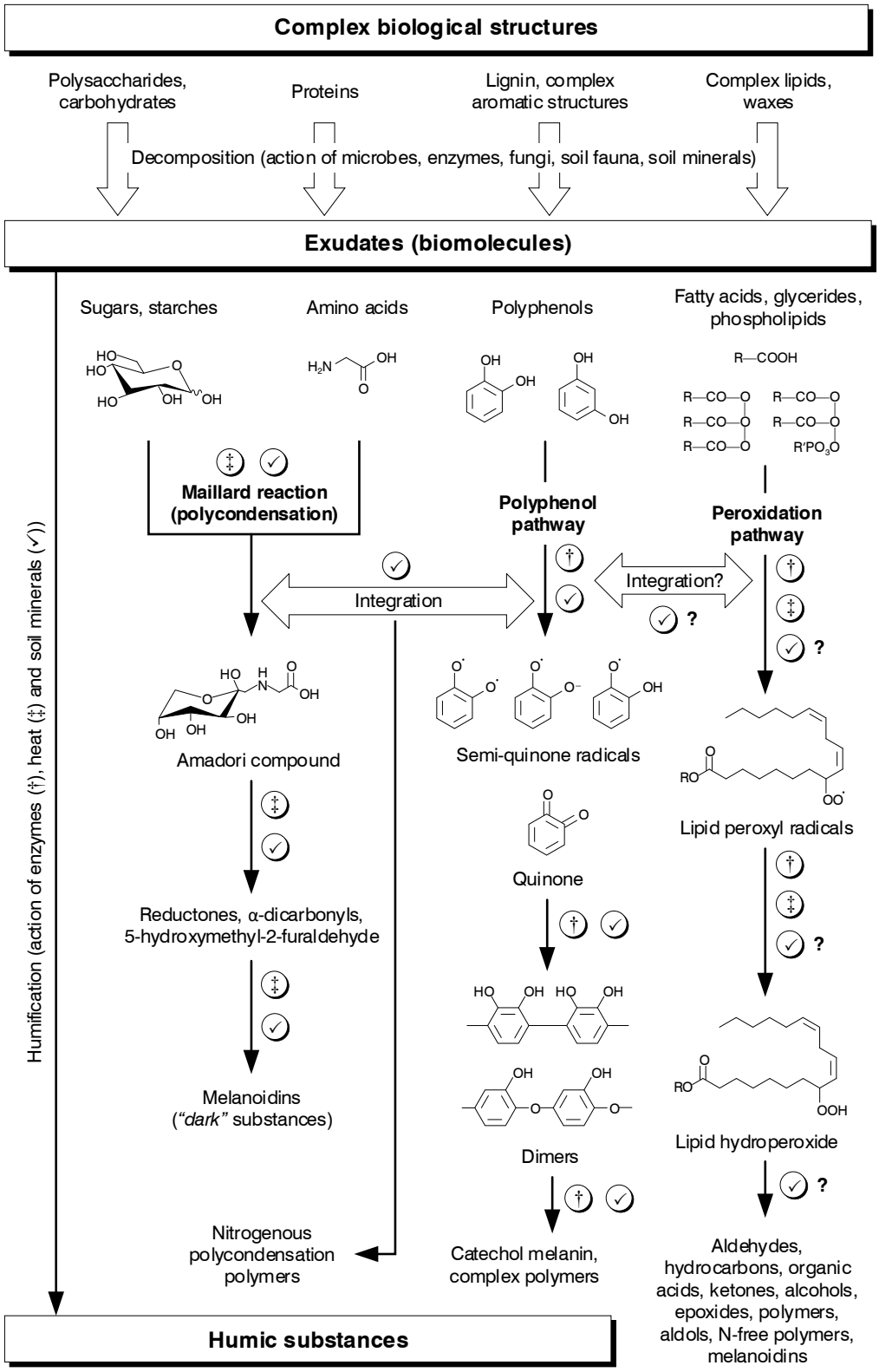

Fig. 2.3 The major pathways of humification, namely the Maillard reaction, polyphenol pathway and lipid peroxidation pathway. Reactions mediated/catalysed by enzymes (†), heat (‡) and soil minerals (✓) are indicated beside the relevant reaction. Question marks (?) indicate the gaps in knowledge that exist. Modified from images and work in Huang and Hardie (2009), Yin *et al.* (2011) and Wu *et al.* (2012).

The Maillard reaction is also catalysed by several soil minerals, such as manganese oxides (*e.g.* birnessite; Jokic *et al.*, 2001*a*, 2001*b*, 2004*a*, 2005), iron oxides (*e.g.* goethite; Gonzalez and Laird, 2004), clay minerals (*e.g.* smectites, nontronite, kaolinite) and quartz (Arfaioli *et al.*, 1997, 1999; Bosetto *et al.*, 2002; Gonzalez and Laird, 2004).

The polyphenol pathway, on the other hand, can be catalysed by the enzymes tyrosinase and peroxidase, to form quinone and semi-quinone radicals (Dubey *et al.*, 1998; Naidja *et al.*, 1998). These then couple and self-propagate into more complex, aromatic polymers. Numerous minerals, however, can also catalyse the polyphenol pathway. These include short-range iron, aluminium and silicon oxides (Scheffer *et al.*, 1959; Wang *et al.*, 1983*a*, 1983*b*; Shindo and Huang, 1984*a*, 1985; Shindo and Higashi, 1986; Wang and Huang, 1989), manganese oxides (Shindo and Huang, 1982, 1984*a*, 1984*b*; Wang and Huang, 1992; Naidja *et al.*, 1998, 1999), and clay minerals (Wang and Li, 1977; Wang *et al.*, 1978; Wang and Huang, 1986, 1989, 1994).

Another important aspect to consider is the complexity of the soil system. The humification pathways do not occur in isolation, but rather occur as integrated pathways (see Fig. 2.3), each synthesizing very complex humic substances with a wide range of chemical compositions, aromaticity and nitrogen content. The integrated pathways between the Maillard reaction (or components of it) and the polyphenol pathway are readily catalysed by soil minerals. Birnessite, for example, catalyses the reaction between Maillard reaction components and polyphenols (Wang and Huang, 1987; Jokic *et al.*, 2004*b*; Hardie *et al.*, 2007, 2010; Zhang *et al.*, 2015), and this pathway has become known as the polyphenol-Maillard pathway (or catechol-Maillard pathway for example when a specific polyphenol is referred to; *e.g.* Hardie *et al.*, 2010; Zhang *et al.*, 2015). As mentioned, specific components of the Maillard reaction (*e.g.* amino acids) can also react and humify with polyphenols. These reactions are also catalysed by soil minerals. Fukushima *et al.* (2009) studied the catalytic effect of a soil rich in the aluminosilicate allophane on the integrated humification reaction between catechol and glycine.

One of the least understood humification pathways (in terms of soil processes and especially mineral catalysis thereupon) is the lipid peroxidation pathway (Fig. 2.3). Whilst the reaction is well-known from a food science and health perspective (see *e.g.* Kanner *et al.*, 1987; St. Angelo *et al.*, 1996; German, 1999; Halliwell, 2000; Waraho *et al.*, 2011; Falade and Oboh, 2015; Johnson and Decker, 2015; Yang and Stockwell, 2016), it is still not fully understood how this reaction occurs in soils, and how the resulting lipid hydroperoxides are incorporated into humic substances.

The lipid peroxidation reaction is a free-radical reaction and can be initiated and further catalysed by the enzymes lipoxygenase and hydroperoxide lyase (Schneider *et al.*, 2008; Repetto *et al.*, 2012), reactive oxygen species (Smith and Murphy, 2008), heat (Litwinienko *et al.*, 2000; Litwinienko and Kasprzyc-

ka-Guttman, 2000; Jaarin and Kamisah, 2012), iron species, in particular Fe^{2+} (Braughler *et al.*, 1986; Minotti and Aust, 1992; Chen and Ahn, 1998; Gogvadze *et al.*, 2003; Sochor *et al.*, 2012), as well as ultraviolet (UV)-radiation (Chatterjee and Agarwal, 1983; Moysan *et al.*, 1993; Chen and Ahn, 1998).

Whether soil minerals can catalyse the lipid peroxidation reaction in soil is still unknown. While some authors such as Vandenbroucke and Largeau (2007), and Wu *et al.* (2012) have hinted at the possibility in reviews, no definitive literature exists to support this possible reaction mechanism. To the best of our knowledge, this study would be the first to investigate whether soil minerals can initiate, mediate or even catalyse the lipid peroxidation reaction.

2.4 Organic matter recalcitrance

Previously (p. 12), the concept of labile *versus* recalcitrant (active *versus* passive) carbon was introduced. In recent years, the general "*inherent molecular structure determines the recalcitrance*" paradigm has been brought into question by several studies such as Kleber *et al.* (2011), Schmidt *et al.* (2011) and Min *et al.* (2015). Some authors such as Lehmann and Kleber (2015) even go so far as to argue that high molecular weight, inherently stable "*humic substances*" as such do not actually exist and are an artefact of alkaline extraction analytical methods for studying SOM. Instead, they propose that SOM is composed of a variety of substances that lie on a continuum of increasing degree to which they have been degraded. This degree of degradation is influenced by a number of factors (*e.g.* biological action of microbes, fungi and plants as well as abiotic action of soil mineral phases). The possibly high variability in SOM stability that may arise from the influence of all these factors is illustrated fairly well in Table 2.1, which lists the residence times of various types of organic substances in soils. Immediately noticeable are the large ranges in residence time (*i.e.* recalcitrance) for some organic substances. The available data on SOM recalcitrance therefore does not lend much support the idea of there existing highly stable humic substances in soils (Lehmann and Kleber, 2015). This point of contention therefore presents the opportunity to investigate further and gather more data—such is the aim of this study—to learn more about the interaction between lipids and soil mineral phases.

Also observed from Table 2.1 is that lipids and lipid-derived humic substances (mostly aliphatic structures) constitute one of the most recalcitrant forms of SOM, with a residence time in soils in the order of several years to centuries (Lorenz and Lal, 2010). They therefore contribute mostly to the passive fraction of soil carbon, the fraction where sequestered carbon is found, and the fraction which is most likely to control the stability of any carbon fluxes between the terrestrial sink and the atmosphere.

Table 2.1 The residence times of various plant residues, organic compounds and biomarkers in the terrestrial ecosystem (After Lorenz and Lal, 2010; reproduced with permission from Springer Nature).

Organic matter / compound	Residence time
Plant residues	
Leaf litter	Months to years
Root litter	Years
Bark	Decades to centuries
Wood	Decades to centuries
Soil organic matter (SOM)	Years to centuries
Available SOM [a]	Years to decades
Stable SOM [b]	Millennia
Black carbon (BC)	Decades to millennia
Organic compounds	
Cellulose	Years to decades
Lignin	Years to decades
Lipids	Decades
Proteins	Decades
Biomarkers	
Lignin-derived phenols	Years to decades
Aliphatic structures	Years to centuries
Carbohydrates	Hours to decades
Proteins	Decades
Phospholipid fatty acids	Decades to centuries
Amino sugars	Years to decades

[a] Active fraction
[b] Passive fraction

In a changing environment, these stabilities could very well change, and it is not entirely trivial as to whether the recalcitrance of a certain type of SOM would increase or decrease, without investigating all the potential factors that may influence its stability in an altered environment. Several types of SOM may shift from the passive to active fraction, and *vice versa*.

2.5 Lipid chemistry

2.5.1 Introduction and nomenclature

There are several classes of lipids that occur in nature. Two specific classes that will be focused on in this study are the *free fatty acids* and their *glycerides*. Free fatty acids (FFAs) are long-chain aliphatic saturated (no double bonds) or mono/poly-unsaturated (one or more double bonds, respectively) molecules with a carboxylic acid functional group at one end. The carbon at this end is designated the first carbon in the molecule, and the first carbon atom immediately following it is known as the α-carbon (alpha-carbon), and the most distant carbon at the other end of the molecule, in the final position, is known as the ω-carbon (omega-carbon) (Litchfield, 1972; O'Keefe, 2002; Lobb and Chow, 2008).

The glycerides of fatty acids are fatty acid esters that are bonded *via* glycerol as the backbone (see Table 2.2 for examples). The glycerides are further split into three categories, namely *mono*glycerides where one fatty acid molecule is bonded to one of the three alcoholic functional groups on glycerol, *di*glycerides where two fatty acid molecules are bonded to two of the three alcoholic functional groups on glycerol, and *tri*glycerides where three fatty acid molecules are bonded to all three of the three alcoholic functional groups on glycerol (Table 2.2). The di- and tri-glycerides are further differentiated on the basis of whether the fatty acid molecules they contain are all identical (*homo*diglycerides and *homo*triglycerides) or different (*hetero*diglycerides and *hetero*triglycerides) (Tang *et al.*, 1978; Komnick, 1988; Wang *et al.*, 2012).

In terms of nomenclature, there exist both common or trivial names as well as systematic names derived from the IUPAC (International Union of Pure and Applied Chemistry) naming system for fatty acids and glycerides (Table 2.2). In this study, the focus is on fatty acids that contain eighteen carbon atoms, but carbon chain lengths can vary anywhere from two (Brown *et al.*, 2003; Le Poul *et al.*, 2003; Nilsson *et al.*, 2003) to over fifty carbon atoms (Qureshi *et al.*, 1984). Litchfield (1972) and the IUPAC-IUB Commission on Biochemical Nomenclature (CBN) (1967) outlined the basic rules for shorthand nomenclature of fatty acids and glycerides. In the case of linoleic acid for example, C18:2 ω-6, the number 18 indicates the total number of carbon atoms in the molecule, the number 2 indicates the number of double bonds in the molecule, and ω-6 indicates the position of the first double bond counted from the final (ω) carbon in the molecule. An alternative notation is also used which replaces the ω term with "*n*", so the notation would read C18:2 *n*-6. As observed, this ω-notation does not provide all the information, as it remains unclear where the second double bond is located along the carbon chain. To deal with this, the shorthand notation has been modified to show where the double bonds occur as well as their stereochemistry.

Table 2.2 Various examples of free fatty acids and glycerides, with references that either discuss or describe them in detail. Nomenclature and molecular weight (MW) data were obtained from either the National Institutes of Health's PubChem database (National Institutes of Health, 2019) or the Royal Society of Chemistry's ChemSpider database (Royal Society of Chemistry, 2019).

C_{18} saturated fatty acid	
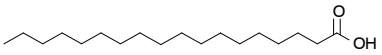	**Stearic acid**, $C_{18}H_{36}O_2$ octadecanoic acid C18:O MW = 284 g mol^{-1} Grande *et al.* (1970)
C_{18} mono-unsaturated fatty acid	
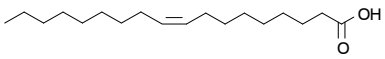	**Oleic acid**, $C_{18}H_{34}O_2$ (9*Z*)-octadec-9-enoic acid C18:1 ω-9, C18:1-9*c* MW = 282 g mol^{-1} Moore and Knauft (1989)
C_{18} poly-unsaturated fatty acids	
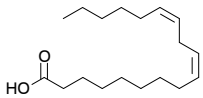	**Linoleic acid**, $C_{18}H_{32}O_2$ (9*Z*,12*Z*)-octadeca-9,12-dienoic acid C18:2 ω-6, C18:2-9*c*, 12*c* MW = 280 g mol^{-1} Wilson (2004)
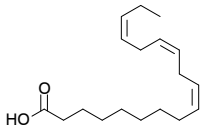	**α-Linolenic acid**, $C_{18}H_{30}O_2$ (9*Z*,12*Z*,15*Z*)-octadeca-9,12,15-trienoic acid C18:3 ω-3, C18:3-9*c*, 12*c*, 15*c* MW = 278 g mol^{-1} Blondeau *et al.* (2015)
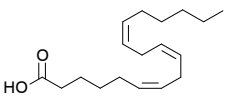	**γ-Linolenic acid**, $C_{18}H_{30}O_2$ (6*Z*,9*Z*,12*Z*)-octadeca-6,9,12-trienoic acid C18:3 ω-6, C18:3-6*c*, 9*c*, 12*c* MW = 278 g mol^{-1} Horrobin (1992)

Table 2.2 *Continued.*

Monoglyceride

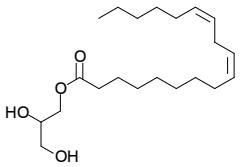

1-Monolinolein, $C_{21}H_{38}O_4$
1-linoleoyl-*rac*-glycerol
2,3-dihydroxypropyl (9*Z*,12*Z*)-octadeca-9,12-dienoate
MW = 354.5 g mol^{-1}
Daubert and Baldwin (1944)

Homodiglyceride (monoacid diglyceride)

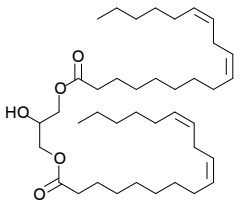

1,3-Dilinolein, $C_{39}H_{68}O_5$
1,3-dilinoleoyl-*rac*-glycerol
[2-hydroxy-3-[(9*Z*,12*Z*)-octadeca-9,12-dienoyl]oxypropyl] (9*Z*,12*Z*)-octadeca-9,12-dienoate
MW = 617 g mol^{-1}
Liu *et al.* (1993)

Heterodiglyceride (diacid diglyceride)

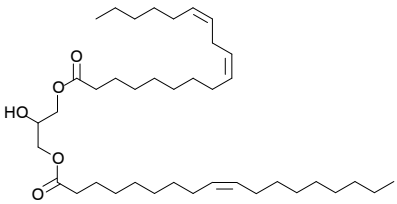

1-Linoleic-3-olein, $C_{39}H_{70}O_5$
1-oleoyl-3-linoleoyl-*rac*-glycerol
[2-hydroxy-3-[(9*Z*,12*Z*)-octadeca-9,12-dienoyl]oxypropyl] (9*Z*)-octadec-9-enoate
MW = 619 g mol^{-1}
Lo *et al.* (2004*a*, 2004*b*)

Homotriglycerides (monoacid triglycerides)

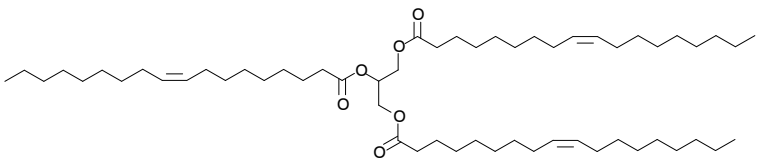

Triolein, $C_{57}H_{104}O_6$
glyceryl trioleate
2,3-*bis*[[(9*Z*)-octadec-9-enoyl]oxy]propyl (9*Z*)-octadec-9-enoate
MW = 885 g mol^{-1}
Ebiura *et al.* (2005)

Table 2.2 *Continued.*

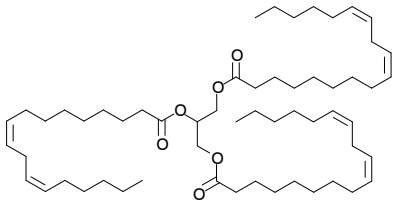	**Trilinolein**, $C_{57}H_{98}O_6$ glyceryl trilinoleate 2,3-*bis*[[(9*Z*,12*Z*)-octadeca-9,12-dienoyl]oxy]propyl (9*Z*,12*Z*)-octadeca-9,12-dienoate MW = 879 g mol^{-1} Koch *et al.* (1958)
Heterotriglyceride (triacid triglyceride)	
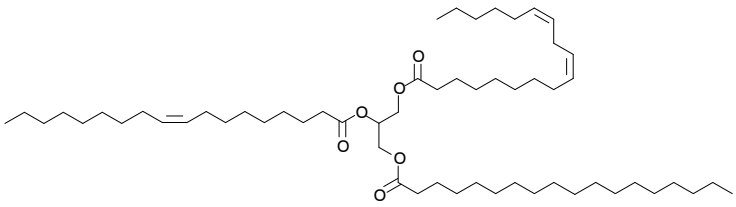	**1-Stearin-2-linolein-3-olein**, $C_{57}H_{104}O_6$ 1-linoleoyl-2-oleoyl-3-stearoyl-*rac*-glycerol 2-[(9*Z*)-9-octadecenoyloxy]-3-(stearoyloxy)propyl (9*Z*,12*Z*)-9,12-octadecadienoate MW = 885 g mol^{-1} Li *et al.* (2014)

Linoleic acid has a *cis*-configuration for both its double bonds, so the shorthand notation becomes C18:2-9*c*, 12*c*. Note that in this case the carbons have also been counted from the other (carboxylic) end of the molecule now, so that the double bond that was in position C6 according to the ω system, is now located at C12, from the carboxylic carbon. The *cis*-configuration is stated by the letter "*c*" after each double bond. Likewise, the *trans*-configuration would be indicated by the letter "*t*". This system has also been partially applied to shorthand notations for the triglycerides (Li *et al.*, 2014), however, without stating any double bond positions or their stereochemistry. For example, 1-stearin-2-linolein-3-olein is simply written as 18:0–18:2–18:1.

The position of substituents on the carbon chain (*e.g.* OH) can also be indicated, as a suffix. For example, the C_{18} fatty acid ricinoleic acid has a hydroxy group situated on the 12th carbon. In its shorthand notation, this is indicated with the suffix "-12OH", so that the shorthand notation reads C18:1 9*c*-12OH (see Table 2.3).

Table 2.3 A summary of the standard abbreviations and shorthand notations used for fatty acids. Modified from Litchfield (1972).

Abbreviation	and name	Shorthand notation	Relevant Reference
A	Azelaic acid	C9:0	Mehmood *et al.* (2008)
HAc	Acetic acid	C2:0	De Jong and Badings (1990)
Ad	Arachidic acid	C20:0	Xu *et al.* (1999)
An	Arachidonic acid	C20:4-5*c*, 8*c*, 11*c*, 14*c*	Zambonin *et al.* (2006)
B	Butyric acid	C4:0	Lima *et al.* (2002)
Be	Behenic acid	C22:0	Xu *et al.* (1999)
D	Decanoic acid	C10:0	Christensen *et al.* (1995)
E	Erucic acid	C22:1-13*c*	Schmidt and Heinz (1993)
El	Elaidic acid	C18:1-9*t*	Gebauer *et al.* (2007)
HFo	Formic acid	C1:0	Reiner *et al.* (1999)
G	Gondoic acid (Eicosenoic acid)	C20:1-11*c*	Jabeen and Chaudhry (2011)
H	Hexanoic acid	C6:0	Lalman and Bagley (2000)
L	Linoleic acid	C18:2-9*c*, 12*c*	Agatha *et al.* (2004)
	Conjugated linoleic acid (CLA)	C18:2-9*c*, 11*t*/ C18:2-10*t*, 12*c*	Banni (2002)
La	Lauric acid	C12:0	Denke and Grundy (1992)
Lg	Lignoceric acid	C24:0	Ramos *et al.* (2009)
Ln	α-Linolenic acid	C18:3-9*c*, 12*c*, 15*c*	de Melo *et al.* (2014)
	γ-Linolenic acid	C18:3 6*c*, 9*c*, 12*c*	Mjøs (2004)
M	Myristic acid	C14:0	Denke and Grundy (1992)
N	Nervonic acid	C24:1-15*c*	Jham *et al.* (2009)
O	Oleic acid	C18:1-9*c*	Lima *et al.* (2002)
Oc	Octanoic acid (Caprylic acid)	C8:0	Jensen *et al.* (1994)
P	Palmitic acid	C16:0	Jham *et al.* (2009)
Pe	Petroselinic acid	C18:1-6*c*	Cahoon and Ohlrogge (1994)
Po	Palmitoleic acid	C16:1-9*c*	Svensson *et al.* (2003)
R	Ricinoleic acid	C18:1-9*c*-12OH *	Andrikopoulos *et al.* (1991)
St	Stearic acid	C18:0	Ramos *et al.* (2009)
V	Vaccenic acid	C18:1-11*t*	AbuGhazaleh and Jenkins (2004)
Ve	Vernolic acid	C18:1-9*c*-12,13-epoxy *	Buisman (1999)

* The additional suffixes refer to substituents situated on the carbon chain (see text for explanation).

Another term also features in the shortened naming conventions for glycerides. In several cases, especially for the heteroglycerides, the second carbon in the glycerol backbone is chiral, so there exist two enantiomers (mirror images) of the same molecule. This is the reason why the abbreviation "*rac*" is inserted into the names of these glycerides, to indicate the term *racemate*—an equal mixture of two enantiomers. If the enantiomeric configuration of the glyceride is known, the additional terms *R* or *S* would be added into its IUPAC systematic name but can be added to trivial names too.

The fatty acids also have standard abbreviations designated to them (Table 2.3). This system also enables another shorthand notation for glycerides to be written (see Table 2.2). The system is once again described in Litchfield (1972) and used by several authors (*e.g.* Martín-Carratalá *et al.*, 1999; Andrikopoulos *et al.*, 2001; Aranda *et al.*, 2004). Using the abbreviation for oleic acid (O), the abbreviation for triolein triglyceride is OOO. For the heterotriglyceride stearin-linolein-olein, the abbreviation is StLO.

To indicate specific positions, the numbers of the carbon atoms in the glycerol backbone are used. The first carbon's oxy group is designated *sn*-1, the second carbon's oxy group *sn*-2, and the third carbon's oxy group *sn*-3. In this way, if the configuration is known for StLO, for example 1-Stearin-2-linolein-3-olein (Table 2.2), then the shorthand notation is *sn*-StLO—the positions 1, 2 and 3 are implicitly stated by writing St, L and O in *that specific order*.

If the fatty acid chain on position *sn*-2 (*e.g.* L) is known, but the order of those on *sn*-1 and *sn*-3 are unknown (*e.g.* either St or O), then the prefix "β" is used, for instance β-StLO. This would be a variable proportion of *sn*-StLO and *sn*-OLSt. If the proportion of both cases are exactly equal, we have two equally proportioned enantiomers, and thus a racemate, so the notation *rac*-StLO is used in this case.

For the diglycerides the position and fatty acid chains are simply linked. For instance, 1,3-dilinolein is written as 1,3-LL (Lo *et al.*, 2004*b*). No shorthand notations for monoglycerides were found in the literature. This is in all likelihood because there would be no difference between the shorthand notation for monoglycerides and the abbreviations for the free fatty acids.

2.5.2 Lipid compositions

In any reaction involving lipids, knowing the original or starting chemical composition of the lipid mixture is crucial, so that any changes can be monitored during the reaction. The lipid composition of olive oil is a good example. The lipid fraction of olive oil is predominantly composed of the triglycerides of oleic acid (*e.g.* OOO, SOO, POO, OLO), with minor amounts of the triglycerides of linoleic acid (*e.g.* LLL, PLL), stearic acid (*e.g.* SSO, SOL), linolenic acid (*e.g.* OLLn, PLLn), arachidic acid (*e.g.* OLA) and palmitic acid (*e.g.* PPP, PPL; Andrikopoulos

et al., 2001; Aranda *et al.*, 2004; Beltrán *et al.*, 2004). In the examples mentioned above, the predominance of oleic acid (O) in most of these triglycerides is notable. Minor quantities of the free fatty acids (mostly oleic acid and linoleic acid) are also present in olive oil. The typical lipid composition of olive oil is summarised in Table 2.4.

Table 2.4 The typical lipid composition of olive oil, given as a percentage of each fatty acid. Note that fatty acids can be bonded either in triglycerides in several configurations or occur freely as individual molecules. Modified from Assy *et al.* (2010), with additional data from Aranda *et al.* (2004) and Beltrán *et al.* (2004).

Fatty acid	Percentage
Total saturated fatty acids	**13.2–15**
Palmitic acid (C16:0)	11–11.9
Stearic acid (C18:0)	2.2–3.1
Total mono-unsaturated fatty acids	**73.3–80.5**
Oleic acid (C18:1 9*c*)	72.5–79.3
Palmitoleic acid (C16:1 9*c*)	0.8–1.2
Total poly-unsaturated fatty acids	**3.3–8.5**
Linoleic acid (C18:2 9*c*, 12*c*) *	3.0–7.9
a-Linolenic acid (C18:3 9*c*, 12*c*, 15*c*)	0.3–0.6

* No information or distinction provided for conjugated linoleic acid (CLA) specifically.

Isomers of linoleic acid. Whilst only one form of oleic acid exists, namely the C18:1 9c isomer (or ω-9 fatty acid), for linoleic acid, there are several isomers that exist. The first one is the ω-6 fatty acid, with its two double bonds both in the *cis*-configuration, the previously discussed C18:2-9*c*, 12*c* isomer. A second isomer has the furthest double bond at position 11 instead of 12, and in the *trans*-configuration, so that the two double bonds are conjugated (see Fig. 2.4). This isomer is consequently known as *conjugated linoleic acid* (CLA) (O'Quinn *et al.*, 2000; Agatha *et al.*, 2004; Raff *et al.*, 2008; see Table 2.3) with the configuration C18:2-9*c*, 11*t* (Agatha *et al.*, 2004). There also exists another isomer of CLA, which has the configuration C18:2-10*t*, 12*c* (Fig. 2.4). In total, there exist 28 isomers of linoleic acid (Banni, 2002).

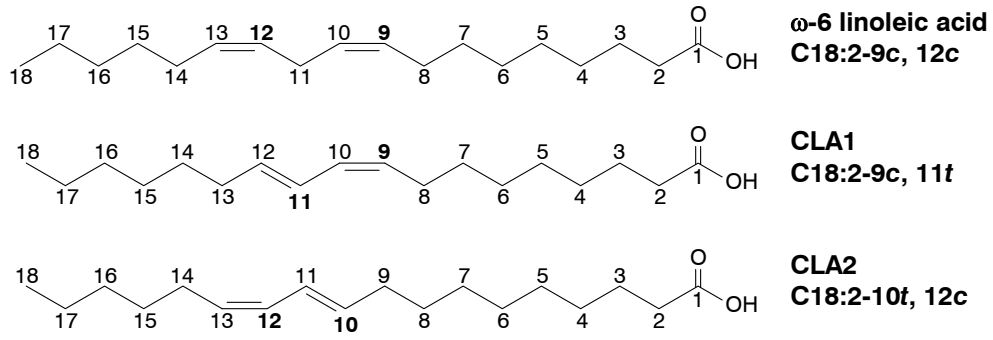

Fig. 2.4 Three of the most important isomers of linoleic acid. CLA = conjugated linoleic acid. Modified from Bhatt (2013).

Isomers of the same molecule can present and behave very differently, both physically and chemically. In the health sciences, the health benefits of consuming CLA have are well-known (Lee *et al.*, 1994; Houseknecht *et al.*, 1998; Basu *et al.*, 2000; Raff *et al.*, 2008), but chemically, the conjugated double bonds in CLA means it is generally less reactive (or more stable) than its non-conjugated counterpart. For example, Allen *et al.* (1949) found that the autoxidation (a reaction of lipids that will be dealt with in the coming sections) of CLA did not occur as rapidly as that of the non-conjugated linoleic acid.

Joo *et al.* (2002) found that increased CLA content in pork loin (attained by adjusting the diet of pigs) inhibited the discolouration (yellowing) of the meat, and they inferred that there was an inhibition of lipid oxidation, compared to control pork loin with greater non-conjugated linoleic acid content.

The implications of these various isomers of linoleic acid would be that it would very likely affect the reactivity of linoleic acid towards soil minerals, just as they affected the reactivity of linoleic acid in the previously mentioned examples. It is very likely that soil minerals would attack linoleic acid at the alkene functional groups most of all, so the added stability of the conjugated double bond in CLA would potentially make it less prone to mineral attack, and therefore lower its reactivity towards soil minerals, compared to the ω-6 isomer of linoleic acid.

Free-radical scavengers and pigments. Natural oils such as olive oil can contain various components outside triglycerides and fatty acids (Fig. 2.5), that are capable of colouring the oil as well as affecting its stability (resistance to oxidation). Typically, olive oil can contain 800–12,000 mg kg^{-1} of squalene ($C_{30}H_{50}$)—an anti-oxidant (Nenadis and Tsimidou, 2002). Squalene is well-known as a free-radical scavenger, especially of singlet oxygen (O_2 ($^1\Delta_g$)) (Kohno *et al.*, 1995; Owen *et al.*, 2000), a key component in lipid peroxidation, as will be discussed later. It does so by undergoing peroxidation itself (Auffray, 2007).

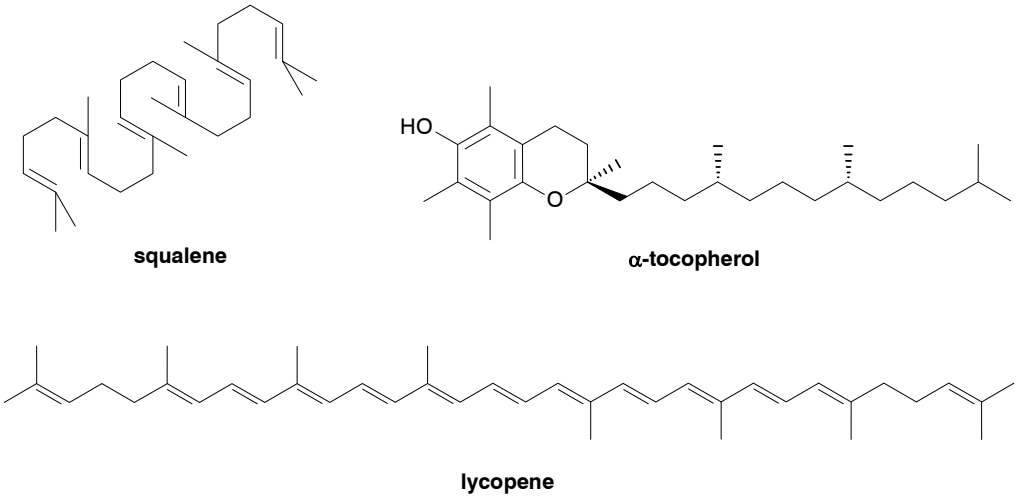

Fig. 2.5 Chemical structures of some of the radical scavengers and pigments typically found in olive oil.

In a manner similar to squalene, polyphenols present in olive oil such as hydroxytyrosol and *p*-tyrosol (Wiseman *et al.*, 1996; Manna *et al.*, 2002) also scavenge free-radicals. Other free-radical scavengers present (in mostly mg kg^{-1} quantities) include tocopherols (Psomiadou and Tsimidou, 1998; Cert *et al.*, 2000; Sagratini *et al.*, 2013), yellow-orange to reddish carotenoid pigments (*e.g.* α-carotene, β-carotene, lycopene/ψψ-carotene, lutein) (Psomiadou and Tsimidou, 1998; Cert *et al.*, 2000; Covas *et al.*, 2006; Sagratini *et al.*, 2013) and green chlorophyll pigments (*e.g.* chlorophyll *a* and pheophytin *a*) (Psomiadou and Tsimidou, 1998; Cert *et al.*, 2000; Covas *et al.*, 2006).

By acting as radical scavengers, these have the capacity to inhibit the peroxidation of lipids (Cabrini *et al.*, 2001; Manna *et al.*, 2002; Psomiadou and Tsimidou, 2002). This has potential implications for the reaction between soil minerals and olive oil as well, by either limiting the reaction and the mineral's potential catalytic effect, or by the mineral sorbing or reacting itself with these compounds in preference to the fatty acids and triglycerides, thereby slowing the lipid-mineral reaction or enhancing it (removal of protective radical scavengers).

2.5.3 Hydrolysis and esterification

Triglyceride hydrolysis / saponification. Triglycerides can undergo hydrolysis under acidic and alkaline conditions to form their constituent free fatty acids (*FFA*) and glycerol. This involves the breaking of their three ester bonds, to form one mole of glycerol and three moles of fatty acid for every mole of triglyceride (*TG*), as per the general equation 2.4:

$$1\,\text{mol}\,TG + H^+/OH^- \rightarrow 3\,\text{mol}\,FFA/\text{soaps} + 1\,\text{mol}\,glycerol \qquad (2.4)$$

An example of triolein (OOO) hydrolysis is shown in Fig. 2.6. Under acidic conditions, the free fatty acids are present in their protonated form, whilst under alkaline conditions (saponification reaction), they are present as carboxyl salts of the cation (soaps) which was present in the base (*e.g.* K^+, Na^+, *etc.*).

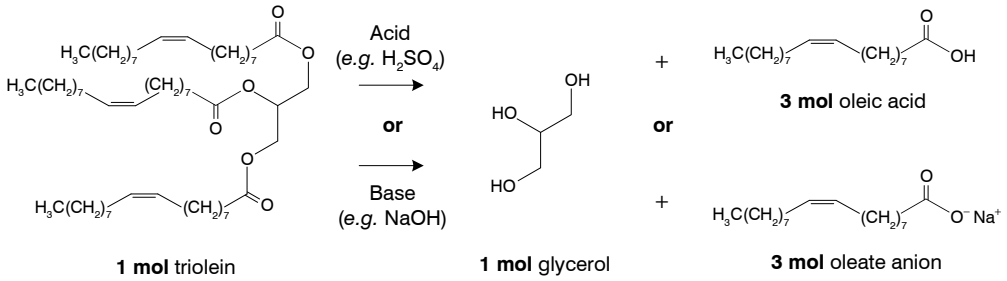

Fig. 2.6 The acid and alkaline hydrolysis of the triglyceride triolein (OOO).

Triglyceride hydrolysis is also catalysed by enzymes, chief among which are hormone sensitive lipases (HSL) and lipoprotein lipases (LPL) (Oscai *et al.*, 1990), found in both humans and animals (Blankenhorn and Ahrens Jr, 1955; Rogalska *et al.*, 1993). The fungus *Rhizopus arrhizus* is able to hydrolyse triglycerides *via* the solid-phase enzyme lipase (Bell *et al.*, 1981), and the skin yeast *Malassezia globosa* has evolved a specific lipase gene (LIP1) to hydrolyse triglycerides (DeAngelis *et al.*, 2007). There are also several species of microbes that produce the lipase enzyme to catalyse triglyceride hydrolysis. These include *Candida antarctica*, as well as several species of *Pseudomonas* and *Geotrichum* (Rogalska *et al.*, 1993). These species are also stereo-selective and can selectively hydrolyse specific positions on the glycerol backbone of the triglyceride molecule (*e.g. sn*1, *sn*2, or *sn*3).

Transesterification and methylation. Triglycerides and free fatty acids can also be transformed into *fatty acid methyl esters* (FAMEs). In this reaction, the free fatty acids (either initially free or derived from glycerides) are reacted with methanol in the presence of a catalyst to form the relevant FAME (see Fig. 2.7). These reactions are important in the production of biodiesel from vegetable oils (Meher *et al.*, 2006; Leung *et al.*, 2010; Abbaszaadeh *et al.*, 2012) and the derivatisation of fatty acids and glycerides for analysis by gas chromatography (GC) (Ichihara *et al.*, 1996; Indarti *et al.*, 2005; Masood *et al.*, 2005). A distinction is made for glycerides and free fatty acids, in terms of what the reaction is called. For glycerides, since they are already esters, the reaction is called *transesterification*, because the ester is being transformed from one ester to a methyl ester. Free fatty acids are not esters, so their reaction can be called *methylation* or simply *esterification*.

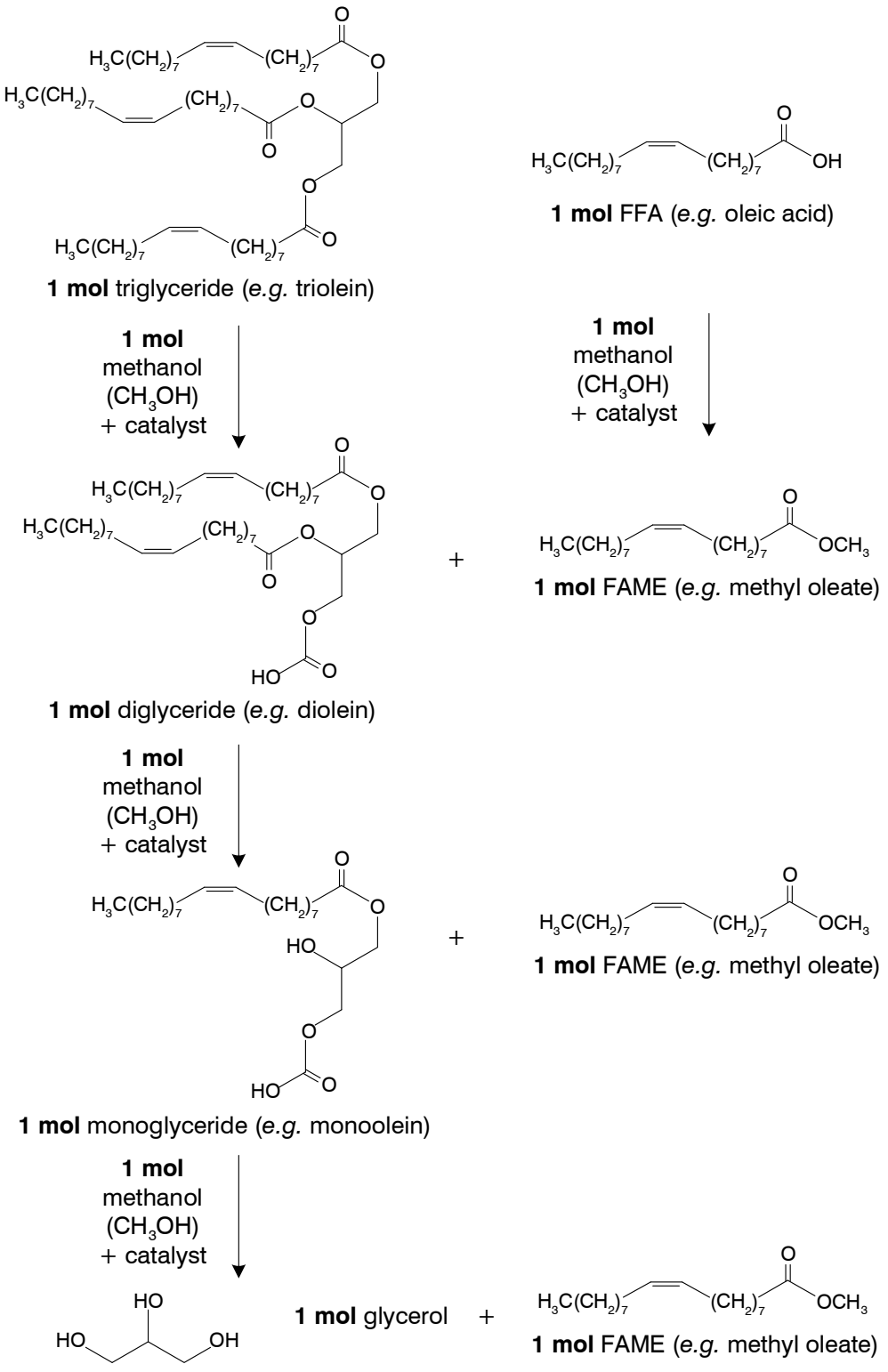

Fig. 2.7 The transesterification/methylation reaction in lipids. FAME = fatty acid methyl ester, FFA = free fatty acid.

The transesterification of triglycerides is a three-step reaction (Fig. 2.7; Meher *et al.*, 2006; Borges and Díaz, 2012), with diglycerides and monoglycerides being the intermediates. The overall reaction (Meher *et al.*, 2006; Lam *et al.*, 2010; Borges and Díaz, 2012) is given in equation 2.5:

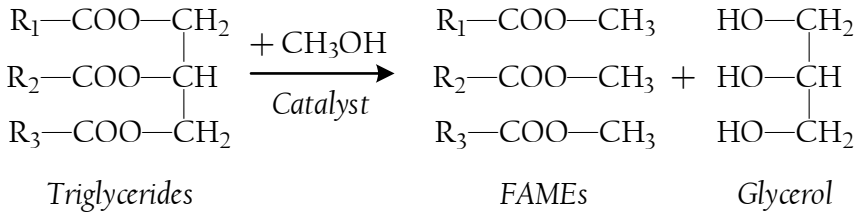

(2.5)

where R_1, R_2 and R_3 represent the fatty acid hydrocarbon chain.

The reaction is catalysed by a vast array of catalysts, which have been detailed in various reviews (Lam *et al.*, 2010; Abbaszaadeh *et al.*, 2012; Borges and Díaz, 2012). Catalysts range from *homogeneous* (where the substance being catalysed, and the catalyst are both in the same phase during the reaction, *e.g.* both liquids) and *heterogeneous* inorganic catalysts (where the substance being catalysed, and the catalyst are both in different phases, *e.g.* liquid being catalysed by a solid catalyst) to enzymes (biological catalysts).

The inorganic catalysts essentially rely on their Lewis or Brønsted-Lowry acid/base capacity to catalyse the reaction. Homogenous inorganic catalysts include several mineral acids such as sulphuric acid (H_2SO_4) and phosphoric acid (H_3PO_4) as well as Lewis acids such as boron trifluoride (BF_3) and ferric sulphate ($Fe_2(SO_4)_3$). The BF_3-methanol gas chromatography (GC)-FAMEs method is recognised by the Association of Official Analytical Chemists (AOAC) as the standard method for the analysis of fatty acids and glycerides by GC (AOAC, 2016). Homogenous bases include strong bases such as sodium hydroxide (NaOH) and potassium hydroxide (KOH). Solid heterogeneous catalysts include acidic catalysts such as zeolites and transition-metal (*e.g.* tungsten (W), titanium (Ti), tin (Sn) and zirconium (Zr)) oxides and silicates, as well as solid heterogeneous alkaline catalysts such as basic metal oxides (*e.g.* calcium oxide (CaO) and magnesium oxide (MgO)).

Biological catalysis is achieved by the lipase enzyme which has been extracted from several species of fungi and yeasts including those of the genera *Candida*, *Penicillium* and *Rhizopus*, and several species of microbes of the genera *Bacillus* and *Pseudomonas* (see Lam *et al.* (2010) and Borges and Díaz (2012) for more details regarding specific species and strains, as well as more details on the aforementioned inorganic catalysts).

Some of the catalysts (*e.g.* BF_3 and H_2SO_4) also require heating at various stages during the transesterification reaction, with reaction temperatures in the range of 80–100°C. This means added heat is part of the catalytic process. Enzyme-catalysed transesterification is considered much milder for this reason, as it proceeds at environmental temperatures at around 40°C. However,

the technology required to perform enzyme catalysis is relatively costly compared to the inorganic catalysts, and during some instances of the reaction, where the methanol to oil ratio may exceed 1:1, the lipase enzyme can be subject to methanol poisoning (Musa, 2016).

Both the hydrolysis and transesterification/methylation reactions have the same basic mechanism. In both cases, a nucleophile attacks the carbon of the carbonyl group to yield esters or carboxyl functional groups. The difference only lies in the nucleophile, which is water in the hydrolysis reaction and methanol in the transesterification/methylation reaction.

2.5.4 Peroxidation (Autoxidation)

The peroxidation of lipids involves the addition of oxygen (O_2) to the hydrocarbon chain in lipids, especially onto the allylic carbons associated with double bonds (*e.g.* carbons 8 and 11 in oleic acid or 8, 11 and 14 in ω-6 linoleic acid). The reaction is also known as the lipid autoxidation reaction and is the main cause of rancidity in oils. The reaction is a free-radical reaction, and follows three main steps (Yin *et al.*, 2011; Zielinski and Pratt, 2017):

Step 1: Initiation—free radicals are generated from initiator molecules (*In*—*In*):

$$In\text{—}In \rightarrow In^{\bullet} + In^{\bullet} \tag{2.6}$$

Common initiator radicals include azo compounds, products of gamma (γ) and UV-radiation, radicals produced by various oxidase, synthase, lipoxygenase and myeloperoxidase enzymes, as well as reactive oxygen and nitrogen species produced by various organisms and free-radical mechanisms. The initiator radical attacks and abstracts a hydrogen atom from a lipid molecule (*L*—H). The hydrogen atom in question is mostly one located on an allylic carbon. Hydrogens in this position are the most weakly bound hydrogens on the molecule, making them the most likely candidates for abstraction (Yin *et al.*, 2011). This leads to the formation of quenched initiator-hydrogen complexes (*In*—H) and lipid radicals ($L^{\bullet}$):

$$In^{\bullet} + L\text{—H} \rightarrow In\text{—H} + L^{\bullet} \tag{2.7}$$

Step 2: Propagation: oxygen addition—in this step, molecular oxygen (O_2) is added to the lipid radical ($L^{\bullet}$) to form a lipid peroxyl radical (*L*—O—$O^{\bullet}$).

$$L^{\bullet} + O_2 \rightarrow L\text{—O—}O^{\bullet} \tag{2.8}$$

The addition occurs on the carbon from where the hydrogen was abstracted. The lipid peroxyl radical (L—O—O$^{\bullet}$) itself now abstracts a hydrogen atom from a second lipid molecule (L—H) to form yet another lipid radical ($L^{\bullet}$):

$$L\text{—O—O}^{\bullet} + L\text{—H} \rightarrow L\text{—O—OH} + L^{\bullet} \tag{2.9}$$

which allows the reaction to loop (equation 2.8) and thus generate a self-propagating chain reaction, hence the term propagation step.

Step 3: Termination—two lipid peroxyl radicals (L—O—O$^{\bullet}$) are also able to couple, forming dimer intermediates [L—OO—OO—L], non-radical products (NRPs) and molecular oxygen (O_2):

$$2(L\text{—O—O}^{\bullet}) \rightarrow [L\text{—OO—OO—}L] \tag{2.10a}$$

$$[L\text{—OO—OO—}L] \rightarrow \text{NRPs} + O_2 \tag{2.10b}$$

The NRPs formed can include a multitude of various oxidised structures. The oxidised lipid can cleave to form various volatile compounds such as aldehydes, ketones and alcohols or polymerise to form complex structures.

Metal cation and hydroperoxide homolysis radical initiation. The oxygen-oxygen bond in hydroperoxide (—O—O—) can undergo several subsequent reactions after its formation, chief among which include its one-electron reduction by a metal cation (M^{n+}) (equation 2.11*a*) and spontaneous homolysis (equation 2.11*b*) to form highly reactive alkoxyl (L—O$^{\bullet}$) and hydroxyl (HO$^{\bullet}$) radicals, as well as hydroxide anions (OH^{-}) (Zielinski and Pratt, 2017):

$$L\text{—O—OH} + M^{n+} \rightarrow L\text{—O}^{\bullet} + M^{(n+1)+} + OH^{-} \tag{2.11a}$$

$$L\text{—O—OH} \rightarrow L\text{—O}^{\bullet} + \text{HO}^{\bullet} \tag{2.11b}$$

A metal cation that is known to reduce lipid hydroperoxide in this manner is ferrous iron (Fe^{2+}) (Driomina *et al.*, 1993; Waraho *et al.*, 2011; Zielinski and Pratt, 2017). The formation of the lipid radical then proceeds in a manner very similar to the reaction depicted in equation 2.7:

$$L\text{—O}^{\bullet} + L\text{—H} \rightarrow L\text{—OH} + L^{\bullet} \tag{2.12a}$$

$$\text{HO}^{\bullet} + L\text{—H} \rightarrow H_2O + L^{\bullet} \tag{2.12b}$$

From here, the propagation step occurs, and the chain reaction proceeds as before.

Reactive oxygen species (ROS). Several reactive oxygen species (ROS) also exist which can react directly with lipids, abstracting a hydrogen atom, and not proceeding *via* the initiation step, rendering the initial formation of lipid radicals ($L^{\bullet}$) redundant. These include radical species such as the superoxide anion ($^{\bullet}O_2^-$) and hydroxyl radicals ($HO^{\bullet}$), as well as a non-radical, but highly reactive, excited state of molecular oxygen known as singlet oxygen (O_2 ($1\Delta_g$)). Oxygen radicals are generated in many biological reactions, an example of which is the autoxidation of linoleic acid catalysed by the xanthine oxidase enzyme (Kellogg III and Fridovich, 1975; Thomas *et al.*, 1978). This enzyme produces both the superoxide anion and hydrogen peroxide (H_2O_2) (Thomas *et al.*, 1978):

$$2\ {}^{\bullet}O_2^- + 2H^+ \rightarrow H_2O_2 + O_2 \tag{2.13}$$

The produced H_2O_2 and the superoxide anion radical then react to form hydroxyl radicals ($HO^{\bullet}$), hydroxide (OH^-) and singlet oxygen (Kellogg III and Fridovich, 1975):

$$^{\bullet}O_2^- + H_2O_2 \rightarrow HO^{\bullet} + OH^- + O_2\ (1\Delta_g) \tag{2.14}$$

However, Thomas *et al.* (1978) noted that kinetically, the reaction in equation 2.14 is much too slow to produce significant quantities of the radical and oxygen products and suggested that it is mediated or catalysed by cations such as Fe^{3+} (also King *et al.* (1975)), biologically chelated with adenosine diphosphate (ADP) for example:

$$^{\bullet}O_2^- + \text{ADP-}Fe^{3+} \rightarrow O_2\ (\text{possibly } 1\Delta_g) + \text{ADP-}Fe^{2+} \tag{2.15}$$

In a manner similar to Fenton-type reactions (Fe^{2+}/H_2O_2), hydroxyl radicals are formed:

$$\text{ADP-}Fe^{2+} + H_2O_2 \rightarrow \text{ADP-}Fe^{3+} + HO^{\bullet} + OH^- \tag{2.16}$$

These radicals can also be generated in true Fenton systems, which means in theory, lipid peroxidation should proceed by advanced oxidation processes (AOPs). The reality is more complex however, with competition for Fe^{2+} (equation 2.11*a*) and the presence of radical scavengers in non-FFA systems such as real olive oil having marked inhibitory effects on the reactivity of pure Fenton reagents (Polyakov *et al.*, 2001).

Superoxide anion radicals can react directly with lipid molecules (L—H) to form lipid hydroperoxides, *via* the following steps:

$$^{\bullet}O_2^- + L\text{—H} \rightarrow L^{\bullet} + {}^{\bullet}OOH \tag{2.17a}$$

$$L^{\bullet} + {}^{\bullet}\mathrm{OOH} \rightarrow L\text{—}\mathrm{OOH} \qquad (2.17b)$$

The reactive lipid hydroperoxides (L—OOH) can also once again react with the superoxide anion radical to form highly reactive alkoxyl radicals (L—O$^{\bullet}$; Thomas *et al.*, 1978):

$$^{\bullet}\mathrm{O}_2^- + L\text{—}\mathrm{OOH} \rightarrow L\text{—}\mathrm{O}^{\bullet} + \mathrm{O}_2 \qquad (2.18)$$

In the reaction with singlet oxygen, the highly reactive O_2 ($1\Delta_g$) molecule itself abstracts the hydrogen situated on the allylic carbon and adds onto this carbon (Frankel, 1980):

$$L\text{—}\mathrm{H} + \mathrm{O}_2\,(1\Delta_g) \rightarrow L\text{—}\mathrm{OOH} \qquad (2.19)$$

Reactive oxygen species can also be generated by reducing metal cations (Frankel, 1980), yielding superoxide anion radicals which, by losing an electron, can form singlet oxygen, or by gaining a proton (H^+), can form hydroperoxyl radicals:

$$M^{n+} + \mathrm{O}_2 \rightarrow M^{(n+1)+} + {}^{\bullet}\mathrm{O}_2^- \begin{cases} -e^- \rightarrow \mathrm{O}_2\,(1\Delta_g) \\ +\mathrm{H}^+ \rightarrow {}^{\bullet}\mathrm{HO}_2^- \end{cases} \qquad (2.20)$$

With the presence of free radicals, and the chemical transformation of the formed lipid hydroperoxides, several subsequent (secondary oxidation) reactions occur which leads to the formation of either more complex and more polymerised reaction products, or cleavage of the hydroperoxides into smaller, more volatile aldehydes, alcohols, other vinylic compounds and hydrocarbons.

Peroxidation mechanism. The mechanism of oxygen addition to lipids is depicted in Fig. 2.8, for oleic acid (one double bond, monounsaturated) and linoleic acid (two double bonds, polyunsaturated). Once the oxygen molecule is added to one of the allylic positions, the double bonds can undergo several rearrangements. In the case of linoleic acid, the two double bonds often rearrange into a conjugated configuration, with the *cis*-9 double bond becoming *trans*-10, or *cis*-12 becoming *trans*-11 (see Fig. 2.4; Yin *et al.*, 2011; and Zielinski and Pratt, 2017). The same happens for oleic acid, its single double bond also moves one carbon position up or down the chain, but the final configuration can be either *cis* or *trans* (see Fig. 2.8).

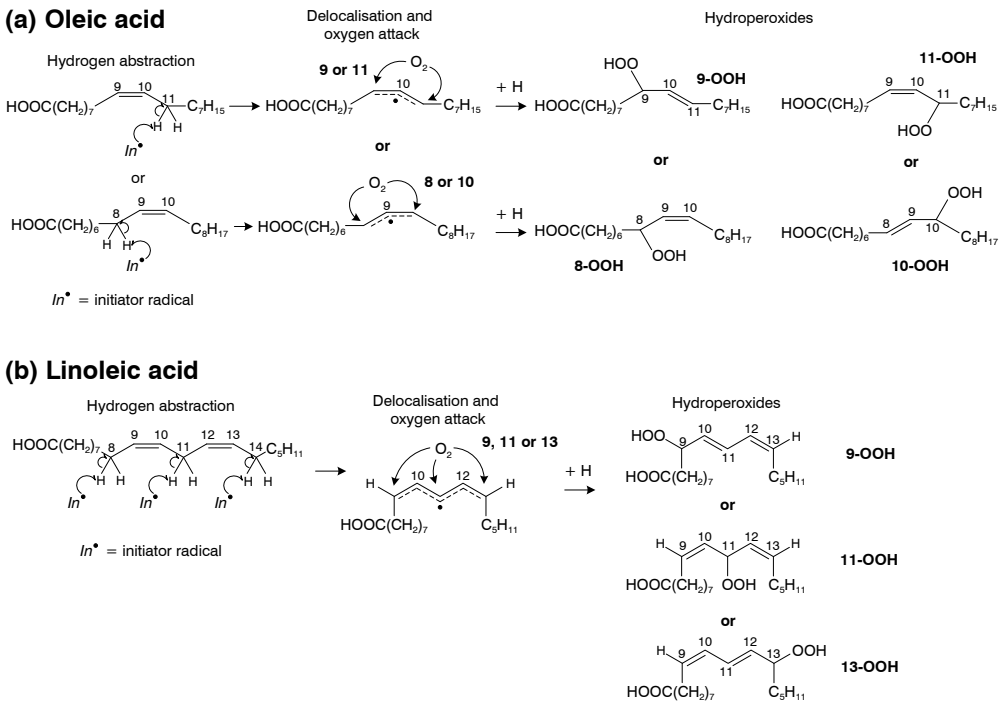

Fig. 2.8 The reaction mechanism of lipid peroxidation, for (a) oleic acid and (b) linoleic acid. Modified from Frankel (1980), Yin *et al.* (2011) and Zielinski and Pratt (2017).

As per equation 2.9, the lipid peroxyl radical abstracts an allylic hydrogen from another lipid molecule, and the chain reaction ensues, with the formation of hydroperoxides. Other stereoisomeric changes are also possible for double bonds not initially involved, sometimes changing from the *cis* to the *trans* configuration.

Secondary oxidation products. With the decay of the lipid hydroperoxides (see equations 2.11*a* and *b*), there are several secondary oxidation products that can form (Frankel, 1980; Schneider *et al.*, 2008; Yin *et al.*, 2011; Zielinski and Pratt, 2017; see Fig. 2.9).

The double bonds in both oleic acid and linoleic acid hydroperoxides can interact with the —O—OH bond to generate an epoxide and hydroxide (Frankel, 1980; Nieva-Echevarría *et al.*, 2017), hemi-acetals (Schneider *et al.*, 2008), furanoids/ring structures and isofurans (Yin *et al.*, 2011; Berdeaux *et al.*, 2012), as well as ketones and alcohols (Berdeaux *et al.*, 2012). The fatty acid chain can also cleave at the double bond, whilst interacting with the hydroperoxide group, to form shorter chain aldehydes (Schneider *et al.*, 2008; Yin *et al.*, 2011; Berdeaux *et al.*, 2012; Zielinski and Pratt, 2017). In biological systems, further reduction reactions and cleavage can form very short chain hydrocarbons (Dumelin and Tappel, 1977). The structures of these secondary oxidation products are depicted in Fig. 2.9.

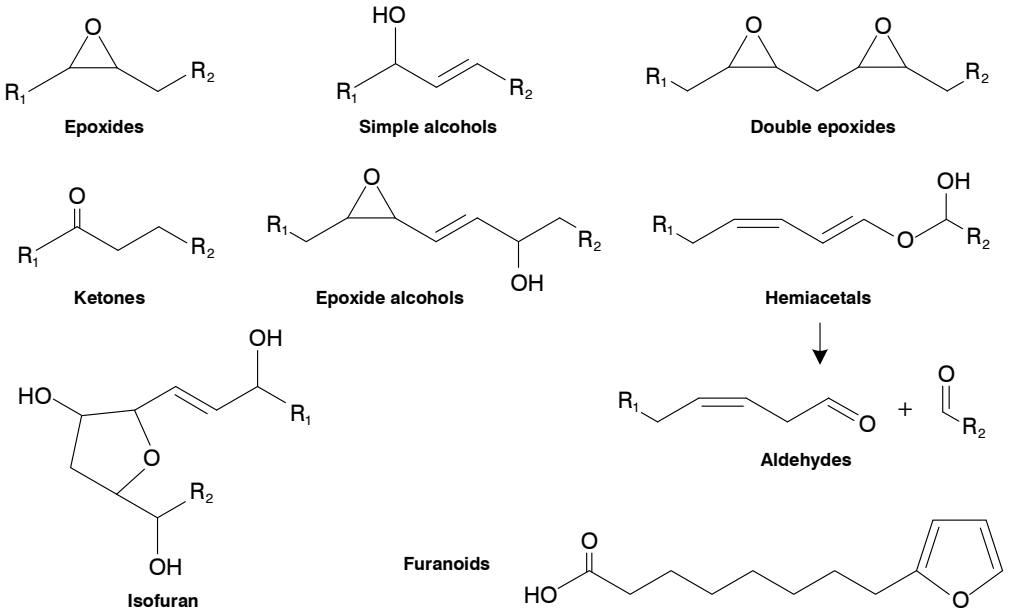

Fig. 2.9 Secondary oxidation products resulting from the further reaction (decay) of lipid hydroperoxides. R_1/R_2 = rest of lipid molecule ($R_1 \neq R_2$).

Polymerisation products. The hydroperoxides and secondary oxidation products, as well as radicals, can couple to form dimers and couple further to form high molecular weight compounds (Gomez *et al.*, 2011; Yin *et al.*, 2011; Omonov *et al.*, 2016; Zielinski and Pratt, 2017). The epoxides and alcohols formed from hydroperoxides (Fig. 2.9) often act as intermediates to polymerisation (Gomez *et al.*, 2011; Omonov *et al.*, 2016). Double alcohols form *via* the addition of water to epoxides, causing the ring structure to cleave (Frankel, 1980):

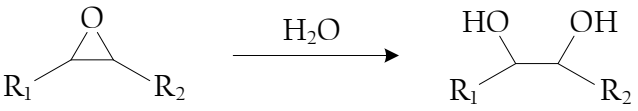

(2.21)

Omonov *et al.* (2016) also demonstrated the formation of polymers through polycondensation reactions, with the formation of ester bonds between alcohols and the carboxylic acid functional groups present on the oxidised and unoxidised free fatty acids. Gomez *et al.* (2011) demonstrated that coupling reactions *via* hydroxyl (alcoholic) functional groups and epoxides among fatty acid chains also occur within and between triglycerides, creating high molecular weight compounds (>2,000 Da). The structures become more and more complex to characterise as coupling continues and molecules grow larger. Some of the typical structures (*e.g.* dimers and polyesters) are shown in Fig. 2.10.

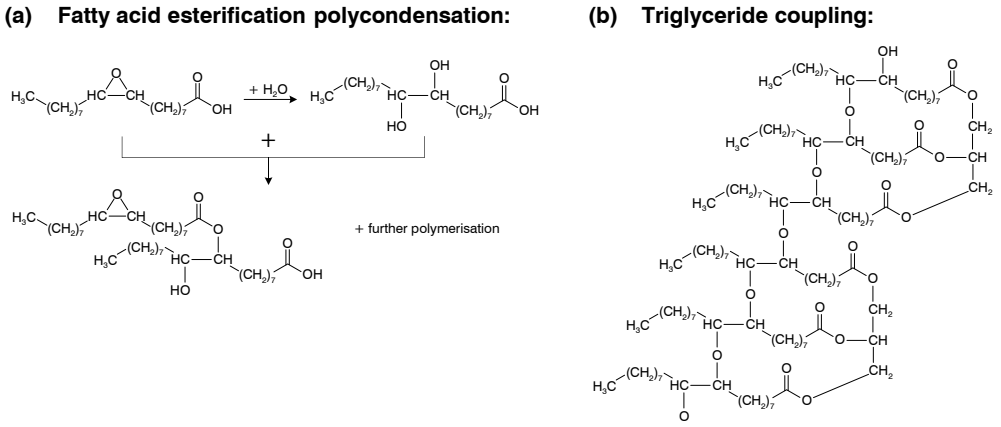

Fig. 2.10 The polymerisation (coupling) of (a) free fatty acid and (b) triglyceride oxidation products. Modified from Gomez *et al.* (2011) and Omonov *et al.* (2016).

2.5.5 Non-peroxidative polymerisation of oleic acid

Non-oxygenous polymerisation products. Free fatty acids and glycerides also undergo polymerisation *via* a non-peroxidative mechanism. In particular, oleic acid is known to form various non-oxygenous, polymerised products that include dimers, trimers, and various ring structures such as cyclobutanes and lactones (see Fig. 2.11 below; den Otter, 1968; Garssen *et al.*, 1972).

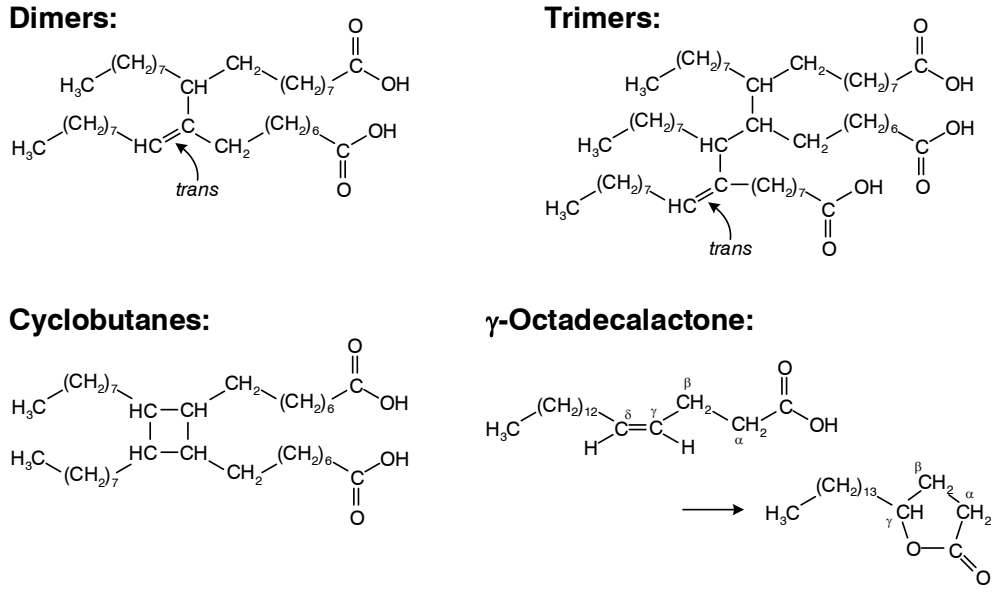

Fig. 2.11 The non-peroxidative (non-oxygenous) polymerised products and ring structures of oleic acid. Modified after den Otter (1968).

The polymerisation products arise specifically due to a lack of oxygen (*e.g.* anaerobic conditions), hence no peroxidation occurs. The reaction can be catalysed directly by heat (*c.* 300°C for *c.* 2 hours; Sen Gupta, 1966; Koley, 1971) or by other means at similar or lower temperatures, including electric discharges (den Otter, 1968), atomic hydrogen (H; den Otter, 1968), hydrogen peroxide (H_2O_2, at 135°C for 48 hours; Cowan, 1962), Lewis acids such as stannic chloride ($SnCl_4$; at 100°C for 10 hours), zinc chloride ($ZnCl_2$), aluminium chloride ($AlCl_3$), antimony chloride ($SbCl_3$) and bismuth chloride ($BiCl_3$; den Otter, 1968) as well as Lewis acid-Brønsted acid pairs such as boron trifluoride (BF_3) with phosphoric acid (H_3PO_4, at 20–100°C) or hydrogen fluoride (HF; Croston *et al.*, 1952). The dimerisation of oleic acid is also catalysed by montmorillonite (smectite) in an inert atmosphere at temperatures between 180 and 300°C for 2–4 hours (den Otter, 1968).

Reaction mechanism. As illustrated in Fig. 2.11, many of the polymerised products possess double bonds in the trans configuration. This alludes to one of the first steps of the reaction mechanism, the re-arrangement of the *cis*- to the more reactive *trans*- geometric isomer (den Otter, 1968):

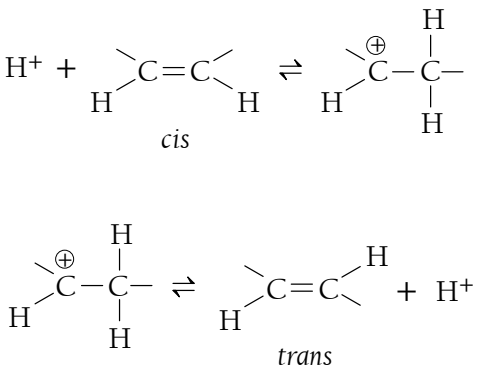

(2.22)

The re-arrangement of geometric isomers is catalysed by acids or acid-activated montmorillonite (den Otter, 1968). It is not well-known how the reaction proceeds from this point, but one possibility would be the abstraction of an H atom from one oleic acid molecule to produce a vinylic carbanion as well as an alkyl carbocation intermediate in the abstracting molecule, with subsequent nucleophilic attack by the carbanion:

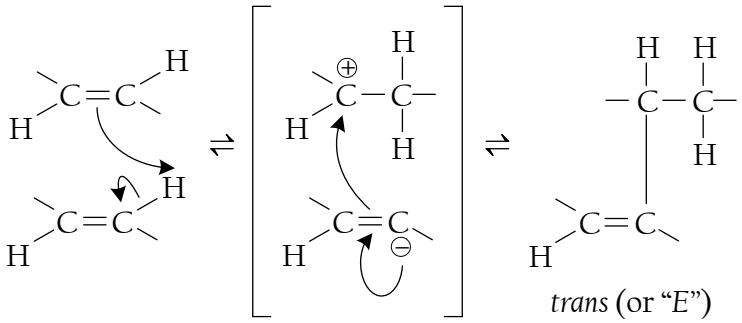

(2.23)

2.5.6 Kinetics of lipid reactions

For the peroxidation reactions, the rate-limiting step is the propagation step (see equation 2.9), particularly hydrogen atom transfer (HAT). The rate of HAT is related to the strength of the allylic C—H bond from which the H atom is abstracted by the peroxyl radical. An increasing degree of undersaturation relates to a weaker C—H bond and a faster HAT reaction rate. For example, the typical rate constants for the propagation step (k_p) for oleic acid are in the order of 0.9 $mol^{-1}\,l^{-1}\,s^{-1}$ whilst those for linoleic acid are greater, at 62 $mol^{-1}\,l^{-1}\,s^{-1}$ (Zielinski and Pratt, 2017). For the initiation step (see equation 2.7), the initiation rate constants (k_i) are usually in the order of 60 $mol^{-1}\,l^{-1}\,s^{-1}$, whilst those for the oxygen addition step (k_{perox}; equation 2.8) and termination step (k_t; equation 2.10*a*) are much greater, with $k_{perox} = 10^9$ $mol^{-1}\,l^{-1}\,s^{-1}$ and $k_t = 10^5$–10^7 $mol^{-1}\,l^{-1}\,s^{-1}$ (Yin *et al.*, 2011).

Rate expressions for the peroxidation reactions are overall not simple zero, first or second order rate laws, and are often fractional (Zielinski and Pratt, 2017), but they are first order with respect to lipid concentration, *i.e.* [*L*—H] (A supplementary, more in-depth discussion regarding rate laws, rate constants, reaction orders and other useful kinetic parameters can be found in Appendix A).

Several studies have reported the activation energy (E_a) of the limiting propagation step during oleic acid peroxidation (*e.g.* Litwinienko and Kasprzycka-Guttman, 2000; Litwinienko, 2001). Values typically range in the order of 88–94 kJ mol^{-1}. In the presence of metal cations (*e.g.* Cu^{2+}, Fe^{2+}, see § 2.5.4), the E_a can be lowered to as low as 63 kJ mol^{-1} (Choe and Min, 2006), thereby catalysing the reaction. For non-peroxidative polymerisation, the E_a for H-atom transfer (HAT; first part of equation 2.23) is slightly higher than the E_a for the HAT during the peroxidation propagation step, with values more in the order of 151 kJ mol^{-1} (den Otter, 1968).

2.6 The properties and chemistry of soil clays

This section aims to shed more light on the minerals of the clay fraction that have been selected for this study—their properties, their chemistry and what is already known about how they interact with organic compounds.

2.6.1 Mineral surface chemistry

At the edges of mineral crystals, one finds the mineral surface. This surface is the (often reactive) interface between the mineral and any phases that are in contact with it. Surface oxygen atoms attract protons (H^+) and the terminal oxygens on a mineral edge or surface is thus often in the form of a hydroxyl

functional group (—OH) rather than an oxygen atom. The hydroxyl functional group can be illustrated in a simple manner as ≡*M*—OH, where *M* represents the central metal cation in the mineral surface structure. In the same manner as Brønsted[2] acids and bases, these hydroxyl functional groups protonate and deprotonate at decreasing and increasing solution pH, respectively, for example when suspended in aqueous solution. Under acidic conditions, the hydroxyl functional group can accept an additional proton to form a protonated hydroxyl group ($\equiv M—OH_2^+$), whilst under basic conditions the hydroxyl functional group can lose a proton to form a deprotonated oxy functional group ($\equiv M—OH^-$).

Water molecules can also interact with the surface central cation (represented as ≡*M*), thereby adsorbing onto the surface. This can be illustrated by equation 2.24:

$$\equiv M + H_2O \rightleftharpoons \equiv M^{\delta+}\ldots{}^{\delta-}OH_2 \tag{2.24}$$

2.6.2 The capacity of clays to influence organic reactions

It is fairly well-known that minerals of the clay fraction can transform a vast array of organic compounds in soils, including pesticides, explosives, polyaromatic hydrocarbons (PAHs), organophosphates and halogenated organics to name a few (McBride, 1994; Huang and Hardie, 2012). More importantly, however, as discussed in § 2.3.1, several clay phases have the capacity to catalyse humification reactions and influence the stability of the humified products.

Several properties act collectively to provide clays with the capacity to influence soil organic reactions. Each individual mineral phase can possess one, several or all of these properties. The oxides of Mn and Fe possess fairly high oxidation-reduction (redox) potential, relative to most other organic and inorganic substances in nature. As a result, they are able to oxidize a vast array of compounds in the environment (Huang and Hardie, 2012). Minerals such as smectite on the other hand possess significant cation exchange capacity (CEC), attracting numerous hydrolysed cations (written in the general form as $[M(H_2O)_p]^{n+}$ where *M* is the cation, *p* is the number of water molecules in its hydration sphere and *n*+ is the charge of the cation). Hydrated, highly electronegative cations can polarize water molecules to the point where one of the O—H bonds is broken (hydrolysis) and in so doing can generate Brønsted acidity. This is especially true for cations such as Al^{3+} and Fe^{3+}. The central cations in mineral edges/surfaces (≡*M*) are also capable of polarizing adsorbed water molecules (refer again to equation 2.24) in the same manner, also generating Brønsted acidity. Increased acidity often initiates mineral-organic reactions (Shin and Cheney, 2005; Huang and Hardie, 2012). In water absent systems,

[2] A Brønsted acid is a substance that releases protons (H^+), whilst a Brønsted base is a substance that accepts protons (H^+).

the electronegativities of the adsorbed and/or central cations cause them to act as Lewis acids, allowing them to accept electron pairs from organic nucleophiles.

Redox potential. The oxides of Mn^{4+}, Mn^{3+} and Fe^{3+} have the capacity to oxidize organic compounds because they possess significantly higher oxidation-reduction (redox) potential (E) relative to many organic molecules. The oxides themselves undergo reduction. The reduction half-reactions for several oxides are provided below (Stone and Morgan, 1984*a*, 1984*b*; Stone, 1987; LaKind and Stone, 1989; Huang and Hardie, 2012):

$$Mn^{3+}O_2H(s) + 3H^+ + e^- \rightarrow Mn^{2+} + 2H_2O, \quad E^\circ = +1.50\,V \qquad (2.25a)$$

$$Mn^{4+}O_2(s) + 4H^+ + 2e^- \rightarrow Mn^{2+} + 2H_2O, \quad E^\circ = +1.23\,V \qquad (2.25b)$$

$$Fe^{3+}O_2H(s) + 3H^+ + e^- \rightarrow Fe^{2+} + 2H_2O, \quad E^\circ = +0.67\,V \qquad (2.25c)$$

$$Fe_2^{3+}O_3(s) + 6H^+ + 2e^- \rightarrow 2Fe^{2+} + 3H_2O, \quad E^\circ = +0.66\,V \qquad (2.25d)$$

where E° is the standard electrode potential relative to the standard hydrogen electrode (SHE; pH = 0, $T = 25°C$, $P_{H_2} = 1$ bar) and e^- is a single electron. The corresponding oxidation half-reaction involves the oxidation of the organic compound in question, transforming it into various oxidation products (sometimes CO_2). The oxidation half-reaction of catechol to quinone is a good example (LaKind and Stone, 1989; Huang and Hardie, 2012):

$$C_6H_4(OH)_2 \rightarrow C_6H_4O_2 + 2H^+ + 2e^-, \quad E^\circ = +0.70\,V \qquad (2.26)$$

Mulyani *et al.* (2014) studied the electrochemical oxidation of oleic acid (the model lipid of this study) to CO_2. Using stoichiometric relationships and their obtained cyclic voltammograms, the following potential oxidation half-reaction can be written for oleic acid:

$$C_{18}H_{34}O_2(\ell) \rightarrow 18CO_2(g) + 34H^+ + 34e^-, \quad E^\circ = +0.41\,V \qquad (2.27)$$

Since the redox potential of $Mn^{4+}O_2$ is greater than that of oleic acid, it is thermodynamically favourable that $Mn^{4+}O_2$ would oxidize oleic acid as it does various other organic compounds.

The presence of Mn^{3+} in the structures of Mn-oxides also affects the redox potential of these minerals. Trivalent Mn has a greater redox potential than $Mn^{4+}O_2$ (Kostka *et al.*, 1995; Yadav *et al.*, 2016):

$$Mn^{3+} + e^- \rightarrow Mn^{2+}, \quad E^\circ = +1.51\,V \qquad (2.28)$$

The release of Mn cations from the Mn-oxide mineral lattice occurs once Mn^{3+} is reduced to Mn^{2+} (Ulrich and Stone, 1989). In this manner, solid Mn-oxides are dissolved (Stone and Morgan, 1984*a*, 1984*b*; Stone, 1987). In a similar manner, solid Fe-oxides are also dissolved reductively, by reducing Fe^{3+} to Fe^{2+} (equations 2.25*c* and *d*; Schwertmann, 1991; Rueda *et al.*, 1992).

Dissolved Mn^{2+} is stable under acidic to neutral conditions, whilst dissolved Mn^{3+} is unstable under the same conditions (Brookins, 1988; Kostka *et al.*, 1995; Klewicki and Morgan, 1998; Topolski, 2011), unless stabilized by complexation with ligands such as pyrophosphate, EDTA,[3] several porphyrins (*e.g.* TPP),[4] polyphenols, di-hydroxy-substituted benzoic acids, dopamine, organic sulphonates and citrate (Dismukes *et al.*, 1987; Kostka *et al.*, 1995; Klewicki and Morgan, 1998; Nico and Zasoski, 2001; Madison *et al.*, 2011; Marafatto *et al.*, 2015; Oldham *et al.*, 2015, 2017). If not complexed by ligands, Mn^{3+} undergoes a disproportionation reaction to form Mn^{2+} and $Mn^{4+}O_2$ (Kostka *et al.*, 1995; Klewicki and Morgan, 1998):

$$2Mn^{3+} + 2H_2O \rightarrow Mn^{2+} + Mn^{4+}O_2(s) + 4H^+, \quad E^\circ = +0.53\ V \tag{2.29}$$

Despite Mn^{3+} being unstable under these conditions however, it is still detected widely in natural environments, and is in fact sometimes the most prevalent species of Mn present (>90%), especially in anoxic to sub-oxic aqueous and marine environments (Trouwborst *et al.*, 2006; Madison *et al.*, 2011, 2013; Oldham *et al.*, 2015) as well as oxygenated environments, where Mn^{3+} is stabilised by humic ligands (Oldham *et al.*, 2017), and waste water treatment works where Mn-oxides are in contact with organic-rich sludges (Johnson *et al.*, 2018).

Similar to Mn^{3+}, Fe^{2+} is unstable under certain conditions—neutral pH and oxidising environments, unless stabilised by a similar array of ligands to those that stabilise Mn^{3+}, such as EDTA and citrate (Schwertmann, 1991; Rueda *et al.*, 1992). If not stabilised, Fe^{2+} readily oxidises to Fe^{3+}-oxides by the reverse of the reactions in equations 2.25*c* and *d*.

Brønsted acidity. Hydrated cations ($[M(H_2O)_p]^{n+}$) sorbed onto mineral surfaces and situated in interlayers polarise water molecules located in their hydration spheres until hydrolysis occurs (modified from McBride, 1994; Laird and Koskinen, 2008; Wu *et al.*, 2012):

$$[M(H_2O)_p]^{n+} \rightleftharpoons [M(OH)(H_2O)_{p-1}]^{(n-1)+} + H^+ \tag{2.30}$$

where M is a hypothetical hydrolysed cation with charge $n+$ and p is the number of water molecules in the hydration sphere. This generates Brønsted acidity, which can protonate acidic and basic functional groups on organic molecules,

[3] EDTA = ethylenediaminetetraacetate
[4] TPP = tetraphenylporphyrin

altering their reactivity, especially toward the mineral surface. The order of cation polarising potential is $K^+ < Na^+ < Ca^{2+} < Mg^{2+} < Al^{3+} < Fe^{3+}$ (Li *et al.*, 1998; Laird and Koskinen, 2008).

Adsorbed water molecules on mineral surfaces (see equation 2.24) can also be polarised in a similar manner, due to the electronegativities of the surface cations (≡*M*):

$$\equiv M^{\delta+} \ldots {}^{\delta-}OH_2 \rightleftharpoons \equiv M(OH) + H^+ \tag{2.31}$$

Increased acidity increases the redox potential of Mn- and Fe-oxide minerals (Brookins, 1988; Skoog *et al.*, 2004; Clarke *et al.*, 2012). This can be demonstrated using the Nernst equation (Skoog *et al.*, 2004) which relates the general redox potential under any conditions (E or pε), to the equilibrium constant (K) and the number of electrons transferred (z) during a redox reaction:

$$E = E^\circ - \frac{RT}{z\mathscr{F}} \ln K \tag{2.32a}$$

$$p\varepsilon = p\varepsilon^\circ + \frac{1}{z} \log K \tag{2.32b}$$

where R is the universal gas constant (8.314 J K^{-1} mol^{-1}), T is the temperature in Kelvin (K) and $\mathscr{F}$ is Faraday's constant (9.648×10^4 C mol^{-1}).[5] The H^+ concentration term is located within the equilibrium constant expression, so mathematical manipulation ($pH = -\log[H^+]$) can be used to show that pε is dependent on pH:

$$p\varepsilon + c_1\, pH = c_2 \tag{2.33}$$

where c_1 and c_2 are simply mathematical constants. Since the sum of pε and pH is constant, an increase in acidity (decrease in pH) therefore leads to an increase in redox potential.

Increased acidity also leads to the protonation of hydroxyl functional groups (≡*M*—OH) on mineral surfaces (Stone and Morgan, 1984*a*; Schwertmann, 1991):

$$\equiv M\text{—}OH + H^+ \rightleftharpoons \equiv M\text{—}OH_2^+ \tag{2.34}$$

The protonated hydroxyl group (—OH_2^+) is more electron withdrawing than the unprotonated hydroxyl group (—OH), meaning the ≡*M*—OH_2^+ bond is easier to break than the ≡*M*—OH bond. This facilitates exchange reactions on the mineral surface, such as inner-sphere sorption reactions and anion ex-

[5] C = Coulomb—a unit of charge (elementary charge/charge on an electron = 1.602×10^{-19} C).

change. This is further enhanced when at lower pH values, the exchanging ligands are likely protonated as well (modified from Shin and Cheney, 2005):

$$\equiv M\text{—}OH_2^+ + Lig.^+\text{—}H \rightleftharpoons \equiv M\text{—}Lig.^+\text{—}H + H_2O \qquad (2.35)$$

where $Lig.^+$—H is a hypothetical protonated ligand. This first sorption step is often crucial for the initiation of several mineral-organic reactions (Stone and Morgan, 1984*a*; Ulrich and Stone, 1989; Shin and Cheney, 2005).

Lewis acidity. In systems where moisture plays no role (*e.g.* dehydrated systems), cations on the surfaces of minerals (edge/surface cations as well as sorbed cations) can also act as Lewis acids—*i.e.* electron pair acceptors (Brown and Rhodes, 1997; Wu *et al.*, 2012). This means cations can accept electrons from nucleophilic organic functional groups (*e.g.* carboxyl, amino, phenol, *etc.*), and is noted as potentially one of the major mechanisms of kerogen cracking into lighter hydrocarbons during the formation of crude oil (Wu *et al.*, 2012).

Lewis acidity is closely related to electronegativity, and for some of the most common cations such as those found in mineral structures and on mineral surfaces, the values are $Mn^{4+} = 1.55$, $Fe^{3+} = 1.83$, $Al^{3+} = 1.61$ and $Si^{4+} = 1.90$ (Huang and Hardie, 2012). There generally exists an inverse relationship between Brønsted acidity and Lewis acidity, as Brønsted acidity becomes, by definition, no longer relevant in systems without water. Lewis acidity generally increases with dehydration (*e.g.* through heating; Brown and Rhodes, 1997), whilst Brønsted acidity decreases, as water molecules are being removed (Wu *et al.*, 2012). However, this rudimentary rule of thumb is complicated slightly during the process of drying. During drying, the polarisation of water molecules increases, as the reaction is driven to the right (McBride, 1994):

$$[M(H_2O)_p]^{n+} \rightleftharpoons [M(OH)_q(H_2O)_{(p-q)}]^{(n-q)+} + qH^+, q \rightarrow p \qquad (2.36a)$$

$$[(\equiv M)_p \ldots (H_2O)_p]^{n+} \rightleftharpoons [(\equiv M)_p(OH)_q(H_2O)_{(p-q)}]^{(n-q)+} + qH^+, q \rightarrow p \qquad (2.36b)$$

where q is the number of hydrolysed water molecules and protons formed, and q approaches p (original number of unhydrolysed water molecules) with increased drying. This generates increased Brønsted acidity (McBride, 1994; Clarke *et al.*, 2011, 2012), which continues to increase as the volume of water decreases (concentration of H^+ increases; Huang and Hardie, 2012). At the same time, Lewis acidity would become more important as well (a dehydrating system), potentially generating extremely acidic and reactive surfaces (Russell *et al.*, 1968; McBride, 1994).

Oxides as terminal electron acceptors. In sub-oxic to anaerobic environments, oxides of Mn and Fe, along with several other chemical species (*e.g.* nitrate (NO_3^-) and sulphate (SO_4^{2-})), can act as electron acceptors instead of oxygen (O_2) during the dissimilatory oxidation of organic compounds by microorganisms. The degradation of BTEX (benzene, toluene, ethylbenzene and xylene) petroleum compounds resulting from subterranean gasoline spills are a good example of this (Roychoudhury and Merrett, 2006). In this manner, oxide minerals assist biological reactions. However, this topic will not be discussed further as it falls outside the scope of this current study.

2.6.3 Potential lipid-mineral surface interactions

Free fatty acids such as oleic acid all terminate with the carboxylic acid moiety (Table 2.2). These functional groups, in both protonated (carboxylic acid) and deprotonated form (carboxylate anion) can interact with the hydroxyl functional groups on mineral surfaces, often bonding directly to the central cation through an exchange reaction (modified from Wu *et al.* (2012) and Johnson *et al.* (2015)):

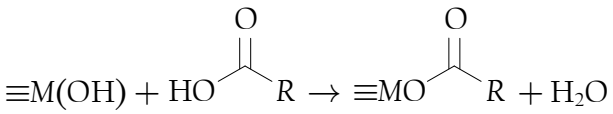

$$\equiv M(OH) + HO\text{–}C(=O)\text{–}R \rightarrow \equiv MO\text{–}C(=O)\text{–}R + H_2O \qquad (2.37a)$$

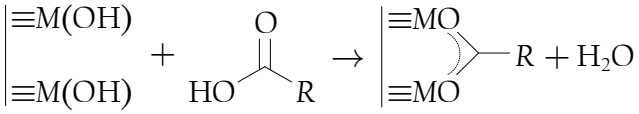

$$\left|\begin{matrix}\equiv M(OH)\\ \equiv M(OH)\end{matrix}\right. + HO\text{–}C(=O)\text{–}R \rightarrow \left|\begin{matrix}\equiv MO\\ \equiv MO\end{matrix}\right\rangle\!\!-R + H_2O \qquad (2.37b)$$

where *R* is the aliphatic chain attached to the carboxyl group and $|\equiv M(OH)$ is one of two surface hydroxyl groups involved in the exchange reaction. Note that the protonated form of the carboxylic acid is shown here. Under more alkaline conditions, one would expect this group to be deprotonated (carboxylate anion form, $RCOO^-$) as well as the surface hydroxyl group ($|\equiv MO^-$). The exchange reaction, however, remains the same. The mineral hydroxyl group can also act as a Brønsted base, removing a proton from the carboxylic acid group, which is then followed by the exchange reaction (adapted from Yariv (2002*a*) and (2002*b*)):

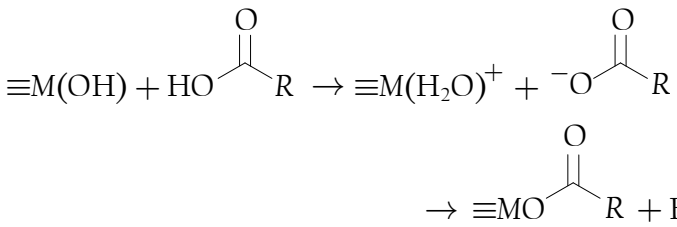

$$\equiv M(OH) + HO\text{–}C(=O)\text{–}R \rightarrow \equiv M(H_2O)^+ + {}^-O\text{–}C(=O)\text{–}R$$
$$\rightarrow \equiv MO\text{–}C(=O)\text{–}R + H_2O \qquad (2.38a)$$

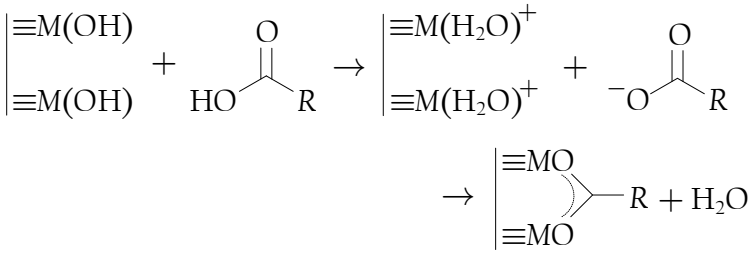

(2.38*b*)

These bonds to the mineral surface *via* the central cation create a "*bridge*" *via* which electron transfer reactions can occur if redox-active cations such as Mn^{4+}, Mn^{3+} and Fe^{3+} are involved (Ulrich and Stone, 1989; Shin and Cheney, 2005). Stone (1987) and Ulrich and Stone (1989) described the steps during which electron transfer from Mn^{3+} in the oxide lattice to chlorophenols (represented by ArOH) occurs *via* the bridging bond:

Step 1—surface complex formation:

$$\equiv Mn^{3+}(OH) + ArOH \rightleftharpoons \equiv Mn^{3+}\text{—}OAr + H_2O \qquad (2.39a)$$

Step 2—electron transfer:

$$\equiv Mn^{3+}\text{—}OAr \rightleftharpoons (\equiv Mn^{2+}, {}^{\bullet}OAr) \qquad (2.39b)$$

Step 3—release of phenoxy radical:

$$(\equiv Mn^{2+}, {}^{\bullet}OAr) + H_2O \rightleftharpoons \equiv Mn^{2+}\text{—}OH_2 + {}^{\bullet}OAr \qquad (2.39c)$$

Step 4—release of reduced Mn:

$$\equiv Mn^{2+}\text{—}OH_2 \rightleftharpoons Mn^{2+} + \equiv\square \qquad (2.39d)$$

where $\equiv\square$ represents a free (vacant) underlying site in the Mn-oxide lattice. At the same time, the Mn-oxide mineral is dissolved. It is still not clear whether the fatty acids transfer electrons in this manner, but it is a possibility (Wu *et al.*, 2012).

2.7 Summary

The lipids found in natural oils are found in two major forms—free fatty acids (FFAs) and triglycerides. Both may undergo a multitude of reactions that can be classed into three groups. The first group of reactions include the hydrolysis (de-esterification) of triglycerides into glycerol and their constituent fatty

acids. Both triglycerides and FFAs can also undergo methylation, in the form of methyl-transesterification for the triglycerides and methyl-esterification for the FFAs. These reactions are catalysed by acids or bases (homogenous catalysts) and solid catalysts (heterogeneous catalysts) with acidic and basic functions (*e.g.* Lewis acidity) such as alkaline metal oxides, silicates and oxides of the transition metals. Biologically, they are also catalysed by the lipase enzymes, produced by various species of fungi and other microorganisms. The second group of reactions include the peroxidation of lipids *via* the lipid-peroxidation radical reaction mechanism, to form a vast array of hydroperoxides which undergo further reactions to form secondary oxidation products. The secondary oxidation products consist of both smaller molecules that result from the cleaving of the lipid hydroperoxide (*e.g.* aldehydes, ketones, alcohols, epoxides, furanoids) and larger molecules that result from the polymerisation or coupling of the oxidized products of lipid peroxidation. Lipid peroxidation consists of three main steps, namely (1) initiation, (2) propagation and (3) termination. The reactions within these steps are driven by reactive oxygen species (ROS), most notably the peroxyl free radicals. These ROS are generated in various ways, namely *via* the activity of the enzymes oxidase, synthase, lipoxygenase and myeloperoxidase, as well as the inherent reactivity of singlet oxygen and electron transfer reactions between oxygen and metal cations. This latter part is especially important as it opens the possibility that soil minerals could drive or catalyse the lipid peroxidation mechanism, given the array of metal cations contained within their structures. The third group of reactions lipids undergo involves non-peroxidative polymerisation, catalysed mostly by heat, acids and montmorillonite clay, to form dimers, trimers and ring structures that lack oxygen relative to peroxidative polymerisation products. This reaction involves isomeric rearrangement and an H-atom transfer (HAT) step.

Despite it being currently unknown whether soil clays oxidize, transform or even humify lipids, their known properties render them very likely candidates for such reactions. Their chemical composition, mineral structures and surfaces contribute to their properties such as CEC, redox potential and Brønsted as well as Lewis acidity, which provide them with the capacity to be very reactive towards organics such as lipids.

CHAPTER 3

Lipid-clay interactions: screening mineral reactivity and products formed

3.1 Introduction

This chapter focuses on the first aim of this study, which is to identify the products formed by interactions between lipids and minerals of the soil clay fraction.

The lipid that was chosen for this chapter is the free fatty acid (FFA) *oleic acid*, the chemical structure of which is depicted in Fig. 3.1 on the next page.

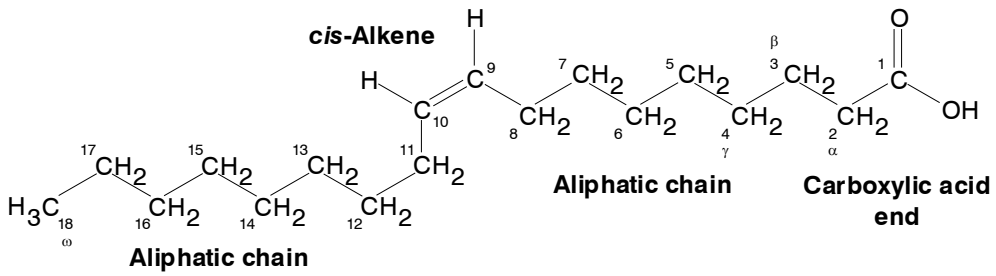

Fig. 3.1 The chemical structure of the oleic acid molecule, showing carboxylic acid functional group and *cis*-configuration double bond.

Oleic acid was selected because it shows the lowest degree of autoxidation in air, compared to linoleic acid and natural oils (see Fig. E.1 in Appendix E). This renders oleic acid most applicable for this model study, as any significant changes would most likely be from the influence of the mineral phases, and not autoxidation that would have occurred regardless of the presence or absence of mineral phases.

Oleic acid was reacted with discrete, end-member, synthetic versions of typical minerals found in the soil clay fraction. These included two Mn-oxides, namely birnessite (δ-$K^{+}(Mn^{3+}, Mn^{4+}, \square)_7O_{14}{\cdot}2.8H_2O$; where $\square$ represents a vacant octahedral cation site) and pyrolusite (β-$Mn^{4+}O_2$), the Fe-oxide goethite (α-$Fe^{3+}O_2H$), the Al-oxide gibbsite (α-$Al^{3+}(OH)_3$), and the Si-oxide quartz (α-$Si^{4+}O_2$). Two natural clay minerals were also selected as mineral phases, including the non-swelling 1:1 clay mineral kaolinite, and a series of swelling 2:1 montmorillonites—one in its natural state, and three with their interlayers saturated with Al^{3+}, Fe^{3+} and Ca^{2+}.

This chapter has a very broad purpose. It can be considered a broad-spectrum "*treatment*" of oleic acid with various soil clays, in order to screen which mineral phases are most reactive toward this model lipid, given equal (but not necessarily optimum) experimental conditions. Along that line, two simple, rapid and cost-effective methods were employed to analyse the products formed from the lipid-clay reactions, namely visual inspection of the darkening reaction and attenuated total reflectance—Fourier transform infrared (ATR-FTIR) spectroscopy. After the initial visual cues that a reaction is occurring *via* the observation of a distinct colour change (refer again to Fig. 2.2 and § 2.3), the disappearance of original chemical bonds, the forming of new bonds, and new interactions between existing bonds, is effectively studied using the FTIR technique. As some of the materials investigated were potentially highly oxidative and acidic, a diamond ATR-FTIR spectroscopy system was selected for this study. Studying the bonds formed from the reaction, and altered during the reaction, provides information relating to the structure of the new molecules

formed, as well as the associations it may or may not form with the mineral surfaces.

It was decided to undertake a model study in order to eliminate the complexities of trying to study a natural system. Instead of looking at a vast array of possible reactions that could be taking place between minerals and lipids in true natural systems, it was decided that isolating the specific case of the reaction between soil clays and oleic acid would be far more beneficial and advantageous than studying a highly variable natural scenario and giving it the "*black box*" treatment (Johnson *et al.*, 2015).

3.2 Materials and methods

3.2.1 Materials

All chemicals were purchased from Sigma-Aldrich® (St. Louis, MO, USA) at the highest purities available (≥99%), except oleic acid, which was technical grade quality (90% pure). All chemicals were used without further purification.

Synthetic versions of minerals typical to the soil clay fraction were used in order to eliminate any potential variability that may be introduced resulting from the inhomogeneities and complexities typically found in mineral phases sampled from real soils.

Birnessite and pyrolusite were selected as model Mn-oxides, given their prevalence in soils (Taylor *et al.*, 1964; McKenzie, 1971). These two Mn-oxides also represent two very different internal crystalline structures, with birnessite being a typically layered "*phyllomanganate*" (Lanson *et al.*, 2000; Lopano *et al.*, 2009; Subramanian *et al.*, 2014; Ivanets *et al.*, 2017) and pyrolusite, a TiO_2-like structured "*tectomanganate*" (Post, 1999; Manceau *et al.*, 2012). Birnessite was synthesized by the method detailed in McKenzie (1971) in which 2 moles of hydrochloric acid (*e.g.* 165 ml of 37% HCl) is added dropwise to 2.5 l of boiling 0.4 M potassium permanganate ($KMnO_4$). The brown suspension was washed with ultrapure deionised water (resistivity of 18.2 MΩ·cm and total organic carbon (TOC) <5 ppb)[6] from a Millipore MilliQ® ultrapure type 1 water dispenser (Millipore Corporation (now Merck), Burlington, MA, USA) by repeatedly centrifuging the mixture at 10,000 rpm (10,621 × *g*)[7] and then re-suspending in deionized water. Once the suspension no longer settled due to centrifugation, the mixture was then placed into cellulose dialysis tubing and dialysed with deionised water for approximately 1 week by regularly changing the water. The water decanted was continuously tested for the presence of Cl^- ions using 1 M $AgNO_3$. Once the formation of the white AgCl precipitate was no

[6] ppb = parts per billion, in this case $\mu g\, l^{-1}$.
[7] *g* = G-force ($g_n = 9.81\ m\ s^{-2}$)

longer observed, the solid was removed from the dialysis tubing, and the water removed using a vacuum filter and 0.1 μm Whatman® Nylon® filter membrane (Whatman® plc, Maidstone, UK). The solid was dried by vacuum freeze-drying. First, it was frozen overnight at −77°C (NuAire GlacierTM NU-9668E −86°C Ultralow Freezer). The frozen solid was then freeze-dried under vacuum for 24 h (VirTis SP Scientific, BenchTop Pro with OmnitronicsTM) at −86.2°C and 19–20 mTorr (0.13 Pa). The dry solid was ground into a homogeneous powder using a quartz pestle-in-a-mortar and a sample was analysed with powder XRD analysis. Broad peaks were obtained that correspond to poorly crystalline birnessite (Potter and Rossman, 1979; Golden *et al.*, 1986; Hudson Institute of Mineralogy, 2018*a*). The relevant *d*-spacings were 7.08 Å, 3.55 Å, 2.47 Å, 2.33 Å and 1.43 Å (see Appendix B, Fig. B.1*a*). The identity of the solid was further confirmed as birnessite with FTIR spectroscopy (Potter and Rossman, 1979; McBride, 1989; Li *et al.*, 2007; Gao *et al.*, 2008; Zhao *et al.*, 2012; see Appendix C, Fig. C.1*a*). Commercial pyrolusite was purchased and confirmed by XRD analysis. The mineral phase was found to be highly crystalline with sharp peaks occurring at the relevant *d*-spacings, namely 3.11 Å, 2.41 Å, 2.11 Å, 1.62 Å, 1.31 Å and 1.30 Å (Hudson Institute of Mineralogy, 2018*b*; Appendix B, Fig. B.1*b*). The FTIR spectrum of pyrolusite is given in Appendix C, Fig. C.1*b*, and corresponds with spectral features mentioned in Potter and Rossman (1979).

The commonly occurring Fe-oxide goethite (Schwertmann, 1991; Rueda *et al.*, 1992; Cornell and Schwertmann, 1996) was synthesized according to the method outlined in Schwertmann and Cornell (2000), where 5 M KOH is added to a solution of $Fe(NO_3)_3{\cdot}9H_2O$ to form 2-line ferrihydrite, which upon aging for one week at 70°C, produces goethite. The yellow-brown solid was washed with deionized water and freeze-dried in a procedure similar to that for birnessite. The presence of residual salts was tested for by performing the diphenylamine test for nitrate (Grotz, 1973). Analysis by XRD confirmed the identity of goethite, with relevant *d*-spacings at 4.18 Å, 2.69 Å and 2.45 Å (Hudson Institute of Mineralogy, 2018*c*; Appendix B, Fig. B.1*c*). The FTIR spectrum of the synthesized goethite corresponds with those of studies such as Prasad *et al.* (2006) and Namduri and Nasrazadani (2008), and is depicted in Fig. C.1*c*, Appendix C.

The Al-oxide gibbsite was synthesized by the method in Rosenqvist and Casey (2004) which involved the titration of 1 l of a 1 M $AlCl_3$ solution with 4 M NaOH until a pH of 4.6 was reached. Thereafter the mixture was heated at 40°C overnight and then centrifuged (10,621 × *g*) with methanol (CH_3OH). The solid was dialysed for 4 weeks at 50°C. Si-dioxide (quartz) was purchased. The identities of the oxides were confirmed by XRD analysis (Appendix B, Figs B.1*d* and *e*) with relevant *d*-spacings of 4.85 Å, 4.38 Å and 4.33 Å for gibbsite (Hudson Institute of Mineralogy, 2018*d*) and 4.26 Å, 3.34 Å and 1.82 Å for quartz (Hudson Institute of Mineralogy, 2018*e*). The FTIR spectra of gibbsite

and quartz (Figs C.1*d* and *e*; Appendix C) correspond to those in the studies of Schroeder (2002) and Palayangoda and Nguyen (2012), respectively.

The clay minerals kaolinite (KGa-1b from Washington County, Georgia) and montmorillonite (STx-1b from Gonzales County, Texas) were purchased from the Clay Minerals Society. The respective XRD analyses (Appendix B, Figs B.1*f* and *g*) show the relevant *d*-spacings for this kaolinite are 7.17 Å, 4.37 Å, 3.58 Å, 1.62 Å and 1.59 Å (Hudson Institute of Mineralogy, 2018*f*) whilst those for this montmorillonite are 15.0 Å, 5.01 Å, 4.50 Å, 3.02 Å and 1.50 Å (Hudson Institute of Mineralogy, 2018*g*). The FTIR spectra of these clay minerals are depicted in Figs C.1*f* and *g*, Appendix C and correspond with those in studies such as Madejová and Komadel (2001), Schroeder (2002) and Madejová (2003).

Ion-saturated smectites were generated by washing 20 g of STx-1b montmorillonite with 1 N solutions of $AlCl_3$, $FeCl_3$ and $CaCl_2$ to produce Al^{3+}-, Fe^{3+}- and Ca^{2+}-saturated smectite (Russell *et al.*, 1968). Washing was performed in the same suspension-centrifugation manner as washing with deionized water during the oxide syntheses. Once saturation was reached, excess salts were once again washed off with deionized water and tested for the presence of Cl^- using 1 M $AgNO_3$.

The mineral phases used in this study were further characterised by determination of their Brunauer-Emmett-Teller (BET) surface areas (5-point nitrogen (N_2)-adsorption isotherm method) and bulk pH in solution (according to the ISO 10390:2005 method, 1:5 solid to water volume ratio) and the results are provided in Table 3.1. A more detailed description of analytical methods and instruments used are provided in § 3.2.3.

3.2.2 Experimental procedure

Experiments were conducted using 100 ml glass vials previously soaked in 5% nitric acid (HNO_3) and washed in acetone, after which they were baked at 110°C and finally rinsed with ultrapure deionized water to remove all organics. To eliminate any possible interference from biological reactions, 2 mg of thimerosal ($C_9H_9HgNaO_2S$) was added to each vial (Hardie *et al.*, 2007). In previous studies (*e.g.* Wang *et al.*, 1983*b*), thimerosal was found not to interfere with any of the mineral-organic reactions being studied.

To each vial, 1.00 g of the solid mineral phase (clay) was added (with no further adjustments to pH or any other properties), followed by 10.0 g of oleic acid. The solid lying at the bottom of the vial was gently mixed with the oleic acid, but in a manner so as to not suspend it in the liquid but only coat the solid phase in its entirety. The mixtures were not disturbed again for as long as the reaction took place. The vials were incubated for 6 months (180 days) at 25°C in the dark. A control vial was also set up in which 10.0 g of oleic acid with no mineral phase added was allowed to react under the same conditions.

Table 3.1 BET surface area and bulk pH characterisation of the mineral phases used in this study.

Mineral phase	Determined BET surface area ($m^2\ g^{-1}$)	BET surface area literature values ($m^2\ g^{-1}$)	Bulk pH (ISO 10390:2005)
Birnessite	52.72 ± 0.65	32 [a]	7.23
Pyrolusite	4.35 ± 0.02	3 [a]	6.15
Goethite	55.58 ± 0.34	20 [b]	10.37
Gibbsite	292.43 ± 2.95 †	11.2 [c], 19.6 [d], 120 [e]	3.74
Quartz	5.88 ± 0.01	2.50 [f]	2.60
Kaolinite (KGa-1b)	10.1 ‡	16.1 [g]	4.75
Montmorillonite (STx-1b)	83.8 ‡	82.9 [g]	8.39
Al^{3+}-saturated	–	–	4.69
Fe^{3+}-saturated	–	–	3.40
Ca^{2+}-saturated	–	–	8.00

a. McKenzie (1971)
b. Schwertmann and Cornell (2000)
c. Redden *et al.* (1998)
d. Rosenqvist and Casey (2004)
e. Langmuir (1997)
f. European Commission Joint Research Centre (2018)—BCR-172 Quartz reference material
g. Sanders *et al.* (2010)
† Possible dehydration and transformation to boehmite (γ-AlO_2H) during analysis (Zhu *et al.*, 2010) with BET surface area in the order of 264 $m^2\ g^{-1}$ (Alex *et al.*, 2013), or due to poor crystallinity (see diffractogram in Appendix B, Fig. B.1*d*).
‡ Pre-determined by the Clay Minerals Society.

The vials were removed after the incubation period and then photographed against a uniform white sheet as background using an artificial, fixed indoor light source (a regular neon light in a room with no windows). Thereafter, the product formed in each vial was analysed by ATR-FTIR spectroscopy.

The reactions were conducted without adding water for practical reasons. Although it is more representative of true soils for water to be involved in the reaction, in this case, when mixing water along with the mineral phases and oleic acid, the hydrophobic oleic acid phase forms a heterogeneous matrix of droplets within the aqueous phase. Some droplets reach the mineral phase whilst many coalesce and float above it, but with mineral phase incorporated or in contact with them. The different mineral phases also disperse differently

in water. When considering all these aspects, adding water adds too much complexity and removes a lot of practical control and uniformity/inter-comparability.

3.2.3 Analytical methods

X-ray diffraction (XRD) analysis was performed using the powder-XRD technique, on a Bruker multi-purpose D8 powder diffractometer. Diffractograms were collected using an X-ray beam from a Cu-Kα source at a wavelength of 1.54 Å and a 2θ-range of 0–90°.

For ATR-FTIR analysis, approximately 5–10 mg of the product formed in each vial was sampled using a small stainless-steel spatula in a part of the vial where a mixture of both the liquid (*quasi*-solid) phase and mineral phase could be sampled simultaneously. The sample was placed on a *c.* 2 × 2 mm diamond ATR crystal that formed part of a Bruker Alpha Platinum-ATR system. Acquisition was performed in the range 4000–400 cm^{-1} using 16 co-added scans at a resolution of 4 cm^{-1} and processing was performed using Bruker OPUS software version 7.5.18.

Brunauer-Emmett-Teller (BET) surface area analysis was performed using a 5-point N_2-adsorption-desorption isotherm, on a Micromeritics® system. Volatiles were removed from the Mn-oxide surfaces prior to analysis by heating (≤100°C) and placing the powders under vacuum. The analysis bath temperature was 77 K and thermal correction was employed. Processing was performed using 3Flex software, version 4.00.

Determination of pH was performed using a Metrohm® glass electrode and a Metrohm® pH lab 744 system as interface (Metrohm®, Herisau, Switzerland). The electrode was calibrated before each session using pH 4 and pH 7 buffers.

3.3 Results and discussion

3.3.1 Visual inspection

After the six-month incubation period, the vials were removed and inspected. The vials showed a large variation in the degree of colour change and darkening for the various mineral phases (Fig. 3.2). Except for quartz, all the mineral phases showed a greater degree of darkening and colour change relative to the control. As was the case for the control, the most prevalent colour change for most of the mineral phases appeared to be a yellowing.

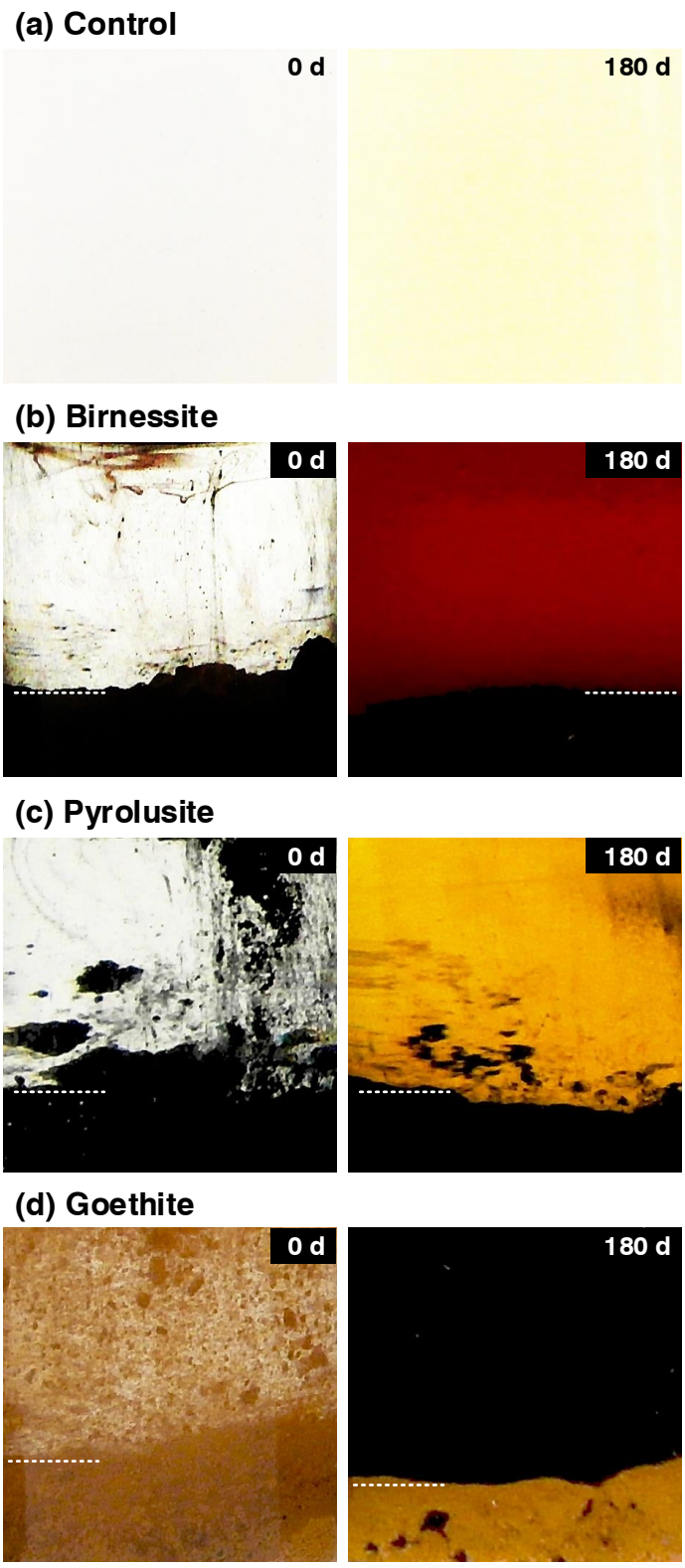

Fig. 3.2 Visual changes to (a and l) oleic acid control and (b–k) oleic acid treatment with clays after 6 months incubation at 25°C in the dark. Dashed lines (----) indicate mineral-liquid interface (mineral below).

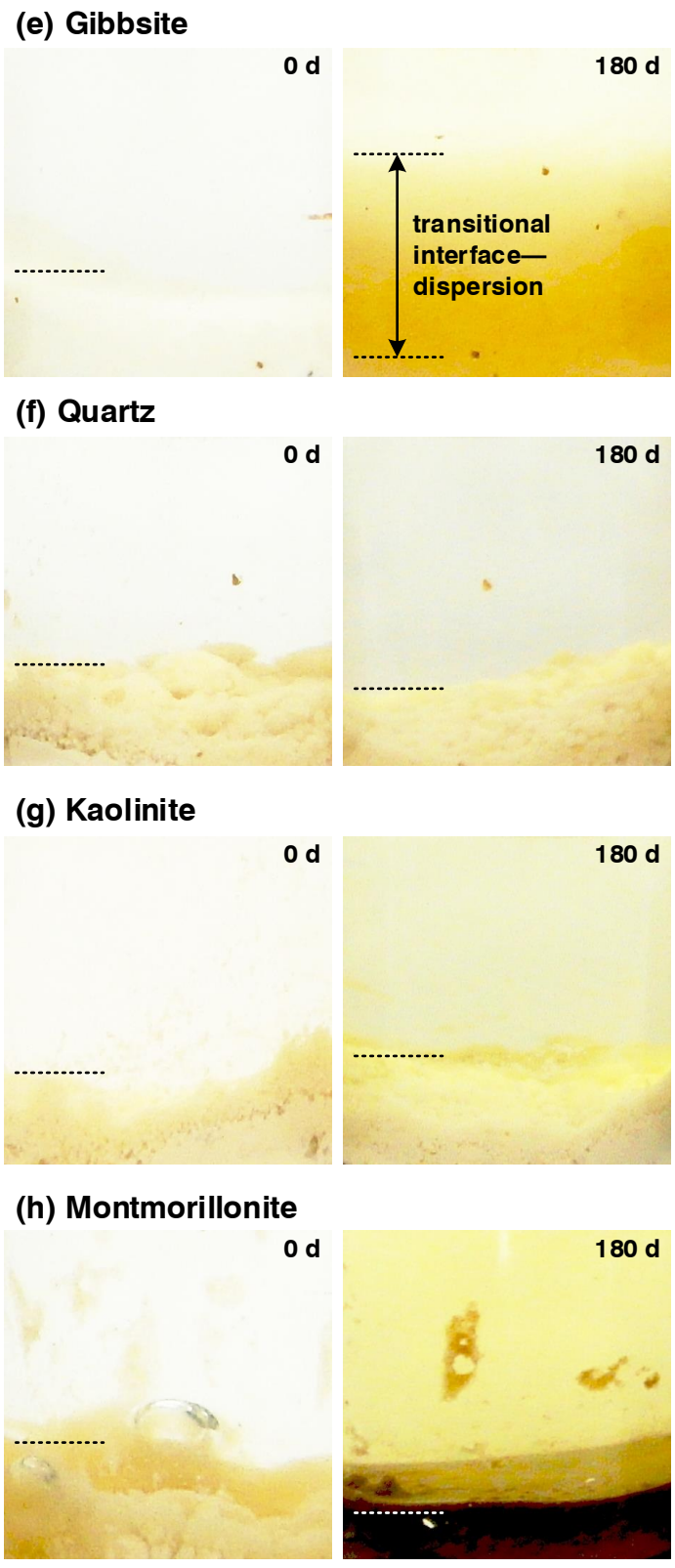

Fig. 3.2 *Continued.*

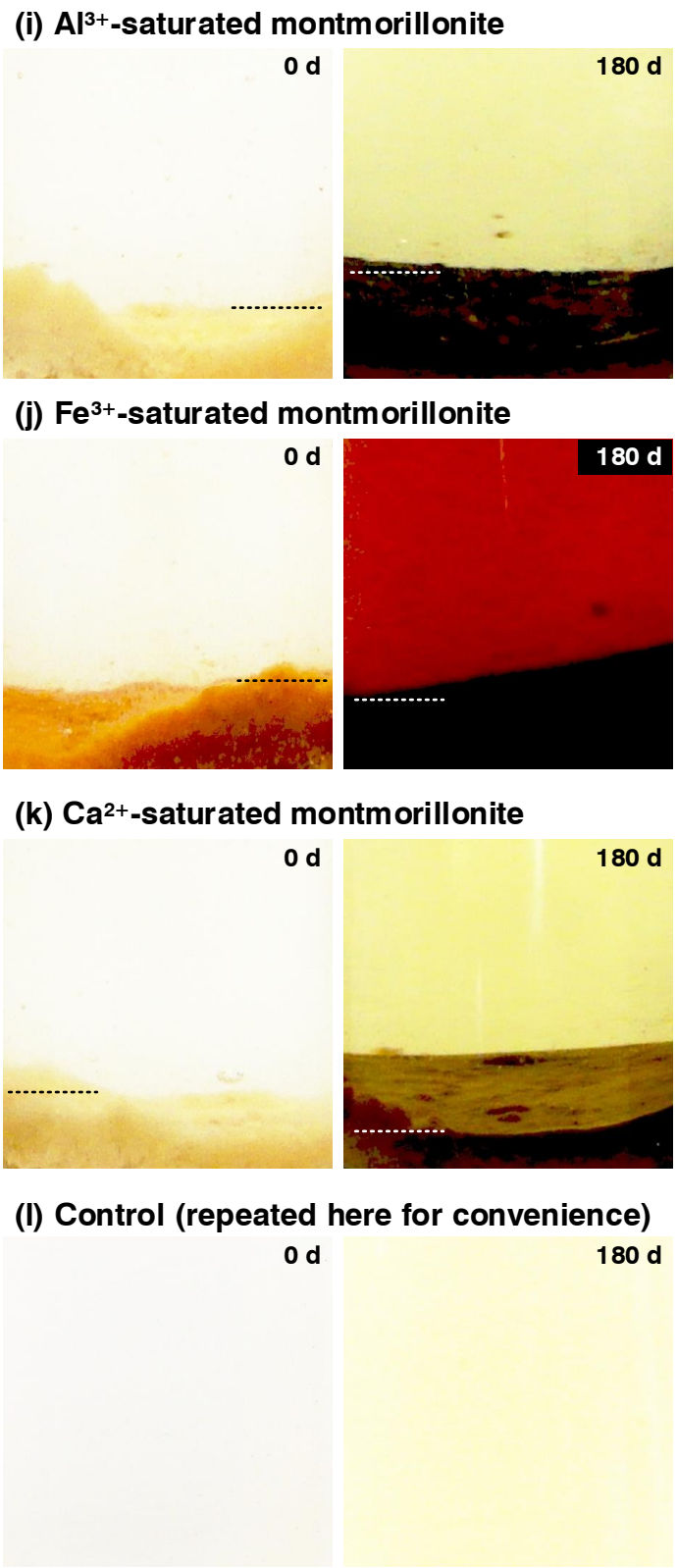

Fig. 3.2 *Continued.*

The exceptions to this are the mineral phases containing redox-active cations, such as Mn^{4+}, Mn^{3+} and Fe^{3+}, whether in the mineral lattice/surface itself (Mn- and Fe-oxides) or the smectite interlayer (Fe^{3+}-saturated montmorillonite). For these, the colour change was a significant darkening to red-brown-black colours.

Birnessite was the most reactive toward oleic acid, and this sample had darkened the most, to a deep red-brown colour. The contents of the pyrolusite vial was markedly less dark and coloured, having an orange-yellow colour to it. Closer inspection of the contents in the birnessite vial revealed that the birnessite had been partially dissolved by reaction with oleic acid during the incubation period. The dark-red liquid phase of the birnessite vial had also become much more viscous than the original oleic acid, whilst the liquid phase of the pyrolusite vial had no noticeable difference in viscosity relative to oleic acid.

The thickening and darkening observed was similar to observations reported by Gomez *et al.* (2011) and Omonov *et al.* (2016). Further inspection found a noticeable increase in viscosity (relative to original oleic acid) in the cases of birnessite and gibbsite, especially closer to the clay-liquid interface, but not for the remaining mineral phases and the control. The *quasi*-solids formed are potentially polymeric products resulting from the lipid-clay reaction. These were analysed by ATR-FTIR and will be discussed later, after the presentation of the ATR-FTIR data. At this point, the discussion will focus on the colour changes observed and the apparent dissolution of the birnessite mineral phase.

Reaction of oleic acid with redox-active clays. The higher degree of reaction between oleic acid and birnessite versus oleic acid and pyrolusite can be attributed to two main factors. Firstly, the greater BET surface area of birnessite as opposed to pyrolusite (53 *v.* 4 m^2g^{-1}) renders it more reactive. Secondly, birnessite possibly possesses octahedral sites that contain Mn^{3+} cations instead of Mn^{4+} (Stone and Morgan, 1984*a*, 1984*b*; Ulrich and Stone, 1989; Manceau *et al.*, 2012). Trivalent Mn has a greater redox potential ($E° = +1.51$ V) than Mn^{4+} ($E° = +1.23$ V), also therefore contributing to possible greater reactivity of birnessite. Given the disappearance of birnessite during the reaction, it is likely that the oleic acid-Mn-oxide reaction is a reductive dissolution reaction, with Mn-oxide acting as oxidant and oleic acid acting as reductant.

Both goethite and Fe^{3+}-saturated montmorillonite also show considerable darkening and reddening. It is possible that Fe-containing phases also undergo reduction by oleic acid. Little to no dissolution of goethite or Fe^{3+}-saturated montmorillonite was observed, however. This is possibly due to Fe-oxides possessing lower redox potential ($E° = +0.67$ V) than Mn-oxides and being possibly less reactive toward oleic acid.

It is noteworthy that the dark-red colour is only visible in the cases of redox-active mineral phases. Red colouration possibly results from the formation of some particular type of oleic acid oxidation product potentially only forming

in these cases, or it could form from the presence of dissolved trivalent forms of Mn and Fe. Both Mn^{3+} and Fe^{3+} are known for their sometimes-intense pink-red and orange-red colours in solution, respectively. When complexed with ligands such as pyrophosphate, EDTA and porphyrins, the Mn^{3+} ion possesses a magenta (red) colour (Kostka *et al.*, 1995; Klewicki and Morgan, 1998; Madison *et al.*, 2011; Oldham *et al.*, 2015, 2017), whilst Fe^{3+} produces orange colours with ligands such as citrate and EDTA (Schwertmann, 1991; Rueda *et al.*, 1992; Cornell and Schwertmann, 1996).

To test if Mn^{3+} and Fe^{3+} cations were actually present, a set of rudimentary chemical tests (not mentioned in the materials and methods section, § 3.2) were employed. A *c.* 1 ml aliquot of the liquid phase from each of the red liquid phases was pipetted into a 50 ml BD Falcon™ centrifuge tube. For the purposes of the greatest possible colour change/result, pyrolusite was excluded from the test and birnessite was used singularly to represent Mn-oxides/Mn^{3+}. For the case of the birnessite liquid, 10 ml of a 50 mM tetra-sodium pyrophosphate decahydrate ($Na_4P_2O_7{\cdot}10H_2O$) solution, which was adjusted to a pH of 6.5 (Kostka *et al.*, 1995; Nico and Zasoski, 2001; Marafatto *et al.*, 2015), was added to the 1 ml aliquot extracted from birnessite. The mixture was then vortexed, and it turned cloudy-brown. After settling for approximately 2 hours, the mixture separated into a cloudy-brown layer floating above a crimson pink aqueous layer and this was photographed (see Fig. 3.3*a*).

This crimson layer also forms temporarily, but rapidly disappears when using 10 ml of a 0.01 M HCl solution instead of 50 mM pyrophosphate for example (see Fig. 3.3*b*). This could point to the presence of Mn^{3+}, as it is known that Mn^{3+}, when not complexed with ligands such as pyrophosphate and under acidic conditions, is unstable (Brookins, 1988).

Addition of 1 M NaOH to an aliquot of the crimson aqueous 50 mM pyrophosphate-extracted layer forms a cloudy-brown suspension at first, which darkens after standing, grading darker towards the top end of the mixture (Fig. 3.3*c*), suggesting formation of Mn oxide phases. Addition of 1 M Na-dithionite reducing agent ($Na_2S_2O_4$) to an aliquot of the crimson aqueous 50 mM pyrophosphate-extracted layer causes the disappearance of the crimson colour (Fig. 3.3*d*).

The reaction governing the colour change in an acidic medium and with the addition of Na-dithionite is:

$$Mn^{3+} + e^- \rightarrow Mn^{2+} \tag{3.1}$$

The reaction governing the colour change in a basic medium with the addition of NaOH is the precipitation of the brown $Mn^{4+}O_2$-solid:

$$Mn^{3+} + 4OH^- \rightarrow Mn^{4+}O_2(s) + 2H_2O + e^- \tag{3.2}$$

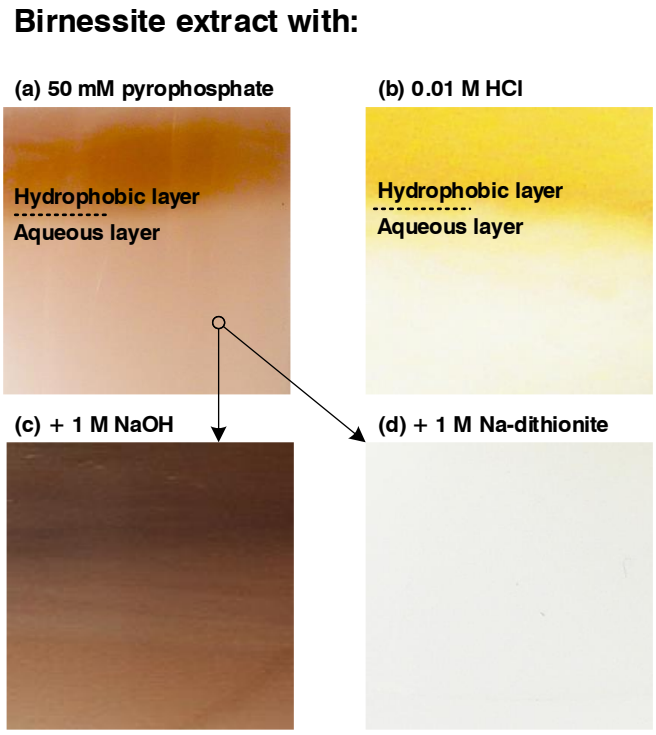

Fig. 3.3 The colour changes that occur to the birnessite extract when adding (a) 50 mM pyrophosphate solution and (b) 0.01 M HCl solution, as well as the colour changes when samples of the 50 mM pyrophosphate-extracted solution are treated with (c) 1 M NaOH and (d) 1 M Na-dithionite reducing agent.

In the case of the extracts from goethite and Fe^{3+}-saturated montmorillonite, the 1 ml liquid aliquots were extracted with 10 ml of a 50 mM EDTA solution. The mixtures were vortexed and turned a cloudy orange-brown. When left to settle for 2 hours as well, two layers form: a cloudy-orange-brown layer floating atop a pale yellow-orange aqueous layer (see Figs 3.4*a* and *b*). Upon addition of 1 M Na-dithionite reductant to the EDTA extracts, the pale yellow-orange colour fades somewhat (Figs 3.4*c* and *d*). The reaction governing this colour change is:

$$Fe^{3+} + e^{-} \rightarrow Fe^{2+} \tag{3.3}$$

In equations 3.1 and 3.3, the corresponding oxidation reactions are the oxidation of the dithionite molecule *via* a sulphur dioxide radical step (Balahura and Johnson, 1987):

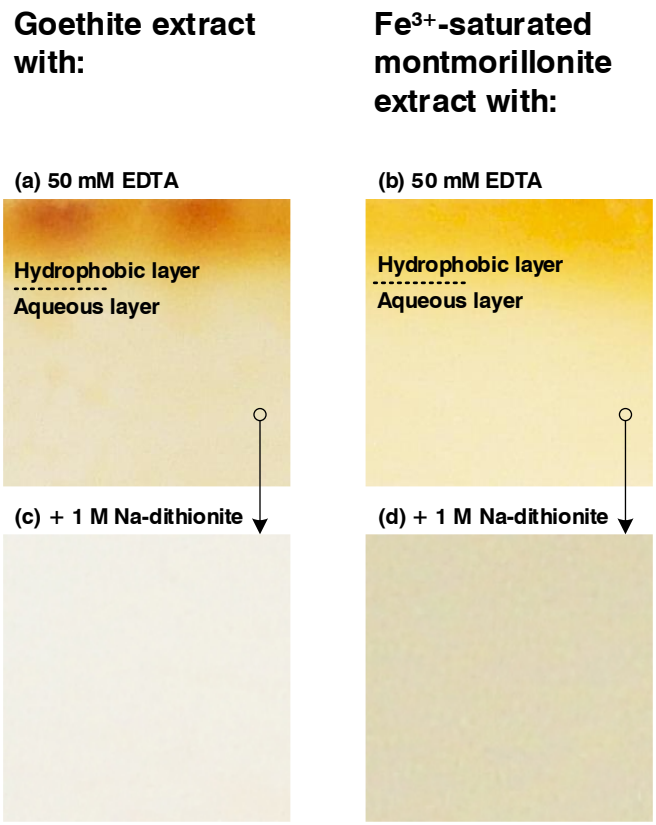

Fig. 3.4 The colour changes that occur to the goethite and Fe^{3+}-saturated montmorillonite extracts when adding (a, b) 50 mM EDTA solution as well as the colour changes that occur when samples of the 50 mM EDTA-extracted solutions are treated with (c, d) 1 M Na-dithionite reducing agent.

$$S_2O_4^{2-} \rightleftharpoons 2^{\bullet}SO_2^- \tag{3.4a}$$

$$^{\bullet}S^{3+}O_2^- \rightarrow S^{4+}O_2(g) + e^- \tag{3.4b}$$

whilst the corresponding reduction reaction in the oxidation of Mn^{3+} (equation 3.2) is possibly the reduction of oxygen (in basic medium):

$$O_2(g) + 2H_2O + 4e^- \rightarrow 4OH^- \tag{3.5}$$

The colour changes in Figs 3.3 and 3.4 are strong indicators that trivalent species of Mn and Fe are possibly present in the liquid phase of the redox-active oleic acid-clay treatments.

Reaction of oleic acid with non-redox-active clays. In the cases of gibbsite, quartz, kaolinite and the smectites, the reaction with oleic acid produced varying degrees of yellowing (Figs 3.2*e–i*, *k*). Gibbsite was the most reactive (greatest degree of yellowing) and what was also interesting to note was that most yellowing and darkening occurred in the area of the clay, with a transition into the lighter-coloured liquid phase. Unlike the other clay phases, there appeared to be no clear layer of solid-phase settled at the bottom of the vial (Fig. 3.2*e*, 180 days). The solid phase appeared to be well dispersed in the liquid phase. Inspection with a stainless-steel spatula revealed that the viscosity of the liquid phase increased dramatically toward the bottom, forming a *quasi*-solid which seems to be a thorough mixture of gibbsite particles and organic products.

Whilst significant yellowing is observed in the case of smectites, no appreciable increase in viscosity or clay-phase dispersion was observed as was with gibbsite. The mineral phase is well settled with a sharp clay-liquid interface (Fig. 3.2*h*, *i* and *k*). No discernible differences in the degree of yellowing and darkening of the liquid phase are observed among the different montmorillonites (Al^{3+}-, Ca^{2+}- and unsaturated). This would suggest that differences in acidity (Lewis or Brønsted) of the interlayer cation does not play a major role in the possible oleic acid polymerisation reaction. The polymerisation mechanism associated with clay minerals (den Otter, 1968; see equations 2.22 and 2.23) would suggest that the more acidic Al^{3+}-saturated smectite would provide the acidity needed for the reaction to initiate, over less acidic or basic clay minerals such as Ca^{2+}-saturated smectite or unsaturated smectite. However, given the reaction conditions employed by den Otter (1968) such as high temperatures (*c.* 300°C) compared to this study (25°C), it is likely that Al^{3+}-saturated montmorillonite is providing the acidity needed, but there is an energy barrier (high activation energy step) located somewhere in the polymerisation mechanism, which is simply not being overcome as effectively under the conditions employed in *this* study.

An interesting observation specific to the cases of the montmorillonites is that the mineral phases themselves appear to be darkening considerably as a result of the interaction with oleic acid (see Figs 3.2*h–k*). Several possibilities could explain these observations, ranging from the formation of dark organo-clay complexes to changes in the structure of the clay mineral itself. It was decided at this point that visual observation alone could not provide a sufficient explanation and therefore this darkening of the smectite phase is discussed in a later section of this chapter—§ 3.3.3. This later section follows further investigation of the organic phase by ATR-FTIR spectroscopy as well as investigation of the reacted mineral phase itself by XRD analysis. The additional insights provided by these techniques allows for a more informed interpretation of the observed mineral phase darkening.

The least reactive clay phases toward oleic acid are kaolinite and quartz (Figs 3.2*g* and *f*), both with seemingly very little influence on the degree of yellowing relative to the control experiment. Despite possessing significant acidity (surface pH = 2.6 and contains a strong Lewis acid—Si^{4+}), which is often necessary in initiating mineral-organic reactions (*e.g.* equation 2.35), quartz is virtually unreactive toward oleic acid. The two factors that play a role in the non-reactivity of kaolinite and quartz is firstly that kaolinite, despite having an interlayer, possesses a low CEC and so fewer exchangeable cations compared to smectite. Secondly, and most importantly, these two minerals possess a much lower BET surface area than smectite (Table 3.1; 10 $m^2\,g^{-1}$ for kaolinite and 6 $m^2\,g^{-1}$ for quartz versus 84 $m^2\,g^{-1}$ for smectite). In this case, the relatively low effective surface area impacts reactivity in the same manner as it did in the case of pyrolusite (despite possessing Mn^{4+} which has high Lewis acidity and redox potential).

3.3.2 Polymerised products—ATR-FTIR spectroscopy

The yellowing and darkening resulting from the oleic acid-mineral reactions are likely a result of the formation of various types of polymerised products (den Otter, 1968; Gomez *et al.*, 2011; Omonov *et al.*, 2016; see Figs 2.10 and 2.11). Yellow and light colours are indicative of dimer products, whilst darker colours are indicative of products possessing higher molecular weights, such as trimers, esters and peroxidation-polymerised products (den Otter, 1968).

The ATR-FTIR technique provides a highly useful, rapid and cost-effective method for probing the identities of these potential polymerised products. For all of the cases studied (Fig. 3.2), the corresponding ATR-FTIR spectra were collected, and these are provided in Fig. 3.5. In each case, optimum sampling was performed—in the cases where the liquid had changed colour but still remained liquid, the liquid was sampled as close to the mineral phase as possible, in the clay-liquid interface. In the cases where *quasi*-solids had formed, these were sampled as far as possible in preference to the liquid, and still from the clay-organic interface.

The most prominent features of the pure oleic acid ATR-FTIR spectrum (Fig. 3.5) include the strong band at 1,706 cm^{-1} related to the carbonyl (C=O) stretch vibration of the carboxylic acid functional group. This peak has a somewhat variable frequency, sometimes being located more in the region of 1,713 cm^{-1} (Klokkenburg *et al.*, 2007). The features located at 936, 2,670 and 3,097 cm^{-1} are related to the stretching of the —OH bond in the carboxylic acid functional group.

The features at 1,286 and 1,413 cm^{-1} are related to the stretching of the C—OH in the same functional group, whilst those at 2,925 and 2,856 cm^{-1} correspond to stretching vibrations of the —CH_2— group, with the corresponding bending vibration occurring at 1,461 cm^{-1}.

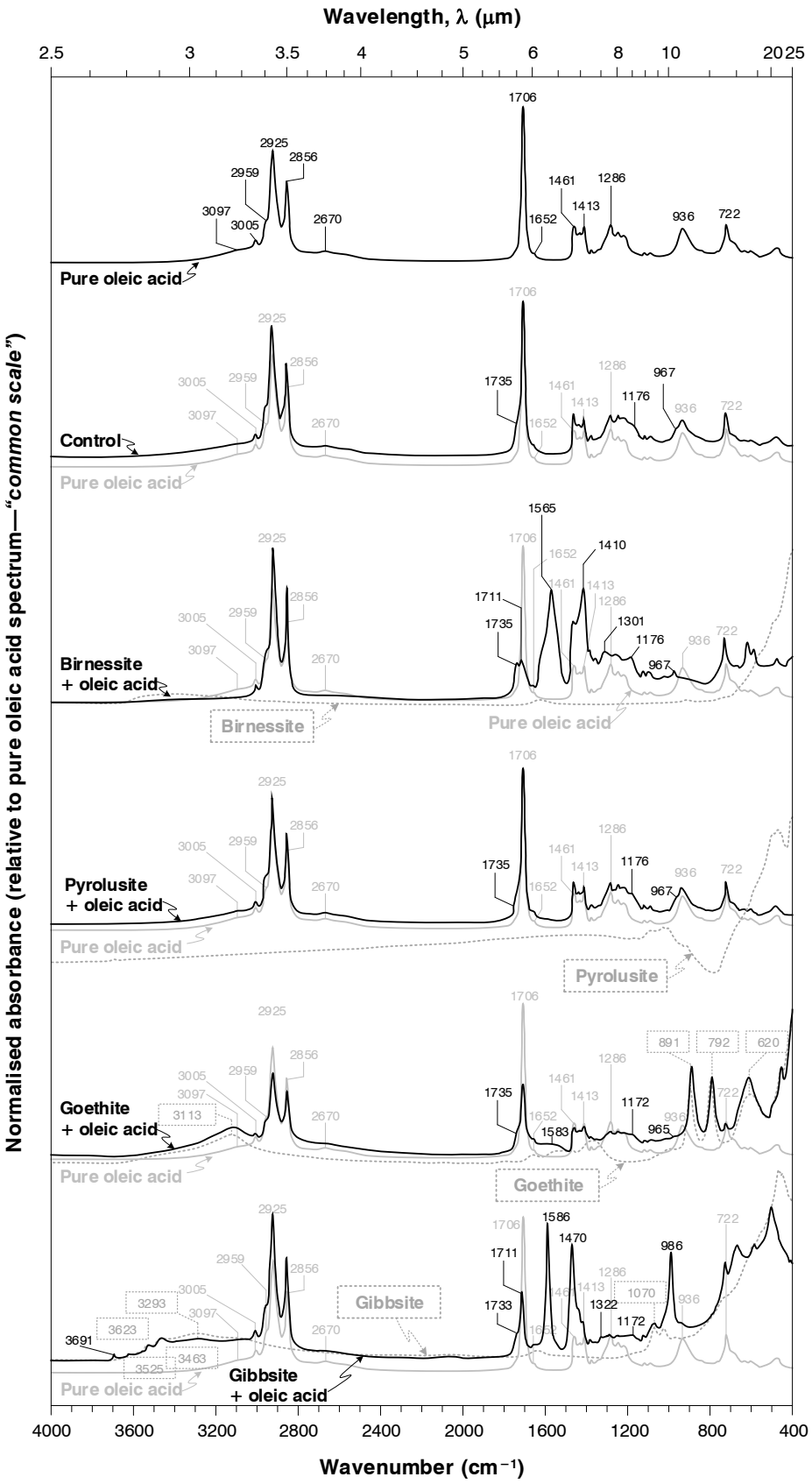

Fig. 3.5 The ATR-FTIR spectra of the various clay-oleic acid treatments (incubated for 6 months at 25°C in the dark).

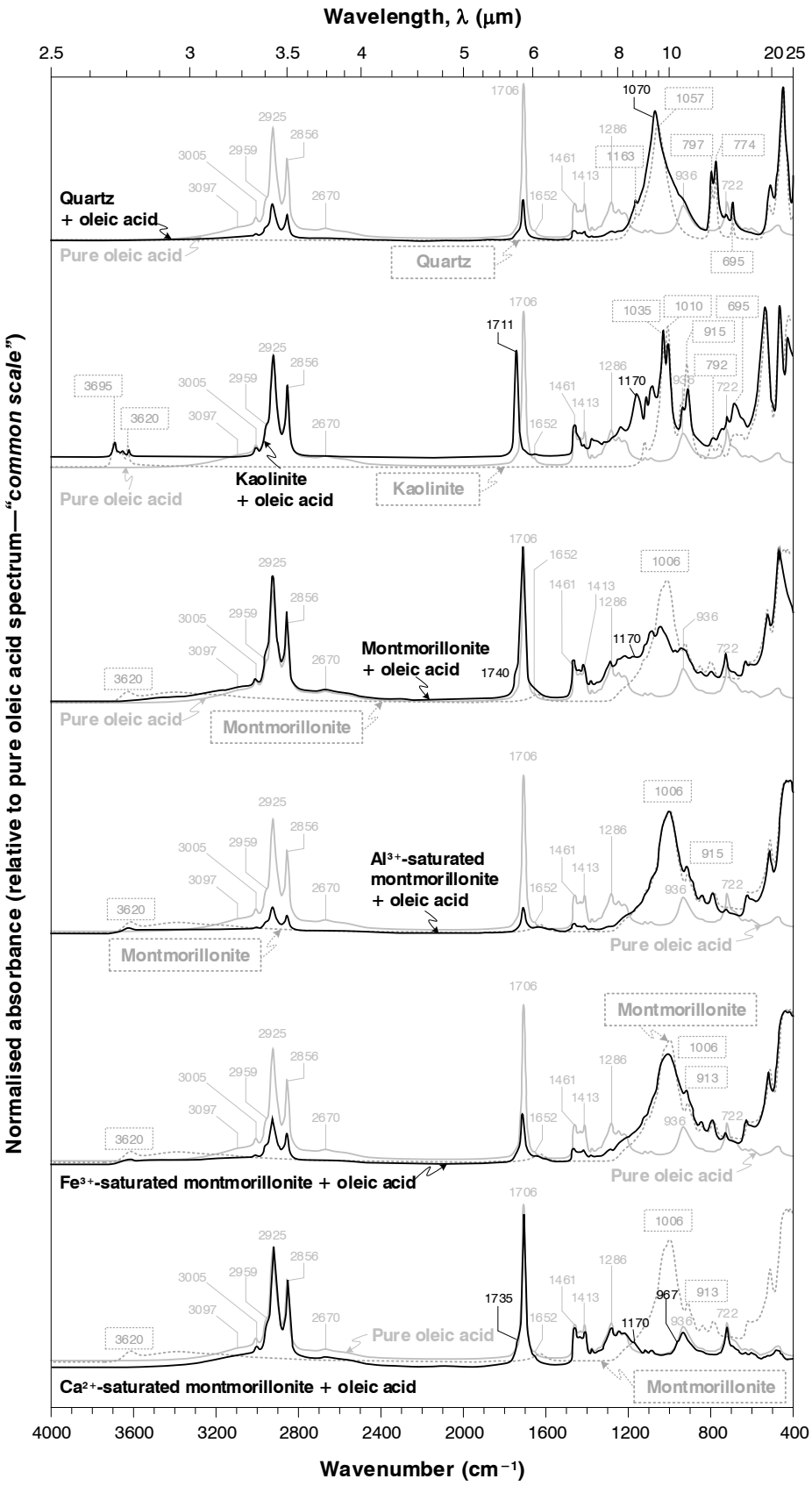

Fig. 3.5 *Continued.*

The features at 3,005 and 1,652 cm^{-1} relate to stretching vibrations associated with the alkene functional group (*e.g.* —CH=). The peak at 722 cm^{-1} is ever-present in all long-chain molecules, and is another feature related to the —CH_2— group.

In all of the treatments, the greatest changes in band position and the formation of new bands was observed for the case of oleic acid reacting with birnessite (Fig. 3.5). Inspection of the birnessite plus oleic acid spectrum reveals that the broad feature located at approximately 2,500–3,500 cm^{-1} with shoulders at 3,097 and 2,670 cm^{-1} has disappeared in the spectrum of birnessite plus oleic acid in comparison to the pure oleic acid spectrum. This broad feature corresponds to the O—H stretch vibration of the —OH group in the carboxylic acid functional group on oleic acid (Premaratne *et al.*, 2013).

No changes to the peak at 3,005 cm^{-1}, which corresponds to the C—H stretch attached to a double-bond (Premaratne *et al.*, 2013; Dzhatdoeva *et al.*, 2016; Omonov *et al.*, 2016), means double-bonds are not disappearing as a result of the reaction. The formation of epoxides would cause the disappearance of the *cis*-double bond in oleic acid as the π-bond shifts to close the oxirane ring structure. The absence of a peak at 826 cm^{-1} (Omonov *et al.*, 2016) confirms that there are no epoxides forming. A small shoulder feature at 1,652 cm^{-1} confirms that there are double-bonds (Johnson *et al.*, 2015). However, despite the double-bonds not disappearing, many have transformed from *cis-* to *trans*-configuration. This is deduced from the peak forming at 967 cm^{-1} (Yoshida *et al.*, 2009; Poiana *et al.*, 2015).

No disappearance of the peak at 720 cm^{-1} occurred indicating that long-chain structures are still prevalent, as this peak corresponds to the rocking motion of the chain —CH_2— groups (Premaratne *et al.*, 2013; Omonov *et al.*, 2016). The disappearance of the peak at 936 cm^{-1} relates to the disappearance of the out-of-plane OH stretch in carboxylic acid (Premaratne *et al.*, 2013; Dzhatdoeva *et al.*, 2016; Omonov *et al.*, 2016). This corresponds to the disappearance of the broad OH stretch between 2,500–3,500 cm^{-1}. The disappearance of peaks related to the carboxylic acid group and the formation of a new carbonyl stretch at 1,735 cm^{-1}, as well as a peak at 1,176 cm^{-1} (relating to C—O—C) bonds, suggest the formation of esters (Johnson *et al.*, 2015; Omonov *et al.*, 2016). A decrease in the relative peak intensity and a slight shift to 1,711 cm^{-1} is also noticed for the original carbonyl stretch of the carboxylic acid group at 1,706 cm^{-1} (Premaratne *et al.*, 2013; Omonov *et al.*, 2016). The disappearance of the peak at 1,286 cm^{-1} (associated with the stretch vibration of the C—O bond in —COOH; Premaratne *et al.*, 2013; Johnson *et al.*, 2015) and emergence of a new peak at 1,301 cm^{-1} also supports the notion of esters forming. The peak at 1,301 cm^{-1} is not allocated as such but could be the indication of a strengthening of the C—O bond. This would make sense as the H atom attached to the O atom in the C—OH bond (carboxylic acids) is more electron withdrawing than a —CH_2— group attached to the O atom in the C—O—C bond (esters), meaning carbox-

ylic acids have a weaker (lower frequency—1,286 cm^{-1}) C—O bond than the stronger (higher frequency—1,301 cm^{-1}) C—O bond in esters. The formation of esters would explain the thickening (increase in viscosity) observed, as this is a form of polymerisation reaction. As no free alcohol group's OH-stretch vibrations (usually *c.* 3,400 cm^{-1}) can be observed, it would suggest that all or most of the hydroxy groups, once formed (possibly near the double bond), react instantly with any available carboxylic acid groups, or that the reaction does not proceed in such a manner at all, and rather by some radical mechanism. The lack of any hydroperoxide peaks (*e.g.* the —O—O— stretch at 879 cm^{-1} and stretching vibrations of the free OH group at 3,620 cm^{-1}; Dzhatdoeva *et al.*, 2016) suggests that hydroperoxides (or its derivatives, *e.g.* alcohol groups or epoxides) are either very short-lived or not present at all.

A hypothetical structure of the ester-bonded polymer has been suggested in Fig. 3.6 below. It builds on the original idea of Omonov *et al.* (2016) who suggested ring opening of epoxides to form —OH groups that then couple with carboxylic acid functional groups (see Fig. 2.10).

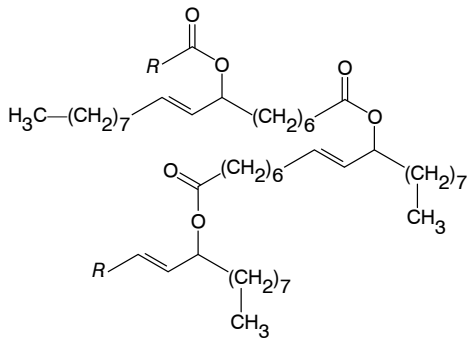

◀ **Fig. 3.6** A possible structure for the polyester potentially forming in the reaction between birnessite and oleic acid (modified from Omonov *et al.* (2016)). *R* = rest of molecule.

Noticeable from Fig. 3.5 is the low organic signal that arises from the cases of quartz and the natural clay minerals. For the cases where *quasi*-solid phases had formed, sampling near the mineral-liquid interface provides a well-proportioned sample between organic phase and mineral phase, producing well-defined peaks especially for the organic phase. In the cases of quartz and the clay minerals, the liquid phase was still fairly fluid, and as a result, sampling near the liquid-mineral interface saw much of the liquid phase run off the stainless-steel spatula, leaving behind a sample which was mostly mineral phase. This had two major effects on the spectra obtained. One is the acquisition of a relatively low organic signal which means it is more difficult to detect any changes (*i.e.* polymerisation) in comparison with the organic phases of the birnessite and gibbsite treatments for example. The second effect is the strong signal of unreacted mineral phase, which overshadows any possible changes that may be occurring right at the liquid-mineral interface (a layer probably only a fraction of a μm or nm thick).

Other notable observations from the birnessite-oleic acid ATR-FTIR spectrum are two more significant peaks at 1,565 and 1,410 cm^{-1}. These bands at 1,565 and 1,410 cm^{-1} correspond to the asymmetrical and symmetrical carboxyl ($—COO^-$) stretch vibrations, respectively (Premaratne *et al.*, 2013; Johnson *et al.*, 2015). The peak formed at 1,410 cm^{-1} overlaps with the original smaller peak at 1,413 cm^{-1} which corresponds to the in-plane bend of the C—H bond on double bonds (Dzhatdoeva *et al.*, 2016). The manner of bonding between carboxylic acid (or carboxylate) groups and the oxide surface were depicted in equations 2.37*a*–*b* and 2.38*a*–*b*:

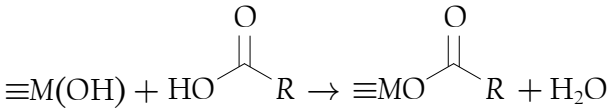

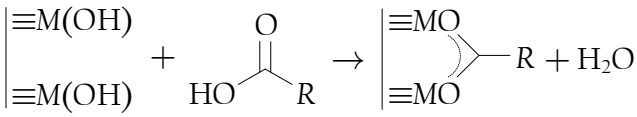

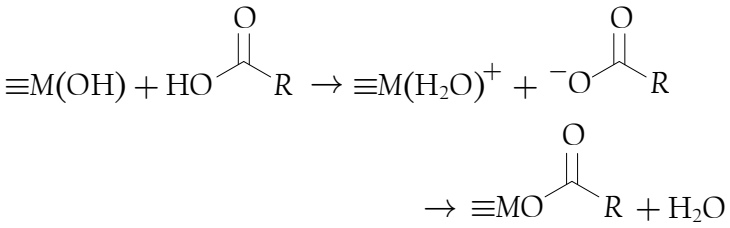

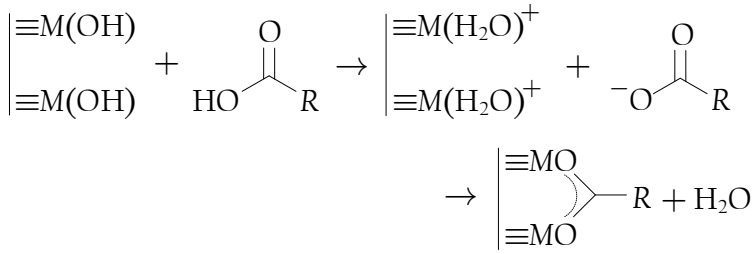

These surface bonding schemes were suggested by studies such as Johnson *et al.* (2015) because of peaks found in FTIR spectra which were located at 1,595 and 1,565 cm^{-1}, corresponding to asymmetric stretching vibrations of the carboxylate group (Yariv, 2002*a*, 2002*b*, Johnson *et al.*, 2015). Whilst Yariv (2002*a*) and Yariv (2002*b*) did not study Mn-oxides specifically as Johnson *et al.* (2015) did, he found similar peaks for the interaction of stearic acid (saturated analogue of oleic acid—$C_{18}H_{36}O_2$) with cations adsorbed on smectites. Under hydrated conditions, peaks were observed in the region of 1,500–1,585 cm^{-1}, but shifted upon drying, and this shift was cation-specific. The conclusion was that

the carboxylate group had bonded directly with the cation. In all the cases of Yariv (2002*a*, 2002*b*) and Johnson *et al.* (2015), the symmetric carboxylate stretching vibration at 1,400–1,405 cm^{-1} was also present. It is therefore highly likely that the observed peaks at 1,565 and 1,410 cm^{-1} are indicative of the exchange reaction between the carboxyl groups of oleic acid and the surface functional groups on Mn-oxide.

It is possible that complexation or chelation of Mn^{3+} (and Fe^{3+}) potentially occurs, from the mineral phase into the liquid phase. Since these frequencies relating to the carboxylate group may also appear when complexing with specific cations as well (Yariv, 2002*a*, 2002*b*), it is possible that complexation of Mn^{3+} (and Fe^{3+}) *via* the carboxyl group of oleic acid potentially also occurs, and these interactions may possibly also be contributing to the observed peaks for the asymmetrical and symmetrical —COO^- stretch.

In comparison to the birnessite-oleic acid spectrum, the spectra of pyrolusite-oleic acid and the control experiment do not show much change from the original (neat) oleic acid spectrum. This agrees with the initial visual observations. The pyrolusite-oleic acid spectrum shows slight shoulder features at 1,735, 1,176 and 967 cm^{-1}, which is consistent with the formation of the discussed polyester (Fig. 3.6), with its ester bonds and *trans*-configuration double bonds. Similar shoulders occur for the control experiment spectrum, which would have undergone autoxidation (since there is no mineral present).

Relative to the case for birnessite, goethite showed markedly less reactivity toward oleic acid, in terms of lipid polymerisation. Similar to the control and pyrolusite plus oleic acid ATR-FTIR spectrum, only small shoulder features at 1,735, 1,176 and 967 cm^{-1} are observed (Fig. 3.5). No significant shifts were observed for the peaks located at 3,113, 891 and 792 cm^{-1}, which are related to stretching and bending vibrations of the surface ≡Fe—OH functional groups on goethite, and likewise, only a slight shoulder was observed in the region of 1,583 cm^{-1}, which would correspond to any direct bonding through ligand exchange by the carboxylate group on oleic acid (no strong peak is visible at 1,460 cm^{-1} either). This result demonstrates that no appreciable exchange (equations 2.37*a*–*b* and 2.38*a*–*b*) is occurring on the goethite surface. One possible reason could be the high surface pH of goethite (∼ 10; see Table 3.1). At this pH, the goethite surface would be mostly deprotonated (≡Fe—O^-) and this negatively charged group does not as readily undergo exchange as the protonated group (≡Fe—OH and ≡Fe—OH_2^+). However, this does not account for the appreciable amount of red-colouration observed visually though. For this visibly appreciable amount of Fe^{3+} to be either chelated from the goethite surface or be formed oxidatively *in-situ*, one would expect to see some kind of interaction between the surface hydroxyl functional groups and the carboxylate functional group. Given the relatively low levels of polymerisation products, it is possible that Fe^{3+} in the goethite surface is acting as a radical quench for lipid (peroxide) radicals, in a one-electron reduction step, to form Fe^{2+}, thereby not

directly involving the surface hydroxyl functional groups as such, and inhibiting the polymerisation reaction, which relies upon the propagation of lipid radical species.

In contrast, gibbsite showed marked reactivity toward oleic acid, and its ATR-FTIR spectrum depicts some new peaks, suggesting (a) product(s) very different from the one observed for the birnessite-oleic acid case (Fig. 3.6). Two very strong peaks occur at 1,586 and 1,470 cm^{-1}, relating to the asymmetrical and symmetrical —COO^- stretch, respectively. However, the fact that a strong peak is now observed at 1,470 cm^{-1} rather than the 1,410 cm^{-1} observed for birnessite, suggests a different type of binding interaction with the gibbsite surface, compared to the birnessite surface. In a study by Sharma *et al.* (2015), FTIR peaks at 1,560 and 1,443 cm^{-1} was attributed to oleic acid binding in a bidentate fashion (*e.g.* equations 2.37*b* and 2.38*b*) to magnetite nanocubes. Whilst these frequencies are not the same as those observed in the case of gibbsite in this study, their difference in wavenumber corresponds rather closely to that observed in the gibbsite-oleic acid spectrum. It is therefore highly likely that both oxygen atoms of the carboxylate group are involved and bind in a bidentate manner to the gibbsite surface. In addition, the study by Sharma *et al.* (2015) focused on using oleic acid binding in this manner to magnetite nanocubes in order to disperse them for the purposes of magnetic-resonance imaging (MRI) applications. In *this* study, it was also observed that much dispersion of the gibbsite solid phase appeared to take place in the case of the gibbsite-oleic acid reaction, prompting the consideration that a similar bidentate binding and dispersion process is occurring in *this* case too. Another new, strong peak is observed at 986 cm^{-1}. This peak was assigned to vibrations caused by a bond occurring in the vinyl position of the double-bond in oleic acid (Rege *et al.*, 1984). The size of the peak appears to be so large that it dwarfs (overlaps) any possible distinction of whether the double-bond is *trans* or not (967 cm^{-1}). Despite this, the observation of a bond in the vinyl position, along with the yellow colour of the product, points strongly to the formation of dimeric (and possible trimeric) products (den Otter, 1968) depicted in Fig. 2.11. This structure possesses a linking bond directly from the carbon on the *trans* double-bond (vinyl position) to a second (and thereafter third) oleic acid molecule. The Lewis acidity of Al^{3+} in this case in all likelihood provides the acidity required for the initiation of the reaction (see equations 2.22 and 2.23), although it is not clear how it is doing so—whether by its Lewis acidity directly, or by polarising the hydroxyl functional groups to the point of releasing a proton (H^+).

For the remaining cases, *viz.* quartz, kaolinite and the montmorillonites, no noteworthy peaks were observed in comparison to what was already observed in the control experiment. Small shoulder features are observed throughout, once again at around 1,735/1,740, 1,176/1,170 and 967 cm^{-1}, indicating some reaction, but no appreciable levels thereof. No significant changes to mineral-phase peaks were observed either, except in the case of quartz, where the peak

at 1,057 cm^{-1} which is related to the stretching vibration of the Si—O bond, and specifically the displacement of oxygen along this bond (Lippincott *et al.*, 1958), shifted to 1,070 cm^{-1}. This could indicate some interaction of oleic acid with the quartz surface, but the lack of peaks relating to the asymmetrical and symmetrical —COO^- stretch (*c.* 1,570 and 1,410/1,470 cm^{-1}) indicates that there is no appreciable direct binding to the quartz surface, and any interactions are in all likelihood through hydrogen bonding for example, between the carboxylic acid group and surface silanol groups (≡Si—OH and ≡Si—OH_2^+).

3.3.3 Darkening of the smectite mineral phase

Upon closer inspection of Figs 3.2*h–k*, which depicts the colour change resulting from the reaction of the montmorillonites with oleic acid, it is noticeable that the smectite mineral phase itself has darkened considerably in all cases. The observed darkening may be due to the formation of organo-clay complexes or the physical alteration of the smectite mineral structure itself (refer again to § 3.3.1). In order to investigate such possible changes, one of the smectite phases was sampled (post-reaction) and analysed using XRD, and the results compared with the unreacted smectite phases (pre-reaction). The case that was selected was that of Al^{3+}-saturated montmorillonite as it had darkened the most and was thus deemed to be the case in which the smectite mineral phase had been altered the most. The diffractograms obtained for Al^{3+}-saturated montmorillonite before the reaction compared with after the reaction are depicted in Figs 3.7*a* and *b*, respectively.

The diffractogram for Al^{3+}-saturated montmorillonite after reaction (Fig. 3.7*b*) shows a shift of the peak at 15 Å, associated with the basal plane (*hkl* = [001]) reflection of the smectite interlayer, to approximately 14 Å. The associated reflections at 5 and 3 Å (planes *hkl* = [003] and *hkl* = [005], respectively) have also disappeared. These shifts in *d*-spacing indicate a slight collapsing of the smectite interlayer (originally 15 Å).

Several possibilities may account for the collapsing of the smectite interlayer, but a likely scenario involves the interactions between functional groups on oleic acid (or polymerised products) and interlayer cations (*e.g.* Al^{3+}) as well as between organic functional groups and hydroxyl groups or central Si^{4+}/Al^{3+} cations in the tetrahedral sheet bordering the interlayer. An illustration of the possible interactions between organic functional groups and clay functional groups is provided in Fig. 3.8.

Referring again to the ATR-FTIR spectrum of the Al^{3+}-saturated montmorillonite plus oleic acid case (Fig. 3.5), a weak organic signal relative to the mineral signal possibly hides any spectral features in the region near 1,560 cm^{-1} (which indicates the presence of the —COO^- group and the possible inner-sphere direct-binding mode between the carboxyl group and central Si^{4+}/Al^{3+} cations, or interlayer Al^{3+}).

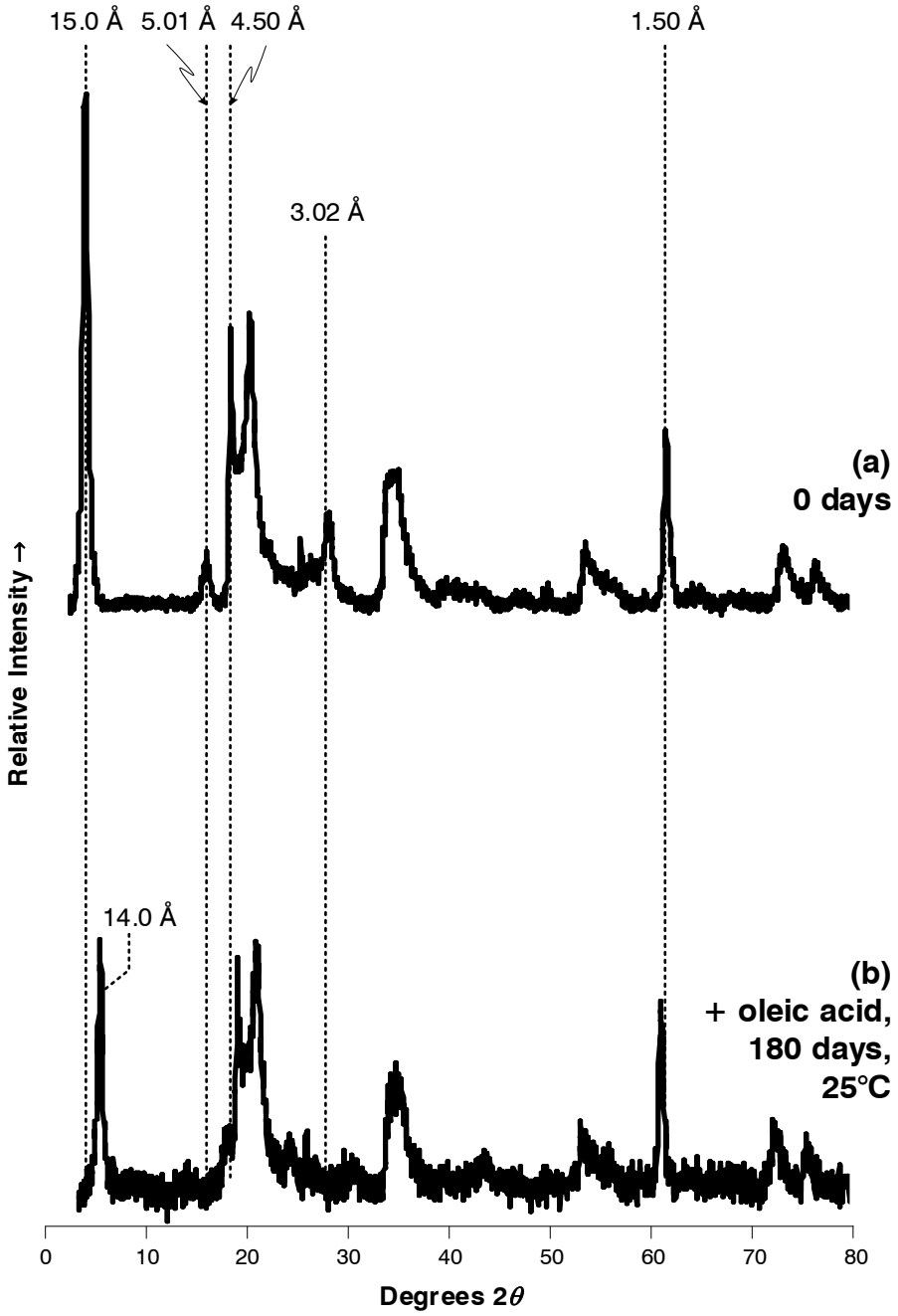

Fig. 3.7 The X-ray diffractograms of Al^{3+}-saturated montmorillonite (a) before and (b) after reaction with oleic acid for 180 days at 25°C.

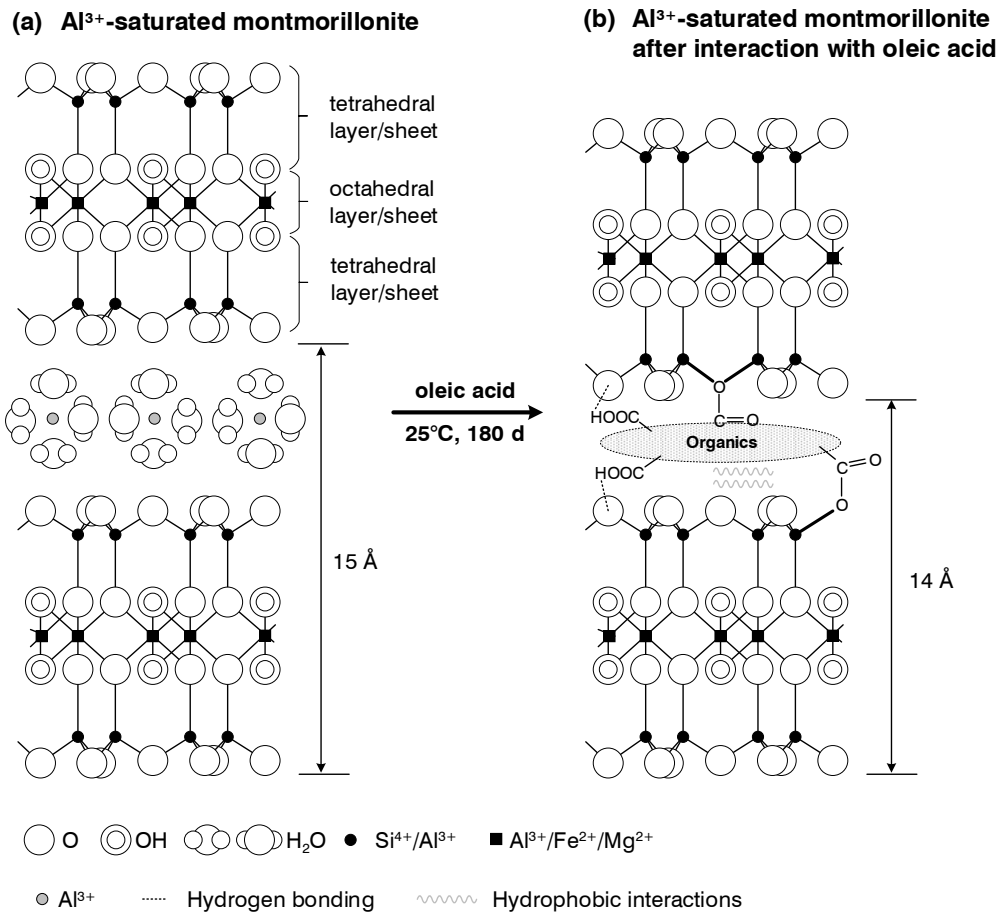

Fig. 3.8 The atomic models of (a) unreacted Al^{3+}-saturated montmorillonite and (b) Al^{3+}-saturated montmorillonite after reaction with oleic acid, showing the possible interactions between organic functional groups and the mineral surface.

Therefore, it remains a possibility that carboxyl groups are binding directly to central cations in the tetrahedral sheet/interlayer cations. However, if one were to rule out such a possibility, then interactions would most likely occur in an outer-sphere manner, with the carboxyl group interacting with hydroxyl groups on the mineral surface *via* hydrogen bonding, as well as hydrophobic interactions between the aliphatic chain of oleic acid and hydrophobic micro-sites present on the mineral surface (Laird and Koskinen, 2008).

The collapse of the interlayer could also possibly be due to displacement of co-ordinated water molecules surrounding interlayer Al^{3+} by oleic acid carboxyl functional groups *via* the potential exchange reaction:

$$[Al(H_2O)_6]^{3+} + n(HOOC{-}C_{17}H_{33}) \rightleftharpoons [Al(HOOC{-}C_{17}H_{33})_n(H_2O)_{6-n}]^{3+} + nH_2O \quad (3.6)$$

and possibly in deprotonated forms, with likely preference for exchange with hydrolysed water molecules forming hydroxyl groups (—OH) around Al^{3+}:

$$[Al(OH)_n(H_2O)_{(6-n)}]^{(3-n)+} + q(^{-}OOC—C_{17}H_{33}) \rightleftharpoons [Al(^{-}OOC—C_{17}H_{33})_q(OH)_{n-q}(H_2O)_{6-n}]^{(3-n)+} + qOH^{-} \quad (3.7)$$

It is possible that in this sense the carboxylic acid functional group (and more so the carboxylate group) may complex Al^{3+} more strongly, leading to overall shorter bonds, and therefore perhaps a slight collapsing of the smectite interlayer.

If it is indeed the case that molecules in the organic phase are able to collapse the smectite interlayer in the proposed manner, and this collapsed interlayer is "*locked*" in place, then this could represent another mechanism of organic molecule protection in nature by clay minerals, in a manner similar to the one suggested by Johnson *et al.* (2015). However, this would also possibly affect the reactivity or catalytic capacity of the smectite mineral phase, as the capacity to exchange cations potentially disappears. The implications are therefore two-tiered—on one hand there is the promotion of the formation of potentially stable or protected organo-clay complexes, whilst on the other hand, this limits any further transformation of lipids into stable, higher molecular weight compounds by the smectite mineral phase.

3.3.4 Trivalent Mn and Fe species

The dark red colour observed in the liquid phases of the redox-active clay-oleic acid cases has been interpreted previously as possibly being due to trivalent species of Mn and Fe (refer again to Figs 3.3 and 3.4). The presence of these trivalent species can be explained by two major possible pathways—*viz.* reductive dissolution of the Mn- and Fe-oxide (birnessite, pyrolusite and goethite) or direct chelation/complexation of Mn^{3+} and Fe^{3+} from the mineral structure. Complexation would also explain the presence of Fe^{3+} in the liquid phase of Fe^{3+}-saturated montmorillonite, as the Fe^{3+} cation is situated in the interlayer (no dissolution of the mineral phase in this case).

If these trivalent cations are forming *via* redox pathways, two possible steps are involved. The first step is the reductive dissolution of the mineral phase to form divalent Mn and Fe (Stone and Morgan, 1984*a*, 1984*b*; Ulrich and Stone, 1989):

For birnessite and pyrolusite, within the mineral surface structure:

$$\equiv Mn^{4+} + e^{-} \rightarrow \equiv Mn^{3+} \quad (3.8a)$$

$$\equiv Mn^{3+} + e^{-} \rightarrow (\equiv Mn^{2+}) \rightarrow Mn^{2+} \quad (3.8b)$$

with the overall reaction being the familiar Mn-oxide reductive dissolution reaction (equation 2.25*b*):

$$Mn^{4+}O_2(s) + 4H^+ + 2e^- \rightarrow Mn^{2+} + 2H_2O \quad (3.9)$$

In some octahedral sites of birnessite that already contain Mn^{3+}, the reaction would start from equation 3.8*b*. The overall reaction would simply be:

$$Mn^{3+} + e^- \rightarrow Mn^{2+} \quad (3.10)$$

For the Fe-containing phases, similar potential reduction reactions are possible:

for goethite (*e.g.* equation 2.25*c*):

$$Fe^{3+}O(OH)(s) + 3H^+ + e^- \rightarrow Fe^{2+} + 2H_2O \quad (3.11)$$

for Fe^{3+} in the smectite interlayer:

$$Fe^{3+} + e^- \rightarrow Fe^{2+} \quad (3.12)$$

The second step would involve the oxidation of the divalent cation to its trivalent form. This occurs *via* two possible reactions. The first is the one-electron reduction of lipid hydroperoxides (*e.g.* equation 2.11*a*):

$$L\text{—}O\text{—}OH + Mn^{2+} \rightarrow L\text{—}O^{\bullet} + Mn^{3+} + OH^- \quad (3.13a)$$

$$L\text{—}O\text{—}OH + Fe^{2+} \rightarrow L\text{—}O^{\bullet} + Fe^{3+} + OH^- \quad (3.13b)$$

where *L*—O—OH represents the lipid hydroperoxide which could have formed from either oleic acid being oxidized to its hydroperoxide by the redox-active mineral phases or by reaction with oxygen/reactive oxygen species (ROS), and *L*—O$^{\bullet}$ is an alkoxyl radical. One-electron oxidation of the divalent metal cation to form ROS would also yield the trivalent species (*e.g.* equation 2.20):

For Mn^{2+}:

$$Mn^{2+} + O_2 \rightarrow Mn^{3+} + {}^{\bullet}O_2^- \quad (3.14a)$$

$^{\bullet}O_2^-$ $\xrightarrow{-e^-}$ O_2 ($1\Delta_g$)

$^{\bullet}O_2^-$ $\xrightarrow{+H^+}$ $^{\bullet}HO_2^-$

For Fe^{2+}:

$$Fe^{2+} + O_2 \rightarrow Fe^{3+} + {}^{\bullet}O_2^- \begin{cases} \xrightarrow{-e^-} O_2\ (1\Delta_g) \\ \xrightarrow{+H^+} {}^{\bullet}HO_2^- \end{cases} \quad (3.14b)$$

As mentioned, another possible scenario to explain the presence of trivalent Mn and Fe species is the direct chelation or complexation of the trivalent Mn and Fe cations from birnessite, goethite and Fe^{3+}-saturated montmorillonite. This scenario is also a possibility because in the cases of the Fe-containing mineral phases, no significant reaction between these Fe-containing clays and oleic acid was observed with ATR-FTIR spectroscopy, indicating perhaps that no significant redox reactions (to form divalent Fe species and polymerised organic products) are occurring in the case of Fe-containing phases. This would also mean that lipid peroxidation products and ROS (that would lead to polymerisation) are not very prevalent in the liquid phase, so the reactions in equations 3.11, 3.12, 3.13*b* and 3.14*b*, whilst possible, are probably not occurring.

The idea that trivalent Mn and Fe species are being complexed directly from the mineral phase into the liquid phase is supported by the possibility that oxygen diffusion from the atmosphere through the entire column of the oily liquid phase to the mineral-liquid interface is probably quite limited (in industry some metals are stored in oil to prevent corrosion), meaning that an alternative non-redox mechanism may be taking place, leading to the presence of trivalent Mn and Fe species in the liquid phase. In this manner, oleic acid may not necessarily be transformed by especially the more non-reactive mineral phases (such as the Fe-containing clays), but instead acts as a ligand to complex and solubilise Mn^{3+} and Fe^{3+}. The reaction would have a general form (modified from Schwertmann, 1991):

$$\equiv Mn^{3+} + nLig. \rightarrow [Mn^{3+}(Lig._n)]^{(3-n)+} + \equiv\square \quad (3.15a)$$

$$\equiv Fe^{3+} + nLig. \rightarrow [Fe^{3+}(Lig._n)]^{(3-n)+} + \equiv\square \quad (3.15b)$$

where *Lig.* is a general ligand and $\equiv\square$ is an empty octahedral site in the mineral lattice/surface.

Referring back to Figs 3.3 and 3.4, another observation is made. In the hydrophobic layer floating above the pink pyrophosphate extract of the birnessite-oleic acid case (Fig. 3.3*a*), there appears to be a reasonably strong brown colouration. Extraction with 0.01 M HCl (*i.e.* pH = 2) instead of pyrophosphate (pH = 6.5), yields a dark yellow hydrophobic layer, floating above the clear

aqueous layer (Fig. 3.3*b*). Whilst there exists the possibility that dark brown oleic acid polymerised products have formed, especially if trimeric or rich in oxygen (den Otter, 1968), this brown colour in the hydrophobic layer disappears under acidic conditions, which may indicate the presence of solid (perhaps colloidal, <0.45 μm) Mn-oxide phases—either from dispersion of the original birnessite phase, or formed authigenically (*in-situ* in the original liquid phase). This solid Mn-oxide phase would dissolve reductively under acidic conditions, changing from brown solid particles to colourless Mn^{2+} (Brookins, 1988), and revealing the true possible colour (yellow) of the lipid polymerised/oxidation products.

Authigenic Mn-oxide would form from the oxidation of reduced Mn-species *via* the possible reactions:

Balanced in an alkaline medium:

$$Mn^{3+} + 4OH^- \rightarrow Mn^{4+}O_2(s) + 2H_2O + e^- \quad (3.16a)$$

$$Mn^{2+} + 4OH^- \rightarrow Mn^{4+}O_2(s) + 2H_2O + 2e^- \quad (3.16b)$$

Balanced in an acidic medium:

$$Mn^{3+} + 2H_2O \rightarrow Mn^{4+}O_2(s) + 4H^+ + e^- \quad (3.17a)$$

$$Mn^{2+} + 2H_2O \rightarrow Mn^{4+}O_2(s) + 4H^+ + 2e^- \quad (3.17b)$$

A possible oxidant in this reaction would be oxygen, as per the reduction reaction:

Balanced in an alkaline medium:

$$O_2(g) + 2H_2O + 4e^- \rightarrow 4OH^- \quad (3.18)$$

Balanced in an acidic medium:

$$O_2(g) + 4H^+ + 4e^- \rightarrow 2H_2O \quad (3.19)$$

However, as discussed before, it is questionable if molecular oxygen is able to diffuse all the way down to the mineral-liquid interface, through the oil column. It is thus more likely that authigenic Mn-oxide would possibly form from the oxidation of Mn^{3+} by lipid hydroperoxides (or other radical products) in a manner similar to that in equation 3.13*a*, or by oxidation of Mn^{2+}/Mn^{3+} by adsorption onto the residual birnessite surface.

No significant peaks for Mn-oxides were detected with ATR-FTIR spectroscopy, but it is possible that the relatively strong organic signal overshadows such peaks. It is also possible that the peaks observed at 1,565 and 1,410 cm^{-1} in the case of birnessite plus oleic acid (which were related to binding of the carboxylate group to the Mn-oxide surface), are in fact indicating binding of oleic acid to these suspended authigenic or dispersed Mn-oxide phases, instead of the original birnessite phase.

A similar observation is made in the case of the Fe-containing clays. In Figs 3.4*a* and *b*, upon extraction of the red liquid phases with EDTA, an orange-brown colour is observed in the hydrophobic layer, floating above the very pale yellow-orange aqueous layer. This is very similar to the case of the birnessite-oleic acid pyrophosphate extraction discussed previously. It is possible that in this case, solid Fe-oxide phases could be present in the hydrophobic layer (and thus in the original liquid layer). As was the case with birnessite plus oleic acid, these (possibly colloidal) Fe-oxides could be present either due to dispersion or by forming authigenically. When referring back to Fig. 3.2*d*, goethite appears to disperse automatically (without agitation) by simply adding the oleic acid liquid phase, with a significant amount of solid material located well above the solid-liquid interface. However, after 180 days, the original goethite appears to have settled (possibly by flocculation or aggregation) and the liquid phase seems to possess a much darker (even black) colour. This does lend to the possibility that any solid particles are probably authigenic in nature, and somewhat different to the original goethite.

When referring again to the ATR-FTIR spectrum of the goethite plus oleic acid case, however, no significant reaction appears to be taking place between goethite and oleic acid (unlike the case of birnessite plus oleic acid). This means that the possibility of several redox reactions occurring in this case is somewhat unlikely. As stated previously, the Fe^{3+} responsible for the colouration of the liquid phase is likely due to complexation by oleic acid, from the mineral structure, with no significant redox reactions between oleic acid and goethite being involved (unlike the case of birnessite plus oleic acid). Given that the goethite used in this study was fairly alkaline (pH $\sim$ 10; see Table 3.1), it is possible that authigenic Fe-oxides would most likely form from the precipitation reaction:

$$Fe^{3+} + 3OH^{-} \rightarrow Fe^{3+}(OH)_3(s) \tag{3.20}$$

where $Fe^{3+}(OH)_3$ represents a generalised form of Fe^{3+}-(oxy)hydroxides.

In the case of Fe^{3+}-saturated montmorillonite plus oleic acid, the hydrophobic layer floating above the aqueous layer which forms after extraction with EDTA does not appear to possess as dark an orange-brown colour as that of the goethite-oleic acid case (see Fig. 3.4*b*). Instead, this particular hydrophobic layer is more dark-yellow, similar to the dark-yellow observed when the bir-

nessite-oleic acid case was extracted with acid, and the yellow colours observed for the other clay-oleic acid cases. It is therefore more likely that in the case of Fe^{3+}-saturated montmorillonite plus oleic acid, a lot more of the Fe^{3+} present in the liquid phase is present in complexed form, with less authigenic Fe-oxide present, as opposed to the case of goethite plus oleic acid.

If it is indeed the case that solid Mn- and Fe-phases are present along with the soluble Mn and Fe species, then this would explain the observation that the hydrophobic layer appears to be fairly dark in comparison with the aqueous layer when the various liquid phases are extracted with pyrophosphate and EDTA. The aqueous layers of the extracts (the pale pink layer of the pyrophosphate extract and the pale yellow-orange colour of the EDTA extracts) also show a much less intense colour than the original dark red of the liquid phases from which they were extracted. The presence of solid Mn- and Fe-oxide phases would explain the pale colours of the aqueous layers of the extracted solutions, given that a significant portion of the colour-producing cations are trapped in the solid phase and therefore unavailable to be extracted during the addition of ligands such as pyrophosphate and EDTA. They are therefore not available to contribute to the colour of the extract solution. It is not that these ligands are not capable of dissolving the solid phase and eventually extracting the cations, but that such a process would probably be controlled by the kinetics of the dissolution reaction (it is useful to refer to studies such as Schwertmann (1991), Rueda *et al.* (1992) and Kostka *et al.* (1995) to learn more about the kinetics of these Mn- and Fe-oxide dissolution reactions).

It should be kept in mind that assertions mentioned here are often tested with very powerful techniques such as synchrotron-based X-ray absorption spectroscopy (XAS), which was not employed in the current work. Specific techniques such as X-ray absorption near edge structure (XANES) spectroscopy are able to distinguish specific oxidation states of Mn and Fe species.

It is entirely possible that not only trivalent states of Mn and Fe exist in these lipid-clay cases, but that polyvalent and polyphase Mn and Fe species occur—*viz.* $Mn^{4+}O_2(s)$, Mn^{3+}, Mn^{2+}, $Fe^{3+}(OH)_3(s)$, $Fe^{3+}O(OH)(s)$, Fe^{3+}, Fe^{2+}. When trying to elucidate a lipid-clay reaction mechanism, it is important that all of these species are considered, as they all play a role in the overall reaction and add several layers of complexity to the overall reaction mechanism.

3.4 Summary and conclusions

For the reactions of oleic acid with several soil clay fraction minerals, birnessite and gibbsite are the most reactive toward oleic acid, forming mostly polyester and dimer (possibly trimer) products, respectively. Factors that controlled the reactivity and polymer formation included redox potential, BET surface area and Lewis acidity. For birnessite, it is likely that the combination of higher BET

surface area than pyrolusite (53 *v.* 4 $m^2\ g^{-1}$) and greater redox potential than pyrolusite (due to the possible presence of Mn^{3+} in several cation sites) rendered it much more reactive toward oleic acid as a consequence. Goethite, which has a redox potential which is lower than both birnessite and pyrolusite, appeared much less reactive toward oleic acid. In contrast, gibbsite, which is not redox-active, was likely more reactive due to the Lewis acidity of Al^{3+}, which provided the capacity to dimerise (and perhaps trimerise) oleic acid.

For the minerals that contained redox-active species (typically Mn^{4+}, Mn^{3+} and Fe^{3+}), additional red and dark colouration was observed and attributed to possible solubilised trivalent (and perhaps even polyvalent) Mn- and Fe-species, resulting from a complex set of various redox reactions in combination with chelation/complexation reactions. Several rudimentary chemical tests and visual observations point strongly toward these Mn and Fe species being present.

Visual changes to some of the mineral phases observed—the dissolution of birnessite and the darkening of montmorillonite phases—also suggests changes occurring to the mineral phase during the reaction with oleic acid, or as a result thereof. The analysis of the darkened smectite phases post-reaction by XRD analysis reveal that the smectite interlayer had collapsed somewhat (15–14 Å) as a result of reaction with oleic acid. It is likely that several interactions between carboxyl functional groups on the organic molecules and the mineral surface or interlayer cations (such as hydrogen bonding/outer-sphere interactions and inner-sphere interactions) as well as hydrophobic interactions (between aliphatic structures and the mineral surface) are responsible for this alteration of the smectite mineral phase.

The formation of polymerised products, and various Mn- and Fe-species during these lipid-clay reactions, has potential implications for the formation of lipid-derived humic substances in natural soils as well as several (especially redox) reactions in the soil environment.

CHAPTER 4

Lipid-clay interactions: reaction mechanisms

4.1 Introduction

This chapter probes more deeply into the first aim (a) of this study—which is to identify the products that form when lipids (represented by the free fatty acid oleic acid) interact/react with minerals of the soil clay fraction—in order to reveal more information about the mechanism by which they form, thereby fulfilling the goals of aim the second aim (b) of this study.

From the observations of chapter 3, two main and diverging cases of oleic acid treatment with clays have emerged. The first are the clays that contain redox-active species (Mn^{4+}, Mn^{3+} and Fe^{3+}), producing dark red products along with polyesters, the most reactive clay toward oleic acid being birnessite. The second is the case of gibbsite, which produces non-oxygenous, dimers and possibly trimers. The second case (formation of dimers and trimers) follows an acid-catalysed mechanism that is well-established (den Otter, 1968). The first case (polyester formation in the presence of clays), however, proceeds *via* a mechanism that is currently mostly unknown, even though autoxidation mechanisms have been studied for several years (refer again to § 2.5.4).

For this reason, the focus is now shifted to the cases of the redox-active clays from chapter 3, with most of the focus being on the most reactive case—*viz.* the birnessite-oleic acid reaction. Whilst the mode of binding between oleic acid and the mineral surface was established by ATR-FTIR spectroscopy to be bidentate in the case of gibbsite, the mode of oleic acid binding to the mineral surface in the case of birnessite was not clearly distinguished (not enough clear binding was observed from the spectra of the Fe-phases or for pyrolusite, so for this aspect, birnessite is the focus). The red colours produced during the reaction can be analysed by ultraviolet-visible (UV-VIS) spectroscopy, and specific wavelengths could reveal more pertinent information about the nature of the organo-mineral or organo-metal cation complexes.

Further probing into the identity of the red-coloured products is performed by electron paramagnetic resonance (EPR) spectroscopy. This presents further information about the form in which the (dissolved/precipitated) metal ions (*e.g.* Mn^{4+}, Mn^{3+}, Mn^{2+}, Fe^{3+} and Fe^{2+}) occur within the liquid phase. This aims to shed more light on the red-coloured and dark products formed from the reaction between redox-active clays and oleic acid.

Observed changes to the birnessite phase itself is also considered in this chapter, as it was observed that birnessite was dissolved during the reaction with oleic acid. To investigate the structural changes to birnessite, XRD analysis is employed on unreacted birnessite and compared with the birnessite phase after reaction with oleic acid, in a manner very similar to the case of smectite darkening (see § 3.3.3, Fig. 3.7).

After studying the dark-red products and mineral phases, attention is turned to the polyesters that were formed by the reaction between birnessite and oleic acid. Although useful structural information has already been ob-

tained by ATR-FTIR spectroscopy, more structural information is also obtained with techniques such as direct-injection mass spectrometry (MS). This is achieved by analysing molecular masses of whole molecules and fragments. The direct injection MS technique was also employed to detect any other possible organic oleic acid oxidation products that may have formed alongside the polyesters. Further information about the nature of the polyester product formed is also obtained by investigating the thermal stability of these polymerised products with thermogravimetric analysis (TGA) and differential scanning calorimetry (DSC) analysis.

The preceding analyses cover the deeper probing of aim (a) of this study, and at this point, investigation into aim (b) can be initiated with the information gathered—*viz.* elucidating the reaction mechanism of the polyester-forming reaction between lipids and soil clays. For further clarification, and to investigate the possible importance of the initial surface-binding that is suspected to be a crucial part of the reaction, another experiment is conducted in which olive oil (mostly the triglyceride triolein; refer again to Table 2.2) instead of oleic acid is reacted with birnessite. The visual results are once again studied, but this time along with data obtained from gas chromatography—mass spectrometry (GC-MS). The GC-MS results compare the disappearance of oleic acid (analysed in the form of fatty acid methyl esters (FAMEs)) in both the case of olive oil (oleic acid in triglyceride form) reacting with birnessite as well as pure oleic acid (in free fatty acid form) reacting with birnessite.

4.2 Materials and methods

4.2.1 Materials

The materials used in this chapter are samples taken from the relevant reaction vials in chapter 3. For the purposes of the olive oil-birnessite experiment, commercial-grade extra-virgin olive oil (EVOO) was purchased.

4.2.2 Experimental procedure

The olive oil-birnessite reaction experiment was conducted in the same manner as the oleic acid-clay experiments in chapter 3. To a pre-cleaned glass vial (§ 3.2.2), 10.0 g of olive oil was added to 1.00 g of birnessite, mixed very gently until the clay phase was coated, and then allowed to react in the dark for 6 months at 25°C. A control vial was also set up in which 10.0 g of olive oil with no mineral phase added was allowed to react under the same conditions. As before, 2 mg of thimerosal was added to the vials in order to eliminate any biological interference. After reacting for 6 months, the vials were removed and photographed as before. Thereafter, the product formed in each vial was ana-

lysed by GC-MS. Similarly, an aliquot of the previously reacted birnessite-oleic acid liquid phase was sampled for GC-MS analysis in parallel.

4.2.3 Analytical methods

Ultraviolet-visible (UV-VIS) spectroscopy was performed using a Thermo Scientific Genesys 10uv Scanning UV-VIS spectrophotometer and VisionLite® software (Thermo Fisher Scientific, Waltham, MA, USA). Visible spectra were collected to detect the colour change due to the birnessite-oleic acid reaction as well as to detect the presence and form of dissolved/colloidal Mn. These spectra were collected directly without any dilutions to the sample by pipetting 1 ml aliquots from each reaction vial into separate 1.5 ml Plastibrand® plastic cuvettes, and then collecting spectra in the range 350–700 nm at 1 nm intervals. An empty plastic cuvette was used as baseline (background).

Electron paramagnetic resonance (EPR) was conducted on aliquots from the oleic acid-birnessite, oleic acid-goethite and oleic acid-Fe^{3+}-saturated montmorillonite experiments. These were compared to the spectra obtained for standard solutions of dissolved Mn and Fe. Analysis was performed using a Bruker EMX microX CW-EPR[8] spectrometer. Spectra were collected at the microwave X-band frequency of 9.87 GHz, using an attenuation factor of 20 dB[9] and a power level of 2,046 mW![10] The quality factor (Q) was 10,900. Spectra were collected in a Hall field (magnetic field) range of 2,750–4,250 G,[11] by extracting a sample from each vial using a Blaubrand® intraMARK 50 μl disposable glass micropipette as capillary tube and placing it in the microwave resonance chamber. Spectral acquisition and processing were performed using the Bruker WinEPR software package, version 2.22. X-ray diffraction analysis was performed as described before (§ 3.2.3).

Direct-injection mass spectrometry was also conducted on a sample taken from the reaction between birnessite and oleic acid. The analysis was performed using a Waters® Synapt™ G2 quadrupole time-of-flight (TOF) accurate mass spectrometer (Waters® Corporation, Milford, MA, USA). Mass spectral analysis was conducted by dissolving the sample in acetonitrile and then directly injecting the electrospray ionisation (ESI) probe into the acetonitrile stream. Mass spectra were collected at a scan rate of 0.2 s in the m/z range 100–2,000 in the electrospray positive mode (ESI+), using a cone voltage of 15 V, a capillary voltage of 2.5 kV, a desolvation temperature of 250°C and a desolvation gas (N_2) flow rate of 650 l h^{-1}. All the other MS settings were optimized for the best performance. Accurate mass determination was performed in real time using a lock mass flow rate of 2 μl min^{-1} and leucine enkephalin as

[8] CW-EPR = continuous-wave electron paramagnetic resonance
[9] dB = decibel, 10 times the base-10 logarithm of a quantity
[10] mW = milliwatt
[11] G = Gauss = 0.1 mT (millitesla)

lock mass, acquiring the lock mass data in 20 s intervals. Sodium formate (HCO_2Na) was used to calibrate the instrument. Data acquisition and processing was performed with MassLynx 4.1 software.

Thermogravimetric analysis (TGA) and differential scanning calorimetry (DSC) were performed on a TA Instruments (New Castle, DE, USA) Q500 TGA and Q20 DSC, respectively, employing a temperature range of 20–600°C for TGA and 25–200°C for DSC. Analyses were performed under a N_2 gas purge (50.0 ml min^{-1} flow rate), which for DSC, was coupled to an RCS cooling unit. Both TGA and DSC were performed at a heating rate of 10°C min^{-1}, whilst the DSC cooling rate was 5°C min^{-1}. Non-hermetically sealed aluminium pans were used during analyses. Data processing was performed using the Universal Analysis software package.

The amount of oleic acid remaining after olive oil and oleic acid had reacted with birnessite was determined by GC-MS. Oleic acid was derivatised to its FAME methyl oleate before analysis. The procedure was as follows: approximately 100 mg of sample was pipetted from each vial into a 15 ml glass test tubes with screw caps and Teflon® (PTFE)[12] septa. To each sample tube, 5 ml of hexane (C_6H_{14}) was added and the mixture was vortexed (Scientific Industries Vortex Genie) until the sample was dissolved within the hexane. Next, 100 μl of a C_{17}-standard (100 ppm[13] heptadecanoic acid in hexane) was added to each test tube and the samples were once again vortexed. The samples were ready for methylation at this point, and this was achieved by adding 1.00 ml of 10% sulphuric acid (H_2SO_4) in methanol (CH_3OH) to each sample, with each sample being vortexed again. Thereafter, samples were heated in a water bath at 80°C for 1 hour and then allowed to cool for 30 minutes. To each sample, 2.0 ml of a 20% sodium chloride (NaCl) solution was added and the samples vortexed. The samples now had two layers present in the test tube—a hexane layer containing the FAME floating above an aqueous layer. From each test tube, 1 ml of the hexane layer was transferred into crimp-cap GC vials for analysis. Five levels of calibration standards were generated by diluting a pre-mixed standard solution (250 μl Sigma-Aldrich® FAMES stock solution plus 250 μl hexane) as follows: *level 1*—20 μl standard solution plus 180 μl hexane, *level 2*—40 μl standard solution plus 160 μl hexane, *level 3*—60 μl standard solution plus 140 μl hexane, *level 4*—80 μl standard solution plus 120 μl hexane and *level 5*—100 μl standard solution 100 μl hexane. Standards were then vortexed and transferred to crimp-cap GC vials to be analysed with samples. Chromatographic separation was performed on an Agilent 6890N gas chromatograph (Agilent Technologies Inc., Palo Alto, CA, USA) coupled to an Agilent 5975B inert XL EI/CI mass selective detector (MSD). The GC-MS system was coupled to a CTC Analytics COMBI PAL autosampler. Analysis of the methyl oleate FAME was performed on a non-polar ZB-Semivolatiles Guardian (30 m, 0.25 mm in-

[12] PTFE = polytetrafluoroethylene

[13] ppm = parts per million, in this case mg kg^{-1}.

ternal diameter, 0.25 μm film thickness) B 7HG-G027-11 capillary column. Helium (He) was used as the carrier gas at a flow rate of 1 ml min^{-1}. The injector temperature was maintained at 250°C whilst 1 µl of the sample was injected in a split ratio of 5:1. The oven temperature was programmed as follows: 100°C for 5 min, then ramped up to 180°C at a rate of 5°C min^{-1}, held for 5min at 180°C, and finally ramped up to 330°C at a rate of 8°C min^{-1} where it was held for 5 min. The MS detector was operated in a full scan mode and the source and quad temperatures were maintained at 230°C and 150°C, respectively. The transfer line temperature was maintained at 280°C. The mass spectrometer was operated under EI mode at an ionization energy of 70 eV;[14] scanning from 35 to 500 m/z.[15] The limit of quantitation (LOQ) for methyl oleate FAME was 5.20 mg l^{-1} and the limit of detection (LOD) was 1.56 mg l^{-1}. Data acquisition and processing was performed using Agilent ChemStation software.

4.3 Results and discussion

4.3.1 Possible trivalent cation complexation—UV-VIS spectroscopy

The UV-VIS spectra for the redox-active oleic acid-clay experiments (namely, oleic acid plus birnessite, oleic acid plus pyrolusite, oleic acid plus goethite and oleic acid plus Fe^{3+}-saturated montmorillonite; see Fig. 3.2*b–d* and *j*), which produced the deep red colouration (virtually black for goethite), are depicted in Fig. 4.1. The spectrum for the oleic acid control experiment is also shown (Fig. 4.1) along with each experimental case for reference purposes.

The spectra for oleic acid plus pyrolusite, oleic acid plus goethite and oleic acid plus Fe^{3+}-saturated montmorillonite, whilst showing increased absorbance relative to the pure oleic acid spectrum (due to darkening), do not show any discernible peaks. The spectrum of oleic acid-goethite shows especially strong absorbance, given that it was also the darkest sample observed (Fig. 3.2*d*). Only the UV-VIS spectrum of the oleic acid-birnessite experiment showed any decipherable peaks (Fig. 4.1*a*), with a maximum at 490 nm and shoulder features at 460 and 510 nm.

Since the oleic acid-birnessite case is the sole case providing peaks in the UV-VIS spectral range during this discussion, the focus for now will centre around the possible complexation of Mn^{3+}. The complexation of Mn^{3+} by various ligands produces peaks in the UV-VIS spectrum at several wavelengths.

[14] eV = electron volt = 1.602×10^{-19} joule (J).
[15] m/z = mass-to-charge ratio

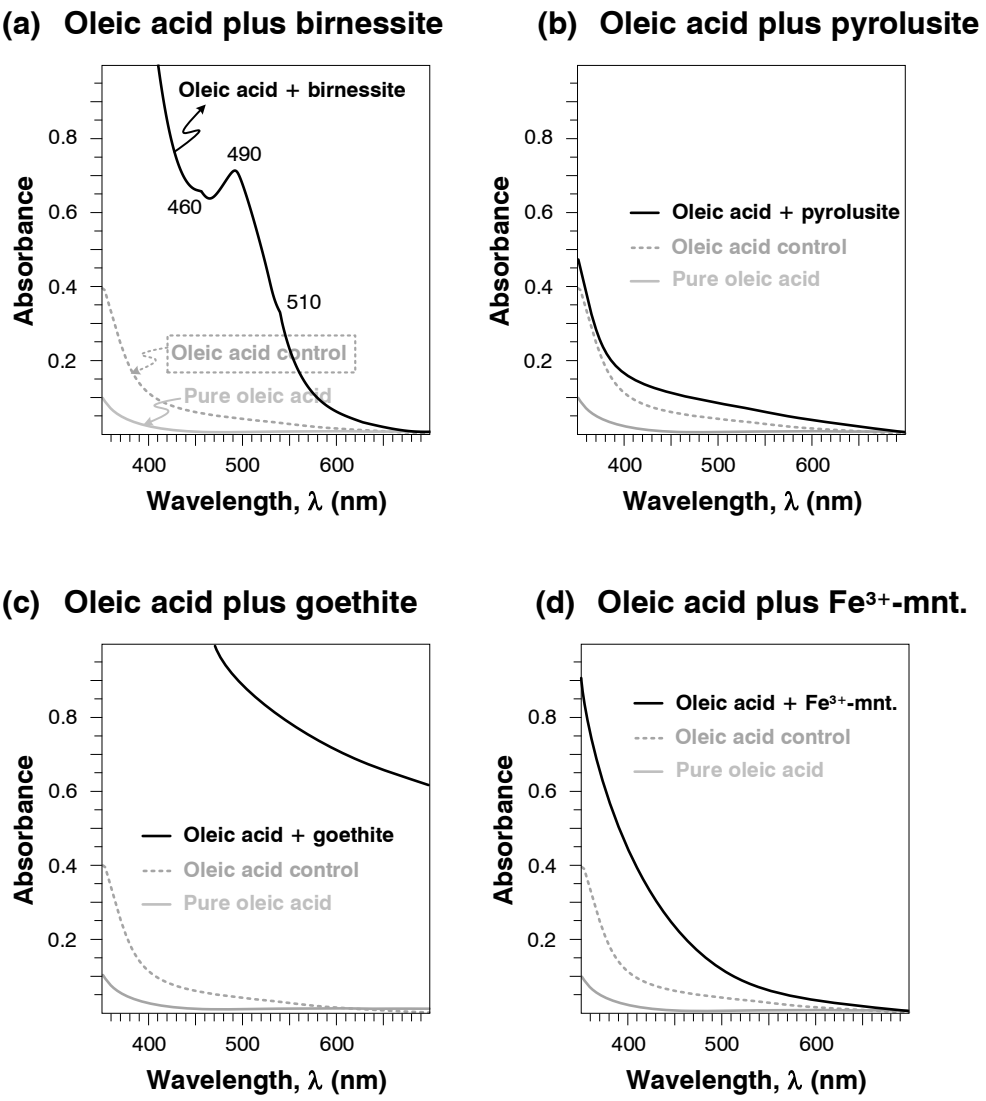

Fig. 4.1 Ultraviolet-visible (UV-VIS) spectra for the case of (a) birnessite plus oleic acid, (b) pyrolusite plus oleic acid, (c) goethite plus oleic acid and (d) Fe^{3+}-saturated montmorillonite (Fe^{3+}-mnt.) plus oleic acid experiments, sampled from the vials described in chapter 3 (incubation at 25°C for 6 months) and compared to pure oleic acid and the oleic acid control experiment.

When complexed with pyrophosphate and porphyrins, Mn^{3+} possesses a magenta (red) colour in solution. The magenta Mn^{3+}-pyrophosphate complexes have an absorption peak at 480–484 nm (Kostka *et al.*, 1995; Klewicki and Morgan, 1998; Oldham *et al.*, 2015), whilst red-orange Mn^{3+}-porphyrin complexes absorb at 468 nm (Madison *et al.*, 2011; Oldham *et al.*, 2015, 2017). Magenta-coloured protonated Mn^{3+}-HEDTA complexes (pH $<$ 5.3) absorb at 488 nm, whilst more red-orange-coloured Mn^{3+}-$EDTA^{-}$ complexes (pH $>$ 5.3) absorb at 450 nm (Klewicki and Morgan, 1998). The magenta-coloured complex of Mn^{3+}-2,3-dihydroxypyridine absorbs at 520 nm (Oldham *et al.*, 2015), whilst

the more yellow-coloured Mn^{3+}-citrate complexes absorb at 430 nm (Klewicki and Morgan, 1998). Several Mn^{3+}-complexes absorb at lower wavelengths too—Mn^{3+}-ferrozine[16] (282 and 316 nm, a doublet peak) Mn^{3+}-desferrioxamine-B (310 nm), Mn^{3+}-dopamine[17] (302 nm) and Mn^{3+}-tiron[18] (292 nm) (Oldham *et al.*, 2015). Benzoic acid derivatives and polyphenols produce blue-green complexes with Mn^{3+}. The blue complex of 2,3-dihydroxybenzoic acid with Mn^{3+} absorbs at 410 and 622 nm, whilst the green complex of Mn^{3+} and catechol (1,2-dihydroxybenzene) absorbs at 356 and 654 nm (Oldham *et al.*, 2015).

The wavelengths observed in Fig. 4.1*a* are very close to those reported for protonated MnHEDTA (488 nm) and deprotonated $MnEDTA^{-}$ (450 nm) by Klewicki and Morgan (1998) as well as the 520 nm for Mn^{3+}-2,3-dihydroxypyridine (Oldham *et al.*, 2015). It is possible that the correspondence of these wavelengths observed with known wavelengths for several Mn^{3+}-complexes with organic ligands may reveal information about the manner in which Mn^{3+} is present in the liquid phase of the birnessite-oleic acid vial—*e.g.* complexed *via* certain specific functional groups. It is possible that the carboxyl groups present on oleic acid (and potentially its products) complex with the free Mn^{3+} cations, perhaps in a similar manner to carboxyl-group-containing ligands such as EDTA and citrate (Klewicki and Morgan, 1998).

If the Mn^{3+} cation is complexed/chelated by carboxylic acid functional groups as suggested, then such interactions involve π-electrons and π-bonds which, through resonance, would yield very similar structures to those possible with the carboxylic acid (carboxyl) moiety on EDTA (Fig. 4.2*a*). The small shoulder feature at 510 nm could also be indicative that there are dihydroxy groups in the region of the *cis*-double bond between carbons 9 and 10 on oleic acid, due to peroxidation reactions. If a double bond is still present between or near the dihydroxy group (possible *trans*-configuration, see peroxidation mechanisms in § 2.5.4), it is possible that such a structure could mimic the one found on 2,3-dihydroxypyridine, especially through resonance (Fig. 4.2*b*).

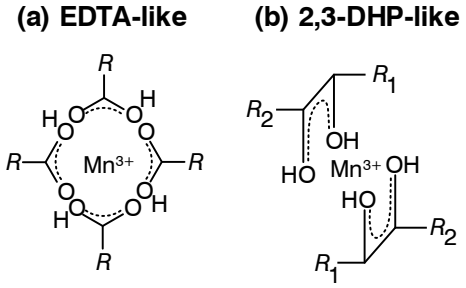

◀ **Fig. 4.2** Possible complexation structures for Mn^{3+} either similar to complexation by (a) EDTA or (b) 2,3-dihydroxypyridine (2,3-DHP). Where *R* represents the rest of the molecular structure ($R_1 \neq R_2$).

[16] Ferrozine = 3-(2-pyridyl)-5,6-diphenyl-1,2,4-triazine-*p,p'*-disulphonic acid monosodium salt hydrate

[17] Dopamine = 3-hydroxytyramine

[18] Tiron = 4,5-dihydroxybenzene-1,3-disulfonate

If only one hydroxy group is present, it is possible that keto-enol resonance structures could complex Mn^{3+} as well. These observations do not prove unequivocally that Mn^{3+} is present in soluble/complexed form in this specific manner but do suggest that it is certainly possible.

Further investigation into Mn^{3+} possibly being present in soluble/complexed form in the birnessite-oleic acid liquid phase was also conducted by collecting a UV-VIS spectrum of the pyrophosphate extract of the liquid phase, conducted in chapter 3 (see Fig. 3.3*a*). This spectrum was compared to a spectrum of a 9 mM Mn^{3+}-acetate dihydrate ($(CH_3COO)_3Mn{\cdot}2H_2O$) in 50 mM pyrophosphate solution (pH = 6.5), as illustrated in Fig. 4.3:

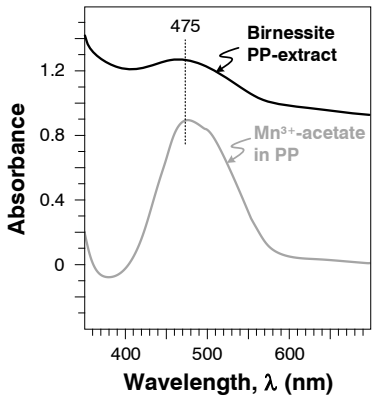

◀ **Fig. 4.3** Visible (VIS) spectrum of the 50 mM pyrophosphate extract of the liquid extracted from the birnessite vial versus the VIS spectrum of 9 mM Mn^{3+}-acetate in 50 mM pyrophosphate. PP = pyrophosphate.

When compared, both UV-VIS spectra show a matching peak at 475 nm. It is therefore possible that Mn^{3+} is present in the liquid phase, but since pyrophosphate can also extract or complex various organic compounds, the red colouration cannot definitely be attributed to the presence of Mn^{3+}, although highly likely given the previous observation of the unstable behaviour of the red colour under acidic (Fig. 3.3*b*), basic (Fig. 3.3*c*) and reducing conditions (Fig. 3.3*d*). The observations from chapter 3 (specifically Fig. 3.3) combined with the birnessite-oleic acid UV-VIS spectrum in Fig. 4.1*a*, demonstrates that in all likelihood polyvalent forms of Mn are present in the liquid phase, with a complex interplay of redox reactions possibly taking place between soluble Mn^{2+}, Mn^{3+} and MnO_2. Again, powerful techniques such as synchrotron-XAS could be employed in future investigations of this reaction mechanism.

The presence of Mn^{3+} in the liquid phase could originate *via* two possible pathways. The first is that oleic acid could be acting as a ligand and complexing Mn^{3+} found in birnessite octahedral sites, removing Mn^{3+} into the liquid phase directly through a complexation-dissolution mechanism, in a manner very similar to goethite dissolution by ligands such as EDTA and citrate in which Fe^{3+} is extracted from surface sites directly (Schwertmann, 1991). The second pos-

sible pathway to explain the presence of Mn^{3+} is the *in-situ* oxidation of Mn^{2+} released from the birnessite surface in a mechanism similar to the reduction of birnessite by aromatics (Stone and Morgan, 1984*a*, 1984*b*; Stone, 1987; Ulrich and Stone, 1989). As discussed before, the diffusion of oxygen into the liquid phase is probably quite limited, so the likely *in-situ* redox process forming Mn^{3+} in the liquid phase is probably the one electron reduction (oxidation of Mn^{2+}) of the unstable hydroperoxides of lipids (L) (modified from equation 2.11*a*):

$$L\text{—O—OH} + Mn^{2+} \rightarrow L\text{—O}^{\bullet} + Mn^{3+} + OH^{-} \tag{4.1}$$

or by the oxidation of Mn^{2+} to Mn^{3+} by the birnessite (or possibly authigenic Mn-oxide) surface itself:

$$\begin{array}{l} (Mn^{4+})_{n-1}(Mn^{3+})_{8-n}O_{14} \leftarrow \\ \\ (Mn^{4+})_{n}(Mn^{3+})_{7-n}O_{14} \leftarrow \end{array} \begin{array}{l} Mn^{2+} \\ \\ Mn^{3+} \end{array} \tag{4.2a}$$

and/or:

$$\begin{array}{l} (Mn^{4+})_{n}(Mn^{3+})_{6-n}(Mn^{2+})O_{14} \leftarrow \\ \\ (Mn^{4+})_{n}(Mn^{3+})_{7-n}O_{14} \leftarrow \end{array} \begin{array}{l} Mn^{2+} \\ \\ Mn^{3+} \end{array} \tag{4.2b}$$

Another possible mechanism is the reduction of Mn^{4+} in surface sites to Mn^{3+}:

$$\equiv Mn^{4+} + e^{-} \rightarrow \equiv Mn^{3+} \tag{4.3}$$

This Mn^{3+} would then either be complexed into the liquid phase directly (refer again to equation 3.15*a*), or it undergoes the one-electron reduction reaction with oleic acid as before to form Mn^{2+} which is then released and oxidised to Mn^{3+} at a later stage (*e.g.* equation 4.1). This is likely the dominant mechanism in pyrolusite which, unlike birnessite, contains no octahedral Mn^{3+} initially.

The red colour present in the liquid phase (Figs 3.2*b* and 4.4*a*) was observed to be fairly stable, as long as the liquid phase remained in contact with birnessite (*i.e.* was left in the vial). Disappearance of the red colour was observed when small aliquots of the liquid were pipetted out of the vial into a small 1.5 ml Eppendorf® microcentrifuge tube or glass HPLC vial for example. The colour that remains after the red colour disappears is dark yellow (Fig. 4.4*b*). A similar red colour liquid is obtained when mixing *c*. 100 mg of Mn^{3+}-acetate dihydrate ($Mn(CH_3COO)_3{\cdot}2H_2O$) into 10 g oleic acid (Fig. 4.4*c*):

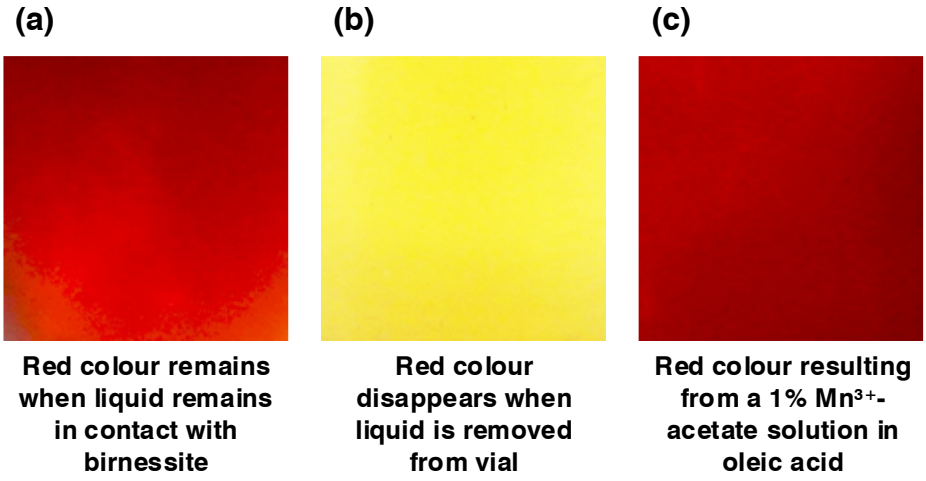

Fig. 4.4 The (a) red colour of the birnessite-oleic acid liquid phase, (b) the yellow colour that remains after the red colour disappears, and (c) the red colour formed when 100 mg of $Mn(CH_3COO)_3{\cdot}2H_2O$ is mixed into 10 g of oleic acid.

The disappearance of the red colour is possibly an indication that the oleic acid-Mn^{3+} complex is not as stable as the pyrophosphate or EDTA complexes of Mn^{3+}. It is possible that Mn^{3+} itself is reacting with one or more radical species generated by the lipid peroxidation reaction (§ 2.5.4) or initiated by the oxidative capacity of birnessite. It therefore appears that the red colour (probably at least partially due to soluble Mn^{3+}) remains intact as long as there is a compensating flux of Mn^{3+} or Mn^{2+} into the liquid phase from the dissolving Mn-oxide phase, as it replaces the Mn^{3+} consumed by reaction with lipid radical species. A UV-VIS spectrum (Fig. 4.5) of the yellow liquid (originally red when in contact with birnessite) was found to be virtually identical to the UV-VIS spectrum of the control experiment (Fig. 4.1) with no useful or discernible peaks:

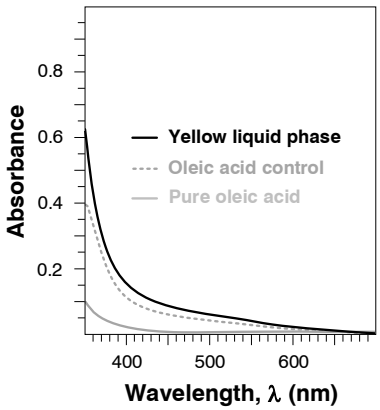

◀ **Fig. 4.5** The UV-VIS spectrum of the yellow-coloured liquid phase originating from the red liquid phase of the birnessite-oleic acid experiment upon separation from birnessite.

From the data of this section, combined with the observations of chapter 3, it has become evident that Mn (and possibly but likely less so Fe) is possibly present in polyvalent/multivalent forms. The following section employs EPR spectroscopy to investigate the possible presence of multivalent Mn and Fe forms further. It will also possibly shed more light on the case of Fe^{3+} (and Fe^{2+}) especially, which could not be discussed due to the observed general lack of Fe-phase (*e.g.* goethite) reactivity toward oleic acid.

4.3.2 Multivalent forms of Mn and Fe—EPR spectroscopy

Aliquots from the liquid phases of the redox-active oleic acid-clay experiments (namely, oleic acid plus birnessite, oleic acid plus goethite and oleic acid plus Fe^{3+}-saturated montmorillonite) were analysed using EPR spectroscopy (Fig. 4.6). The pyrolusite-oleic acid treatment was omitted in order to investigate only the most reactive cases and obtain possibly the most demonstrative spectra.

A 1 mg ml^{-1} manganous sulphate hydrate ($MnSO_4 \cdot H_2O$) solution (*i.e.* the soluble Mn^{2+} cation) produces a strong and sharp 6-line hyperfine structure (Krishnamurti and Huang, 1988; Jokic *et al.*, 2001*b*; Matocha *et al.*, 2001; Khorobrykh *et al.*, 2013), centred at a magnetic field of approximately 3,500 Gauss (350 mT)[19] and around 600 Gauss wide (Fig. 4.6). This is because it contains 5 unpaired electrons in its 5 *d*-orbitals (using noble gas core spdf notation: Mn^{2+}: $[Ar]3d^5$). The solution is colourless to very pale pink, which would mean Mn^{2+} essentially contributes no significant (red) colouration to the liquid phase of the birnessite-oleic acid case, even if present in appreciable quantities.

The EPR spectrum for the birnessite-oleic acid liquid phase shows a similar 6-line hyperfine structure to that of the Mn^{2+} spectrum, albeit it somewhat distorted. The peak positions of the 6-line structure match in both spectra, leading to the conclusion that Mn^{2+} is present in the liquid phase of the birnessite-oleic acid treatment case. This supports the theory that the reaction mechanism between oleic acid and birnessite contains one or several redox steps, involving the reduction of the Mn-oxide (with Mn^{3+} as intermediate or located in octahedral sites), or soluble Mn^{3+} present (complexed) in the liquid phase, to Mn^{2+}. There are no definitive explanations for the distortions observed on the spectrum. The distortion near the centre of the hyperfine structure is possibly from organic radicals present in the reaction vial, such as lipid-peroxyl radicals for example.

[19] mT = millitesla

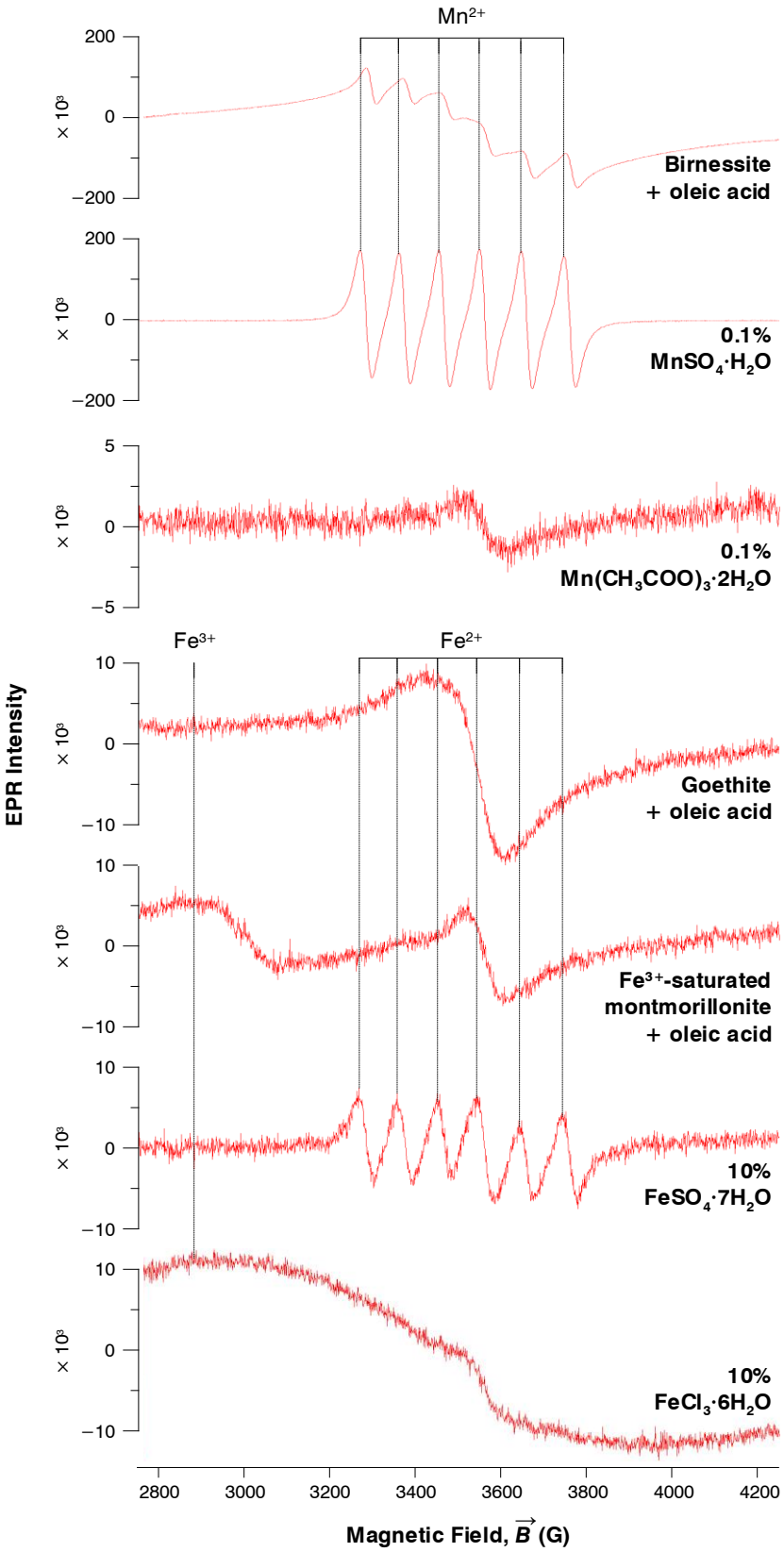

Fig. 4.6 The obtained EPR spectra of the liquid phases of the most reactive redox-active clay-oleic acid treatments, compared with standard solutions of Mn^{2+}, Mn^{3+}, Fe^{2+} and Fe^{3+} species.

The distortions close to the peaks of the Mn^{2+} structure could be the detection of Mn^{3+}, but unfortunately this could not be corroborated as the comparative spectrum for soluble Mn^{3+} (a 1 mg ml^{-1} manganese triacetate dihydrate ($Mn(CH_3COO)_3{\cdot}2H_2O$) solution in 50 mM pyrophosphate at pH 6.5) did not produce any definitive peaks that could be compared to the birnessite plus oleic acid spectrum. Studies of Mn^{3+} by EPR spectroscopy are usually conducted at low temperatures (*e.g.* 10 K; Dismukes *et al.*, 1987) and on solids (see *e.g.* Azamat *et al.*, 2012). The equipment required for cold temperature EPR spectroscopy was not available for this study unfortunately.

For the cases of goethite and Fe^{3+}-saturated montmorillonite, no peaks relating to Fe^{2+} were detected in the liquid phases of these treatments, when the EPR spectra are compared with the spectrum of 100 mg ml^{-1} ferrous sulphate heptahydrate ($FeSO_4{\cdot}7H_2O$) solution. The EPR spectrum for this Fe^{2+} solution also shows a 6-line hyperfine structure, similar to the spectrum of Mn^{2+}, albeit a much weaker signal. The solution was prepared right at the moment of analysis, since it was found that the solution oxidizes rapidly within minutes, and the subsequent 6-line signal disappears accordingly. The spectrum of the Fe^{3+} solution in the form of 100 mg ml^{-1} ferric chloride hexahydrate ($FeCl_3{\cdot}6H_2O$) showed a broad peak with its maximum in the region of 2,900 G. This peak was detected in the case of the Fe^{3+}-saturated montmorillonite-oleic acid liquid phase but not for the goethite-oleic acid liquid phase (Fig. 4.6). This peak was similar to a peak found by Mugnol *et al.* (2008), which was also accompanied by a peak at *c.* 2,250 G (outside the range of the EPR measurements in this study). The spectra collected by Mugnol *et al.* (2008) were collected at a temperature of 11 K, however, bringing into question the reliability of the peak observed in Fig. 4.6. As the spectra were not collected under optimal conditions for Fe^{3+} detection, it is possible that the peak did not appear for those reasons, not because no Fe^{3+} was present. Furthermore, the peak located at 2,250 G (not present in this study) in Mugnol *et al.* (2008) appears to be a stronger peak and the preferred peak for studying the behaviour of Fe^{3+} by EPR spectroscopy.

Whilst conclusive evidence for the presence of Fe^{3+} and Fe^{2+} could not be gathered with EPR spectroscopy and thus confirmed unequivocally, this technique has nonetheless demonstrated that divalent Mn^{2+} is present in the liquid phase of the birnessite-oleic acid experiment, revealing crucial information required when elucidating a reaction mechanism for Mn-oxide clays reacting with oleic acid. The presence of Mn^{2+} confirms that for birnessite, the reaction with oleic acid to form polyesters must, at some point, involve a Mn-oxide or Mn^{3+} reduction step to Mn^{2+}.

Considering the ATR-FTIR spectroscopy findings for the birnessite-oleic acid case in chapter 3, together with the fact that Mn^{2+} is present in the liquid phase, the initial steps of a reaction mechanism can be proposed at this point. The findings of ATR-FTIR spectroscopy revealed the mode of binding between

oleic acid and the Mn-oxide surface (or chelating Mn^{3+}) as occurring through the carboxylate group. It is therefore possible that the electron transfer step of the reaction occurs *via* a cation-carboxyl bridge, very similar in nature to the one proposed by Stone (1987) and Ulrich and Stone (1989) using chlorophenols as an example (see equation 2.39*a*):

Mn^{3+} in birnessite surface sites:

$$\equiv Mn^{3+}\text{—}OOC\text{—}R \rightleftharpoons (\equiv Mn^{2+}, {}^{\bullet}OOC\text{—}R) \tag{4.4}$$

Chelated Mn^{3+}:

$$Mn^{3+}\text{—}OOC\text{—}R \rightleftharpoons Mn^{2+} + {}^{\bullet}OOC\text{—}R \tag{4.5}$$

where *R*—COO— is oleic acid bonded to Mn^{3+} either located in birnessite surface sites ($\equiv Mn^{3+}$) or chelated and $^{\bullet}OOC$—*R* is an oleic acid radical. For Mn^{4+}, an additional first step prior to the reaction in equation 4.4 could also lead to the formation of radicals, if oleic acid is the reductant:

$$\equiv Mn^{4+}\text{—}OOC\text{—}R \rightleftharpoons (\equiv Mn^{3+}, {}^{\bullet}OOC\text{—}R) \tag{4.6}$$

It has also been proposed previously that Mn^{4+} in surface sites ($\equiv Mn^{4+}$) could be reduced to Mn^{3+} in these surface sites ($\equiv Mn^{3+}$). At this point, the formed radicals could abstract hydrogen atoms from other oleic acid molecules and other oleic acid molecules could also be transformed into radicals, with the reaction initiating at the point represented in equation 4.4. It is becoming evident that the reaction between birnessite and oleic acid may involve a series of dynamic and complex sorption-desorption steps, coupled with several redox steps.

Once the point of reduction of surface site Mn^{3+} ($\equiv Mn^{3+}$) to surface site Mn^{2+} ($\equiv Mn^{2+}$) is reached (equation 4.4), an additional step leads to the release of Mn^{2+} into the liquid phase:

$$\equiv Mn^{2+}\text{—}OH_2 \rightleftharpoons Mn^{2+} + \equiv\square \tag{4.7}$$

where, as before, $\equiv\square$ refers to a vacant site in the mineral surface. At this point a propagation step is potentially initiated by Mn^{2+} being oxidised during the one-electron reduction of lipid hydroperoxides:

$$L\text{—}O\text{—}OH + Mn^{2+} \rightarrow L\text{—}O^{\bullet} + Mn^{3+} + OH^{-} \tag{4.8}$$

The Mn^{2+} cations reduce the lipid hydroperoxide to a lipid-alkoxy radical that could abstract another α-hydrogen from another lipid molecule, generating

another lipid radical ($L^{\bullet}$) ready for peroxidation or a coupling reaction with other radicals.

4.3.3 Changes to the birnessite phase—XRD analysis

When considering again the various treatments conducted in chapter 3, two minerals which had undergone significant visual changes after reaction with oleic acid stand out, namely birnessite which had undergone appreciable dissolution and the montmorillonite phases, which had darkened considerably (refer again to Fig. 3.2). In the case of the montmorillonite phases, it was found that the smectite interlayer had collapsed slightly (15 Å down to 14 Å) due to interaction with oleic acid (refer again to § 3.3.3 and Figs 3.7–3.8).

Given the valuable information that was obtained from XRD analysis in the particular case of smectites reacting with oleic acid, it was decided that the similar approach of performing XRD analysis on birnessite which had reacted (partially dissolved) with oleic acid might likewise provide pertinent information with respect to the reaction mechanism of the birnessite-oleic acid reaction. In the same manner as before, the XRD diffractogram of birnessite post-reaction was compared with the diffractogram of unreacted birnessite (refer again to Appendix B, Fig. B.1*a*).

The XRD diffractograms obtained for birnessite before the reaction compared with after the reaction are depicted in Figs 4.7*a* and *b*, respectively. The diffractogram for birnessite after the reaction (Fig. 4.7*b*) shows some marked differences when compared with the diffractogram of unreacted birnessite (Fig. 4.7*a*). The first difference is the disappearance of several peaks related to the basal reflections of the layer structure of birnessite (Cheney *et al.*, 2009), namely the peak at 7 Å (related to $hkl = [001]$) and 3.5 Å (related to $hkl = [002]$). There are also several new peaks that arise at 4.39 Å, 3.07 Å, 2.40 Å, 2.16 Å, 1.83 Å, 1.52 Å and 1.35 Å (Fig. 4.7*b*). These peaks correspond to the Mn-oxide cryptomelane (Hudson Institute of Mineralogy, 2018*h*), which is a K^+-containing end-member of the hollandite group. The presence of K^+ arises from the fact that the original mineral phase reacted was K^+-birnessite as synthesized by the method of McKenzie (1971).

A change in mineral structural morphology is a common observation during the various reactions of Mn-oxides such as those involving synthetic birnessite phases (Elzinga, 2011). The transformation of birnessite to cryptomelane can occur thermally at relatively high temperatures (>600°C; Chen *et al.*, 1986), However, this transformation can occur at much lower temperatures when other chemical species are involved. For example, during the adsorption of Mn^{2+} by birnessite, Tu *et al.* (1994) found that the birnessite phase transformed to cryptomelane at approximately room temperature (21°C) and at a pH of around 4.

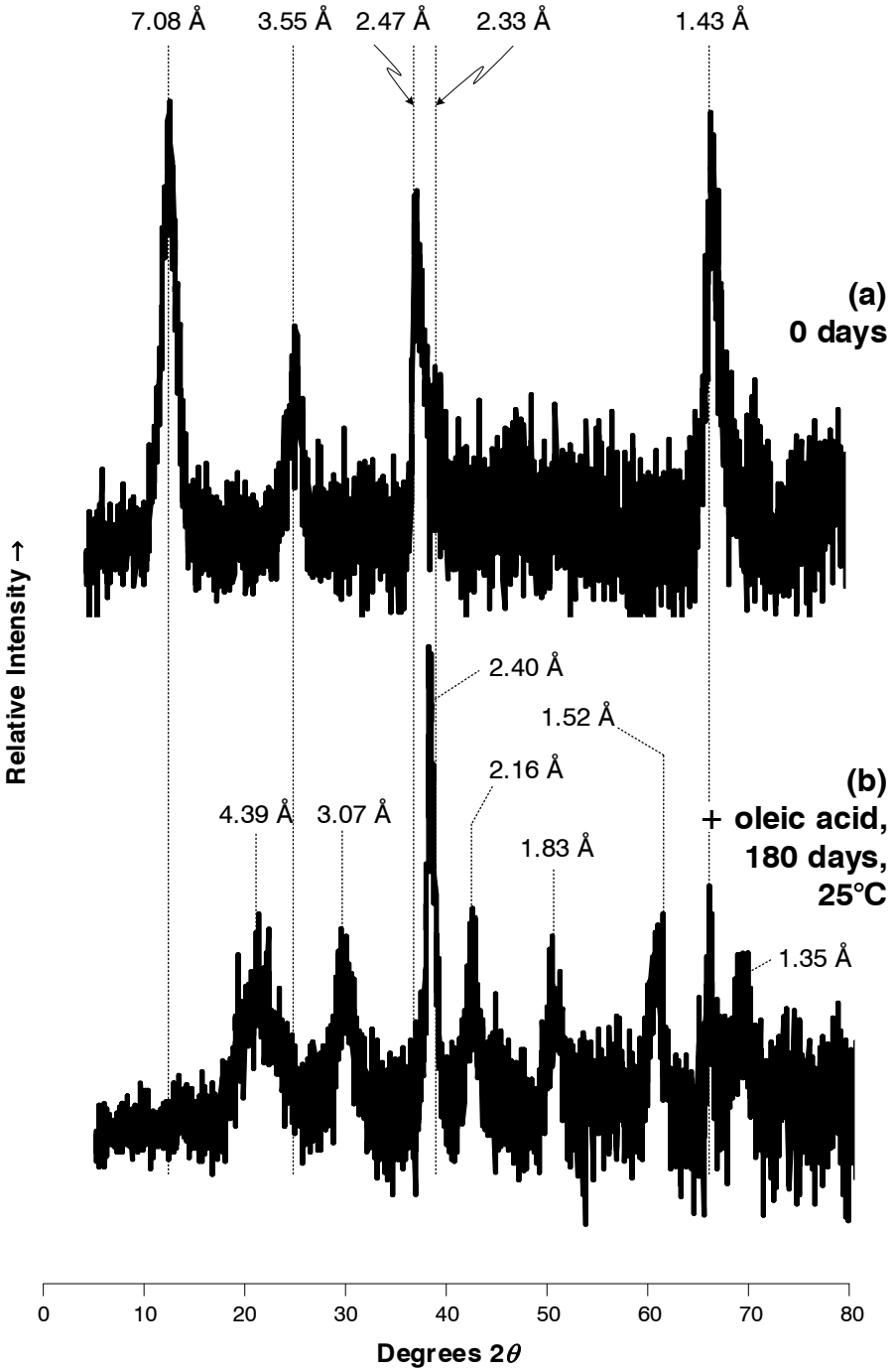

Fig. 4.7 The X-ray diffractograms of (a) birnessite before and (b) birnessite after reaction with oleic acid.

What was also interesting to note is that Tu *et al.* (1994) found no direct oxidation of Mn^{2+} by birnessite had actually occurred, and that Mn^{2+} remained adsorbed to the birnessite surface. They proposed that it was more likely Mn^{2+} was eventually rather incorporated into the Mn-oxide structure than oxidised, and this led to alteration of the Mn-oxide mineral structure. These observations are in contrast to those found in *this* current work, as Mn^{2+} is clearly present

in the liquid phase (detected by EPR spectroscopy), relatively far removed from the birnessite surface.

It is not entirely clear at this point how the birnessite in this study is being transformed to cryptomelane. One possibility is that some of the Mn^{2+} formed within the surface sites ($\equiv Mn^{2+}$) by reactions such as the one in equation 4.4 is not actually being released (equation 4.7) but is retained in the birnessite structure, instead facilitating the transformation to cryptomelane. It is therefore possible that *in-situ* formation of free Mn^{2+} in the liquid phase by the possible reaction between oleic acid and chelated Mn^{3+} (equation 4.5) is a much more important reaction than first anticipated. This pathway of Mn^{2+} formation perhaps even accounts for the majority of Mn^{2+} observed in the liquid phase, with the primary role of surface Mn^{2+} ($\equiv Mn^{2+}$) formed *via* the pathway in equation 4.4 being incorporation into birnessite and subsequent transformation of birnessite into cryptomelane. It is also therefore possible that direct complexation of surface Mn^{3+} ($\equiv Mn^{3+}$) into the liquid phase may perhaps be a more important Mn-release pathway than that of equation 4.7.

4.3.4 Further polymer characterisation—TGA and DSC results

The focus now shifts from the metal cations present in the liquid phase and the mineral phases back to the polymer products formed from the reaction between oleic acid and clay phases first described in chapter 3. More specifically, attention is directed at this point to the polyester product forming from the reaction between birnessite and oleic acid. The use of TGA and DSC is employed in this section to shed more light on the chemical nature of the polyester, including its thermal stability. The resulting curves are depicted in Fig. 4.8:

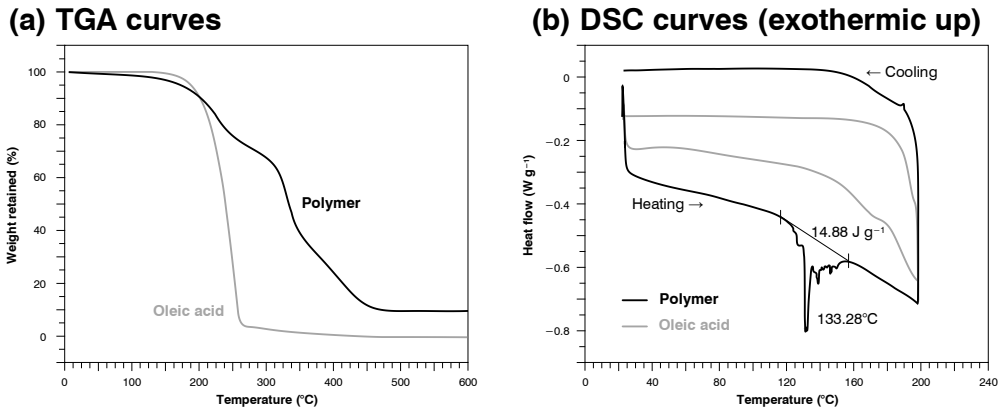

Fig. 4.8 The (a) TGA and (b) DSC curves of oleic acid and the polymer produced from the reaction of oleic acid with birnessite.

The TGA curve of oleic acid shows that it loses over 90% of its weight in one step, between approximately 150°C and 350°C, whilst the TGA curve of the polymer product shows three features. The first is a weight loss event at 150–200°C, which is associated with either the loss of oleic acid poorly bound to a mineral surface (Jadhav *et al.*, 2013) or the first weight loss event of a polyester polymer (Sander *et al.*, 2012). The second weight loss event of 280–350°C represents the oleic acid that has been bound to the surface of birnessite, through the surface exchange complex. This conclusion is drawn since this event corresponds well to the findings of Jadhav *et al.* (2013) who found a similar event on their TGA curve when studying oleic acid bounded to magnetite nanoparticles. The third weight loss event between 350–450°C represents another weight loss event for polyesters (Sander *et al.*, 2012). The polymer product is more thermally stable than the original oleic acid, but still falls below what is considered part of the "*refractory carbon pool*" (only decomposes above 550°C; Johnson *et al.*, 2015).

The DSC curve for oleic acid shows no discernible phase transitions in the temperature range of acquisition (25–200°C). This is because the melting point of oleic acid is generally in the order of approximately 13°C (Knothe and Dunn, 2009). The DSC curve for the polymer product, however, shows an endothermic phase transition at 133°C, which was interpreted as its melting point. This is very close to the melting point for polyesters of 130°C found in the study by Sander *et al.* (2012). The calculated heat of fusion (ΔH_f) for this transition is 14.88 J g^{-1}. This supports the idea further that the reaction of oleic acid with birnessite produces stable, ester-bonded polymerised products (polyesters), first discovered from the ATR-FTIR results (see Figs 3.5 and 3.6). Together with the TGA results, the DSC curves confirm the existence of thermally stable polyester structures, with some of the carboxyl groups still bounded to the birnessite surface.

4.4 Reaction mechanism

4.4.1 Selection of model case for mechanism demonstration

From the data acquired throughout this chapter and chapter 3 (aim (a) of this study), a reaction mechanism for the reaction between oleic acid and soil clays can be proposed (aim (b)). Since the case for birnessite reacting with oleic acid has consistently produced the most conclusive data (compared to the Fe^{3+}-phases for example) as well as the most novel polymer products (polyesters *versus* the known dimers/trimers produced by non-redox active clays), the reaction mechanism proposed will centre around the birnessite-oleic acid reaction, and the various Mn species produced as a result of it.

4.4.2 The formation of divalent and trivalent Mn species

It is believed that the first step of the oleic acid-birnessite reaction involves ligand exchange with Mn^{3+}- and Mn^{4+}-centres ($\equiv Mn^{3+}$, $\equiv Mn^{4+}$) in birnessite, in much the same way as described by Stone (1987) and Ulrich and Stone (1989). Exchange occurs between the Mn^{3+}-/Mn^{4+}-centre and carboxyl moiety, as observed by the ATR-FTIR spectrum obtained for the reaction between birnessite and oleic acid (Fig. 3.5) and as proposed by Johnson *et al.* (2015). These interactions were outlined in equations 2.37*a*–*b* and 2.38*a*–*b*. In this way, the "*bridging bond*" which is crucial for one electron transfer, is established.

Step 1—surface complex formation:

$$\equiv Mn^{3+}(OH) + HOOC{-}R \rightleftharpoons \equiv Mn^{3+}{-}OOC{-}R + H_2O \qquad (4.9a)$$

$$\equiv Mn^{4+}(OH) + HOOC{-}R \rightleftharpoons \equiv Mn^{4+}{-}OOC{-}R + H_2O \qquad (4.9b)$$

where HOOC—*R* represents a lipid such as oleic acid. It is not completely clear at this point though how the single electron transfer to $\equiv Mn^{3+}$/$\equiv Mn^{4+}$ occurs *via* the $\equiv Mn^{3+}$—/$\equiv Mn^{4+}$—OOC—*R* bridge. No definite mechanism has been proposed before. It is possible that a resonance-stabilised radical may simply form within the carboxyl group bonded to the $\equiv Mn^{3+}$/$\equiv Mn^{4+}$ centre.

Step 2—electron transfer:

$$\equiv Mn^{3+}{-}OOC{-}R \rightleftharpoons (\equiv Mn^{2+}, {}^{\bullet}OOC{-}R) \qquad (4.10a)$$

$$\equiv Mn^{4+}{-}OOC{-}R \rightleftharpoons (\equiv Mn^{3+}, {}^{\bullet}OOC{-}R) \qquad (4.10b)$$

It is possible that in the case of equation 4.10*b*, the surface site Mn^{3+} formed ($\equiv Mn^{3+}$) may re-initiate (or loop) the reaction in equation 4.9*a*, which is followed by the subsequent reaction in equation 4.10*a*, or this Mn^{3+} is actually chelated/complexed from the birnessite surface and into the liquid phase (oleic acid acts as ligand after binding to this surface site Mn^{3+}):

$$\equiv Mn^{3+}{-}OOC{-}R \rightleftharpoons Mn^{3+}{-}OOC{-}R + \equiv\square \qquad (4.11)$$

where $\equiv\square$ represents a now vacant surface site on birnessite. The subsequent step is then the formation of the carboxyl radical (${}^{\bullet}OOC{-}R$) *in-situ* in the liquid phase by complexed Mn^{3+} rather than surface site Mn^{3+} ($\equiv Mn^{3+}$), through a possible homolysis reaction:

$$Mn^{3+}{-}OOC{-}R \rightleftharpoons Mn^{2+} + {}^{\bullet}OOC{-}R \qquad (4.12)$$

It is now uncertain whether the following steps, as proposed before (equations 2.39*c–d*), still occur, given the new evidence that has surfaced throughout this chapter (4):

Step 3 (still occurring?)—release of the carboxyl radical:

$$(\equiv Mn^{2+}, {}^{\bullet}OOC{-}R) + H_2O \rightleftharpoons \equiv Mn^{2+}{-}OH_2 + {}^{\bullet}OOC{-}R \qquad (4.13)$$

Step 4 (still occurring?)—release of Mn^{2+}:

$$\equiv Mn^{2+}{-}OH_2 \rightleftharpoons Mn^{2+} + \equiv\square \qquad (4.14)$$

Doubt is especially cast on this final step (equation 4.14), as the transformation of birnessite to cryptomelane observed previously (§ 4.3.3 and Fig. 4.7) would suggest that this Mn^{2+} located within the surface sites ($\equiv Mn^{2+}$) is rather being incorporated into the mineral structure than being released (Tu *et al.*, 1994). Furthermore, a satisfactory plausible Mn-release mechanism (into the liquid phase) *via* complexation has already been proposed (equation 4.11). Another factor to consider is that although the presence of H_2O in this virtually anhydrous system (oil plus mineral) is not impossible (*e.g.* displacement of possibly protonated surface hydroxyl groups by oleic acid during the surface complexation step), one would expect a general lack of water in this type of system. This would strongly inhibit the reaction in step 3 (equation 4.13) and subsequently the reaction in step 4 (equation 4.14).

Apart from steps 3 and 4, the first part of the birnessite-oleic acid reaction mechanism is possibly very similar to the mechanism of the oxidation of aromatic compounds by Mn-oxides to aryl (*e.g.* semi-quinone) radicals (equations 2.39*a–d*). However, at this point the mechanism for lipids departs from the one for aromatics as the carboxyl radicals do not couple to one another. Instead, it is proposed here that they couple with lipid radicals ($L^{\bullet}$) that have lost the α-hydrogen (on carbon number 8 or 11 for oleic acid) to some kind of initiator molecule or lipid-alkoxy radicals ($L{-}O^{\bullet}$) which result from the reduction of lipid hydroperoxides ($L{-}O{-}OH$) by Mn^{2+}:

$$L{-}O{-}OH + Mn^{2+} \rightarrow L{-}O^{\bullet} + Mn^{3+} + OH^{-} \qquad (4.15a)$$

$$L{-}O^{\bullet} + L{-}H \rightarrow L^{\bullet} + L{-}OH \qquad (4.15b)$$

It is possible that the lipid hydroxide ($L{-}OH$; essentially an alcohol group on an oleic acid molecule for example, but with a *trans*-double bond) could bond with the carboxylic acid group on unreacted oleic acid, forming ester bonds by the classic condensation type mechanism. It is possible that the place within the liquid phase where the sample was taken for ATR-FTIR (at the liquid-min-

eral interface) does not contain the hydroperoxides, and that they are located higher up in the liquid column, perhaps near the surface. From there they diffuse downward through the liquid column, reacting with Mn^{2+}.

4.4.3 Polyester coupling reaction

After steps 1 and 2 (and possibly 3 and 4, but unlikely), the next step would be the coupling reaction (in two possible ways) between the carboxyl and lipid radicals or lipid hydroxides and carboxylic acid functional groups, forming ester bonds, and thus polymers:

$$L^{\bullet} + {}^{\bullet}\mathrm{OOC}\text{—}R \rightarrow L\text{—O—(CO)—}R \tag{4.16a}$$

$$L\text{—OH} + \mathrm{HOOC}\text{—}R \rightleftharpoons L\text{—O—(CO)—}R \tag{4.16b}$$

This would explain why the (*trans*) double bond remains intact as the esters are not forming *via* an epoxide-ring-opening to alcohol intermediate mechanism (such as the one in Omonov *et al.*, 2016). Recall that the formation of a *trans*-double bond is one of the first steps during lipid radical generation. Schematics of the reactions in equations 4.16*a* and *b* are depicted in Figs 4.9*a* and *b*, respectively.

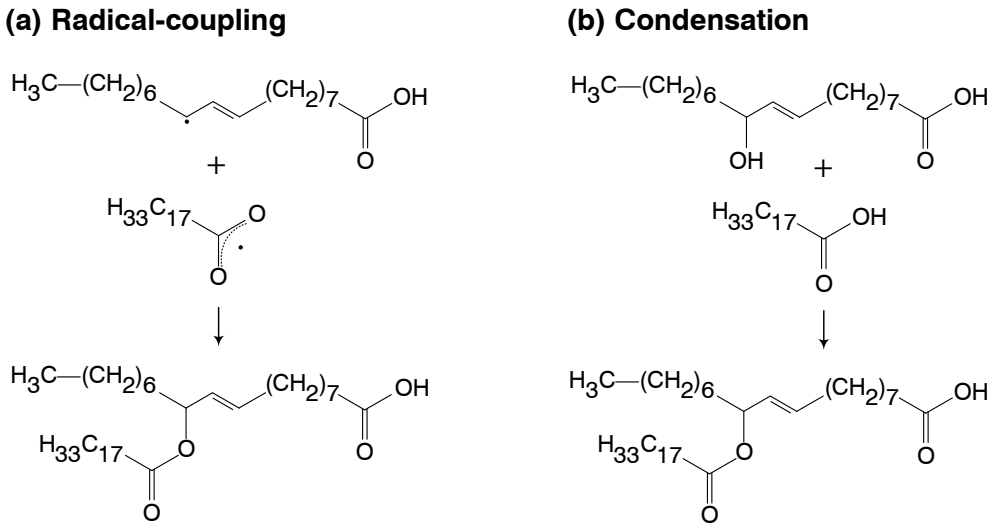

Fig. 4.9 The coupling reaction between an (a) oleic acid radical and an oleic acid carboxyl radical, as well as (b) oleic acid hydroxide and oleic acid to form (poly)esters.

In the ATR-FTIR spectrum collected for the birnessite-oleic acid experiment (Fig. 3.5), there was no indication of lipid hydroperoxides (*L*—O—OH) or lipid hydroxides (*L*—OH) being present in the sample. However, as mentioned, the sample was taken in a relatively deep part of the vial (near the mineral-liquid interface) for ATR-FTIR samples. Closer to the top (surface) of the liquid phase in the vial, atmospheric oxygen (O_2) interacts more readily with the liquid in the vial, as it is not limited by diffusion processes, and it is possible that peroxidation products could be found here. To confirm if this is indeed the case, a small aliquot of the liquid in the birnessite-oleic acid vial was sampled and injected directly into a mass spectrometer running in the ESI+ mode. The mass spectrum is shown in Fig. 4.10 on the next page. Two ions present at m/z values of 321 and 337 correspond to molecular formulae of $C_{18}H_{34}O_3$-Na and $C_{18}H_{34}O_4$-Na, respectively. These are the formulae for oleic acid hydroxide and oleic acid hydroperoxide, which indicates that hydroperoxides and their breakdown products do exist closer to the surface of the liquid phase.

These peroxidation products diffuse downward where they are reduced by upward diffusing Mn^{2+} to radicals, and Mn^{2+} is oxidized to Mn^{3+} (which explains the red colouration of the liquid phase). These radicals continue diffusing downward where they encounter the carboxyl radicals, coupling with them to form ester bonds (not *via* a condensation reaction).

It is also highly probable that given the relatively high redox potential of Mn^{3+} ($E° = +1.51$ V), it would react with carboxyl groups on downward diffusing peroxidation products as well as those of remaining oleic acid.

The speciation of Mn in the liquid phase therefore in all likelihood undergoes a complex cycling between Mn^{3+} and Mn^{2+}, with a compensating flux from the mineral phase below (probably complexed Mn^{3+}). There are thus still a multitude of unexplored reactions between Mn^{3+}, Mn^{2+} and lipid phases such as oleic acid and its (per)oxidation products.

4.4.4 The overall reaction mechanism

Figure 4.11 illustrates the overall reaction mechanism between birnessite and oleic acid to form polyesters. The first step of the reaction involves the protonation of the surface hydroxyl group on the birnessite surface *via* proton abstraction from the carboxylic acid group of oleic acid. The subsequent re-arrangement leads to an exchange between the protonated hydroxyl group on birnessite and the deprotonated carboxyl group of oleic acid (Fig. 4.11*a*). An exchange surface complex has now formed between oleic acid and the central Mn^{4+} cation in the birnessite surface site. The second step of the reaction now involves single electron transfer through homolysis of the Mn—O bond (Fig. 4.11*b*), reducing Mn^{4+} to Mn^{3+} and forming a carboxyl radical. This two-step process is the first way in which a carboxyl radical forms. An alternative mechanism is also possible and is illustrated in Figs 4.11*c* through *d*.

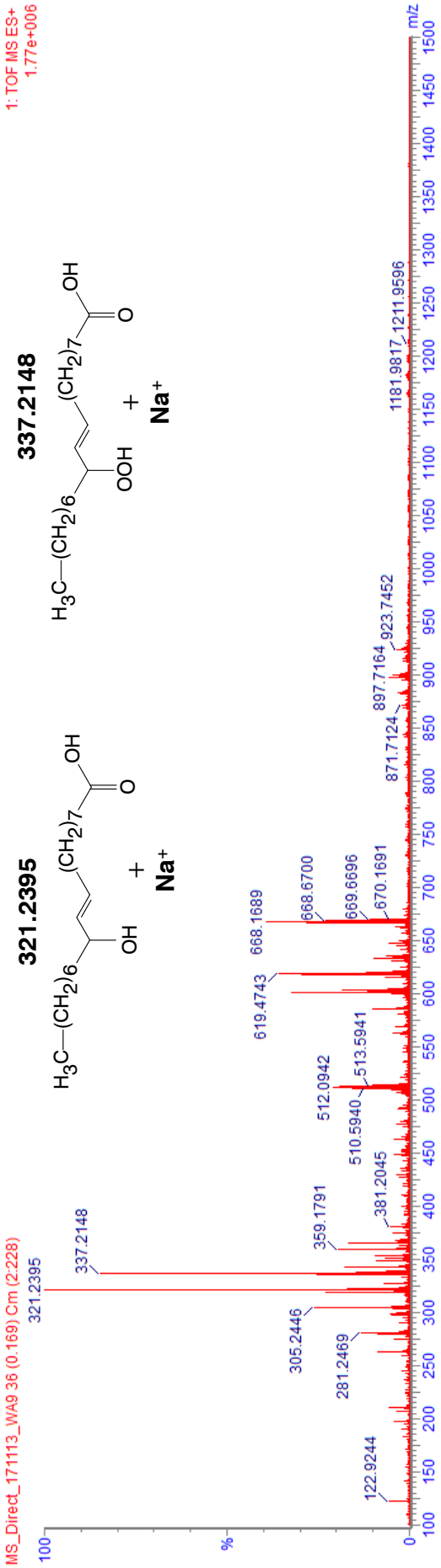

Fig. 4.10 The direct injection time-of-flight electrospray positive (TOF-ESI+) mass spectrum of a sample from the bimessite-oleic acid reaction vial, showing molecular interpretation of the two accurate masses 321.2395 and 337.2148.

(a) Formation of a surface complex

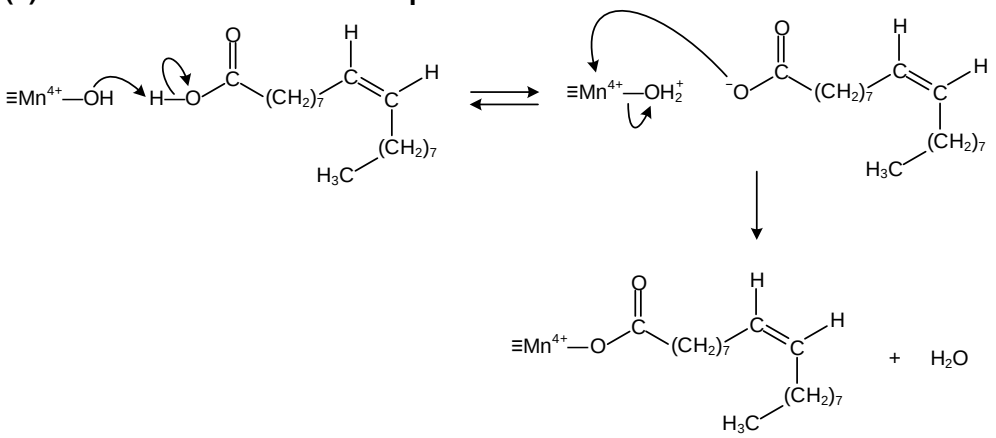

(b) Single electron transfer (homolysis)

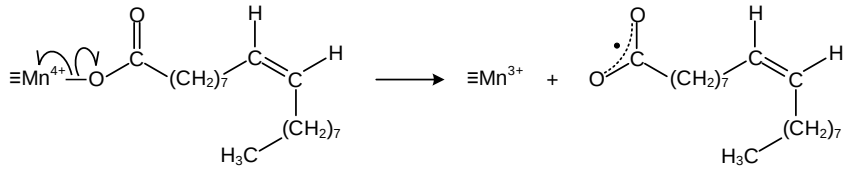

(c) Mn^{3+} chelation from birnessite surface (complex formation as in (a))

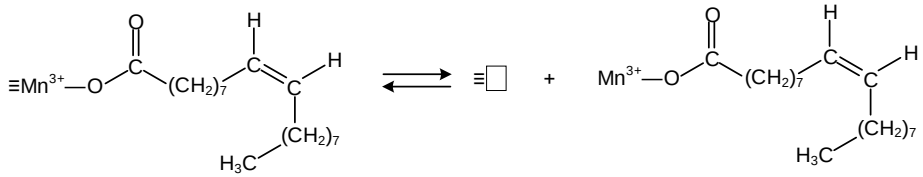

(d) Single electron transfer – *in-situ* formation of Mn^{2+}

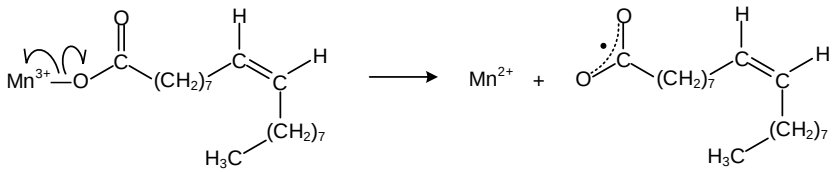

Fig. 4.11 The reaction mechanism between birnessite and oleic acid to form (a-d) carboxyl radicals, followed by (e, next page) radical attack (H-abstraction) of oleic acid to form oleic acid radicals which may then (f, next page) couple with carboxyl radicals to form esters. Subsequent (g) propagation and attack leads to polyester formation. ≡□ = vacant surface site.

(e) Radical attack, H-abstraction

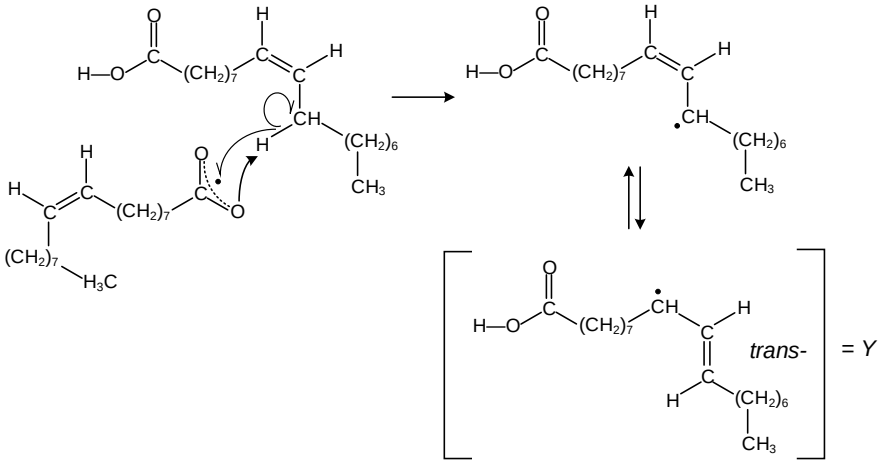

(f) Radical coupling

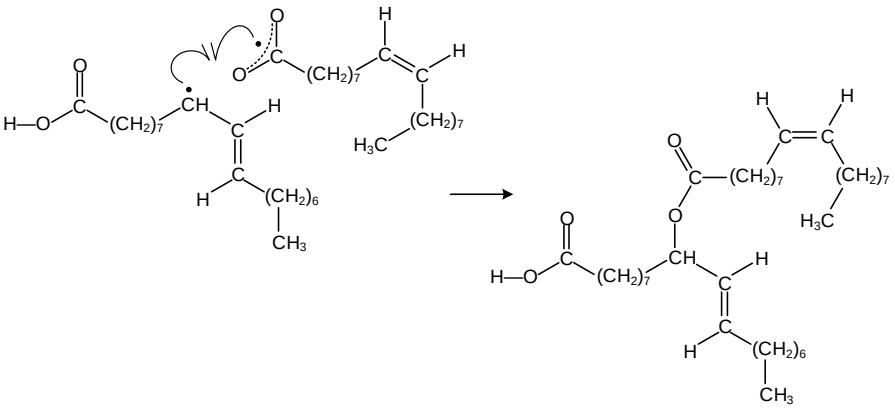

(g) Further attack, homolysis and eventual radical coupling (propagation)

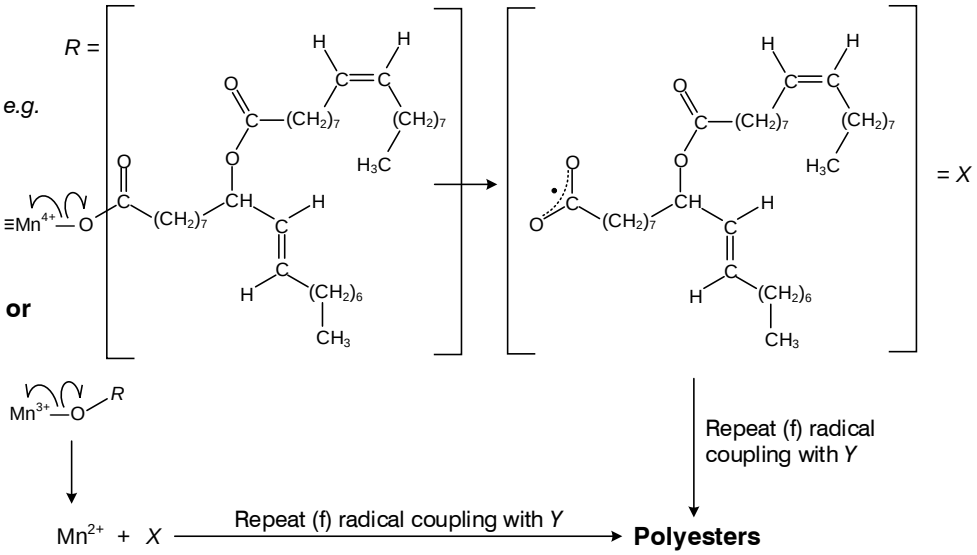

Fig. 4.11 *Continued.*

The first step (Fig. 4.11*c*) this time involves direct chelation of Mn^{3+} (either as initially present in birnessite or formed through steps *a* and *b* previously) *via* a surface exchange complex with oleic acid which forms in the same manner as in Fig. 4.11*a*. This complexed Mn^{3+} is then removed into the liquid phase, leaving behind a vacant cation site in birnessite (Fig. 4.11*c*). This chelated Mn^{3+} is then reduced *via* homolysis in a manner similar to Fig. 4.11*b* to form Mn^{2+} and a carboxyl radical (Fig. 4.11*d*).

The carboxyl radicals formed as a result of the reactions in Figs 4.11*b* and *d* are capable of abstracting a hydrogen atom from an oleic acid molecule in much the same way as during the usual lipid peroxidation reactions discussed in § 2.5.4 (see Fig. 4.11*e*). These oleic acid radicals are then able to couple with unreacted carboxyl radicals to form esters (Fig. 4.11*f*). Any free carboxyl groups on these esters are not exempt from exchanging on the birnessite surface or chelating Mn^{3+} (Figs 4.11*a* and *c*) which means they can also undergo homolysis reactions to form carboxyl radicals (Fig. 4.11*g*). These larger radicals can then also couple with oleic acid radicals (a repeat of the reaction in Fig. 4.11*f*) to form larger ester structures and eventually polyesters.

4.4.5 The importance of the surface exchange complex

The formation of the surface exchange complex between oleic acid and the birnessite surface is considered a crucial part of the mechanism which initiates the birnessite-oleic acid reaction.

In order to verify the importance of this step, a parallel reaction to the birnessite-oleic acid reaction was conducted with birnessite and olive oil, under the same conditions as in chapter 3 (25°C for 6 months). This experiment was performed because oleic acid found in olive oil is not present in its free fatty acid (FFA) form, but rather in the form of glycerides, the most common being triglyceride triolein (refer again to Table 2.2 for chemical structure). By removing the free carboxyl group from the reaction, it is possible to see just how crucial the interaction between the birnessite surface and the free carboxyl group is for the reaction to proceed.

As was the case in chapter 3, the end result of the reaction was photographed, and interpreted visually. However, in addition, samples of the liquid phase were taken from the birnessite-olive oil and olive oil control experiments, as well as from the birnessite-oleic acid and oleic acid control experiments, and the disappearance (assumed to be consumed by reaction) of oleic acid was analysed in each sample by GC-MS. These GC-MS results of all four samples are then compared.

Visual results. Visual observations captured for the reaction between olive oil and birnessite are depicted in Fig. 4.12 (on the next page).

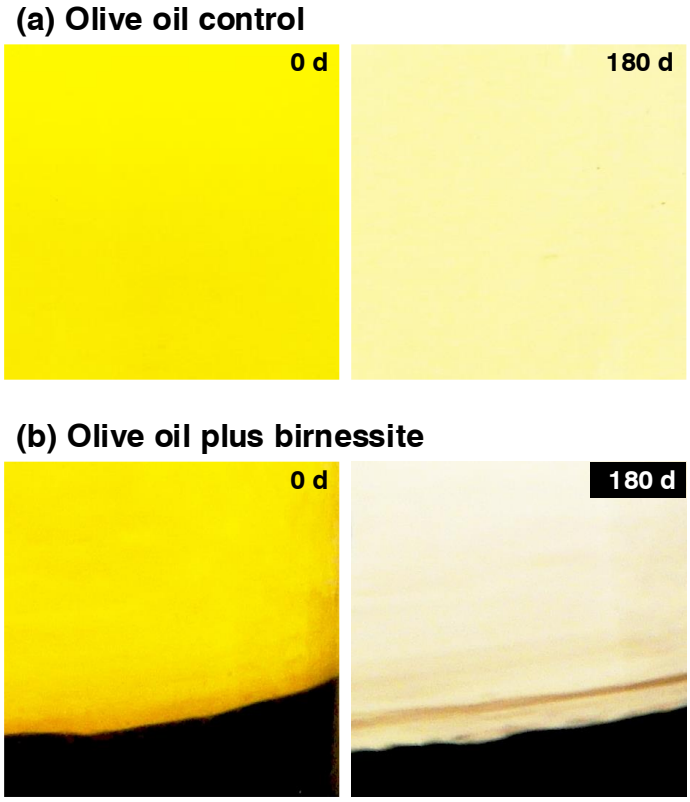

Fig. 4.12 The colour change observed resulting from the (a) olive oil control experiment and (b) the olive oil plus birnessite experiment, when incubated at 25°C in the dark for 6 months.

Olive oil changes colour from a generally yellow-green colour to a pale yellow-clear colour over the 6-month incubation period. The colour change was attributed to sorption or destruction of pigment compounds such as chlorophyll and β-carotene, which commonly occurs during the process of olive oil bleaching (Aued-Pimentel *et al.*, 2013; Asgari *et al.*, 2018). More importantly, however, no darkening or thickening of the liquid phase was detected, which means triolein (the triglyceride form of oleic acid present in olive oil) did not appreciably react with birnessite.

Since triolein has its carboxyl groups bonded to glycerol *via* ester bonds, this lack of reaction of olive oil with birnessite indicates how important it is that the carboxyl or carboxylic acid group be unbounded and thus free to react. This supports the notion that the first crucial step of the reaction between oleic acid and birnessite involves the surface exchange complex between the carboxylic acid/carboxyl group and surface sites on birnessite.

Disappearance of oleic acid—GC-MS results. The results of the GC-MS analyses are provided in Fig. 4.13:

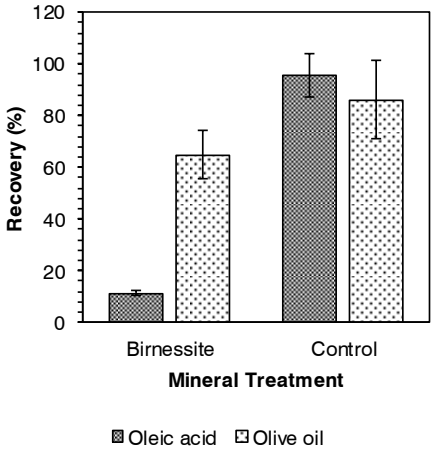

◀ **Fig. 4.13** The percent recovery of oleic acid FAME from the reactions between oleic acid and birnessite, olive oil and birnessite, oleic acid control and olive oil control, after reaction at 25°C in the dark for 6 months. Error bars represent deviation for duplicate ($n = 2$) samples.

Oleic acid in the free fatty acid form showed much greater reactivity toward birnessite than olive oil (triolein triglyceride), with only approximately 10% recovery of the initial oleic acid amount versus 65% recovery in the case of olive oil.

This reinforces the importance of the initial formation of a surface exchange complex during the reaction between lipids and the birnessite surface. The recovery of 65% is, however, somewhat lower than that of the control olive oil experiment (86%). This points to the fact that birnessite is initiating some kind of reaction with the triolein in olive oil. It is possible that the triglyceride is coupling to form a product similar to that depicted in Fig. 2.10*b*, or that birnessite is hydrolysing the ester bond to form free oleic acid which then polymerises, but that kinetically hydrolysis is a much slower reaction than the polymerisation reaction, and the limited supply of oleic acid is thus a rate-limiting factor. It is also possible that the triglyceride is adsorbing to the birnessite surface, through hydrophobic interactions.

4.5 Summary and conclusions

Oleic acid reacts readily with birnessite *via* a surface exchange, radical formation and Mn-reduction mechanism to form several products including polyesters and dissolved multivalent Mn species. It is very plausible that Fe-containing clays react with oleic acid *via* the same mechanism, but evidence for multivalent Fe species was not as conclusive as it was for birnessite. In the case of birnessite, oleic acid binds directly to Mn^{3+}-/Mn^{4+}-centres ($\equiv Mn^{3+}$/$\equiv Mn^{4+}$) on the birnessite surface *via* its carboxyl group to dissolve the mineral

most probably through complexation of surface site Mn^{3+} ($\equiv Mn^{3+}$) into the liquid phase (a preceding reduction step occurs in the case of $\equiv Mn^{4+}$). Subsequent steps that include the reduction of $\equiv Mn^{3+}$ to $\equiv Mn^{2+}$, with the eventual release of Mn^{2+} from the mineral surface, were at first considered important steps for Mn-release to the liquid phase. However, XRD analysis revealed the transformation of the remaining birnessite after reaction with oleic acid to cryptomelane. This suggests that instead of being released, Mn^{2+} located in surface sites ($\equiv Mn^{2+}$) is incorporated into the mineral structure, altering the mineral structure and initiating the mineral transformation.

It is proposed that complexed Mn^{3+} reacts directly with oleic acid and is reduced to Mn^{2+} *in-situ* in the liquid phase (its presence was detected by EPR spectroscopy). This Mn^{2+} diffuses upward through the liquid phase and reacts with products of downward diffusing lipid peroxidation reactions to once again form Mn^{3+}, which is again complexed/chelated by the carboxyl (and other) functional groups on oleic acid. Here it continues to play a role in transforming oleic acid to polymerised products. The deeper probing of the reaction between birnessite and oleic acid using several advanced techniques has unveiled meaningful insight into the lipid-clay reaction mechanism.

Two additional noteworthy deductions can also be inferred from this chapter. The first is that there exists another potential chelator for Mn^{3+} in nature, in the form of lipids, which may shed more light on the observed stability of Mn^{3+} in nature, despite being considered generally unstable chemically. In this manner, lipids continue to reinforce the status of Mn^{3+} as one of the most crucial chemical species of biogeochemical redox reactions in nature. Secondly, this chapter also shows that Mn^{3+} and birnessite both play a vital role in the humification of lipids.

CHAPTER 5

Kinetics of the lipid-clay reaction

5.1 Introduction

In chapters 3 and 4, the two first questions of this study were answered—*what* forms from lipid-clay interactions, and *how* it forms. This section aims to answer the next two questions of this study—how *fast* do the products of lipid-clay interactions form (*i.e.* their *rate* of formation or *reaction rate*) and what effect certain *variables* (*e.g.* temperature, clay surface pH, the initial ratio of clay to lipid phase) have on this reaction rate. This is known as the *kinetics* of the reaction. A background discussion of rate variables, expressions and reaction orders can be found in Appendix A.

For this chapter, the kinetics of the most reactive and most demonstrative lipid-clay reaction from chapters 3 and 4 was selected—which is the darkening reaction occurring between birnessite and oleic acid. The kinetic variables investigated are exactly those mentioned in the previous paragraph.

5.1.1 Rationale for visual-based reaction monitoring

The disappearance of oleic acid can be quantified by methods such as GC-FID[20] (Tvrzická *et al.*, 2002) or GC-MS (Kail *et al.*, 2012; Avula *et al.*, 2017), by derivatization of oleic acid to its FAME (see § 4.2.3). As this method can often be time-consuming, costly and hazardous (requires working with chemicals such as BF_3 and concentrated H_2SO_4), several studies have suggested methods without the derivatization step, for example gas chromatography triple-quadrupole mass spectrometry (GC-TriQ-MS; Lin *et al.*, 2014) and reversed-phase high performance liquid chromatography (RP-HPLC) methods using capacitively coupled contactless conductivity detection (C^4D; Makahleh *et al.*, 2010). Chromatographic methods, despite being time-consuming and costly, are highly accurate, and deliver a wealth of information about a sample. However, problems are encountered when trying to analyse a compound that is found in an environmental matrix within the sample (*e.g.* soils or solids such as mineral phases). Extraction of the compound of interest is often non-trivial and may involve more steps than the chromatographic sample preparation itself. Sorption or binding of the compound to the solid phase would also affect the final concentration determined. These bonds have to be broken in order to fully extract the compound of interest and this may involve many complex steps. Extracted compounds are then often present at very low concentrations, and an added pre-concentration step is required. Suddenly, as one can see, the complexity of the task at hand increases rapidly. In kinetic studies, the tendency is to attempt analysing more samples more rapidly, rather than fewer samples that take longer to prepare and analyse. This increases the number of data points in the study and therefore increases the time resolution. The tendency is thus toward simpler, more rapid analytical methods.

Owing to the different ways in which reaction rate of a particular reaction can be determined, most of the time it is not necessary to monitor the loss of a specific reactant, unless specifically required. Monitoring the concentration of products formed is just as effective in determining reaction rate. This is known as the monitoring of *surrogate parameters* (Roychoudhury and Merrett, 2006). Using this study as an example, monitoring the concentrations of forming radical products, peroxidation products, Mn^{2+}, Mn^{3+} or O_2 consumption (*e.g.* measured reduction in oxygen partial pressure, P_{O_2})) provides a means of de-

[20] FID = flame ionization detection

termining the reaction rate just as effectively as measuring the disappearance of oleic acid.

These surrogate parameters are often monitored by methods that require little sample preparation and short analysis time, such as colorimetric and spectroscopic methods. As observed in chapter 3, the reaction between oleic acid and birnessite turns the liquid phase a deep red colour with time (Fig. 3.2*b*). This phenomenon is readily measured with UV-VIS spectroscopy. This technique is also useful for quantifying the concentration of Mn^{3+} which forms a crimson-magenta coloured complex with pyrophosphate (Fig. 3.3*a*; Kostka *et al.*, 1995, Klewicki and Morgan, 1998, Oldham *et al.*, 2015). The formation of peroxidation products is similarly monitored by UV-VIS spectroscopy (Gomez *et al.*, 2011; Juita *et al.*, 2012) as they show peaks in the region of 250–320 nm. The concentration of Mn^{2+} can be monitored by EPR spectroscopy (see Fig. 4.6) or UV-VIS spectroscopy (Madison *et al.*, 2011). The concentration of Mn^{2+} can also be determined by using inductively coupled plasma—optical emission spectroscopy (ICP-OES) to determine total dissolved Mn ($\Sigma Mn = [Mn^{2+}] + [Mn^{3+}]$) and subtracting the pre-determined concentration of Mn^{3+}.

These spectroscopic methods work well in most cases, but still have their limitations. Concentrations can be monitored effectively as long as the sample is either in liquid form, soluble (in organic solvent or water), extractable by ligands, and there is enough of a sample, or enough samples, to sacrifice a (sub)-sample for extraction and analysis. As is sometimes the case though, this is not always possible. In this study for example, purified or refined commercial compounds such as technical grade (90% pure) oleic acid are very costly, and therefore only a very finite number of replicates are possible. If sacrificing of samples can be avoided, it is to the benefit of the study. Furthermore, the polymerised products that eventually form from the reaction between birnessite and oleic acid are *quasi*-solids and virtually insoluble in a wide range of organic solvents (*e.g.* hexane, methanol, THF[21]; investigated but not shown). A non-destructive, visual method was therefore employed in this study. The colour change that occurs during the reaction was photographed and the images analysed by RGB (red, green and blue) colour channel analysis. This technique was employed on a set of experiments to monitor the birnessite-oleic acid reaction under variable kinetic conditions. A parallel but smaller set of birnessite-oleic acid experiments were conducted but samples sacrificed before the polymerised product could form, and these were analysed to see whether their RGB values relate in any way to parameters that can be measured by UV-VIS spectroscopy for example. In this manner, it was determined whether RGB analysis could substitute for classic techniques (*e.g.* UV-VIS spectroscopy) as a viable technique in cases where these classic techniques are either very difficult or not practical (in terms of kinetics) to employ.

[21] THF = tetrahydrofuran

By employing this RGB technique, the objectives of this chapter are to (i) determine the activation energy (E_a) of the reaction between birnessite and oleic acid, as well as (ii) determine two reaction orders—one with respect to mineral loading (the ratio of mass of birnessite to oleic acid) and the other with respect to the pH of the birnessite surface.

5.2 Materials and methods

5.2.1 Materials

All chemicals were purchased from Sigma-Aldrich® at the highest available purities (≥99%), except oleic acid which was technical grade (90%). Birnessite used in this chapter was the same synthetic birnessite that was employed in chapters 3 and 4. Characterisation and synthesis method of this birnessite was discussed in § 3.2.1 (also refer to Appendix B, Fig. B.1*a* and Appendix C, Fig. C.1*a* for XRD and FTIR characterisation, respectively).

To test the dependence of the birnessite-oleic acid reaction on birnessite surface pH, two 10 g quantities of birnessite were added into a graduated beaker to which 5 times that volume of ultrapure deionized water (18.2 MΩ·cm, TOC <5 ppb (μg l^{-1}), Millipore MilliQ® ultrapure type 1 water dispenser, Millipore Corporation (now Merck), Burlington, MA, USA) was added, as per the ISO 10390:2005 method for bulk-pH determination. The mixtures were stirred until completely suspended, and over the course of three to four days, the bulk pH of each suspension was carefully adjusted (from the original pH of 7.23) using a dropwise addition of 0.1 M HCl whilst stirring. The pH was measured regularly and adjusted until it reached a final, stable pH of 4.06 in one beaker and 5.50 in the other. The mixtures were then centrifuged at 10,000 rpm (10,621 × *g*), the water decanted, and the solids dried in an oven at 50°C.

5.2.2 Experimental setup

Experiments were conducted in 1 ml glass HPLC vials that were treated in the same manner as the glassware in chapters 3 and 4 (soaked in 5% HNO_3, baked at 110°C, rinsed with acetone and deionized water). Potential interference from biological reactions was eliminated by sterilizing the vials with *c*. 0.02% thimerosal as before (Hardie *et al.*, 2007).

To determine the dependence of the birnessite-oleic acid reaction on temperature, 10 mg of birnessite plus 100 mg oleic acid was added to each vial. For each of three different temperatures, a set of triplicate samples was generated. Control experiments for each temperature were set up by adding only 100 mg of oleic acid to each vial. Each set of triplicate samples was incubated at their own temperature, *viz.* 25°C, 37°C and 50°C, for a total time of approximately

three weeks. Samples were photographed at regular intervals (see § 5.2.3 for procedure) to track the change in colour of the reaction over time, for each temperature.

The dependence of the birnessite-oleic acid reaction on birnessite surface pH was investigated by generating triplicate samples for each pH (4, 5.5 and 7), as was done with temperature. To each vial, 10 mg of the specific birnessite plus 100 mg oleic acid was added, and the vials all incubated at 37°C for approximately three weeks. The samples were photographed regularly to track the colour change of the reaction.

The dependence of the birnessite-oleic acid reaction on the initial ratio of birnessite to oleic acid was investigated in a similar manner to temperature and pH. To one set of triplicate vials, 10 mg of birnessite plus 100 mg of oleic acid (1:10 ratio) was added, to another set 20 mg of birnessite plus 100 mg of oleic acid (1:5 ratio) was added, and to a final set, 5 mg birnessite plus 500 mg of oleic acid (1:100 ratio) was added. The samples were incubated at 37°C for approximately three weeks and photographed regularly to track the colour change of the reaction.

To investigate what the colour change during the reaction represents, a parallel experiment was run using three replicates of the pH 4 birnessite plus oleic acid and three replicates of the pH 7 birnessite plus oleic acid (these were not chosen for any specific reason other than to obtain some variation in colour values) which were then sampled after 90 h, 108 h and 161 h after incubating at 50°C. The replicates consisted of 1 g birnessite to which 10 g oleic acid were added inside 100 ml glass vials. Aliquots (*c*. 2 ml) were sampled as before, and UV-VIS spectra collected of them. Separate aliquots were sampled from each and extracted with pyrophosphate and also analysed with UV-VIS spectroscopy for the determination of Mn^{3+} concentration. The measured absorbance of the Mn^{3+}-pyrophosphate complex at 478 nm (Kostka *et al.*, 1995) was correlated to the concentration of Mn^{3+}, as described in § 5.2.3. Total dissolved manganese (ΣMn) present in the liquid phase was determined by performing ICP-OES on the pyrophosphate extract. The concentration of Mn^{2+} present was determined by subtracting the concentration of Mn^{3+} present in the sample from its ΣMn value.

5.2.3 Analytical methods

The samples were photographed in a fixed position against a fixed white screen with a constant light source located in the same position each time. No outside light entered the room. Colour (RGB) values from the images were extracted using the Microsoft® Paint tool. The values were extracted from places in the image that showed uniform colour with no light reflections. It was also attempted to use as far as possible the same spot in different images from different days. The extracted red (y_R), green (y_G) and blue (y_B) values, as well as the sum

of these values ($\Sigma y = y_R + y_G + y_B$) which represented white light, were plotted against time to establish the change in these values over the course of the reaction, reaction rates and rate constants. Rate constants (k) and corresponding reaction rates for each case (u_{y_R}, u_{y_G}, u_{y_B} and $u_{\Sigma y}$) were determined using best-fit curves for the data. Rate orders and Arrhenius parameters (*e.g.* E_a) were calculated using the linear regression modelling tool in the R software package (version 3.5.1). For these rate order and Arrhenius-quantity determinations, an additional parameter, $\bar{u}$, the average of all the individual reaction rates, *i.e.* $\bar{u} =$ `average`$(u_{y_R}, u_{y_G}, u_{y_B}, u_{\Sigma y})$, was also employed.

For the parallel experiment with pH 4 and pH 7 birnessite, two samples were sacrificed (one of the pH 4 birnessite and one of the pH 7 birnessite) at various time points during the reaction, namely 90 h, 108 h and 161 h, after being incubated at 50°C. Several analyses were performed on them.

Absorbance was measured at 270 nm and 490 nm from UV-VIS spectra collected in the same manner as in chapter 4. Discrete visible-only (VIS) spectra were collected directly, by pipetting an undiluted *c*. 1 ml aliquot of the liquid phase into a 1.5 ml Plastibrand® plastic cuvette and analysing between 350 and 700 nm at 1 nm intervals. The absorbance maximum was found to be at approximately 2 absorbance units. Those samples that exceeded the absorbance maximum were diluted with hexane until they fell within the measurable range (<2 absorbance units). The dilution factor was later accounted for in data processing. Discrete ultraviolet-only (UV) spectra were collected by diluting a 5 mg sample of the liquid phase in 5 ml of hexane, as hexane does not absorb UV-radiation above 200 nm and was thus deemed a suitable non-interfering solvent (McMaster, 2005). The diluted sample was analysed between 200 and 350 nm at 1 nm intervals using a 1 ml Starna® 6Q quartz cuvette. Spectra were collected with a Thermo Scientific Genesys 10uv Scanning UV-VIS spectrophotometer (Thermo Fisher Scientific, Waltham, MA, USA) and VisionLite® software.

The concentration of Mn^{3+} present in each sample was quantified by absorbance at 478 nm after extraction *via* the following method: a sample aliquot of approximately 1 g was weighed after being pipetted into a 50 ml BD Falcon™ sterile polypropylene centrifuge tube. To this was added approximately 10 ml (on a 10 ml g^{-1} of sample basis) of a 50 mM tetra-sodium pyrophosphate decahydrate ($Na_4P_2O_7{\cdot}10H_2O$) solution at pH 6.5 (modified from Kostka *et al.* (1995), Nico and Zasoski (2001) and Marafatto *et al.* (2015)), meaning the major complex species would be $MnHP_2O_7$ ($pK_{a_3} = 6$; Klewicki and Morgan, 1998). The mixture in the centrifuge tube was then vortexed (Scientific Industries Vortex Genie). Two layers form, a non-polar layer drifting above a cloudy light magenta-coloured aqueous layer. Using a 10 ml syringe, approximately 3 ml of the light magenta layer was extracted and then passed through a 0.2 μm Whatman® cellulose acetate (CA) syringe filter, directly into a Plastibrand® plastic cuvette, where it was observed to be a clear magenta-coloured solution. The 50mM pyrophosphate solution, subjected to

the same filtration process, was used as a baseline. The spectrum was collected in the same VIS range and interval as the undiluted VIS spectra collected previously. These spectra were then used to quantify the concentration of Mn^{3+} produced, by calibrating for $[Mn^{3+}]$ using dilutions of a solution of Mn^{3+}-acetate dihydrate $(CH_3COO)_3Mn{\cdot}2H_2O$) in the same 50 mM pyrophosphate (pH 6.5) solution (see Appendix D).

Total dissolved Mn (ΣMn) was determined by diluting a 1 ml aliquot of the pyrophosphate extracted solution (used to determine $[Mn^{3+}]$) and diluted to 10 ml using 0.01 M HCl in a sterile 15 ml BD Falcon™ polypropylene centrifuge tube. The solution was vortexed and adjusted to pH = 2 (if not at 2 already) by adding a few drops of 0.1 M HCl and vortexing the solution again. The samples were analysed on a Thermo Scientific iCAP 6300 ICP-AES using argon (Ar) as plasma gas which was fixed at a flow rate of 12 l min^{-1}. Data acquisition and processing was performed with the iTEVA software package.

The determination of pH was performed using the Metrohm® pH lab 744 system (Metrohm®, Herisau, Switzerland) coupled with a Metrohm® glass electrode, calibrated before each session using proprietary pH 4 and pH 7 buffers.

5.3 Results and discussion

5.3.1 Reaction rates, rate orders and activation energy (E_a)

Visual observation (Fig. 5.1) of the reaction between oleic acid and birnessite over time, under different conditions, reveal that temperature and initial solid-to-liquid ratio appear to have an effect on the rate of darkening observed, but not varying pH of the birnessite surface. Increases or decreases in reaction rate due to changes in temperature appear to be non-linear. For example, the marked difference in darkening rate observed between 50°C and 37°C is not seen between 37°C and 25°C. A more linear change is observed for the mass-loading variable though, where discernible differences are observed among the 1:100, 1:10 and 1:5 birnessite to oleic acid initial mass ratios. No real discernible differences are observed for the different pH values of the birnessite surface.

The course of the birnessite-oleic acid reaction under various conditions was monitored by extracting the RGB values from snapshots such as those depicted in Fig. 5.1. Plots of the red (y_R), green (y_G), blue (y_B) and sum of RGB values (Σy) are plotted versus time in Fig. 5.2. The reaction rates from each plot for each colour component (*i.e.* $u_{y_R} = d(y_R)/dt$, $u_{y_G} = d(y_G)/dt$, $u_{y_B} = d(y_B)/dt$ and $u_{\Sigma y} = d(\Sigma y)/dt$) were determined by the initial rate method (see *e.g.* Lasaga, 1981) in which the reaction rate of interest is determined at the initial part of the curve, where it is fastest, and the concentration of products formed have not reached a level where they influence the reaction rate.

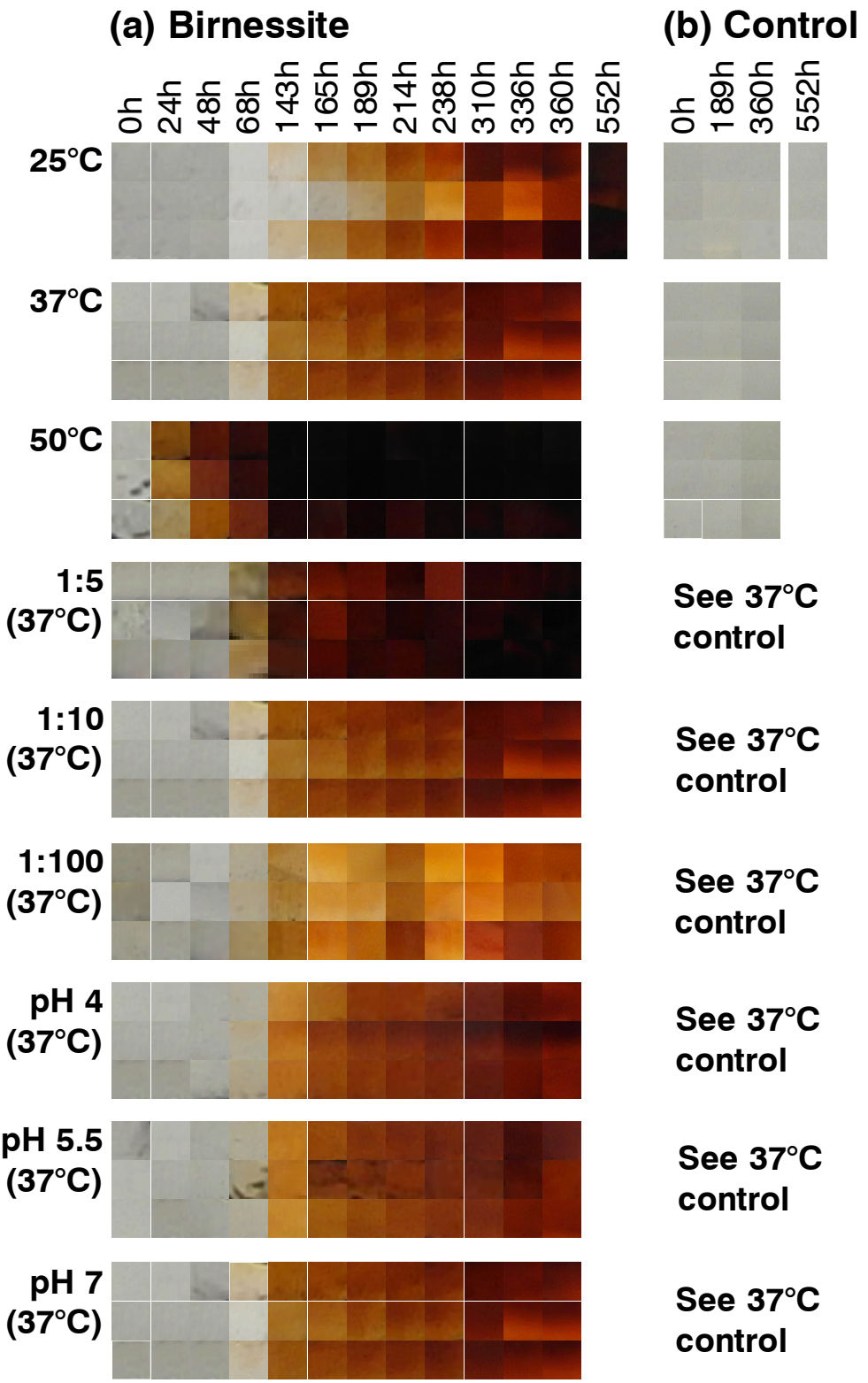

Fig. 5.1 Snapshots of the course of the (a) birnessite-oleic acid reaction and (b) control oleic acid only reaction under varying conditions. The ratios 1:5, 1:10 and 1:100 refer to the initial birnessite to oleic acid ratio for the mass-loading variable.

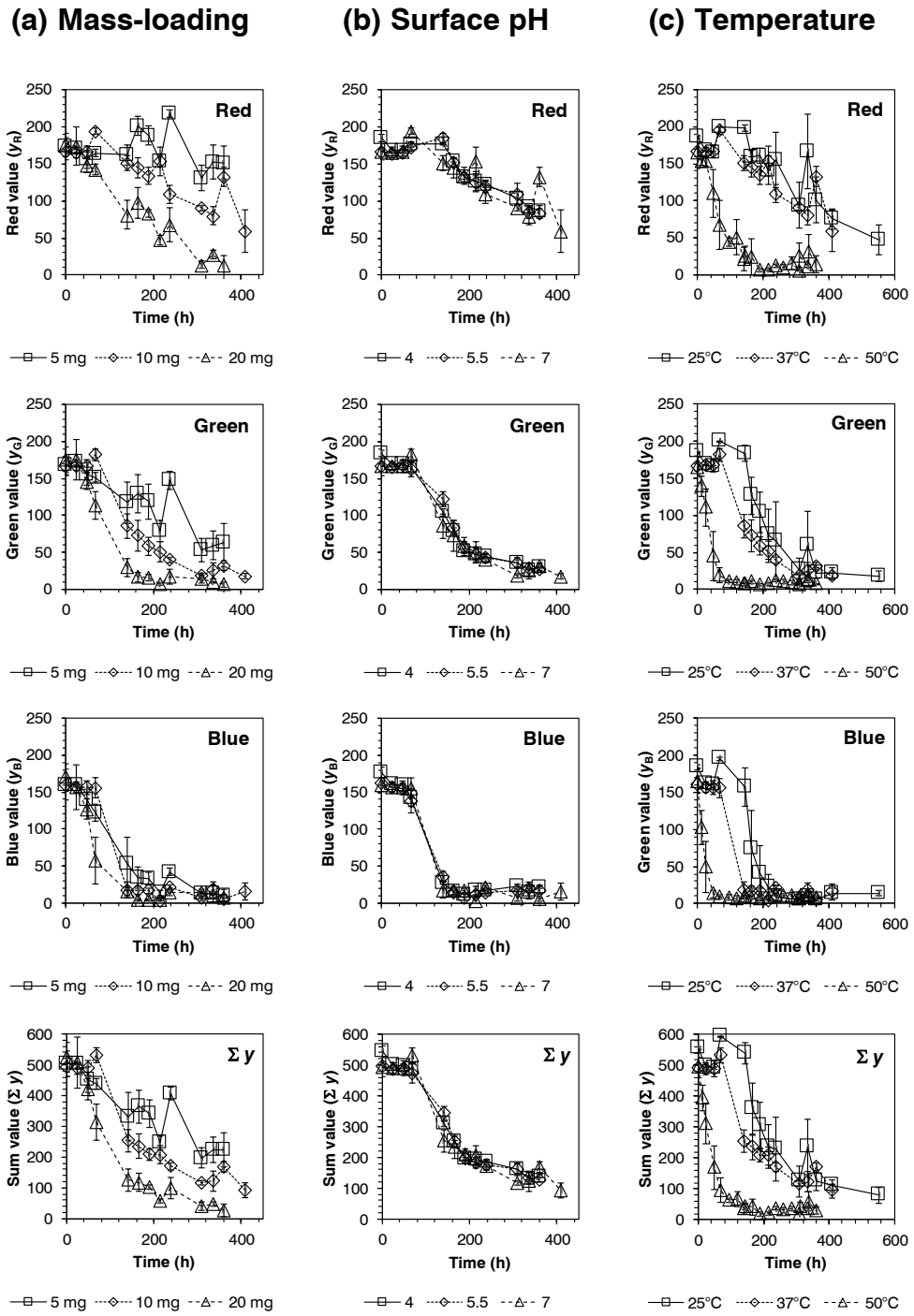

Fig. 5.2 Plots of red (y_R), green (y_G), blue (y_B) and sum of red, green and blue (Σy) colour component values *versus* time for the birnessite-oleic acid reaction. The effects of (a) mass-loading of birnessite—5 mg (1:100 birnessite-oleic acid ratio), 10 mg (1:10 birnessite-oleic acid ratio), 20 mg (1:5 birnessite-oleic acid ratio)—(b) birnessite surface pH (4, 5.5 and 7) and (c) temperature (25, 37 and 50°C) on the rate of darkening are illustrated. Error bars = standard deviation for triplicate samples ($n = 3$).

The initial rate values were determined from the best-fit curves to mostly the first few points of the colour component-time curves in Fig. 5.2. The best-fit models for each case are provided in the first column of Table 5.1 (on the next page). For most of the plots in Fig. 5.2, there appears to be a time period of no reaction for approximately the first 68 h. Thereafter the reaction initiates fairly quickly, and the samples darken rapidly (large decreases in colour component values), indicating that rapid initial kinetics dominate for the birnessite-oleic acid reaction. This initial *c*. 68 h period of no reaction before the reaction rapidly initiates was, however, not observed for cases such as the 50°C case of the temperature variable and the 1:5 (20 mg birnessite) case for the birnessite mass-loading variable.

In many of the cases in Fig. 5.2, the initial part of the curve chosen for the initial rate determination was linear or near-linear, and this allowed for linear regression (straight line) best-fit modelling to be employed on the data. In these cases, the initial rate was simply taken as the slope of the linear regression model. However, in some cases the initial kinetics was more rapid, showing curvature within the first few points after the reaction initiated. In these cases, linear regression models modelled the data more poorly when compared to non-linear regression modelling. Therefore, non-linear models such as exponential models as well as negative power (of t) models were employed for curve-fitting in some cases. For these curves, the initial rate was taken as the first derivative of the curve at the first point of the curve (the point in time when the reaction initiated). The various linear, exponential and power models employed for each case, their time domain and the resulting initial rates for each case are given in Table 5.1.

Reaction order with respect to mass-loading. The reaction order with respect to mass-loading of birnessite was determined by log (rate, u) *v*. log (mass of birnessite/mass of oleic acid, m_b/m_o) plots. The plots are depicted in Fig. 5.3. Here we see the first time that the average rate variable, defined earlier (§ 5.2.3) as $\overline{u} = \texttt{average}(u_{y_R}, u_{y_G}, u_{y_B}, u_{\Sigma y})$, is also employed for the purposes of rate order determination.

The rate orders obtained from the rates of red (u_{y_R}), blue (u_{y_B}), sum ($u_{\Sigma y}$) and average rates of all RGB components ($\overline{u}$) yield the greatest linearity ($r^2 >$ 95%), with a fractional rate order of between 0.65 and 0.85 for the dependence of reaction rate on mass-loading of birnessite relative to oleic acid. This is slightly lower than a typical first order dependence (rate order $\sim$ 1). A linear dependence would mean that if the mass of birnessite doubled, the reaction rate would roughly double as well (linear relationship). A near-unity reaction order was found for studies conducted on birnessite reacting with catechol for example (Matocha *et al.*, 2001). The dependence of reaction rate on mass (essentially effective surface area) indicates the importance of the initial surface exchange complex.

Table 5.1 The best-fit regression models, time domains and determined initial rates extracted from the data in Fig. 5.2.

Regression model (as a function of time, t)	Model domain (h)	r^2	Initial rate (RGB unit h^{-1})
Mass-loading (m_b/m_o)—1:100			
$y_R = 176.91 - 0.0448t$	$t \in [0, 360]$	0.0524	−0.0448
$y_G = 180.68 - 0.4533t$	$t \in [24, 141]$	0.9903	−0.4533
$y_B = 182.07 - 0.9028t$	$t \in [24, 165]$	0.9992	−0.9028
$\Sigma y = 530.16 - 1.4091t$	$t \in [24, 141]$	0.9874	−1.4091
Mass-loading (m_b/m_o)—1:10, Surface pH—7, Temperature—37°C			
$y_R = 226.89 - 0.5007t$	$t \in [68, 189]$	0.9821	−0.5007
$y_G = 19{,}475t^{-1.104}$	$t \in [68, 214]$	0.9952	−2.9981 †
$y_B = 3E{+}06t^{-2.364}$	$t \in [68, 189]$	0.9449	−4.8552 †
$\Sigma y = 19{,}514t^{-0.862}$	$t \in [68, 214]$	0.9772	−6.5121 †
Mass-loading (m_b/m_o)—1:5			
$y_R = 172.2 - 0.4732t$	$t \in [0, 360]$	0.9511	−0.4732
$y_G = 202.98 - 1.2417t$	$t \in [24, 141]$	0.9973	−1.2417
$y_B = 2E{+}06t^{-2.418}$	$t \in [48, 214]$	0.9569	−8.6697 †
$\Sigma y = 28{,}909t^{-1.085}$	$t \in [48, 165]$	0.992	−9.7966 †
Surface pH—4			
$y_R = 307.28 - 0.9236t$	$t \in [141, 189]$	1.00	−0.9236
$y_G = 231 - 0.9289t$	$t \in [68, 189]$	0.9936	−0.9289
$y_B = 613.07e^{-0.022t}$	$t \in [68, 189]$	0.9961	−3.0215 †
$\Sigma y = 648.3 - 2.4071t$	$t \in [68, 189]$	0.9999	−2.4071
Surface pH—5.5			
$y_R = 11{,}063t^{-0.835}$	$t \in [141, 238]$	0.9481	−1.0513 †
$y_G = 3E{+}06t^{-2.066}$	$t \in [141, 238]$	0.968	−1.5949 †
$y_B = 4E{+}13t^{-5.625}$	$t \in [141, 189]$	0.9997	−1.2990 †
$\Sigma y = 179{,}824t^{-1.281}$	$t \in [141, 238]$	0.9139	−2.8842 †
Temperature—25°C			
$y_R = 262.75 - 0.531t$	$t \in [141, 310]$	0.8599	−0.531
$y_G = 805.57e^{-0.011t}$	$t \in [141, 238]$	0.9722	−1.8380 †
$y_B = 10{,}134e^{-0.029t}$	$t \in [141, 238]$	0.9927	−4.6469 †
$\Sigma y = 9E{+}06t^{-1.958}$	$t \in [141, 214]$	0.9746	−7.4229 †
Temperature—50°C			
$y_R = 201.44 - 1.957t$	$t \in [24, 68]$	0.0524	−1.957
$y_G = 172.33 - 2.6349t$	$t \in [12, 48]$	0.9903	−2.6349
$y_B = 163.56 - 4.8333t$	$t \in [0, 24]$	0.9992	−4.8333
$\Sigma y = 483.53 - 6.7t$	$t \in [0, 48]$	0.9874	−6.7

† Determined from first-derivative value at left-most point of model domain.

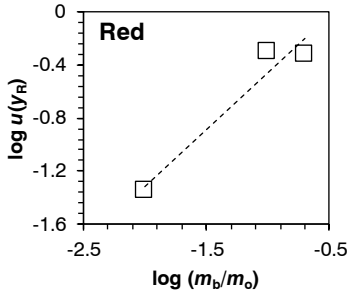


```
Intercept: 0.3931 ± 0.2863
Rate order: 0.8525 ± 0.2116
Multiple r-squared: 0.9419
Adjusted r-squared: 0.8839
```

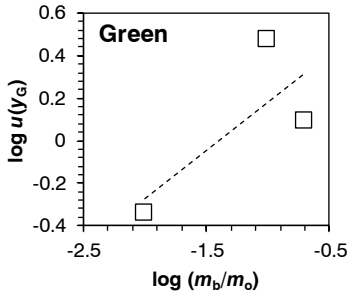


```
Intercept: 0.6404 ± 0.5301
Rate order: 0.4579 ± 0.3919
Multiple r-squared: 0.5772
Adjusted r-squared: 0.1544
```

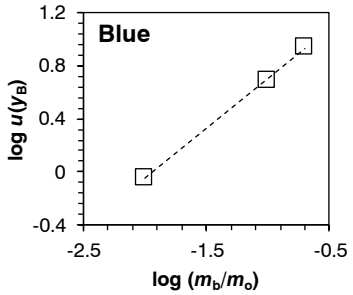


```
Intercept: 1.45005 ± 0.02682
Rate order: 0.74895 ± 0.01983
Multiple r-squared: 0.9993
Adjusted r-squared: 0.9986
```

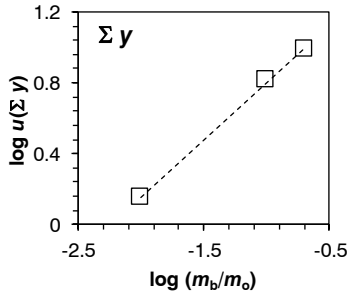


```
Intercept: 1.45476 ± 0.01916
Rate order: 0.65168 ± 0.01417
Multiple r-squared: 0.9995
Adjusted r-squared: 0.9991
```

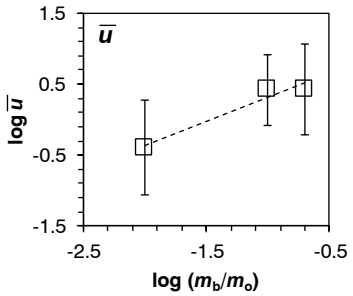


```
Intercept: 0.9846 ± 0.2022
Rate order: 0.6778 ± 0.1495
Multiple r-squared: 0.9536
Adjusted r-squared: 0.9072
```

Fig. 5.3 The log (rate, *u*) *versus* log (mass birnessite/mass oleic acid, m_b/m_o) plot to determine the rate order of the birnessite-oleic acid reaction with respect to mass-loading—for the colour components red (y_R), green (y_G), blue (y_B), sum (Σy) and average rate ($\bar{u}$).

However, the fractional rate order indicates that the formation of the surface exchange complex is not entirely controlled by effective surface area. Another possible factor that would influence the sorption of oleic acid onto the birnessite surface (and subsequent exchange reaction) is the pH of the birnessite surface. It was therefore chosen as the next kinetic variable to be investigated.

Reaction order with respect to birnessite surface pH. Figure 5.4 shows the log (rate, u) *v.* pH plots used to determine the reaction order with respect to pH of the birnessite surface. In this case, the rates derived from the green (u_{y_G}) component showed the strongest linearity ($r^2 \sim 1$) with respect to pH, with a fractional rate order of approximately 0.2. This low rate order value indicates that the birnessite-oleic acid reaction rate has very little dependence on the pH of the birnessite surface. This finding is similar to that of Matocha *et al.* (2001) for the reaction between birnessite and catechol, with rate orders obtained being close to zero. This confirms the original suspicion that pH of the birnessite surface does not have a strong influence on the birnessite-oleic acid reaction rate, when observing the lack of discernible differences among the experiments conducted at different pH levels (see Fig. 5.1), even though many natural Mn-mediated reactions are pH dependent. This small dependence (~ 0.2), however, may explain the deviation from linearity found previously with respect to mass-loading. The reaction rate is thus mostly controlled by mass-loading (effective surface area) with a minor influence from mineral surface pH.

The weak dependence of the reaction rate on birnessite surface pH was also interpreted in terms of the initial surface exchange complex that initiates the birnessite-oleic acid reaction. At low pH levels, the hydroxyl groups on birnessite are protonated and an exchange reaction occurs between the carboxyl group on oleic acid and the protonated hydroxyl group on birnessite. At higher pH levels, the hydroxyl group (or possibly deprotonated, negatively charged oxy-group) of birnessite acts as a Brønsted base, removing a proton donated by the carboxylic acid functional group on oleic acid (Brønsted acid) thereby protonating the hydroxyl functional group. The deprotonated carboxyl group then exchanges with the protonated hydroxyl group on birnessite in the same manner as at lower pH levels. In this manner, the surface complexation/exchange reaction is not strongly dependent on pH.

Activation energy. In order to determine the activation energy (E_a) of the birnessite-oleic acid reaction, the rate constants of the reactions at 25, 37 and 50°C have to be determined. This was achieved by using the best-fit equations established for the initial rates of each colour component (Table 5.1). For the straight-line best-fit curves of the form:

$$y = y_0 - kt \tag{5.1}$$

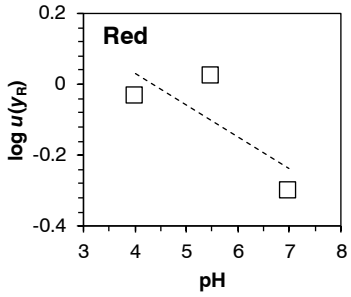


```
Intercept: 0.38309 ± 0.41033
Rate order: -0.08864 ± 0.07282
Multiple r-squared: 0.597
Adjusted r-squared: 0.194
```

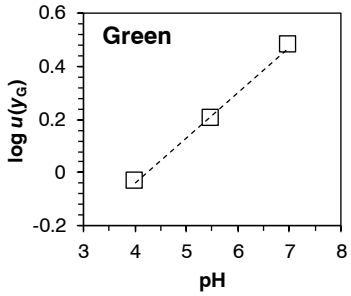


```
Intercept: -0.717094 ± 0.042671
Rate order: 0.169626 ± 0.007573
Multiple r-squared: 0.998
Adjusted r-squared: 0.996
```

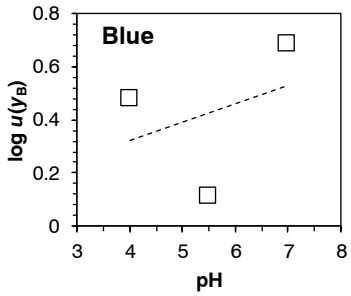


```
Intercept: 0.04904 ± 1.01848
Rate order: 0.06866 ± 0.18075
Multiple r-squared: 0.1261
Adjusted r-squared: -0.7478
```

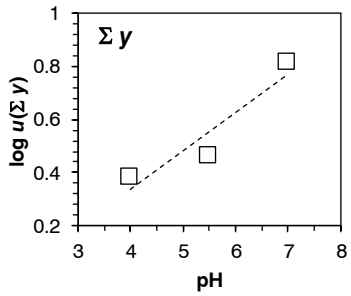


```
Intercept: -0.24071 ± 0.29837
Rate order: 0.14408 ± 0.05295
Multiple r-squared: 0.881
Adjusted r-squared: 0.762
```

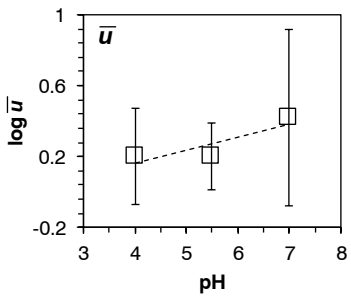


```
Intercept: -0.13142 ± 0.23730
Rate order: 0.07343 ± 0.04211
Multiple r-squared: 0.7525
Adjusted r-squared: 0.505
```

Fig. 5.4 The log (rate, *u*) *versus* pH plot to determine the rate order of the birnessite-oleic acid reaction with respect to pH of the birnessite surface—for the colour components red (y_R), green (y_G), blue (y_B), sum (Σy) and average rate ($\bar{u}$).

where y is the value of the colour component (y_R, y_G, y_B, Σy) and y_0 is the point of the start of the reaction ($(y_R)_0$, $(y_G)_0$, $(y_B)_0$, $(\Sigma y)_0$). In equation 5.1, the rate constant k is the slope of the straight line. The aim is to plot an Arrhenius plot ($\ln k$ v. $1/T$), and the value of k itself is positive, even if the rate is negative. For exponential best-fits, the rate constant is located within the power of the natural exponential function:

$$y = y_0 e^{-kt} \tag{5.2}$$

For the power best-fits, the rate constant is somewhat implicitly stated and has to be extracted by mathematical manipulation. For the general n^{th} order y v. t curve, a typical rate expression containing the rate constant can be conveniently defined as:

$$\frac{dy}{dt} = -kt^{n-1} \tag{5.3}$$

Integration between y_0 (at time 0 for demonstrative simplicity here, but not necessarily at 0 h of reaction, as seen in Table 5.1) and some y at time t:

$$\int_{y_0}^{y} dy = -k\int_{0}^{t} (t^{n-1})dt \tag{5.4}$$

gives the power function, the same form in some of the best-fit curves in Table 5.1:

$$y - y_0 = -\frac{k}{n}t^n \tag{5.5}$$

A negative power of t means n has a negative value, and the term containing k is positive, as seen in Table 5.1. For the sake of simplicity, the rate constants were extracted from the initial rates in Table 5.1, regarding the initial part of the rate as effectively a straight line (equation 5.1).

The natural logarithm of the rate constants obtained ($\ln k$) were plotted against the reciprocal of temperature ($1/T$) in an Arrhenius plot for each colour component (k_{y_R}, k_{y_G}, k_{y_B}, $k_{\Sigma y}$) and the average rate ($k_{\bar{u}}$) in Fig. 5.5. The rate constants originating from the average of all the components ($k_{\bar{u}}$) yielded the best-fitting linear model ($r^2 = 90\%$) with a slope of −1,541.4. This yields an activation energy of 12.8 ± 4.2 kJ mol^{-1}, which is lower than the reported ranges of 88–94 kJ mol^{-1} for lipid peroxidation (Litwinienko and Kasprzycka-Guttman, 2000; Litwinienko, 2001) and 63 kJ mol^{-1} for lipid peroxidation catalysed by certain metal ions (Choe and Min, 2006).

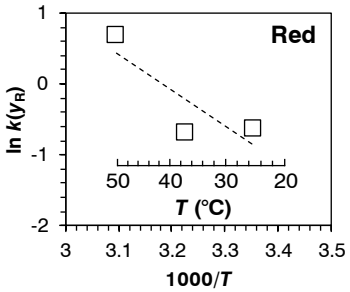


```
Intercept: 15.98 ± 10.20
Slope: -5021.70 ± 3161.51
Act. Energy:  41.750 ± 26.285
                kJ per mole
Multiple r-squared: 0.7161
Adjusted r-squared: 0.4323
```

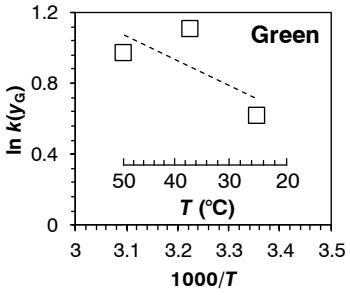


```
Intercept: 5.366 ± 4.436
Slope: -1386.906 ± 1374.520
Act. Energy:  11.531 ± 11.428
                kJ per mole
Multiple r-squared: 0.5045
Adjusted r-squared: 0.008971
```

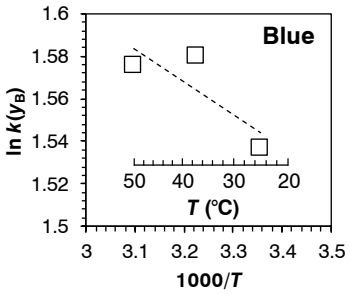


```
Intercept: 2.052 ± 0.347
Slope: -151.440 ± 107.500
Act. Energy:  1.259 ± 0.894
                kJ per mole
Multiple r-squared: 0.6649
Adjusted r-squared: 0.3299
```

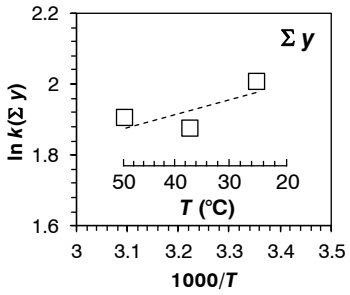


```
Intercept: 0.654 ± 1.143
Slope: 394.549 ± 354.166
Act. Energy:  -3.280 ± 2.945
                kJ per mole
Multiple r-squared: 0.5538
Adjusted r-squared: 0.1076
```

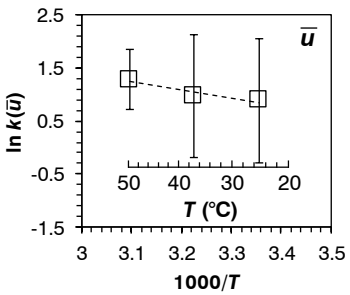


```
Intercept: 6.013 ± 1.641
Slope: -1541.374 ± 508.414
Act. Energy:  12.815 ± 4.227
                kJ per mole
Multiple r-squared: 0.9019
Adjusted r-squared: 0.8038
```

Fig. 5.5 The Arrhenius plots used to determine the activation energy (E_a) for the birnessite-oleic acid reaction—for the colour components red (y_R), green (y_G), blue (y_B), sum (Σy) and average rate ($\bar{u}$).

5.3.2 Correlation of RGB values with other parameters

Parallel experiments that were run using pH 4 birnessite and oleic acid as well as pH 7 birnessite and oleic acid were sampled at 90 h, 108 h and 161 h reaction time, after incubating at 50°C. The results of their measured UV-VIS absorbance at 490 and 270 nm (A_{490} and A_{270}, respectively), their Mn^{3+}, Mn^{2+} and total dissolved Mn (ΣMn) concentrations ($[Mn^{3+}]$, $[Mn^{2+}]$ and ΣMn, respectively), as well as their RGB values (y_R, y_G, y_B, Σy) are given in Table 5.2.

Table 5.2 The results of extracted red (y_R), green (y_G), blue (y_B) and sum (Σy) values, UV-VIS analysis as well as $[Mn^{3+}]$, $[Mn^{2+}]$ and ΣMn determination for the pH 4 and pH 7 birnessite-oleic acid experiments sampled after 90, 108 and 161 h of incubation at 50°C.

	Sample					
	pH 4 birnessite + oleic acid			**pH 7 birnessite + oleic acid**		
	90 h	**108 h**	**161 h**	**90 h**	**108 h**	**161 h**
A_{490} *	9.508	8.032	12.922	5.344	7.044	11.333
A_{270}	0.427	0.420	0.667	0.377	0.402	0.664
ΣMn †	0.972	0.092	1.355	0.399	0.700	0.128
$[Mn^{3+}]$ ‡	0.119	0.044	0.148	0.041	0.054	0.070
$[Mn^{2+}]$ ¥	0.853	0.048	1.207	0.359	0.646	0.058
y_R	91	127	68	110	138	68
y_G	18	21	27	25	28	13
y_B	9	1	25	5	1	10
Σy	118	149	120	140	167	91

* The maximum absorbance at which detector saturation occurred was 2, samples exceeding 2 were diluted until below 2, and then their true absorbances back-calculated using the dilution factor.

† $\Sigma Mn = [Mn^{3+}] + [Mn^{2+}]$, in mmol per 10g sample.

‡ in units of mmol per 10g sample.

¥ $[Mn^{2+}] = \Sigma Mn - [Mn^{3+}]$, in mmol per 10g sample.

To see if any useful relationships exist between y_R, y_G, y_B, Σy and measured parameters such as UV-VIS absorbance, $[Mn^{3+}]$, $[Mn^{2+}]$ and ΣMn, a Pearson correlation matrix was generated for all parameters concerned and is presented in Table 5.3.

Table 5.3 Pearson correlation matrix for the various parameters—*viz.* red (y_R), green (y_G), blue (y_B), sum (Σy), UV-VIS absorbance at 270 nm (A_{270}), absorbance at 490 nm (A_{490}), $[Mn^{3+}]$, total Mn concentration (ΣMn) and $[Mn^{2+}]$. Concentrations of Mn species are, as before, in units of mmol per 10 g sample.

	y_R	y_G	y_B	Σy	A_{270}	A_{490}	$[Mn^{3+}]$	ΣMn	$[Mn^{2+}]$
y_R	1								
y_G	0.46	1							
y_B	−0.84	0.08	1						
Σy	0.93	0.75	−0.58	1					
A_{270}	−0.85	−0.31	0.78	−0.75	1				
A_{490}	−0.82	−0.31	0.82	−0.70	0.91	1			
$[Mn^{3+}]$	−0.70	0.03	0.88	−0.47	0.57	0.80	1		
ΣMn	−0.33	0.49	0.71	−0.02	0.23	0.44	0.86	1	
$[Mn^{2+}]$	−0.29	0.52	0.69	0.02	0.19	0.40	0.83	1.00	1

A strong positive correlation exists between blue (y_B) values and $[Mn^{3+}]$ (r = 88%), with the negative correlation of red (y_R) values *v.* absorbance at 270 nm and 490 nm following close behind ($r = -85\%$ and -82%, respectively). Moderately strong positive correlations exist between blue values and absorbance at 490 nm, absorbance at 270 nm and ΣMn (r = 82, 78 and 71%, respectively).

Moderate negative correlations also exist between Σy and absorbance at 270 and 490 nm ($r = -75$ and -70%, respectively) as well as red values and $[Mn^{3+}]$ ($r = -70\%$). There also exists a moderate positive correlation between blue values and $[Mn^{2+}]$ (r = 69%), whilst a weaker positive correlation exists between green values and $[Mn^{2+}]$ (r = 52%) and green values and ΣMn (r = 49%). A fairly weak negative correlation exists between Σy and $[Mn^{3+}]$ ($r = -47\%$). Weak negative correlations exist between red values and ΣMn ($r = -33\%$), green values and absorbances at 270 and 490 nm ($r = -31\%$), as well as red values and $[Mn^{2+}]$ ($r = -29\%$). Between Σy and ΣMn, Σy and $[Mn^{2+}]$, and between green values and $[Mn^{3+}]$, virtually no relationship exists (r = 2 and −2%, respectively).

The relationships reveal that Mn^{3+}, which is red in solution, is potentially responsible for much of the colour present in these experiments too, but not for all of it. Some of the darkening must therefore also be attributed to the peroxidation, oxidation or polymerisation reactions that are taking place. In the data comparisons presented, it is apparent that not one particular Mn-species' concentration or another parameter can be completely correlated with the colour components. This is demonstrative of the difficulties involved when trying to study the kinetics of complex systems, where there exist reactions

such as the continuous redox cycling between Mn-species for example (Mn^{3+} and Mn^{2+}). This means measurement of parameters such as [Mn^{3+}] may not be a useful parameter to track reaction kinetics of darkening after all.

Despite the liquid phase being a typically red colour, green and blue values in some cases prove to be more reliable in tracking colour changes. This unreliability of the red colour has been noted in other studies using colour values as a quantification tool (see *e.g.* Shokrollahi and Shokrollahi, 2014). The red value not following the trends of the green and blue value is also observed in Fig. 5.2 and Table 5.1, with red values generally requiring a different best-fit curve to the green and blue values.

As expected, weaker relationships exist with respect to [Mn^{2+}] and ΣMn, and this is attributed to Mn^{2+} being a colourless ion in solution. However, there do exist some moderate relationships between blue and [Mn^{2+}] and blue and ΣMn. Blue is also the colour that has the strongest relationship with [Mn^{3+}]. This interrelationship between these three Mn quantities and the blue colour values could be as a result of a moderately strong relationship between [Mn^{3+}] and [Mn^{2+}] (r = 83%) and a very strong relationship between ΣMn and [Mn^{2+}] (r = 100%). This very strong relationship between ΣMn and [Mn^{2+}] could be related to the fact that in many cases, Mn^{2+} comprises most of the total dissolved Mn (see Table 5.2; Fig. 5.6 below).

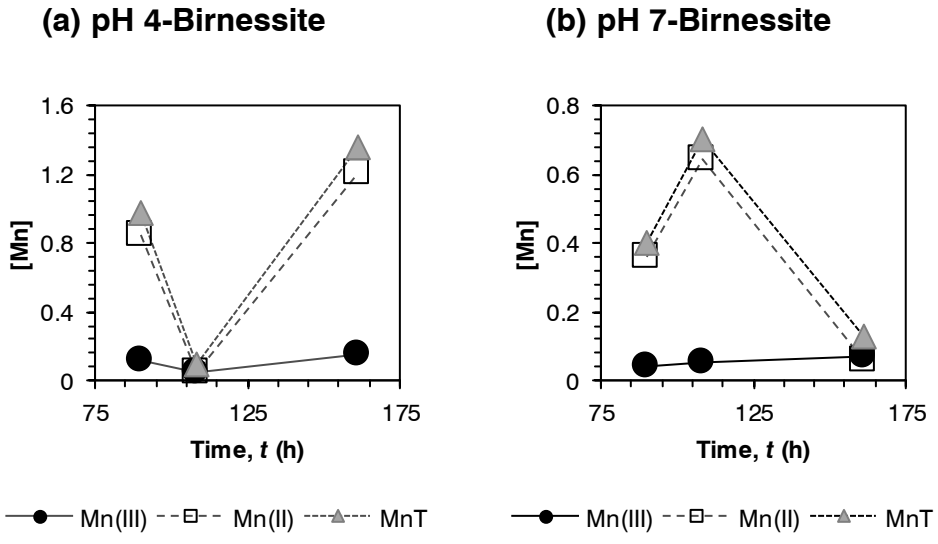

Fig. 5.6 The generation of dissolved Mn species (Mn(III) = Mn^{3+}; Mn(II) = Mn^{2+}; MnT = [Mn^{3+}] + [Mn^{2+}] ≈ ΣMn) over time for the reaction of (a) pH 4 birnessite with oleic acid and (b) pH 7 birnessite with oleic acid, at 50°C and sampled at 90, 108 and 161 h. [Mn] = concentration of various Mn-species in mmol per 10 g sample.

5.4 Summary and conclusions

The course of the darkening reaction that occurs between birnessite and oleic acid was quantified with a non-destructive, RGB colour component monitoring method under various conditions. Variation in mass-loading of the mineral to oleic acid ratio, the pH of the birnessite surface, and the temperature of incubation revealed pertinent kinetic information about the reaction.

The birnessite-oleic acid reaction rate is fractionally, but almost linearly, dependent on the initial mass of birnessite to oleic acid ratio (rate order ~ 0.75; *i.e.* a doubling of effective surface area roughly doubles the reaction rate) whilst only weakly dependent on the pH of the birnessite surface (rate order ~ 0.2). The findings also correspond to similar observations in other studies where birnessite was reacted with organics such as catechol. The virtual independence of the reaction rate with respect to pH reveals that the formation of the surface complex is a favourable reaction over a pH range of *c.* 4 to 7.

Variation in reaction incubation temperature revealed the activation energy (E_a) of the birnessite-oleic acid reaction to be 12.8 ± 4.2 kJ mol^{-1}. Despite having a lower E_a than the lipid peroxidation reaction ($E_a = 88$–94 kJ mol^{-1}), it is believed that a unique reaction exists between birnessite and oleic acid, and that birnessite does not simply catalyse (*i.e.* lower the E_a of) the lipid peroxidation reaction. The lipid peroxidation reaction is a reaction happening independently of the birnessite-oleic acid surface reaction, and possibly at a slower rate. This was inferred from the observation that the dominant form of dissolved Mn in the liquid phase was in the divalent state (Mn^{2+}), which results from the oxidation of oleic acid by Mn^{3+}.

Moderate correlation between Mn^{3+} formation and darkening of the liquid phase also suggests that the red colour of Mn^{3+} alone is not responsible for all the darkening observed. It was however difficult to establish which chemical species was specifically responsible for the observed darkening during the birnessite-oleic acid reaction.

In terms of the application of the RGB colour analysis technique, this non-destructive method provides a simple and cost-effective means of reaction monitoring. As this is the first attempt at using such a method for this purpose, a few improvements are inevitable. The initial lag which is observed for all the samples at or below 37°C until 68 h reaction time is followed by a sudden initiation of the reaction and rapid darkening. Between 68 h and approximately 143 h of reaction time, greater time resolution (*i.e.* more photographs) is needed to resolve that particular time period of fast kinetics. A time interval of 2 or even 1 h would improve time resolution of this region of the curve dramatically. Further future applications of this method may include an automatic photographic system or capturing the reaction progress with high-definition video recording.

CHAPTER 6

Environmental significance and implications

6.1 Introduction

The findings of this study indicate that several mineral phases of the soil clay fraction are able to interact with, and transform, lipids. In particular, birnessite, an Mn-oxide commonly found in the soil clay fraction, reacts with oleic acid, a free fatty acid lipid, to form higher molecular weight, polyester compounds. This sheds new light on the potential fate of free fatty acids in nature, which originate from various biological and abiotic reactions (*e.g.* triglyceride hydrolysis; see § 2.5.3 and Fig. 2.6).

When studying the rates of the darkening reaction between birnessite and oleic acid (chapter 5), approximately 90% of the total amount of darkening occurs anywhere between *c.* 15 days at 25°C to 3 days at 50°C.

Whilst darkening could not be attributed to any one specific chemical species being generated or removed, it is regarded as an approximate tracer of the course of the polymerisation reaction in general. One has to bear in mind though, this is a model study and the results obtained in this work do not necessarily translate directly into what will be observed in nature. Many biological reactions have the capacity to either constructively (positively) or destructively (negatively) interfere with clay-lipid interactions.

6.2 Interactions with natural reactions and processes

6.2.1 Biotic and abiotic interactions

One of the major barriers to the birnessite-lipid reaction appears to be the initial form in which the lipid is found when it encounters the mineral surface. When in free fatty acid form, the carboxyl end is free to exchange with Mn-centres on the mineral surface, at a relatively wide pH range, and this step appears to be a crucial first step in the lipid-birnessite reaction. However, when the lipid is in triglyceride form, the carboxyl groups are ester-bonded to glycerol and not free to exchange with the oxide surface. This was inferred from the fact that olive oil (where oleic acid is in its triglyceride form, triolein) does not seem to darken or thicken in the presence of birnessite. In a natural system, however, the various biological and abiotic triglyceride hydrolysis reactions may transform the triglycerides into free fatty acids, which are then free to react with the Mn-oxide surface. In this manner, reactions occurring beyond specifically lipid-Mn-oxide reactions may support the lipid-Mn-oxide reaction. The lipid-Mn-oxide reaction may also be hindered by outside reactions too though. Under some conditions, lipids may be outcompeted for sites on the Mn-oxide surface by other organic or even inorganic substances. A possible example would be under anaerobic conditions where a lack of O_2 may render Mn-oxides preferred terminal electron acceptors for several natural redox reactions.

6.2.2 Stabilisation of environmental oxidants

The redox-active clay phases (those containing Mn and Fe) were shown to potentially produce various multivalent forms of Mn and Fe species during their reaction with oleic acid. For Mn-oxide phases, it was found that the reaction with oleic acid produced both Mn^{2+} and Mn^{3+}, and whilst not conclusively proven, it is believed that for the Fe-containing clay phases (*e.g.* Fe-oxides), the reaction with oleic acid produces soluble Fe^{3+} (and possibly, but not likely, Fe^{2+} as well). The presence of Mn and Fe species, and with them possibly being complexed and stabilised by carboxyl or hydroxyl functional groups on the lipid, has significant implications for several redox reactions in soils and nature

in general. The trivalent form of Mn has a very high relative redox potential versus most other chemical species in nature, and as a result is one of the most imperative oxidants in the environment. It is a crucial initiator of the oleic acid-Mn oxide reaction itself, as it was observed that birnessite (which contains Mn^{3+} in many of its octahedral sites) was far more reactive than pyrolusite (which contains no Mn^{3+}). The "*Achilles heel*" of Mn^{3+} so to speak has always been its perceived chemical instability, but over the last few years it has been revealed that it is one of the dominant forms of Mn found in nature. This is achieved by various stabilisation mechanisms, and if Mn^{3+} is indeed produced as a result of lipid-Mn-oxide reactions, and stabilised by lipids or lipid-oxidation products, then this would be another significant mechanism by which Mn^{3+} is potentially stabilised in nature, providing a platform from where it can influence numerous biogeochemical reactions as a powerful oxidant. Similarly, Fe^{3+} is one of the most ubiquitous oxidants in the environment, and its reduced counterpart, Fe^{2+}, is one of the most important reducing agents in the natural environment, especially in biogeochemical systems such as the microbiological sulphate-sulphide system. Likewise, Mn^{2+} is another significant reducing agent in the environment.

If these species of Mn and Fe are stabilised by lipids or lipid oxidation products, and their mineral-phase counterparts (*e.g.* Mn- and Fe-oxides) facilitate the formation of thickened, polymerised products from lipids, the possibility exists of these combined products forming hydrophobic yet oxidative or reductive coatings on several mineral grains in nature. The polymer would potentially have the capacity to coat redox inactive mineral grains in soils, such as quartz (SiO_2) and clay minerals, potentially rendering them redox active and able to sorb/transform various hydrophobic organic compounds in nature that they normally would not have. These potential organo-mineral *quasi*-solid associations, if present, possibly play currently unknown key roles in the soil environment, driving several processes whose mechanisms are still not clear to this day—*e.g.* the abiotic formation of reduced species such as carbon monoxide (CO) in what are considered fairly aerobic soil environments. These natural hydrophobic yet redox-active organo-mineral associations would also find potential industrial applications as a means of creating highly oxidative/reductive yet hydrophobic catalysts, using readily available material (*e.g.* sand or clay particles) as a substrate and coating it with a catalytic coating—usually only the surface of a solid catalyst participates in a catalytic reaction. This is very similar to the current practice of functionalising of nanoparticle surfaces with the catalytic functional group of interest, whilst the main core of the nanoparticle is simply an unreactive substrate.

6.3 Environmental remediation applications

There exists a potential further application of this study, with respect to waste effluents and solid residues of the olive oil milling process, a waste product known collectively as olive mill waste (OMW; Azbar *et al.*, 2004). Annually, around 1.8 mega-tonnes of olive oil are produced globally (Al-Khatib *et al.*, 2009), and with each tonne of olives milled, approximately 400–600 kg of solid waste and 0.4–1.8 m^3 of waste water effluent (Tomati and Galli, 1992; Azbar *et al.*, 2004) are produced. The disposal of OMW poses a major environmental pollution risk, as these wastes are rich in polyphenols, proteins, lipids, sugars, tannins and nitrogen (Azbar *et al.*, 2004), all of which have to be removed and the waste effluent treated effectively, before it can be released back into the environment. Many absorbent and catalytic matrices are known to remove the pollutants from OMW, and these include activated carbon, *Azolla* spp. ferns, zeolite and titanium dioxide (TiO_2) nanoparticles (Badawy *et al.*, 2010; Carlozzi *et al.*, 2015). It has already been demonstrated that minerals of the soil clay fraction can transform and catalyse the humification of most of the pollutant compounds mentioned. The only unknown transformation thus far has been the possible humification of lipids by soil clays. Since this study demonstrates that lipid humification, transformation or removal is facilitated by soil minerals, then another potential application of this study would be an OMW treatment step or process which can remove lipids from OMW, to form stable, passive and environmentally beneficial soil carbon. In brief, soil clays would be assisting in transforming an environmental pollution problem into an environmentally and ecologically beneficial scenario.

The apparent hinderance to this process is the fact that olive oil is present in triglyceride form. However, if combined with a biological or catalytic first step (as mentioned in § 6.2.1) which converts triglycerides to free fatty acids (*e.g. via* lipase enzymes or acid catalysis), then these free fatty acids are then free to react with soil clay phases, transforming hydrophobic compounds that would have been considered potential pollutants into stabilised soil organic matter (SOM) in the form of polymerised products. These polymerised products could act as hydrophobic *quasi*-solids, formed as an *in-situ* product of the reaction, but ultimately acting as a potential sorbent for several hydrophobic components of OMW that are considered either toxic to the environment or general environmental pollutants.

If such a scenario is not possible however, for example if soil mineral phases appear to be totally unreactive toward the triglycerides and even fatty acids for some reason, then highly oxidative clay phases such as Mn-oxides might still find a use in OMW treatment as an anti-oxidant scavenger. In § 2.5.2, it was discussed how there exist many free-radical scavengers in olive oil that hinder reactions such as lipid peroxidation, many of which are pigments. Whilst Mn-oxides did not transform or polymerise the triglycerides when reacted with ol-

ive oil, it did "*bleach*" the oil (see Fig. 4.12), removing the pigmentation of the oil and the free-radical scavengers present in the oil. Therefore, it is possible that OMW treatment with Mn-oxide could be added as an initial step, to enhance the rate of (biotic or abiotic) lipid peroxidation by removing free-radical scavengers that hinder the reaction.

The clay-lipid reactions demonstrated in this model study have potentially far-reaching environmental implications and have thus generated the scope for numerous future studies on the topics outlined.

CHAPTER 7

General conclusions and future work

7.1 General conclusions

The present work set out to investigate whether lipids could be humified into dark, high-molecular weight lipid-derived humic substances by the action of mineral phases that are commonly found in the soil clay fraction (<2 μm size particles). A model lipid, oleic acid, was reacted with several clay phases, and three key aspects were focused on regarding this clay-lipid reaction, including (a) identifying the products formed, (b) elucidating the reaction mechanism and (c) studying the kinetics of this reaction. By focusing on these three aspects (which became the three objectives of this study), the question could be answered as to whether soil clays have the capacity to humify lipids.

The results of this study indicate that the different mineral phases (or clays) selected each reacted to varying degrees and in different ways to the lipid oleic acid. The reactivity of the clays and the products that they formed as a result of interaction with oleic acid could be roughly grouped into two major groups—the *redox-active* clays (minerals containing Mn and Fe) and the *redox-inactive* or *non-redox-active* clays (minerals containing mostly Al and Si).

These two groups produced vastly different reaction products and showed varying degrees of reactivity toward oleic acid within each group. The redox-active clays polymerised oleic acid into polyesters, whilst themselves being possibly dissolved and releasing soluble forms of Mn and Fe into the liquid phase. This was demonstrated clearly for the Mn-oxide birnessite, which produced both Mn^{3+} and Mn^{2+} as a result of the reaction. However, the reductive dissolution (or chelation-dissolution for that matter) of Fe-oxide phases such as goethite and the reduction or chelation of Fe^{3+} in Fe^{3+}-saturated montmorillonite could not be demonstrated unequivocally, as no conclusive evidence of dissolved Fe species (Fe^{3+}/Fe^{2+}) was found. The redox-inactive clays on the other hand polymerised oleic acid into dimers and possibly trimers, most likely *via* a Lewis-acid mechanism. The Al-oxide mineral gibbsite was the most reactive clay of this group towards oleic acid.

The formation of environmentally significant dissolved Mn species such as Mn^{3+} prompted deeper probing into the reaction mechanism of the reaction between birnessite and oleic acid. The formation of these polyesters by the action of birnessite does not form *via* the classic epoxidation ring-opening and subsequent condensation mechanism, as no epoxidation products or loss of unsaturation (*i.e.* double bonds) occurs. Instead, the *cis*-configured double bond changes to a *trans*-configuration (indicative of peroxidation) and remains virtually intact, forming part of the final polyester structure.

It is therefore concluded that several soil clays indeed polymerise (humify) the lipid oleic acid, into varying polymerised products (depending on the clay phase) and *via* very specific mechanisms, also dependent on the specific clay phase that is mediating the humification reaction.

Considering the reaction of birnessite with oleic acid once more, it provides the most demonstrative case for investigating the kinetics of the lipid-clay reaction. The fact that birnessite was (i) the most reactive toward oleic acid, (ii) showed the greatest degree of darkening and polymerisation (lipid humification) and (iii) produced conclusively detectable soluble (and one coloured) Mn species, made it the ideal case to employ a simple visual monitoring technique in order to study the kinetics of the lipid-clay reaction.

The fractional, but near-linear dependence of the birnessite-oleic acid reaction rate on the mass of mineral present (effective surface area) indicates the importance of the formation of the mineral surface complex formation as the first step in the reaction mechanism. The direct binding of the carboxylate group with metal centres on the mineral surface is a crucial first step for initiation of the reaction. The importance of this first step was demonstrated by the lack of reactivity olive oil showed toward birnessite, since it has its carboxyl groups bonded *via* glycerol in triglyceride form and thus unavailable for surface exchange. Whilst this first surface exchange step is crucial, it is not greatly influenced by the surface pH of the mineral surface, as kinetic studies indicated a virtual independence of reaction rate on surface pH.

Kinetic studies with respect to temperature revealed that the darkening reaction between birnessite and oleic acid appeared to be more spontaneous (E_a = 12.8 kJ mol^{-1}) than regular peroxidation/autoxidation ($E_a \sim$ 80 kJ mol^{-1}). It is therefore concluded that whilst birnessite lowers the activation energy (energy barrier) of lipid humification, it does not catalyse the peroxidation reaction *per se*, as it itself is consumed during the reaction and the reaction proceeds *via* a unique mechanism, with peroxidation occurring as a completely independent reaction in another part of the reaction vial, despite its peroxidation products influencing the eventual oxidation of Mn^{2+} to Mn^{3+}.

The formation of stable polyesters and stable associations with Mn^{3+}, Mn^{2+} (and possibly Fe^{3+}, Fe^{2+}) has wide-ranging implications for biogeochemical redox cycling in natural systems, as these species play central roles in environmental redox reactions. The formation of Mn^{3+}- or Fe^{3+}-polyester *quasi*-solid structures for example could mimic the role of oxidants such as Mn- and Fe-oxides in nature. Their hydrophobic aliphatic structures would attract several hydrophobic organics, allowing them to adsorb onto the polymer surface and then be oxidised by the trivalent cation present in the polymer structure. This is potentially very important in the transformation of toxic xenobiotic organics to innocuous compounds for example and may be an overlooked mechanism in the transformation of these xenobiotic compounds already occurring in soils during their natural breakdown.

In this purely abiotic study, birnessite does not catalyse the lipid peroxidation reaction, and the formation of lipid peroxidation products (such as hydroperoxides) is the limiting factor in the oxidation of Mn^{2+} to Mn^{3+}. In nature however, the birnessite-lipid reaction would occur alongside several other reactions, such as lipid peroxidation by peroxidase enzymes, as well as triglyceride hydrolysis by lipase enzymes. In this way, biotic reactions provide the substrates such as hydroperoxides and free fatty acids that are required for the lipid-Mn oxide reaction to eventually form polyesters. This combined abiotic and biotic approach could therefore be useful in the mitigation of pollution by olive oil mill wastewater (OMW) for example. A biotic step first transforms the lipids into a form that can react with Mn-oxides, and then the abiotic step follows where lipids are converted into polymerised products by Mn-oxides. Birnessite also removes radical-scavengers, potentially increasing the efficiency of existing lipid peroxidation reactions.

This combined biotic-abiotic mechanism could also be closer to the true mechanism of humified (polymerised) lipid products in soils. The present study investigated one part of the possible abiotic component of the lipid humification mechanism in nature. By doing so, it thus served to shed more light on the combined lipid humification mechanism in nature, by highlighting reaction mechanisms formerly not known to take part in the humification of lipids as well as the stabilisation of lipids and lipid-derived humic substances in nature.

These mechanisms influence the stability of soil organic matter (SOM) and therefore impact the global carbon budget and ultimately global climate.

7.2 Future work

Future work on the topic of this present study would most certainly revolve around the mechanism and kinetics of the Mn- and Fe-oxide-lipid reaction—this present study is only the first one on this topic and could not possibly have covered all the bases. Techniques such as X-ray absorption near edge structure (XANES) spectroscopy could be employed to study the mineral-lipid reaction *in-situ*, tracking the changes to the oxidation state of Mn and Fe during the reaction, in real time, and proving or disproving the existence of various multivalent Mn and Fe species in the liquid phase. Real time *in-situ* investigation of the reaction using a dedicated FTIR system would also reveal valuable information about specific bonds appearing and disappearing in real time—yielding indispensable information on the reaction mechanism and kinetics of specific species and crucial moments of specific bond formation/breaking during the reaction. Considering the kinetics of the reaction further, automated image capturing systems (still or video) would greatly aid much greater time resolutions, especially at the initial parts of the reaction where fast kinetics dominate.

Another important aspect to investigate would be the possible role (or lack of a role) that oxygen plays in these lipid-polymerisation reactions. In the current work, it was suggested that oxygen diffusion through the entire liquid (oil) column to the mineral-liquid interface may not be occurring. Future studies may involve measuring the partial pressure of oxygen (P_{O_2}) in the liquid phase down to the mineral-liquid interface, to determine the depth of oxygen diffusion, and whether oxygen (and thus peroxidation) play a role in the lipid-mineral reaction mechanism.

The reaction of oleic acid with smectites as well as birnessite also altered the mineral phases themselves. As mentioned, birnessite was dissolved, whilst the interlayer of smectite had collapsed slightly after reaction with oleic acid. An investigation into parameters such as smectite CEC before and after reaction with oleic acid may reveal if organic phases are being trapped in the interlayer, "*locking*" it in place. Investigations with techniques such as high-resolution transmission electron microscopy (HR-TEM) may reveal more information about the morphology of mineral dissolution in the case of the redox-active phases, especially birnessite. This technique would also possibly detect the formation of any newly formed, authigenic, nano-sized Mn- or Fe-oxide phases forming *in-situ* due to the lipid-mineral reaction.

Many studies could also investigate the formation and reactivity of the potential Mn^{3+}-polyester hydrophobic oxidative coatings of non-redox active soil mineral particles mentioned previously. These studies might be extended

to the coating of otherwise unreactive nanoparticles, in the formation of high surface area nano-catalysts. Such catalysts would need to be characterised in order to determine their suitability for industrial applications.

As mentioned previously, in nature, these abiotic clay-lipid reactions would not occur in isolation, so several studies would be required to investigate the effect of addition of biological catalysts such as lipase and peroxidase enzymes on the formation of polyesters and potential Mn and Fe cation stabilisation in nature. The clay-lipid reaction would also potentially occur under anoxic or anaerobic conditions, where there is no O_2 present for the lipid peroxidation reaction mechanism, and where Mn- and Fe-oxides for example are also being competed for by other biological reactions for a terminal electron acceptor. All of these scenarios would be significant research topics, with the application being to try and place these model clay-lipid reactions demonstrated in this study into a natural-soil-environmental context.

The fact that the clay-lipid reactions would not occur in isolation in real soils also means that there is the possibility of overlap or integration with other humification pathways (*e.g.* Maillard reaction and polyphenol pathway) in the same way that a well-known integration mechanism already exists between the Maillard reaction and polyphenol pathway. Furthermore, the fact that this integrated pathway is catalysed by soil clays could be a precursor that a potential lipid-polyphenol or lipid-Maillard integrated pathway could also be catalysed by soil minerals present in the clay phase. Such a pathway would potentially lead to the formation of aliphatic structures that also contain nitrogen or aromatic structures, thereby potentially influencing the stability of humic substances (and thus SOM) dramatically in currently unknown ways.

References

Abbaszaadeh, A., Ghobadian, B., Omidkhah, M.R., Najafi, G. (2012). Current biodiesel production technologies: a comparative review. *Energy Conversion and Management*, vol. 63, pp. 138–148.

AbuGhazaleh, A.A., Jenkins, T.C. (2004). Docosahexaenoic acid promotes vaccenic acid accumulation in mixed ruminal cultures when incubated with linoleic acid. *Journal of Dairy Science*, vol. 87, no. 4, pp. 1047–1050.

Agatha, G., Voigt, A., Kauf, E., Zintl, F. (2004). Conjugated linoleic acid modulation of cell membrane in leukemia cells. *Cancer Letters*, vol. 209, no. 1, pp. 87–103.

Aiken, G.R., McKnight, D.M., Wershaw, R.L., MacCarthy, P. (eds) (1985). *Humic substances in soil, sediment and water: Geochemistry, isolation and characterization*. Wiley: New York, NY. 692pp. ISBN: 0471882747

Al-Khatib, A., Aqra, F., Al-jabari, M., Yaghi, N., Basheer, S., Sabbah, I., Al-hayek, B., Mosa, M. (2009). Environmental pollution resulting from olive oil production. *Bulgarian Journal of Agricultural Science*, vol. 15, no. 6, pp. 544–551.

Allen, R.R., Jackson, A., Kummerow, F.A. (1949). Factors which affect the stability of highly unsaturated fatty acids. I. Differences in the oxidation of conjugated and nonconjugated linoleic acid. *Journal of the American Oil Chemists' Society*, vol. 26, no. 8, pp. 395–399.

Alex, T.C., Kumar, R., Roy, S.K., Mehrotra, S.P. (2013). Leaching behaviour of high surface area synthetic boehmite in NaOH solution. *Hydrometallurgy*, vol. 137, pp. 23–32.

Anderson, T.R., Hawkins, E., Jones, P.D. (2016). CO_2, the greenhouse effect and global warming: from the pioneering work of Arrhenius and Callendar to today's earth system models. *Endeavour*, vol. 40, no. 3, pp. 178–187.

Andrikopoulos, N.K., Brueschweiler, H., Felber, H., Taeschler, C. (1991). HPLC analysis of phenolic antioxidants, tocopherols and triglycerides. *Journal of the American Oil Chemists' Society*, vol. 68, no. 6, pp. 359–364.

Andrikopoulos, N.K., Giannakis, I.G., Tzamtzis, V. (2001). Analysis of olive oil and seed oil triglycerides by capillary gas chromatography as a tool for the detection of the adulteration of olive oil. *Journal of Chromatographic Science*, vol. 39, no. 4, pp. 137–145.

Aranda, F., Gómez-Alonso, S., Rivera del Álamo, R.M., Salvador, M.D., Fregapane, G. (2004). Triglyceride, total and 2-position fatty acid composition of Cornicabra virgin olive oil: comparison with other Spanish cultivars. *Food Chemistry*, vol. 86, no. 4, pp. 485–492.

Arfaioli, P., Ristori, G.G., Bosetto, M., Fusi, P. (1997). Humic-like compounds formed from L-tryptophan and D-glucose in the presence of Cu (II). *Chemosphere*, vol. 35, no. 3, pp. 575–584.

Arfaioli, P., Pantani, O.L., Bosetto, M., Ristori, G.G. (1999). Influence of clay minerals and exchangeable cations on the formation of humic-like substances (melanoidins) from D-glucose and L-tyrosine. *Clay Minerals*, vol. 34, no. 3, pp. 487–497.

Arrhenius, S. (1896). On the influence of carbonic acid in the air upon the temperature of the ground. *The London, Edinburgh, and Dublin Philosophical Magazine and Journal of Science: Series* 5, vol. 41, no. 251, pp. 237–276.

Asgari, S., Sahari, M.A., Barzegar, M. (2018). Ultrasound-assisted bleaching of olive oil: kinetics, isotherms and thermodynamics. *Journal of Food Engineering*, vol. 224, pp. 37–44.

Association of Official Analytical Chemists (AOAC) (2016). Method 41: oils and fats. In: Latimer Jr, G.W. (ed.), *Official Methods of Analysis*, 20th edn. AOAC: Rockville, MD.

Assy, N., Nassar, F., Grosovski, M. (2010). Monounsaturated fat enriched with olive oil in non-alcoholic fatty liver disease. In: Preedy, V.R., Watson, R.R. (eds), *Olives and Olive Oil in Health and Disease Prevention*, pp. 1151–1156. Academic Press: London.

Aued-Pimentel, S., da Silva, S.A., Takemoto, E., Cano, C.B. (2013). Stigmastadiene and specific extitntion (270 nm) to evaluate the presence of refined oils in virgin olive oil commercialized in Brazil. *Food Science and Technology*, vol. 33, no. 3, pp. 479–484.

Aufdenkampe, A.K., Mayorga, E., Raymond, P.A., Melack, J.M., Doney, S.C., Alin, S.R., Aalto, R.E., Yoo, K. (2011). Riverine coupling of biogeochemical cycles between land, oceans, and atmosphere. *Frontiers in Ecology and the Environment*, vol. 9, no. 1, pp. 53–60.

Auffray, B. (2007). Protection against singlet oxygen, the main actor of sebum squalene peroxidation during sun exposure, using Commiphora myrrha essential oil. *International Journal of Cosmetic Science*, vol. 29, no. 1, pp. 23–29.

Avula, S.G.C., Belovich, J.M., Xu, Y. (2017). Determination of fatty acid methyl esters derived from algae *Scenedesmus dimorphus* biomass by GC–MS with one-step esterification of free fatty acids and transesterification of glycerolipids. *Journal of Separation Science*, vol. 40, no. 10, pp. 2214–2227.

Azamat, D.V., Dejneka, A., Lancok, J., Trepakov, V.A., Jastrabik, L., Badalyan, A.G. (2012). Electron paramagnetic resonance studies of manganese centers in $SrTiO_3$: Non-Kramers Mn^{3+} ions and spin-spin coupled Mn^{4+} dimers. *Journal of Applied Physics*, vol. 111, no. 10, p. 104119 (6pp.).

Azbar, N., Bayram, A., Filibel, A., Muezzinoglu, A., Sengul, F., Ozer, A. (2004). A review of waste management options in olive oil production. *Critical Reviews in Environmental Science and Technology*, vol. 34, no. 3, pp. 209–247.

Badawy, M.I., Ghaly, M.Y., Zawrah, M.F., Ali, M.E.M., El Gohary, F. (2010). Abatement of organic pollutants from olive mill effluent by TiO_2 nano-particles using catalytic wet air oxidation (CWAO) technique. *Afinidad*, vol. LXVII (67), no. 549, pp. 386–392.

Balahura, R.J., Johnson, M.D. (1987). Outer-sphere dithionite reductions of metal complexes. *Inorganic Chemistry*, vol. 26, no. 23, pp. 3860–3863.

Banni, S. (2002). Conjugated linoleic acid metabolism. *Current Opinion in Lipidology*, vol. 13, no. 3, pp. 261–266.

Basu, S., Smedman, A., Vessby, B. (2000). Conjugated linoleic acid induces lipid peroxidation in humans. *FEBS Letters*, vol. 468, no. 1, pp. 33–36.

Battin, T.J., Luyssaert, S., Kaplan, L.A., Aufdenkampe, A.K., Richter, A., Tranvik, L.J. (2009). The boundless carbon cycle. *Nature Geoscience*, vol. 2, no. 9, pp. 598–600.

Beltrán, G., del Rio, C., Sánchez, S., Martínez, L. (2004). Influence of harvest date and crop yield on the fatty acid composition of virgin olive oils from cv. Picual. *Journal of Agricultural and Food Chemistry*, vol. 52, no. 11, pp. 3434–3440.

Bell, G., Todd, J.R., Blain, J.A., Patterson, J.D.E., Shaw, C.E.L. (1981). Hydrolysis of triglyceride by solid phase lipolytic enzymes of *Rhizopus arrhizus* in continuous reactor systems. *Biotechnology and Bioengineering*, vol. 23, no. 8, pp. 1703–1719.

Berdeaux, O., Fontagné, S., Sémon, E., Velasco, J., Sébédio, J.L., Dobarganes, C. (2012). A detailed identification study on high-temperature degradation products of oleic and linoleic acid methyl esters by GC–MS and GC–FTIR. *Chemistry and Physics of Lipids*, vol. 165, no. 3, pp. 338–347.

Bhatt, N. (2013). Conjugated linoleic acid as an immunity enhancer: a review. *Canadian Journal of Clinical Nutrition*, vol. 1, no. 2, pp. 34–49.

Blankenhorn, D.H., Ahrens Jr, E.H. (1955). Extraction, isolation, and identification of hydrolytic products of triglyceride digestion in man. *Journal of Biological Chemistry*, vol. 212, no. 1, pp. 69–81.

Blondeau, N., Lipsky, R.H., Bourourou, M., Duncan, M.W., Gorelick, P.B., Marini, A.M. (2015). Alpha-linolenic acid: an omega-3 fatty acid with neuroprotective properties—ready for use in the stroke clinic? *BioMed Research International*, vol. 2015, article no. 519830 (8pp.).

Bollag, J.-M., Dec, J., Huang, P.M. (1998). Formation mechanisms of complex organic structures in soil habitats. In: Sparks, D.L. (ed.), *Advances in Agronomy*, vol. 63, pp. 237–266. Academic Press: San Diego, CA.

Borges, M.E., Díaz, L. (2012). Recent developments on heterogeneous catalysts for biodiesel production by oil esterification and transesterification reactions: a review. *Renewable and Sustainable Energy Reviews*, vol. 16, no. 5, pp. 2839–2849.

Bosetto, M., Arfaioli, P., Pantani, O.L. (2002). Study of the Maillard reaction products formed by glycine and D-glucose on different mineral substrates. *Clay Minerals*, vol. 37, no. 1, pp. 195–204.

Braughler, J.M., Duncan, L.A., Chase, R.L. (1986). The involvement of iron in lipid peroxidation: importance of ferric to ferrous ratios in initiation. *The Journal of Biological Chemistry*, vol. 261, no. 22, pp. 10282–10289.

Brookins, D.G. (1988). *Eh-pH Diagrams for Geochemistry*. Springer-Verlag: Berlin. 176pp. ISBN: 978-3-642-73095-5 (print) / 978-3-642-73093-1 (online).

Brown, A.J., Goldsworthy, S.M., Barnes, A.A., Eilert, M.M., Tcheang, L., Daniels, D., Muir, A.I., Wigglesworth, M.J., Kinghorn, I., Fraser, N.J., Pike, N.B., Strum, J.C., Steplewski, K.M., Murdock, P.R., Holder, J.C., Marshall, F.H., Szekeres, P.G., Wilson, S., Ignar, D.M., Foord, S.M., Wise, A., Dowell, S.J. (2003). The orphan G protein-coupled receptors GPR41 and GPR43 are activated by propionate and other short chain carboxylic acids. *The Journal of Biological Chemistry*, vol. 278, no. 13, pp. 11312–11319.

Brown, D.R., Rhodes, C.N. (1997). Brønsted and Lewis acid catalysis with ion-exchanged clays. *Catalysis Letters*, vol. 45, no. 1–2, pp. 35–40.

Buisman, G.J.H. (1999). Biodegradable binders and cross-linking agents from renewable resources. *Surface Coatings International. Part B: Coatings Transactions*, vol. 82, no. 3, pp. 127–130.

Bullock, P. (2005). Climate change impacts. In: Hillel, D. (ed.), *Encyclopedia of Soils in the Environment*, pp. 254–262. Elsevier: Amsterdam.

Cabrini, L., Barzanti, V., Cipollone, M., Fiorentini, D., Grossi, G., Tolomelli, B., Zambonin, L., Landi, L. (2001). Antioxidants and total peroxyl radical-trapping ability of olive and seed oils. *Journal of Agricultural and Food Chemistry*, vol. 49, no. 12, pp. 6026–6032.

Cahoon, E.B., Ohlrogge, J.B. (1994). Metabolic evidence for the involvement of a Δ^4-palmitoyl-acyl carrier protein desaturase in petroselinic acid synthesis in coriander endosperm and transgenic tobacco cells. *Plant Physiology*, vol. 104, no. 3, pp. 827–837.

Callendar, G.S. (1938). The artificial production of carbon dioxide and its influence on temperature. *Quarterly Journal of the Royal Meteorological Society*, vol. 64, no. 275, pp. 223–240.

Canadell, J.G., Le Quéré, C., Raupach, M.R., Field, C.B., Buitenhuis, E.T., Ciais, P., Conway, T.J., Gillett, N.P., Houghton, R.A., Marland, G. (2007). Contributions to accelerating atmospheric CO_2 growth from economic activity, carbon intensity, and efficiency of natural sinks. *Proceedings of the National Academy of Sciences (PNAS) of the United States of America*, vol. 104, no. 47, pp. 18866–18870.

Carlozzi, P., Padovani, G., Cinelli, P., Lazzeri, A. (2015). An innovative device to convert olive mill wastewater into a suitable effluent for feeding purple non-sulfur photosynthetic bacteria. *Resources*, vol. 4, no. 3, pp. 621–636.

Catling, D.C., Zahnle, K.J., McKay, C.P. (2001). Biogenic methane, hydrogen escape, and the irreversible oxidation of early earth. *Science*, vol. 293, no. 5531, pp. 839–843.

Cert, A., Moreda, W., Pérez-Camino, M.C. (2000). Chromatographic analysis of minor constituents in vegetable oils. *Journal of Chromatography A*, vol. 881, no. 1–2, pp. 131–148.

Chatterjee, S.N., Agarwal, S. (1983). Lipid peroxidation by ultraviolet light and high energy α particles from a cyclotron. *Radiation and Environmental Biophysics*, vol. 21, no. 4, pp. 275–280.

Chen, X., Ahn, D.U. (1998). Antioxidant activities of six natural phenolics against lipid oxidation induced by Fe^{2+} or ultraviolet light. *Journal of the American Oil Chemists' Society*, vol. 75, no. 12, pp. 1717–1721.

Chen, C.-C., Golden, D.C., Dixon, J.B. (1986). Transformation of synthetic birnessite to cryptomelane: an electron microscopic study. *Clays and Clay Minerals*, vol. 34, no. 5, pp. 565–571.

Cheney, M.A., Jose, R., Banerjee, A., Bhowmik, P.K., Qian, S., Okoh, J.M. (2009). Synthesis and characterization of birnessite and cryptomelane nanostructures in presence of Hoffmeister anions. *Journal of Nanomaterials*, vol. 2009, p. 940462 (8pp.).

Choe, E., Min, D.B. (2006). Mechanisms and factors for edible oil oxidation. *Comprehensive Reviews in Food Science and Food Safety*, vol. 5, no. 4, pp. 169–186.

Christensen, M.S., Høy, C.-E., Becker, C.C., Redgrave, T.G. (1995). Intestinal absorption and lymphatic transport of eicosapentaenoic (EPA), docosahexaenoic (DHA), and decanoic acids: dependence on intramolecular triacylglycerol structure. *The American Journal of Clinical Nutrition*, vol. 61, no. 1, pp. 56–61.

Clarke, C.E., Aguilar-Carrillo, J., Roychoudhury, A.N. (2011). Quantification of drying induced acidity at the mineral–water interface using ATR-FTIR spectroscopy. *Geochimica et Cosmochimica Acta*, vol. 75, no. 17, pp. 4846–4856.

Clarke, C., Tourney, J., Johnson, K. (2012). Oxidation of anthracene using waste Mn oxide minerals: the importance of wetting and drying sequences. *Journal of Hazardous Materials*, vol. 205–206, pp. 126–130.

Cornell, R.M., Schwertmann, U. (1996). *The Iron Oxides*. VCH Verlagsgesellschaft: Weinheim, Germany. 573pp. ISBN: 3527285768.

Covas, M.-I., Ruiz-Gutiérrez, V., de la Torre, R., Kafatos, A., Lamuela-Raventós, R.M., Osada, J., Owen, R.W., Visioli, F. (2006). Minor components of olive oil: evidence to date of health benefits in humans. *Nutrition Reviews*, vol. 64, no. (suppl.) 4, pp. S20–S30.

Cowan, J.C. (1962). Dimer acids. *Journal of the American Oil Chemists' Society*, vol. 39, no. 12, pp. 534–545.

Croston, C.B., Tubb., I.L., Cowan, J.C., Teeter, H.M. (1952). Polymerization of drying oils. VI. Catalytic polymerization of fatty acids and esters with boron trifluoride and hydrogen fluoride. *Journal of the American Oil Chemists' Society*, vol. 29, no. 8, pp. 331–333.

Datta, R., Kelkar, A., Baraniya, D., Molaei, A., Moulick, A., Meena, R.S., Formanek, P. (2017). Enzymatic degradation of lignin in soil: a review. *Sustainability*, vol. 9, no. 7, p. 1163 (18pp.).

Daubert, B.F., Baldwin, A.R. (1944). Unsaturated synthetic glycerides. VII. Preparation and properties of synthetic 1-monoglycerides and simple triglycerides of linoleic and linolenic acids. *Journal of the American Chemical Society*, vol. 66, no. 6, pp. 997–1000.

De Jong, C., Badings, H.T. (1990). Determination of free fatty acids in milk and cheese procedures for extraction, clean up, and capillary gas chromatographic analysis. *Journal of Separation Science*, vol. 13, no. 2, pp. 94–98.

de Melo, I.L.P., de Carvalho, E.B.T., Mancini-Filho, J. (2014). Pomegranate seed oil (Punica Granatum L.): a source of punicic acid (conjugated α-linolenic acid). *Journal of Human Nutrition & Food Science*, vol. 2, no. 1, p. 1024 (11pp.).

DeAngelis, Y.M., Saunders, C.W., Johnstone, K.R., Reeder, N.L., Coleman, C.G., Kaczvinsky Jr, J.R., Gale, C., Walter, R., Mekel, M., Lacey, M.P., Keough, T.W., Fieno, A., Grant, R.A., Begley, B., Sun, Y., Fuentes, G., Youngquist, R.S., Xu, J., Dawson Jr, T.L. (2007). Isolation and Expression of a *Malassezia globosa* Lipase Gene, *LIP1*. *Journal of Investigative Dermatology*, vol. 127, no. 9, pp. 2138–2146.

Denke, M.A., Grundy, S.M. (1992). Comparison of effects of lauric acid and palmitic acid on plasma lipids and lipoproteins. *The American Journal of Clinical Nutrition*, vol. 56, no. 5, pp. 895–898.

den Otter, M.J.A.M. (1968). The clay-catalysed dimerization of oleic acid. Ph.D. Thesis. *Technische Hogeschool te Eindhoven (Eindhoven University of Technology)*. 197pp.

Dismukes, G.C., Sheats, J.E., Smegal, J.A. (1987). Mn^{2+}/Mn^{3+} and Mn^{3+}/Mn^{4+} mixed valence binuclear manganese complexes of biological interest. *Journal of the American Chemical Society*, vol. 109, no. 23, pp. 7202–7203.

Driomina, E.S., Sharov, V.S., Vladimirov, Y.A. (1993). Fe^{2+}-induced lipid peroxidation kinetics in liposomes: the role of surface Fe^{2+} concentration in switching the reaction from acceleration to decay. *Free Radical Biology & Medicine*, vol. 15, no. 3, pp. 239–247.

Dubey, S., Singh, D., Misra, R.A. (1998). Enzymatic synthesis and various properties of poly(catechol). *Enzyme and Microbial Technology*, vol. 23, no. 7–8, pp. 432–437.

Dumelin, E.E., Tappel, A.L. (1977). Hydrocarbon gases produced during in vitro peroxidation of polyunsaturated fatty acids and decomposition of preformed hydroperoxides. *Lipids*, vol. 12, no. 11, pp. 894–900.

Dzhatdoeva, A.A., Polimova, A.M., Proskurnina, E.V., Proskurnin, M.A., Vladimirov, Y.A. (2016). Determination of lipids and their oxidation products by IR spectrometry. *Journal of Analytical Chemistry*, vol. 71, no. 6, pp. 542–548.

Ebiura, T., Echizen, T., Ishikawa, A., Murai, K., Baba, T. (2005). Selective transesterification of triolein with methanol to methyl oleate and glycerol using alumina loaded with alkali metal salt as a solid-base catalyst. *Applied Catalysis A: General*, vol. 283, no. 1–2, pp. 111–116.

Elzinga, E.J. (2011). Reductive transformation of birnessite by aqueous Mn(II). *Environmental Science & Technology*, vol. 45, no. 15, pp. 6366–6372.

European Commission Joint Research Centre (2018). BCR-172 Quartz. *Certified reference materials catalogue*. Available: https://crm.jrc.ec.europa.eu/p/40456/By-analyte-group/BCR-172-QUARTZ-2-50-m2-g-nitrogen-BET-specific-surface-area/BCR-172 [Accessed: 23 October 2018].

Falade, A.O., Oboh, G. (2015). Thermal oxidation induces lipid peroxidation and changes in the physicochemical properties and β-carotene content of arachis oil. *International Journal of Food Science*, vol. 2015, p. 806524 (7pp.).

Falkowski, P., Scholes, R.J., Boyle, E., Canadell, J., Canfield, D., Elser, J., Gruber, N., Hibbard, K., Högberg, P., Linder, S., Mackenzie, F.T., Moore III, B., Pedersen, T., Rosenthal, Y., Seitzinger, S., Smetacek, V., Steffen, W. (2000). The global carbon cycle: a test of our knowledge of earth as a system. *Science*, vol. 290, no. 5490, pp. 291–296.

Falkowski, P.G. (2003). 8.05 Biogeochemistry of primary production in the sea. In: Holland, H.D., Schlesinger, W.H., Turekian, K.K. (eds), *Treatise on Geochemistry*, vol. 8, pp. 185–213. Elsevier: Amsterdam.

Fourier, J.-B.J. (1827). Mémoire sur les temperatures du globe terrestre et des espaces planétaires. *Mémoires de l'Académie des sciences de l'Institut de France*, vol. 7, pp. 569–604.

Frankel, E.N. (1980). Lipid oxidation. *Progress in Lipid Research*, vol. 19, no. 1–2, pp. 1–22.

Fukushima, M., Miura, A., Sasaki, M., Izumo, K. (2009). Effect of an allophanic soil on humification reactions between catechol and glycine: spectroscopic

investigations of reaction products. *Journal of Molecular Structure*, vol. 917, no. 2–3, pp. 142–147.

Gao, T., Glerup, M., Krumeich, F., Nesper, R., Fjellvåg, H., Norby, P. (2008). Microstructures and spectroscopic properties of cryptomelane-type manganese dioxide nanofibers. *The Journal of Physical Chemistry C*, vol. 112, no. 34, pp. 13134–13140.

Garssen, G.J., Vliegenthart, J.F.G., Boldingh, J. (1972). The origin and structures of dimeric fatty acids from the anaerobic reaction between soya-bean lipoxygenase, linoleic acid and its hydroperoxide. *Biochemical Journal*, vol. 130, no. 2, pp. 435–442.

Gebauer, S.K., Psota, T.L., Kris-Etherton, P.M. (2007). The diversity of health effects of individual *trans* fatty acid isomers. *Lipids*, vol. 42, no. 9, pp. 787–799.

German, J.B. (1999). Food processing and lipid oxidation. In: Jackson L.S., Knize M.G., Morgan J.N. (eds), Impact of Processing on Food Safety. *Advances in Experimental Medicine and Biology*, vol. 459, pp. 23–50. Springer, Boston, MA.

Gogvadze, V., Walter, P.B., Ames, B.N. (2003). The role of Fe^{2+}-induced lipid peroxidation in the initiation of the mitochondrial permeability transition. *Archives of Biochemistry and Biophysics*, vol. 414, no. 2, pp. 255–260.

Golden, D.C., Dixon, J.B., Chen, C.C. (1986). Ion exchange, thermal transformations, and oxidizing properties of birnessite. *Clays and Clay Minerals*, vol. 34, no. 5, pp. 511–520.

Gomez, N.A., Abonia, R., Cadavid, H., Vargas, I.H. (2011). Chemical and spectroscopic characterization of a vegetable oil used as dielectric coolant in distribution transformers. *Journal of the Brazilian Chemical Society*, vol. 22, no. 12, pp. 2292–2303.

Gonzalez, J.M., Laird, D.R. (2004). Role of smectites and Al-substituted goethites in the catalytic condensation of arginine and glucose. *Clays and Clay Minerals*, vol. 52, no. 4, pp. 443–450.

Grande, F., Anderson, J.T., Keys, A. (1970). Comparison of effects of palmitic and stearic acids in the diet on serum cholesterol in man. *The American Journal of Clinical Nutrition*, vol. 23, no. 9, pp. 1184–1193.

Grotz, L.C. (1973). Blue violet for nitrate ion. *Journal of Chemical Education*, vol. 50, no. 1, p. 63.

Halliwell, B. (2000). Lipid peroxidation, antioxidants and cardiovascular disease: how should we move forward? *Cardiovascular Research*, vol. 47, no. 3, pp. 410–418.

Hardie, A.G., Dynes, J.J., Kozak, L.M., Huang, P.M. (2007). Influence of polyphenols on the integrated polyphenol-Maillard reaction humification pathway as catalyzed by birnessite. *Annals of Environmental Science*, vol. 1, pp. 91–110.

Hardie, A.G., Dynes, J.J., Kozak, L.M., Huang, P.M. (2009*a*). The role of glucose in abiotic humification pathways as catalyzed by birnessite. *Journal of Molecular Catalysis A: Chemical*, vol. 308, no. 1–2, pp. 114–126.

Hardie, A.G., Dynes, J.J., Kozak, L.M., Huang, P.M. (2009*b*). Biomolecule-induced carbonate genesis in abiotic formation of humic substances in nature. *Canadian Journal of Soil Science*, vol. 89, no. 4, pp. 445–453.

Hardie, A.G., Dynes, J.J., Kozak, L.M., Huang, P.M. (2010). Abiotic catalysis of the Maillard and polyphenol-Maillard humification pathways by soil clays from temperate and tropical environments. In: Xu, J., Huang, P.M. (eds), *Molecular Environmental Soil Science at the Interfaces in the Earth's Critical Zone*, Conference Proceedings, pp. 26–28. Zhejiang University Press: Hangzhou and Springer: Verlag.

Hershey, R.L., Eberhardt, J.E., Hottel, H.C. (1936). Thermodynamic properties of the working fluid in internal-combustion engines. *SAE Transactions*, vol. 31, pp. 409–424.

Horrobin, D.F. (1992). Nutritional and medical importance of gamma-linolenic acid. *Progress in Lipid Research*, vol. 31, no. 2, pp. 163–194.

Houseknecht, K.L., Vanden Heuvel, J.P., Moya-Camarena, S.Y., Portocarrero, C.P., Peck, L.W., Nickel, K.P., Belury, M.A. (1998). Dietary conjugated linoleic acid normalized impaired glucose tolerance in the Zucker diabetic fatty *fa/fa* rat. *Biochemical and Biophysical Research Communications*, vol. 244, no. 3, pp. 678–682.

Huang, P.M., Hardie, A.G. (2009). Formation mechanisms of humic substances in the environment. In: Senesi, N., Xing, B., Huang, P.M. (eds), *Biophysico-Chemical Processes Involving Natural Nonliving Organic Matter in Environmental Systems*, vol. 2, pp. 41–109. John Wiley & Sons: Hoboken, NJ.

Huang, P.M., Hardie, A.G. (2012). Role of abiotic catalysis in the transformation of organics, metals, metalloids, and other inorganics. In: Huang, P.M., Li, Y.,

Sumner, M.E. (eds), *Handbook of Soil Sciences: Properties and Processes*, 2nd edn, pp. 18-1–18-40. CRC Press: Boca Raton, FL.

Hudson Institute of Mineralogy, 2018*a*. Birnessite. *Mindat.org*. Available: https://www.mindat.org/min-680.html [Accessed 27 July 2018].

Hudson Institute of Mineralogy, 2018*b*. Pyrolusite. *Mindat.org*. Available: https://www.mindat.org/min-3318.html [Accessed 27 July 2018].

Hudson Institute of Mineralogy, 2018*c*. Goethite. *Mindat.org*. Available: https://www.mindat.org/min-1719.html [Accessed 22 October 2018].

Hudson Institute of Mineralogy, 2018*d*. Gibbsite. *Mindat.org*. Available: https://www.mindat.org/min-1689.html [Accessed 22 October 2018].

Hudson Institute of Mineralogy, 2018*e*. Quartz. *Mindat.org*. Available: https://www.mindat.org/min-3337.html [Accessed: 22 October 2018].

Hudson Institute of Mineralogy, 2018*f*. Kaolinite. *Mindat.org*. Available: https://www.mindat.org/min-2156.html [Accessed: 22 October 2018].

Hudson Institute of Mineralogy, 2018*g*. Montmorillonite. *Mindat.org*. Available: https://www.mindat.org/min-2821.html [Accessed: 22 October 2018].

Hudson Institute of Mineralogy, 2018*h*. Cryptomelane. *Mindat.org*. Available: https://www.mindat.org/min-1164.html [Accessed: 11 November 2018].

Ichihara, K., Shibahara, A., Yamamoto, K., Nakayama, T. (1996). An improved method for rapid analysis of the fatty acids of glycerolipids. *Lipids*, vol. 31, no. 5, pp. 535–539.

Indarti, E., Majid, M.I.A., Hashim, R., Chong, A. (2005). Direct FAME synthesis for rapid total lipid analysis from fish oil and cod liver oil. *Journal of Food Composition and Analysis*, vol. 18, no. 2–3, pp. 161–170.

International Organization for Standardization (ISO) (2005). ISO 10390:2005. *Soil quality -- Determination of pH*. Available: https://www.iso.org/standard/40879.html [Accessed 2 August 2018].

IUPAC-IUB Commission on Biochemical Nomenclature (CBN) (1967). The nomenclature of lipids. *European Journal of Biochemistry*, vol. 2, no. 2, pp. 127–131.

Ivanets, A.I., Prozorovich, V.G., Krivoshapkina, E.F., Kuznetsova, T.F., Krivoshapkin, P.V., Katsoshvili, L.L. (2017). Physicochemical properties of manganese oxides obtained via the sol–gel method: the reduction of potassium permanganate by polyvinyl alcohol. *Russian Journal of Physical Chemistry A*, vol. 91, no. 8, pp. 1486–1492.

Jaarin, K., Kamisah, Y. (2012). Repeatedly heated vegetable oils and lipid peroxidation. In: Catala, A. (ed.), *Lipid Peroxidation*, pp. 211–228. InTechOpen: Rijeka, Croatia.

Jabeen, F., Chaudhry, A.S. (2011). Chemical compositions and fatty acid profiles of three freshwater fish species. *Food Chemistry*, vol. 125, no. 3, pp. 991–996.

Jadhav, N.V., Prasad, A.I., Kumar, A., Mishra, R., Dhara, S., Babu, K.R., Prajapat, C.L., Misra, N.L., Ningthoujam, R.S., Pandey, B.N., Vatsa, R.K. (2013). Synthesis of oleic acid functionalized Fe_3O_4 magnetic nanoparticles and studying their interaction with tumor cells for potential hyperthermia applications. *Colloids and Surfaces B: Biointerfaces*, vol. 108, pp. 158–168.

Jain, N., Bhatia, A., Pathak, H., Gupta, N., Sharma, D.K., Kaushik, R. (2012). Greenhouse gas emissions and global warming. In: Khoiyangbam, R.S., Gupta, N. (eds). *Introduction to Environmental Sciences*, pp. 379–412. TERI: New Delhi.

Jensen, M.M., Christensen, M.S., Høy, C.-E. (1994). Intestinal absorption of octanoic, decanoic, and linoleic acids: effect of triglyceride structure. *Annals of Nutrition & Metabolism*, vol. 38, no. 2, pp. 104–116.

Jham, G.N., Moser, B.R., Shah, S.N., Holser, R.A., Dhingra, O.D., Vaughn, S.F., Berhow, M.A., Winkler-Moser, J.K., Isbell, T.A., Holloway, R.K., Walter, E.L., Natalino, R., Anderson, J.C., Stelly, D.M. (2009). Wild Brazilian mustard (*Brassica juncea* L.) seed oil methyl esters as biodiesel fuel. *Journal of the American Oil Chemists' Society*, vol. 86, no. 9, pp. 917–926.

Johnson, D.R., Decker, E.A. (2015). The role of oxygen in lipid oxidation reactions: a review. *Annual Review of Food Science and Technology*, vol. 6, pp. 171–190.

Johnson, K.L., Purvis, G., Lopez-Capel, E., Peacock, C., Gray, N., Wagner, T., März, C., Bowen, L., Ojeda, J., Finlay, N., Robertson, S., Worrall, F., Greenwell, C. (2015). Towards a mechanistic understanding of carbon stabiliza-

tion in manganese oxides. *Nature Communications*, vol. 6, article no. 7628 (11pp.).

Johnson, K.L., McCann, C.M., Wilkinson, J.-L., Jones, M., Tebo, B.M., West, M., Elgy, C., Clarke, C.E., Gowdy, C., Hudson-Edwards, K.A. (2018). Dissolved Mn(III) in water treatment works: prevalence and significance. *Water Research*, vol. 140, pp. 181–190.

Jokic, A., Frenkel, A.I., Vairavamurthy, M.A., Huang, P.M. (2001*a*). Birnessite catalysis of the Maillard reaction: its significance in natural humification. *Geophysical Research Letters*, vol. 28, no. 20, pp. 3899–3902.

Jokic, A., Frenkel, A.I., Huang, P.M. (2001*b*). Effect of light on birnessite catalysis of the Maillard reaction and its implication in humification. *Canadian Journal of Soil Science*, vol. 81, no. 3, pp. 277–283.

Jokic, A., Wang, M.C., Liu, C., Frenkel, A.I., Huang, P.M. (2004*a*). Integration of the polyphenol and Maillard reactions into a unified abiotic pathway for humification in nature: the role of δ-MnO_2. *Organic Geochemistry*, vol. 35, no. 6, pp. 747–762.

Jokic, A., Schulten, H.-R., Cutler, J.N., Schnitzer, M., Huang, P.M. (2004*b*). A significant abiotic pathway for the formation of *unknown* nitrogen in nature. *Geophysical Research Letters*, vol. 31, no. 5, article no. LO5502 (4pp.).

Jokic, A., Schulten, H.-R., Cutler, J.N., Schnitzer, M., Huang, P.M. (2005). Catalysis of the Maillard reaction by δ-MnO_2: a significant abiotic sorptive condensation pathway for the formation of refractory N-containing biogeomacromolecules in nature. In: Huang, P.M., Violante, A., Bollag, J.-M., Vityakon, P. (eds), *Soil Abiotic and Biotic Interactions and Impact on the Ecosystem and Human Welfare*, pp. 127–152. CRC Press: Enfield, NH.

Joo, S.T., Lee, J.I., Ha, Y.L., Park, G.B. (2002). Effects of dietary conjugated linoleic acid on fatty acid composition, lipid oxidation, color, and water-holding capacity of pork loin. *Journal of Animal Science*, vol. 80, no. 1, pp. 108–112.

Juita, Dlugogorski, B.Z., Kennedy, E.M., Mackie, J.C. (2012). Low temperature oxidation of linseed oil: a review. *Fire Science Reviews*, vol. 1, no. 3, DOI: 10.1186/2193-0414-1-3 (36pp.).

Kail, B.W., Link, D.D., Morreale, B.D. (2012). Determination of free fatty acids and triglycerides by gas chromatography using selective esterification reactions. *Journal of Chromatographic Science*, vol. 50, no. 10, pp. 934–939.

Kanner, J., German, J.B., Kinsella, J.E., Hultin, H.O. (1987). Initiation of lipid peroxidation in biological systems. *Critical Reviews in Food Science and Nutrition*, vol. 25, no. 4, pp. 317–364.

Kellogg III, E.W., Fridovich, I. (1975). Superoxide, hydrogen peroxide, and singlet oxygen in lipid peroxidation by a xanthine oxidase system. *The Journal of Biological Chemistry*, vol. 250, no. 22, pp. 8812–8817.

Khorobrykh, A., Dasgupta, J., Kolling, D.R.J., Terentyev, V., Klimov, V.V., Dismukes, G.C. (2013). Evolutionary origins of the photosynthetic water oxidation cluster: bicarbonate permits Mn^{2+} photooxidation by anoxygenic bacterial reaction centers. *ChemBioChem*, vol. 14, no. 14, pp. 1725–1731.

King, M.M., Lai, E.K., McCay, P.B. (1975). Singlet oxygen production associated with enzyme-catalyzed lipid peroxidation in liver microsomes. *The Journal of Biological Chemistry*, vol. 250, no. 16, pp. 6496–6502.

Kleber, M., Nico, P.S., Plante, A., Filley, T., Kramer, M., Swanston, C., Sollins, P. (2011). Old and stable soil organic matter is not necessarily chemically recalcitrant: implications for modeling concepts and temperature sensitivity. *Global Change Biology*, vol. 17, no. 2, pp. 1097–1107.

Klewicki, J.K., Morgan, J.J. (1998). Kinetic behavior of Mn(III) complexes of pyrophosphate, EDTA, and citrate. *Environmental Science & Technology*, vol. 32, no. 19, pp. 2916–2922.

Klokkenburg, M., Hilhorst, J., Erné, B.H. (2007). Surface analysis of magnetite nanoparticles in cyclohexane solutions of oleic acid and oleylamine. *Vibrational Spectroscopy*, vol. 43, no. 1, pp. 243–248.

Knothe, G., Dunn, R.O. (2009). A comprehensive evaluation of the melting points of fatty acids and esters determined by differential scanning calorimetry. *Journal of the American Oil Chemists' Society*, vol. 86, no. 9, pp. 843–856.

Koch, R.B., Stern, B., Ferrari, C.G. (1958). Linoleic acid and trilinolein as substrates for soybean lipoxidase(s). *Archives of Biochemistry and Biophysics*, vol. 78, no. 1, pp. 165–179.

Kohno, Y., Egawa, Y., Itoh, S., Nagaoka, S.-I., Takahashi, M., Mukai, K. (1995). Kinetic study of quenching reaction of singlet oxygen and scavenging reaction of free radical by squalene in n-butanol. *Biochimica et Biophysica Acta (BBA) - Lipids and Lipid Metabolism*, vol. 1256, no. 1, pp. 52–56.

Koley, S.N. (1971). Comparative study of the polymerization of oleic acid with its methyl ester in an azeotropic saltbath. *Fette, Seifen, Anstrichmittel (European Journal of Lipid Science and Technology)*, vol. 73, no. 12, pp. 725–728.

Komnick, H. (1988). Intestinal absorption of defined lipids by the larval dragonfly *Aeshna cyanea* (Insecta: Odonata): mono- and polyunsaturated free fatty acids and their homotriglycerides. *Journal of Insect Physiology*, vol. 34, no. 2, pp. 105–110.

Kostka, J.E., Luther III, G.W., Nealson, K.H. (1995). Chemical and biological reduction of Mn (III)-pyrophosphate complexes: potential importance of dissolved Mn (III) as an environmental oxidant. *Geochimica et Cosmochimica Acta*, vol. 59, no. 5, pp. 885–894.

Krishnamurti, G.S.R., Huang, P.M. (1988). Influence of manganese oxide minerals on the formation of iron oxides. *Clays and Clay Minerals*, vol. 36, no. 5, pp. 467–475.

Kumada, K. (1965). Studies on the colour of humic acids, part 1 on the concepts of humic substances and humification. *Soil Science and Plant Nutrition*, vol. 11, no. 4, pp. 11–16.

Laidler, K.J. (1984). The development of the Arrhenius equation. *Journal of Chemical Education*, vol. 61, no. 6, pp. 494–498.

Laird, D.A., Koskinen, W.C. (2008). Triazine soil interactions. In: LeBaron, H.M., McFarland, J.E., Burnside, O.C. (eds), *The Triazine Herbicides: 50 years Revolutionizing Agriculture*, pp. 275–299. Elsevier: San Diego, CA.

LaKind, J.S., Stone, A.T. (1989). Reductive dissolution of goethite by phenolic reductants. *Geochimica et Cosmochimica Acta*, vol. 53, no. 5, pp. 961–971.

Lal, R. (2008). Sequestration of atmospheric CO_2 in global carbon pools. *Energy & Environmental Science*, vol. 1, no. 1, pp. 86–100.

Lalman, J.A., Bagley, D.M. (2000). Anaerobic degradation and inhibitory effects of linoleic acid. *Water Research*, vol. 34, no. 17, pp. 4220–4228.

Lam, M.K., Lee, K.T., Mohamed, A.R. (2010). Homogeneous, heterogeneous and enzymatic catalysis for transesterification of high free fatty acid oil (waste cooking oil) to biodiesel: a review. *Biotechnology Advances*, vol. 28, no. 4, pp. 500–518.

Langmuir, D. (1997). *Aqueous Environmental Geochemistry*. Prentice-Hall, Inc.: Upper Saddle River, NJ. 600pp. ISBN: 0-02-367412-1 / 978-0023674129.

Lanson, B., Drits, V.A., Silvester, E., Manceau, A. (2000). Structure of H-exchanged hexagonal birnessite and its mechanism of formation from Na-rich monoclinic buserite at low pH. *American Mineralogist*, vol. 85, no. 5–6, pp. 826–838.

Lasaga, A.C. (1981). Rate laws of chemical reactions. In: Lasaga, A.C., Kirkpatrick, R.J. (eds), *Reviews in Mineralogy: Kinetics of Geochemical Processes*, vol. 8, pp. 1–68. Mineralogical Society of America: Washington, DC.

Le Poul, E., Loison, C., Struyf, S., Springael, J.Y., Lannoy, V., Decobecq, M.E., Brezillon, S., Dupriez, V., Vassart, G., Van Damme, J., Parmentier, M., Detheux, M. (2003). Functional characterization of human receptors for short chain fatty acids and their role in polymorphonuclear cell activation. *The Journal of Biological Chemistry*, vol. 278, no. 28, pp. 25481–25489.

Lee, K.N., Kritchevsky, D., Pariza, M.W. (1994). Conjugated linoleic acid and atherosclerosis in rabbits. *Atherosclerosis*, vol. 108, no. 1, pp. 19–25.

Lehmann, J., Kleber, M. (2015). The contentious nature of soil organic matter. *Nature*, vol. 528, no. 7580, pp. 60–68.

Leung, D.Y.C., Wu, X., Leung, M.K.H. (2010). A review on biodiesel production using catalyzed transesterification. *Applied Energy*, vol. 87, no. 4, pp. 1083–1095.

Li, S., Guo, S., Tan, X. (1998). Characteristics and kinetics of catalytic degradation of immature kerogen in the presence of mineral and salt. *Organic Geochemistry*, vol. 29, no. 5–7, pp. 1431–1439.

Li, L., Pan, Y., Chen, L., Li, G. (2007). One-dimensional α-MnO_2: Trapping chemistry of tunnel structures, structural stability, and magnetic transitions. *Journal of Solid State Chemistry*, vol. 180, no. 10, pp. 2896–2904.

Li, S., Xu, J., Chen, J., Chen, J., Zhou, C., Yan, X. (2014). Characterization of the triacylglycerol profile in marine diatoms by ultra performance liquid chromatography coupled with electrospray ionization–quadrupole time-of-flight mass spectrometry. *Journal of Applied Phycology*, vol. 26, no. 3, pp. 1389–1398.

Lima, T.M., Kanunfre, C.C., Pompéia, C., Verlengia, R., Curi, R. (2002). Ranking the toxicity of fatty acids on Jurkat and Raji cells by flow cytometric analysis. *Toxicology in Vitro*, vol. 16, no. 6, pp. 741–747.

Lin, S., Zhang, J., Gao, Y., Zhang, X., Song, S., Long, Z., Karangwa, E. (2014). Rapid and sensitive gas chromatography-triple quadrupole mass spectrometry method for the determination of organic acids in tobacco leaves. *Analytical Methods*, vol. 6, no. 14, pp. 5227–5235.

Lineweaver, H., Burk, D. (1934). The Determination of Enzyme Dissociation Constants. *Journal of the American Chemical Society*, vol. 56, no. 3, pp. 658–666.

Lippincott, E.R., Van Valkenburg, A., Weir, C.E., Bunting, E.N. (1958). Infrared studies on polymorphs of silicon dioxide and germanium dioxide. *Journal of Research of the National Bureau of Standards*, vol. 61, no. 1, pp. 61–70.

Litchfield, C. (1972). *Analysis of Triglycerides*. Academic Press: New York, NY. 374pp. ISBN: 978-0-12-451950-3.

Litwinienko, G. (2001). Autooxidation of unsaturated fatty acids and their esters. *Journal of Thermal Analysis and Calorimetry*, vol. 65, no. 2, pp. 639–646.

Litwinienko, G., Daniluk, A., Kasprzycka-Guttman, T. (2000). Study on autoxidation kinetics of fats by differential scanning calorimetry. 1. Saturated C_{12}–C_{18} fatty acids and their esters. *Industrial and Engineering Chemistry Research*, vol. 39, no. 1, pp. 7–12.

Litwinienko, G., Kasprzycka-Guttman, T. (2000). Study on the autoxidation kinetics of fat components by differential scanning calorimetry. 2. Unsaturated fatty acids and their esters. *Industrial & Engineering Chemistry Research*, vol. 39, no. 1, pp. 13–17.

Liu, J., Lee, T., Bobik Jr, E., Guzman-Harty, M., Hastilow, C. (1993). Quantitative determination of monoglycerides and diglycerides by high-performance liquid chromatography and evaporative light-scattering detection. *Journal of the American Oil Chemists' Society*, vol. 70, no. 4, pp. 343–347.

Lo, S.K., Baharin, B.S., Tan, C.P., Lai, O.M. (2004*a*). Lipase-catalysed production and chemical composition of diacylglycerols from soybean oil deodoriser distillate. *European Journal of Lipid Science and Technology*, vol. 106, no. 4, pp. 218–224.

Lo, S.K., Baharin, B.S., Tan, C.P., Lai, O.M. (2004*b*). Analysis of 1,2(2,3)- and 1,3-positional isomers of diacylglycerols from vegetable oils by reversed-phase high-performance liquid chromatography. *Journal of Chromatographic Science*, vol. 42, no. 3, pp. 145–154.

Lobb, K., Chow, C.K. (2008). Fatty acid classification and nomenclature. In: Chow, C.K. (ed.), *Fatty Acids in Foods and their Health Implications*, 3rd edn, pp. 1–15. CRC Press: Boca Raton, FL.

Lopano, C.L., Heaney, P.J., Post, J.E. (2009). Cs-exchange in birnessite: reaction mechanisms inferred from time-resolved X-ray diffraction and transmission electron microscopy. *American Mineralogist*, vol. 94, no. 5–6, pp. 816–826.

Lorenz, K., Lal, R. (2010). *Carbon Sequestration in Forest Ecosystems*. Springer: Dordrecht. 279pp. ISBN: 978-90-481-3265-2 (print) / 978-90-481-3266-9 (online).

Madejová, J., Komadel, P. (2001). Baseline studies of the Clay Minerals Society source clays: infrared methods. *Clays and Clay Minerals*, vol. 49, no. 5, pp. 410–432.

Madejová, J. (2003). FTIR techniques in clay mineral studies. *Vibrational Spectroscopy*, vol. 31, no. 1, pp. 1–10.

Madison, A.S., Tebo, B.M., Luther III, G.W. (2011). Simultaneous determination of soluble manganese(III), manganese(II) and total manganese in natural (pore)waters. *Talanta*, vol. 84, no. 2, pp. 374–381.

Madison, A.S., Tebo, B.M., Mucci, A., Sundby, B., Luther III, G.W. (2013). Abundant porewater Mn(III) is a major component of the sedimentary redox system. *Science*, vol. 341, no. 6148, pp. 875–878.

Maillard, L.C. (1912). Action des acides aminés sur les sucres; formation de mélanoïdines par voie méthodique. *Comptes rendus hebdomadaires des séances de l'Académie des Sciences*, vol. 154, pp. 66–68.

Makahleh, A., Saad, B., Siang, G.H., Saleh, M.I., Osman, H., Salleh, B. (2010). Determination of underivatized long chain fatty acids using RP-HPLC with capacitively coupled contactless conductivity detection. *Talanta*, vol. 81, no. 1–2, pp. 20–24.

Manceau, A., Marcus, M.A., Grangeon, S. (2012). Determination of Mn valence states in mixed-valent manganates by XANES spectroscopy. *American Mineralogist*, vol. 97, no. 5–6, pp. 816–827.

Manna, C., D'Angelo, S., Migliardi, V., Loffredi, E., Mazzoni, O., Morrica, P., Galletti, P., Zappia, V. (2002). Protective effect of the phenolic fraction from virgin olive oils against oxidative stress in human cells. *Journal of Agricultural and Food Chemistry*, vol. 50, no. 22, pp. 6521–6526.

Marafatto, F.F., Strader, M.L., Gonzalez-Holguera, J., Schwartzberg, A., Gilbert, B., Peña, J. (2015). Rate and mechanism of the photoreduction of birnessite (MnO_2) nanosheets. *Proceedings of the National Academy of Sciences (PNAS) of the United States of America*, vol. 112, no. 15, pp. 4600–4605.

Martín-Carratalá, M.L., Llorens-Jordá, C., Berenguer-Navarro, V., Grané-Teruel, N. (1999). Comparative study on the triglyceride composition of almond kernel oil. A new basis for cultivar chemometric characterization. *Journal of Agricultural and Food Chemistry*, vol. 47, no. 9, pp. 3688–3692.

Martins, S.I.F.S., Jongen, W.M.F., van Boekel, M.A.J.S. (2000). A review of Maillard reaction in food and implications to kinetic modelling. *Trends in Food Science & Technology*, vol. 11, no. 9–10, pp. 364–373.

Masood, A., Stark, K.D., Salem Jr, N. (2005). A simplified and efficient method for the analysis of fatty acid methyl esters suitable for large clinical studies. *Journal of Lipid Research*, vol. 46, no. 10, pp. 2299–2305.

Matocha, C.J., Sparks, D.L., Amonette, J.E., Kukkadapu, R.K. (2001). Kinetics and mechanism of birnessite reduction by catechol. *Soil Science Society of America Journal*, vol. 65, no. 1, pp. 58–66.

McBride, M.B. (1989). Oxidation of 1,2- and 1,4-dihydroxybenzene by birnessite in acidic aqueous suspension. *Clays and Clay Minerals*, vol. 37, no. 5, pp. 479–486.

McBride, M.B. (1994). *Environmental Chemistry of Soils*. Oxford University Press: New York, NY. 416pp. ISBN: 0195070119 / 978-0195070118.

McKenzie, R.M. (1971). The synthesis of birnessite, cryptomelane, and some other oxides and hydroxides of manganese. *Mineralogical Magazine*, vol. 38, no. 296, pp. 493–502.

McMaster, M.C. (2005). *LC/MS: A Practical User's Guide*. John Wiley & Sons: Hoboken, NJ. 184pp. ISBN: 978-0-471-65531-2.

Meher, L.C., Sagar, D.V., Naik, S.N. (2006). Technical aspects of biodiesel production by transesterification—a review. *Renewable and Sustainable Energy Reviews*, vol. 10, no. 3, pp. 248–268.

Mehmood, S., Orhan, I., Ahsan, Z., Aslan, S., Gulfraz, M. (2008). Fatty acid composition of seed oil of different *Sorghum bicolor* varieties. *Food Chemistry*, vol. 109, no. 4, pp. 855–859.

Min, K., Freeman, C., Kang, H., Choi, S.-U. (2015). The regulation by phenolic compounds of soil organic matter dynamics under a changing environment. *BioMed Research International*, vol. 2015, article no. 825098 (11pp.).

Minotti, G., Aust, S.D. (1992). Redox cycling of iron and lipid peroxidation. *Lipids*, vol. 27, no. 3, pp. 219–226.

Mjøs, S.A. (2004). Quantification of linolenic acid isomers by gas chromatography-mass spectrometry and deconvolution of overlapping chromatographic peaks. *European Journal of Lipid Science and Technology*, vol. 106, no. 5, pp. 307–318.

Monod, J. (1949). The growth of bacterial cultures. *Annual Review of Microbiology*, vol. 3, pp. 371–394.

Montgomery, D.R., Zabowski, D., Ugolini, F.C., Hallberg, R.O., Spaltenstein,

H. (2000). Soils, watershed processes, and marine sediments. In: Jacobson, M.C., Charlson, R.J., Rodhe, H., Orians, G.H. (eds), *Earth System Science: From Biogeochemical Cycles to Global Change*, pp. 159–194. Elsevier Academic Press: London.

Moore, K.M., Knauft, D.A. (1989). The inheritance of high oleic acid in peanut. *Journal of Heredity*, vol. 80, no. 3, pp. 252–253.

Moysan, A., Marquis, I., Gaboriau, F., Santus, R., Dubertret, L., Morlière, P. (1993). Ultraviolet A–induced lipid peroxidation and antioxidant defense systems in cultured human skin fibroblasts. *Journal of Investigative Dermatology*, vol. 100, no. 5, pp. 692–698.

Mugnol, K.C.U., Ando, R.A., Nagayasu, R.Y., Faljoni-Alario, A., Brochsztain, S., Santos, P.S., Nascimento, O.R., Nantes, I.L. (2008). Spectroscopic, structural, and functional characterization of the alternative low-spin state of horse heart cytochrome *c*. *Biophysical Journal*, vol. 94, no. 10, pp. 4066–4077.

Mulyani, R., Noviandri, I., Buchari, B., Ciptati, C., Chailapakul, O. (2014). Electrochemical oxidation of sodium dodecylbenzenesulphonate, cetyltrimethyl-ammonium bromide and oleic acid at platinum and cobalt hydroxide modified platinum electrodes. *International Journal of Electrochemical Science*, vol. 9, no. 5, pp. 2410–2419.

Musa, I.A. (2016). The effects of alcohol to oil molar ratios and the type of alcohol on biodiesel production using transesterification process. *Egyptian Journal of Petroleum*, vol. 25, no. 1, pp. 21–31.

Naidja, A., Huang, P.M., Bollag, J.-M. (1998). Comparison of reaction products from the transformation of catechol catalyzed by birnessite or tyrosinase. *Soil Science Society of America Journal*, vol. 62, no. 1, pp. 188–195.

Naidja, A., Huang, P.M., Dec., J., Bollag, J.-M. (1999). Kinetics of catechol oxidation catalyzed by tyrosinase or δ-MnO_2. In: Berthelin, J., Huang, P.M., Bollag, J.-M., Andreux, F. (eds), *Effect of Mineral-Organic-Microorganism Interactions on Soil and Freshwater Environments*, pp. 181–188. Springer: New York, NY.

Namduri, H., Nasrazadani, S. (2008). Quantitative analysis of iron oxides using Fourier transform infrared spectrophotometry. *Corrosion Science*, vol. 50, no. 9, pp. 2493–2497.

National Institutes of Health, 2019. *PubChem: Open Chemistry Database*. Available: https://pubchem.ncbi.nlm.nih.gov [Accessed: 2 February 2019].

Nenadis, N., Tsimidou, M. (2002). Determination of squalene in olive oil using fractional crystallization for sample preparation. *Journal of the American Oil Chemists' Society*, vol. 79, no. 3, pp. 257–259.

Nico, P.S., Zasoski, R.J. (2001). Mn(III) center availability as a rate controlling factor in the oxidation of phenol and sulfide on δ-MnO_2. *Environmental Science & Technology*, vol. 35, no. 16, pp. 3338–3343.

Nieva-Echevarría, B., Goicoechea, E., Guillén, M.D. (2017). Behaviour of non-oxidized and oxidized flaxseed oils, as models of omega-3 rich lipids, during *in vitro* digestion. Occurrence of epoxidation reactions. *Food Research International*, vol. 97, pp. 104–115.

Nilsson, N.E., Kotarsky, K., Owman, C., Olde, B. (2003). Identification of a free fatty acid receptor, FFA2R, expressed on leukocytes and activated by short-chain fatty acids. *Biochemical and Biophysical Research Communications*, vol. 303, no. 4, pp. 1047–1052.

O'Keefe, S.F. (2002). Nomenclature and classification of lipids. In: Akoh, C.C., Min, D.B. (eds), *Food Lipids: Chemistry, Nutrition, and Biotechnology*, 2nd edn, pp. 1–40. Marcel Dekker: New York, NY.

O'Quinn, P.R., Nelssen, J.L., Goodband, R.D., Tokach, M.D. (2000). Conjugated linoleic acid. *Animal Health Research Reviews*, vol. 1, no. 1, pp. 35–46.

Oades, J.M. (1989). An introduction to organic matter in mineral soils. In: Dixon, J.B., Weed, S.B. (eds), *Minerals in Soil Environments*, 2nd edn, pp. 89–159. Soil Science Society of America: Madison, WI.

Oldham, V.E., Owings, S.M., Jones, M.R., Tebo, B.M., Luther III, G.W. (2015). Evidence for the presence of strong Mn(III)-binding ligands in the water column of the Chesapeake Bay. *Marine Chemistry*, vol. 171, pp. 58–66.

Oldham, V.E., Mucci, A., Tebo, B.M., Luther III, G.W. (2017). Soluble Mn(III)–L complexes are abundant in oxygenated waters and stabilized by humic ligands. *Geochimica et Cosmochimica Acta*, vol. 199, pp. 238–246.

Omonov, T.S., Kharraz, E., Curtis, J.M. (2016). The epoxidation of canola oil and its derivatives. *RSC Advances*, vol. 6, no. 95, pp. 92874–92886.

Oscai, L.B., Essig, D.A., Palmer, W.K. (1990). Lipase regulation of muscle triglyceride hydrolysis. *Journal of Applied Physiology*, vol. 69, no. 5, pp. 1571–1577.

Owen, R.W., Mier, W., Giacosa, A., Hull, W.E., Spiegelhalder, B., Bartsch, H. (2000). Phenolic compounds and squalene in olive oils: the concentration and antioxidant potential of total phenols, simple phenols, secoiridoids,

lignans and squalene. *Food and Chemical Toxicology*, vol. 38, no. 8, pp. 647–659.

Palayangoda, S.S., Nguyen, Q.P. (2012). An ATR-FTIR procedure for quantitative analysis of mineral constituents and kerogen in oil shale. *Oil Shale*, vol. 29, no. 4, pp. 344–356.

Parton, W.J., Schimel, D.S., Cole, C.V., Ojima, D. (1987). Analysis of factors controlling soil organic matter levels in the Great Plains grasslands. *Soil Science Society of America Journal*, vol. 51, no. 5, pp. 1173–1179.

Plaster, E.J. (2014). *Soil Science and Management*, 6th edn. Delmar Cengage Learning: Clifton Park, NY. 544pp. ISBN: 084002438X / 9780840024381.

Poiana, M.-A., Alexa, E., Munteanu, M.-F., Gligor, R., Moigradean, D., Mateescu, C. (2015). Use of ATR-FTIR spectroscopy to detect the changes in extra virgin olive oil by adulteration with soybean oil and high temperature heat treatment. *Open Chemistry*, vol. 13, no. 1, pp. 689–698.

Polyakov, N.E., Leshina, T.V., Konovalova, T.A., Kispert, L.D. (2001). Carotenoids as scavengers of free radicals in a Fenton reaction: antioxidants or pro-oxidants? *Free Radical Biology & Medicine*, vol. 31, no. 3, pp. 398–404.

Post, J.E. (1999). Manganese oxide minerals: crystal structures and economic and environmental significance. *Proceedings of the National Academy of Science (PNAS) of the United States of America*, vol. 96, pp. 3447–3454.

Potter, R.M., Rossman, G.R. (1979). The tetravalent manganese oxides: identification, hydration, and structural relationships by infrared spectroscopy. *American Mineralogist*, vol. 64, no. 11–12, pp. 1199–1218.

Prasad, P.S.R., Prasad, K.S., Chaitanya, V.K., Babu, E.V.S.S.K., Sreedhar, B., Murthy, S.R. (2006). In situ FTIR study on the dehydration of natural goethite. *Journal of Asian Earth Sciences*, vol. 27, no. 4, pp. 503–511.

Premaratne, W.A.P.J., Priyadarshana, W.M.G.I., Gunawardena, S.H.P., De Alwis, A.A.P. (2013). Synthesis of nanosilica from paddy husk ash and their surface functionalization. *Journal of Science of the University of Kelaniya Sri Lanka*, vol. 8, pp. 33–48.

Psomiadou, E., Tsimidou, M. (1998). Simultaneous HPLC determination of tocopherols, carotenoids, and chlorophylls for monitoring their effect on virgin olive oil oxidation. *Journal of Agricultural and Food Chemistry*, vol. 46, no. 12, pp. 5132–5138.

Psomiadou, E., Tsimidou, M. (2002). Stability of virgin olive oil. 1. Autoxidation studies. *Journal of Agricultural and Food Chemistry*, vol. 50, no. 4, pp. 716–721.

Qureshi, N., Sathyamoorthy, N., Takayama, K. (1984). Biosynthesis of C_{30} to C_{56} fatty acids by an extract of *Mycobacterium tuberculosis* H37Ra. *Journal of Bacteriology*, vol. 157, no. 1, pp. 46–52.

Raff, M., Tholstrup, T., Basu, S., Nonboe, P., Sørensen, M.T., Straarup, E.M. (2008). A diet rich in conjugated linoleic acid and butter increases lipid peroxidation but does not affect atherosclerotic, inflammatory, or diabetic risk markers in healthy young men. *The Journal of Nutrition*, vol. 138, no. 3, pp. 509–514.

Ramos, M.J., Fernández, C.M., Casas, A., Rodríguez, L., Pérez, A. (2009). Influence of fatty acid composition of raw materials on biodiesel properties. *Bioresource Technology*, vol. 100, no. 1, pp. 261–268.

Redden, G.D., Li, J., Leckie, J. (1998). Adsorption of U^{VI} and citric acid on goethite, gibbsite, and kaolinite: comparing results for binary and ternary systems. In: Jenne, E.A. (ed.), *Adsorption of Metals by Geomedia: Variables, Mechanisms, and Model Applications*, pp. 291–315. Academic Press: San Diego, CA.

Redfield, A.C. (1934). On the proportions of organic derivatives in sea water and their relation to the composition of plankton. *James Johnstone Memorial Volume*, pp. 176–192. University Press of Liverpool.

Redfield, A.C., Ketchum, B.H., Richards, F.A. (1963). The influence of organisms on the composition of sea-water. In: Hill, M.N. (ed.), *The sea: ideas and observations on progress in the study of the seas*, vol. 2: The composition of seawater: Comparative and descriptive oceanography, pp. 26–77. Wiley Interscience: New York.

Rege, R.V., Webster, C.C., Ostrow, J.D., Carr, S.H., Ohkubo, H. (1984). Validation of infrared spectroscopy for assessment of vinyl polymers of bile-pigment gallstones. *Biochemical Journal*, vol. 224, no. 3, pp. 871–876.

Regnier, P., Friedlingstein, P., Ciais, P., Mackenzie, F.T., Gruber, N., Janssens, I.A., Laruelle, G.G., Lauerwald, R., Luyssaert, S., Andersson, A.J., Arndt, S., Arnosti, C., Borges, A.V., Dale, A.W., Gallego-Sala, A., Goddéris, Y., Goossens, N., Hartmann, J., Heinze, C., Ilyina, T., Joos, F., LaRowe, D.E., Leifeld, J., Meysman, F.J.R., Munhoven, G., Raymond, P.A., Spahni, R., Suntharalingam, P., Thullner, M. (2013). Anthropogenic perturbation of the carbon fluxes from land to ocean. *Nature Geoscience*, vol. 6, no.8., pp. 597–607.

Reiner, T., Möhler, O., Arnold, F. (1999). Measurements of acetone, acetic acid, and formic acid in the northern midlatitude upper troposphere and lower stratosphere. *Journal of Geophysical Research*, vol. 104, no. D11, pp. 13943–13952.

Repetto, M., Semprine, J., Boveris, A. (2012). Lipid peroxidation: chemical mechanism, biological implications and analytical determination. In: Catala, A. (ed.), *Lipid Peroxidation*, pp. 3–30. InTechOpen: Rijeka, Croatia.

Rimstidt, J.D., Barnes, H.L. (1980). The kinetics of silica-water reactions. *Geochimica et Cosmochimica Acta*, vol. 44, no. 11, pp. 1683–1699.

Rogalska, E., Cudrey, C., Ferrato, F., Verger, R. (1993). Stereoselective hydrolysis of triglycerides by animal and microbial lipases. *Chirality*, vol. 5, no. 1, pp. 24–30.

Romero-Olivares, A.L., Allison, S.D., Treseder, K.K. (2017). Decomposition of recalcitrant carbon under experimental warming in boreal forest. *PLOS ONE*, vol. 12, no. 6, article no. e0179674 (11pp.).

Rongsirikul, N., Hongsprabhas, P. (2016). Brown pigment formation in heated sugar–protein mixed suspensions containing unmodified and peptically modified whey protein concentrates. *Journal of Food Science and Technology*, vol. 53, no. 1, pp. 800–807.

Rosenqvist, J., Casey, W.H. (2004). The flux of oxygen from the basal surface of gibbsite (α-$Al(OH)_3$) at equilibrium. *Geochimica et Cosmochimica Acta*, vol. 68, no. 17, pp. 3547–3555.

Royal Society of Chemistry, 2019. *ChemSpider: Search and share chemistry*. Available: http://www.chemspider.com [Accessed: 2 February 2019].

Roychoudhury, A.N., Merrett, G.L. (2006). Redox pathways in a petroleum contaminated shallow sandy aquifer: iron and sulfate reductions. *Science of The Total Environment*, vol. 366, no. 1, pp. 262–274.

Rueda, E.H., Ballesteros, M.C., Grassi, R.L. (1992). Dithionite as a dissolving reagent for goethite in the presence of EDTA and citrate. Application to soil analysis. *Clays and Clay Minerals*, vol. 40, no. 5, pp. 575–585.

Russell, J.D., Cruz, M., White, J.L., Bailey, G.W., Payne, W.R., Pope, J.D., Teasley, J.I. (1968). Mode of chemical-degradation of *s*-triazines by montmorillonite. *Science*, vol. 160, no. 3834, pp. 1340–1342.

Sagratini, G., Allegrini, M., Caprioli, G., Cristalli, G., Giardina, D., Maggi, F., Ricciutelli, M., Sirocchi, V., Vittori, S. (2013). Simultaneous determination of squalene, α-tocopherol and β-carotene in table olives by solid phase extraction and high-performance liquid chromatography with diode array detection. *Food Analytical Methods*, vol. 6, no. 1, pp. 54–60.

Sander, M.M., Nicolau, A., Guzatto, R., Samios, D. (2012). Plasticiser effect of oleic acid polyester on polyethylene and polypropylene. *Polymer Testing*, vol. 31, no. 8, pp. 1077–1082.

Sanders, R.L., Washton, N.M., Mueller, K.T. (2010). Measurement of the reactive surface area of clay minerals using solid-state NMR studies of a probe molecule. *The Journal of Physical Chemistry C*, vol. 114, no. 12, pp. 5491–5498.

Scheffer, F., Meyer, B., Niederbudde, E.A. (1959). Huminstoffbildung unter katalytischer Einwirkung natürlich vorkommender Eisenverbindungen im Modelversuch. *Zeitschrift für Pflanzenernährung, Düngung, Bodenkunde*, vol. 87, no. 1, pp. 26–44.

Schmidt, H., Heinz, E. (1993). Direct desaturation of intact galactolipids by a desaturase solubilized from spinach (*Spinacia oleracea*) chloroplast envelopes. *Biochemical Journal*, vol. 289, part 3, pp. 777–782.

Schmidt, M.W.I, Torn, M.S., Abiven, S., Dittmar, T., Guggenberger, G., Janssens, I.A., Kleber, M., Kögel-Knabner, I., Lehmann, J., Manning, D.A.C., Nannipieri, P., Rasse, D.P., Weiner, S., Trumbore, S.E. (2011). Persistence of soil organic matter as an ecosystem property. *Nature*, vol. 478, no. 7367, pp. 49–56.

Schneider, C., Porter, N.A., Brash, A.R. (2008). Routes to 4-hydroxynonenal: fundamental issues in the mechanisms of lipid peroxidation. *The Journal of Biological Chemistry*, vol. 283, no. 23, pp. 15539–15543.

Scholes, R.J., Monteiro, P.M.S., Sabine, C.L., Canadell, J.G. (2009). Systematic long-term observations of the global carbon cycle. *Trends in Ecology and Evolution*, vol. 24, no. 8, pp. 427–430.

Schroeder, P.A. (2002). Infrared spectroscopy in clay science. In: Rule, A., Guggenheim, S. (eds), *CMS Workshop Lectures*, vol. 11, pp. 181–206. The Clay Mineral Society: Aurora, CO.

Schwertmann, U. (1991). Solubility and dissolution of iron oxides. *Plant and Soil*, vol. 130, no. 1–2, pp. 1–25.

Schwertmann, U., Cornell, R.M. (2000). *Iron Oxides in the Laboratory: Preparation and Characterization*, 2nd edn. Wiley-VCH: Weinheim, Germany. 204pp. ISBN: 978-3-527-29669-9.

Sen Gupta, A.K. (1966). Radikalreaktionen bei der thermischen behandlung von ölsäure-methylester unter ausschluß von sauerstoff. *Fette, Seifen, Anstrichmittel (European Journal of Lipid Science and Technology)*, vol. 68, no. 6, pp. 475–483.

Sharma, V.K., Alipour, A., Soran-Erdem, Z., Aykut, Z.G., Demir, H.V. (2015). Highly monodisperse low-magnetization magnetite nanocubes as simultaneous T_1–T_2 MRI contrast agents. *Nanoscale*, vol. 7, no. 23, pp. 10519–10526.

Shin, J.Y., Cheney, M.A. (2005). Abiotic dealkylation and hydrolysis of atrazine by birnessite. *Environmental Toxicology and Chemistry*, vol. 24, no. 6, pp. 1353–1360.

Shindo, H., Higashi, T. (1986). Polymerization of hydroquinone as influenced by selected inorganic soil components. *Soil Science and Plant Nutrition*, vol. 32, no. 2, pp. 305–309.

Shindo, H., Huang, P.M. (1982). Role of Mn(IV) oxide in abiotic formation of humic substances in the environment. *Nature*, vol. 298, no. 5872, pp. 363–365.

Shindo, H., Huang, P.M. (1984*a*). Catalytic effects of manganese (IV), iron(III), aluminum, and silicon oxides on the formation of phenolic polymers. *Soil Science Society of America Journal*, vol. 48, no. 4, pp. 927–934.

Shindo, H., Huang, P.M. (1984*b*). Significance of Mn(IV) oxide in abiotic formation of organic nitrogen complexes in natural environments. *Nature*, vol. 308, no. 5954, pp. 57–58.

Shindo, H., Huang, P.M. (1985). The catalytic power of inorganic components in the abiotic synthesis of hydroquinone-derived humic polymers. *Applied Clay Science*, vol. 1, no. 1–2, pp. 71–81.

Shokrollahi, A., Shokrollahi, N. (2014). Determination of Mn^{2+} ion by solution scanometry as a new, simple and inexpensive method. *Química Nova*, vol. 37, no. 10, pp. 1589–1593.

Skoog, D.A., West, D.M., Holler, F.J., Crouch, S.R. (2004). *Fundamentals of Analytical Chemistry*, 8th edn. Brooks/Cole, Cengage Learning: Belmont, CA. 1146pp. ISBN: 9780534417970.

Smith, W.L., Murphy, R.C. (2008). Oxidized lipids formed non-enzymatically by reactive oxygen species. *The Journal of Biological Chemistry*, vol. 283, no. 23, pp. 15513–15514.

Sochor, J., Ruttkay-Nedeck, B., Babula, P., Adam, V., Hubalek, J., Kizek, R. (2012). Automation of methods for determination of lipid peroxidation. In: Catala, A. (ed.), *Lipid Peroxidation*, pp. 131–154. InTechOpen: Rijeka, Croatia.

St. Angelo, A.J., Vercellotti, J., Jacks, T., Legendre, M. (1996). Lipid oxidation in foods. *Critical Reviews in Food Science and Nutrition*, vol. 36, no. 3, pp. 175–224.

Stone, A.T. (1987). Reductive dissolution of manganese(III/IV) oxides by substituted phenols. *Environmental Science & Technology*, vol. 21, no. 10, pp. 979–988.

Stone, A.T., Morgan, J.J. (1984*a*). Reduction and dissolution of manganese(III) and manganese(IV) oxides by organics. 1. Reaction with hydroquinone. *Environmental Science & Technology*, vol. 18, no. 6, pp. 450–456.

Stone, A.T., Morgan, J.J. (1984*b*). Reduction and dissolution of manganese(III) and manganese(IV) oxides by organics. 2. Survey of the reactivity of organics. *Environmental Science & Technology*, vol. 18, no. 8, pp. 617–624.

Stumm, W., Morgan, J.J. (1996). *Aquatic Chemistry, Chemical Equilibria and Rates in Natural Waters*, 3rd edn. John Wiley & Sons, Inc.: New York, NY. 1040pp. ISBN: 978-0-471-51185-4.

Subramanian, N., Viswanathan, B., Varadarajan, T.K. (2014). A facile, morphology-controlled synthesis of potassium-containing manganese oxide nanostructures for electrochemical supercapacitor application. *RSC Advances*, vol. 4, no. 64, pp. 33911–33922.

Svensson, M., Mossberg, A.-K., Pettersson, J., Linse, S. (2003). Lipids as cofactors in protein folding: stereo-specific lipid–protein interactions are required to form HAMLET (human α-lactalbumin made lethal to tumor cells). *Protein Science*, vol. 12, no. 12, pp. 2805–2814.

Tang, K.C., Tropp, B.E., Engel, R. (1978). The synthesis of phosphonic acid and phosphate analogues of glycerol-3-phosphate and related metabolites. *Tetrahedron*, vol. 34, no. 19, pp. 2873–2878.

Tavakolipour, H., Mokhtarian, M., Kalbasi-Ashtari, A. (2016). Lipid oxidation kinetics of pistachio powder during different storage conditions. *Journal of Food Process Engineering*, vol. 40, no. 3, article no. e12423 (8pp.).

Taylor, R.M., McKenzie, R.M., Norrish, K. (1964). The mineralogy and chemistry of manganese in some Australian soils. *Australian Journal of Soil Research*, vol. 2, no. 2, pp. 235–248.

Thevenot, M., Dignac, M.-F., Rumpel, C. (2010). Fate of lignins in soils: a review. *Soil Biology & Biochemistry*, vol. 42, no. 8, pp. 1200–1211.

Thomas, M.J., Mehl, K.S., Pryor, W.A. (1978). The role of the superoxide anion in the xanthine oxidase-induced autoxidation of linoleic acid. *Biochemical and Biophysical Research Communications*, vol. 83, no. 3, pp. 927–932.

Tomati, U., Galli, E. (1992). The fertilizing value of wastewater from the olive processing industry. In: Kubát, J. (ed.), *Developments in Agricultural and Managed Forest Ecology: humus, its structure and role in agriculture and environment*, vol. 25, pp. 117–126. Elsevier.

Topolski, A. (2011). Insight into the degradation of a manganese(III)-citrate complex in aqueous solutions. *Chemical Papers*, vol. 65, no. 3, pp. 389–392.

Trouwborst, R.E., Clement, B.G., Tebo, B.M., Glazer, B.T., Luther III, G.W. (2006). Soluble Mn(III) in suboxic zones. *Science*, vol. 313, no. 5795, pp. 1955–1957.

Tu, S., Racz, G.J., Goh, T.B. (1994). Transformations of synthetic birnessite as affected by pH and manganese concentration. *Clays and Clay Minerals*, vol. 42, no. 3, pp. 321–330.

Tvrzická, E., Vecka, M., Staňková, B., Žák, A. (2002). Analysis of fatty acids in plasma lipoproteins by gas chromatography–flame ionization detection: quantitative aspects. *Analytica Chimica Acta*, vol. 465, no. 1–2, pp. 337–350.

Ulrich, H.-J., Stone, A.T. (1989). Oxidation of chlorophenols adsorbed to manganese oxide surfaces. *Environmental Science & Technology*, vol. 23, no. 4, pp. 421–428.

Vaclavik, V.A., Christian, E.W. (2008). *Essentials of Food Science*. Springer: New York, NY. 495pp. ISBN: 978-0-387-69939-4 (print) / 978-0-387-69940-0 (online).

Van Cappellen, P., Qiu, L. (1997). Biogenic silica dissolution in sediments of the Southern Ocean. II. Kinetics. *Deep-Sea Research II*, vol. 44, no. 5, pp. 1129–1149.

Vandenbroucke, M., Largeau, C. (2007). Kerogen origin, evolution and structure. *Organic Geochemistry*, vol. 38, no. 5, pp. 719–833.

Wang, M.C., Huang, P.M. (1986). Humic macromolecule interlayering in nontronite through interaction and phenol monomers. *Nature*, vol. 323, no. 6088, pp. 529–531.

Wang, M.C., Huang, P.M. (1987). Polycondensation of pyrogallol and glycine and the associated reactions as catalyzed by birnessite. *Science of the Total Environment*, vol. 62, pp. 435–442.

Wang, M.C., Huang, P.M. (1989). Catalytic power of nontronite, kaolinite, and quartz and their reaction sites in the formation of hydroquinone-derived polymers. *Applied Clay Science*, vol. 4, no. 1, pp. 43–57.

Wang, M.C., Huang, P.M. (1992). Significance of Mn (IV) oxide in the abiotic ring cleavage of polyphenol in natural environments. *Science of the Total Environment*, vol. 113, no. 1–2, pp. 147–157.

Wang, M.C., Huang, P.M. (1994). Structural role of polyphenols in influencing the ring cleavage and related chemical reactions as catalyzed by nontronite. In: Senesi, N., Miano, T.M. (eds), *Humic Substances in the Global Environment and Implications on Human Health*, pp. 173–180. Elsevier: Amsterdam.

Wang, T.S.C., Li, S.W. (1977). Clay minerals as heterogeneous catalysts in preparation of model humic substances. *Zeitschrift für Pflanzenernährung und Bodenkunde*, vol. 140, no. 6, pp. 669–676.

Wang, T.S.C., Li, S.W., Ferng, Y.L. (1978). Catalytic polymerization of phenolic compounds by clay minerals. *Soil Science*, vol. 126, no. 1, pp. 15–21.

Wang, T.S.C., Wang, M.C., Huang, P.M. (1983*a*) Catalytic synthesis of humic substance by using aluminas as catalysts. *Soil Science*, vol. 136, no. 4, pp. 226–230.

Wang, T.S.C., Wang, M.C., Ferng, Y.L., Huang, P.M. (1983*b*). Catalytic synthesis of humic substances by natural clays, silts, and soils. *Soil Science*, vol. 135, no. 6, pp. 350–360.

Wang, H., Wang, X., Li, X., Zhang, Y., Dai, Y., Guo, C., Zheng, H. (2012). QSAR study and the hydrolysis activity prediction of three alkaline lipases from different lipase-producing microorganisms. *Lipids in Health and Disease*, vol. 11, article no. 124 (9pp.).

Waraho, T., McClements, D.J., Decker, E.A. (2011). Mechanisms of lipid oxidation in food dispersions. *Trends in Food Science & Technology*, vol. 22, no. 1, pp. 3–13.

Wilson, R.F. (2004). Seed Composition. In: Shibles, R.M., Harper, J.E., Wilson, R.F., Shoemaker, R.C. (eds), *Soybeans: Improvement, Production, and Uses*, 3rd edn, pp. 621–678. American Society of Agronomy, Crop Science Society of America, Soil Science Society of America: Madison, WI.

Wiseman, S.A., Mathot, J.N.N.J., de Fouw, N.J., Tijburg, L.B.M. (1996). Dietary non-tocopherol antioxidants present in extra virgin olive oil increase the resistance of low density lipoproteins to oxidation in rabbits. *Atherosclerosis*, vol. 120, no. 1–2, pp. 15–23.

Wu, L.M., Zhou, C.H., Keeling, J., Tong, D.S., Yu, W.H. (2012). Towards an understanding of the role of clay minerals in crude oil formation, migration and accumulation. *Earth-Science Reviews*, vol. 115, no. 4, pp. 373–386.

Xu, H.E., Lambert, M.H., Montana, V.G., Parks, D.J., Blanchard, S.G., Brown, P.J., Sternbach, D.D., Lehmann, J.M., Wisely, G.B., Willson, T.M., Kliewer, S.A., Milburn, M.V. (1999). Molecular recognition of fatty acids by peroxisome proliferator–activated receptors. *Molecular Cell*, vol. 3, no. 3, pp. 397–403.

Yadav, A., Tandon, B., Nag, A. (2016). Reduction of Mn^{3+} to Mn^{2+} and near infrared plasmonics from Mn–Sn codoped In_2O_3 nanocrystals. *RSC Advances*, vol. 6, no. 82, pp. 79153–79159.

Yang, W.S., Stockwell, B.R. (2016). Ferroptosis: death by lipid peroxidation. *Trends in Cell Biology*, vol. 26, no. 3, pp. 165–176.

Yariv, S. (2002*a*) Introduction to organo-clay complexes and interactions. In: Yariv, S., Cross, H. (eds), *Organo-Clay Complexes and Interactions*, pp. 39–112. Marcel Dekker, Inc.: New York.

Yariv, S. (2002*b*). IR spectroscopy and thermo-IR spectroscopy in the study of the fine structure of organo-clay complexes. In: Yariv, S., Cross, H. (eds), *Organo-Clay Complexes and Interactions*, pp. 345–462. Marcel Dekker, Inc.: New York.

Yin, H., Xu, L., Porter, N.A. (2011). Free radical lipid peroxidation: mechanisms and analysis. *Chemical Reviews*, vol. 111, no. 10, pp. 5944–5972.

Yoshida, S., Zhang, Q.Z., Sakuyama, S., Matsushima, S. (2009). Metabolism of fatty acids and lipid hydroperoxides in human body monitoring with Fourier transform infrared spectroscopy. *Lipids in Health and Disease*, vol. 8, article no. 28 (11pp.).

Zambonin, L., Ferreri, C., Cabrini, L., Prata, C., Chatgilialoglu, C., Landi, L. (2006). Occurrence of *trans* fatty acids in rats fed a *trans*-free diet: a free radical-mediated formation? *Free Radical Biology & Medicine*, vol. 40, no. 9, pp. 1549–1556.

Zhang, Y., Dongbei, Y., Ma, H. (2015). Darkening mechanism and kinetics of humification process in catechol-Maillard system. *Chemosphere*, vol. 130, pp. 40–45.

Zhao, W., Liu, F., Feng, X., Tan, W., Qiu, G., Chen, X. (2012). Fourier transform infrared spectroscopy study of acid birnessites before and after Pb^{2+} adsorption. *Clay Minerals*, vol. 47, no. 2, pp. 191–204.

Zhu, B., Fang, B., Li, X. (2010). Dehydration reactions and kinetic parameters of gibbsite. *Ceramics International*, vol. 36, no. 8, pp. 2493–2498.

Zielinski, Z.A.M., Pratt, D.A. (2017). Lipid peroxidation: kinetics, mechanisms, and products. *The Journal of Organic Chemistry*, vol. 82, no. 6, pp. 2817–2825.

Zou, X.M., Ruan, H.H., Fu, Y., Yang, X.D., Sha, L.Q. (2005). Estimating soil labile organic carbon and potential turnover rates using a sequential fumigation–incubation procedure. *Soil Biology & Biochemistry*, vol. 37, no. 10, pp. 1923–1928.

Appendix A

Background discussion on kinetics—rate expressions, rate constants, reaction orders and activation energy

The rate of a reaction can be monitored by measuring either the disappearance of reactants in the reaction, or by monitoring the generation of products. Consider the following hypothetical single-step reaction:

$$nA \rightarrow P \tag{A.1}$$

where A is a reactant, P is a product, and n is the molar ratio of A to P. This straightforward single-step reaction is known as an *elemental reaction*. The reaction rate for an elemental reaction can be defined either in terms of the reactant A or the product P (modified from Stumm and Morgan, 1996):

$$\frac{d[P]}{dt} = k[P] = -\frac{d[A]}{dt} = -k[A]^n \tag{A.2}$$

where $[P]$ is the concentration of product P, $[A]$ is the concentration of reactant A, the constant k is the rate constant, and n is the reaction rate order with respect to the concentration of A and is equal to the molar ratio of A to P (equation A.1; Lasaga, 1981; Stumm and Morgan, 1996). Most reactions in nature, however, may consist of a number of steps or elemental reactions, which can be illustrated by the hypothetical reaction (modified from Lasaga, 1981):

$$aA \rightarrow bB \rightarrow cC \rightarrow P \tag{A.3}$$

where, as was the case in equation A.1, a is the molar ratio of A to P, b is the molar ratio of B to P, and c is the molar ratio of C to P. This reaction is known as an *overall reaction*, and has an *overall rate*, defined as:

$$\frac{d[P]}{dt} = k_{\text{overall}}[A]^n[B]^p[C]^q \tag{A.4}$$

where k_{overall} is an overall rate constant, and n, p and q are the reaction rate orders with respect to the concentrations of A, B and C, respectively. The overall reaction rate order is defined as:

$$r_{\text{overall}} = n + p + q \tag{A.5}$$

In the case of overall reactions, the reaction rate orders are not necessarily equal to the molar ratios (*i.e.* $n \neq a, p \neq b$ and $q \neq c$) as was the case for elemental reactions. These reaction orders are non-trivial and have to be determined experimentally. This quickly becomes a complex mathematical challenge, as there are several variables (*i.e.* $[A]$, $[B]$ and $[C]$) upon which the rate is dependent, and they are all varying at the same time.

A simplification is required, and for natural systems it comes in the form of the fact that many natural reactions proceed fairly slowly. From the initiation of a such a reaction, the concentrations of species such as A, B and C remain virtually constant for several hours after initiation. Practically, the initial situation is thus: $[A] \approx [A]_0$, $[B] \approx [B]_0$ and $[C] \approx [C]_0$, where $[A]_0$, $[B]_0$ and $[C]_0$ are the initial concentrations of A, B and C, respectively, and are fixed values (*i.e.* constants). The initial reaction rate therefore becomes:

$$\left(\frac{d[P]}{dt}\right)_0 = k_{\text{overall}}[A]_0^n[B]_0^p[C]_0^q \tag{A.6}$$

Conducting an experiment in which one of these concentrations is varied, for example the concentration of A ($[A]$), whilst all others remain constant ($[B] \approx [B]_0$, $[C] \approx [C]_0$), allows the reaction rate order with respect to $[A]$ (n) to be determined:

$$\frac{d[P]}{dt} = k_{\text{overall}}[A]^n[B]_0^p[C]_0^q = k'[A]^n \tag{A.7}$$

where k' is a new overall rate constant and is equal to $k_{\text{overall}}[B]_0^p[C]_0^q$. The reaction rate order (n) is determined from a double-logarithmic plot of $\log(dP/dt)$ *v.* $\log([A])$. The result of this plot is a straight line with angular coefficient (slope) n and linear coefficient (y-intercept) equal to $\log k'$:

$$\log\left(\frac{d[P]}{dt}\right) = \log k' + n\log([A]) \tag{A.8}$$

This method of reaction order determination is known as the "*initial rate method*" (Lasaga, 1981). Several methods are employed to ensure that the concentration

of the species not being studied remains constant. One commonly-used approach is to add the component(s) not of interest in excess relative to the one of interest, so that changes in its (their) concentration(s) do not affect the reaction rate:

$$\frac{d[P]}{dt} = k_{\text{overall}}[A]^n[B]^p[C]^q$$

but, $[B]$ and $[C] \gg [A]$, and therefore:

$$\frac{d[P]}{dt} \approx k'[A]^n \tag{A.9}$$

The reaction rate is not only dependent on concentrations of species in the reaction, it can be dependent on a number of other variables, called *kinetic variables*. These include variables such as surface area (when a solid is involved in the reaction), the rate of diffusion (which affects the rate at which reactants can collide to react and the rate at which products are removed so that reactants can react without interference), the pH of the solution (or of a solid surface), and another that affects all reaction rates—temperature.

In the same manner as with reactant and product concentrations, the reaction rate is also related to kinetic variables ($\mathcal{X}$, Y, $\mathcal{Z}\ldots$) *via* reaction orders ($x, y, z\ldots$) in a similar equation as before:

$$\frac{d[P]}{dt} = k_{\text{overall}}\mathcal{X}^x\mathrm{Y}^y\mathcal{Z}^z\ldots \tag{A.10}$$

Here too, the reaction order of one variable can be determined by isolation whilst the others are kept constant during the reaction.

The reaction rate order can also reveal the shape of the curve of a plot between $[A]$ and time (t) for example. Consider the reaction rate equation (equation A.11):

$$\frac{d[A]}{dt} = k[A]^n \tag{A.11}$$

A zero-order ($n = 0$) dependence of reaction rate on $[A]$ means that the reaction rate is independent of $[A]$:

$$\frac{d[A]}{dt} = k \tag{A.12}$$

The $[A]$ versus t curve is readily obtained by integration, from the initial concentration of A ($[A]_0$) at some initial time t_i to some concentration of A at some final time t_f ($[A]$):

$$\int_{[A]_0}^{[A]} d[A] = k \int_{t_i}^{t_f} dt \tag{A.13a}$$

which gives:

$$[A] = [A]_0 + k(t_f - t_i) \tag{A.13b}$$

This is a straight line with y-intercept $[A]_0$ and slope k. A first-order ($n = 1$) dependence means that the reaction rate is linearly dependent on $[A]$:

$$\frac{d[A]}{dt} = k[A] \tag{A.14}$$

Integrating in a similar manner as before:

$$\int_{[A]_0}^{[A]} \frac{d[A]}{[A]} = k \int_{t_i}^{t_f} dt \tag{A.15a}$$

which gives:

$$\ln([A]) = \ln([A]_0) + k(t_f - t_i) \tag{A.15b}$$

$$\Leftrightarrow \qquad [A] = [A]_0 e^{k(t_f - t_i)} \tag{A.15c}$$

This is an exponential curve with y-intercept $[A]_0$. The units of the rate constant (k) also vary depending on the order. In zero-order reaction rate equations, k has units of concentration over time, for example mol l^{-1} s^{-1} or μmol g^{-1} day^{-1} or similar. In first order rate equations, k has units of per time only, for example s^{-1}, h^{-1} or day^{-1}. The units of k and the integrated equations of several rate orders are summarised in Table A.1.

In general, increases in temperature cause an increase in reaction rates (due to more collisions among the molecules/atoms of reagents). The relationship between reaction rates and temperature has been studied throughout the late 19th to early 20th century (Laidler, 1984). The *Arrhenius equation* relates the rate constant (k) to temperature (T) (Rimstidt and Barnes, 1980; Laidler, 1984):

$$k = A' \exp\left(-\frac{E_a}{RT}\right) \tag{A.16}$$

Table A.1 Reaction rate expressions for zero, first and second order rate dependence on the concentration of a species A, their integrated form (between an initial $[A]_0$ at time $t = 0$ and some $[A]$ at time t), and units of their rate constants. Modified from Tavakolipour *et al.* (2016).

Rate order	Differential expression	Integrated expression	Units of rate constant [a]
Zeroth	$\frac{d[A]}{dt} = k$	$[A] = [A]_0 + kt$	$\text{mol}\,\text{l}^{-1}\,t^{-1}$
First	$\frac{d[A]}{dt} = k[A]$	$[A] = [A]_0 e^{kt}$	t^{-1}
Second	$\frac{d[A]}{dt} = k[A]^2$	$\frac{1}{[A]} = \frac{1}{[A]_0} - kt$	$\text{l}\,\text{mol}^{-1}\,t^{-1}$

a. The unit t^{-1} (per unit time) means units such as per second (s^{-1}), per minute (min^{-1}), per hour (h^{-1}), per day (d^{-1}), per week (wk^{-1}), per month (mo^{-1}) or per year (a^{-1}).

where A' is the "*frequency factor*" (a pre-exponential term related to collision frequency and entropy), E_a is the activation energy of the reaction (kJ mol^{-1}), R is the universal gas constant (8.314 J $mol^{-1}\,K^{-1}$) and T is the temperature (K). The logarithmic form of the Arrhenius equation is:

$$\ln k = \ln(A') - \frac{E_a}{R}\left(\frac{1}{T}\right) \tag{A.17}$$

A plot of $\ln k$ *versus* $(1/T)$ yields a straight line with y-intercept $\ln(A')$ and slope $-(E_a/R)$. In this manner, the activation energy of a reaction can be determined by conducting several experiments at various temperatures, plotting the natural logarithm of their obtained rate constants against the reciprocal of temperature, and using the slope of the straight line to determine E_a.

There also exist numerous other types of kinetic models and rate expressions, which are dependent on specific variables. A good example is the growth rate (μ) of microorganisms, being dependent on the concentration of a limiting substrate ([S]) (Monod, 1949):

$$\mu = \frac{\mu_{max}\,[S]}{K_s + [S]} \tag{A.18}$$

where μ_{max} is the maximum growth rate under non-limiting conditions and K_s is the "*half-saturation concentration*" which is the value of [*S*] when the growth rate (μ) is half of the maximum growth rate (μ_{max}), *i.e.* $\mu/\mu_{max} = 0.5$. This expression is in the form of the hyperbolic Michaelis-Menten equation, and the important fitting parameters, *viz.* μ_{max} and K_s, are determined by linearizing equation A.18, by taking the reciprocal of both sides (Lineweaver and Burk, 1934):

$$\frac{1}{\mu} = \frac{K_s}{\mu_{max}\,[S]} + \frac{1}{\mu_{max}} \tag{A.19}$$

A plot of $(1/\mu)$ *versus* $(1/[S])$ produces a straight line with slope (K_s/μ_{max}) and *y*-intercept $(1/\mu_{max})$ from which K_s and μ_{max} can be determined.

Another example of a different type of rate expression is the one that describes the rate of silica dissolution of solid silica in aqueous solution (*via* the formation of silicic acid), as demonstrated by the reaction equation:

$$SiO_2(s) + 2H_2O(\ell) \rightleftharpoons Si(OH)_4(aq) \tag{A.20}$$

The above reaction is reversible, with the forward reaction being dissolution and the reverse reaction being precipitation. The rate of change in silicic acid activity ($\partial a_{Si(OH)_4}/\partial t$) is defined by the differential equation which considers both the forward and reverse reactions (Rimstidt and Barnes, 1980):

$$\left(\frac{\partial a_{Si(OH)_4}}{\partial t}\right)_{P,\,T,\,M,\,\gamma} = \left(\frac{A}{M}\right)(\gamma_{Si(OH)_4})(k_+ a_{SiO_2} a_{H_2O}^2 - k_- a_{Si(OH)_4}) \tag{A.21}$$

where *P* is the pressure (bar), *T* is temperature (K), *M* is the mass of water (kg), γ_i is the activity coefficient of species *i* (*e.g.* $Si(OH)_4$), a_i is the activity of species *i* (*e.g.* $Si(OH)_4$), *A* is the interfacial area between solid and aqueous phases (m^2) and k_+ and k_- are the rate constants for the dissolution and precipitation reactions, respectively. The net rate of change in silicic acid concentration (defined as $d[Si(OH)_4]/dt$) is also dependent on the degree of silica undersaturation in solution (defined as $1 - [Si(OH)_4]/[Si(OH)_4]_{eq.}$)(modified from Rimstidt and Barnes (1980) and Van Cappellen and Qiu (1997):

$$\frac{d[Si(OH)_4]}{dt} = k_{app}\left(\frac{A}{M}\right)\left(1 - \frac{[Si(OH)_4]}{[Si(OH)_4]_{eq.}}\right) \tag{A.22}$$

where k_{app} is the apparent rate constant and $[Si(OH)_4]_{eq.}$ is the solubility of the reacting solid silica at a particular *P*, *T* and ionic solution composition.

Appendix B

Identifying X-ray diffraction (XRD) diffractograms for the clays used in this study

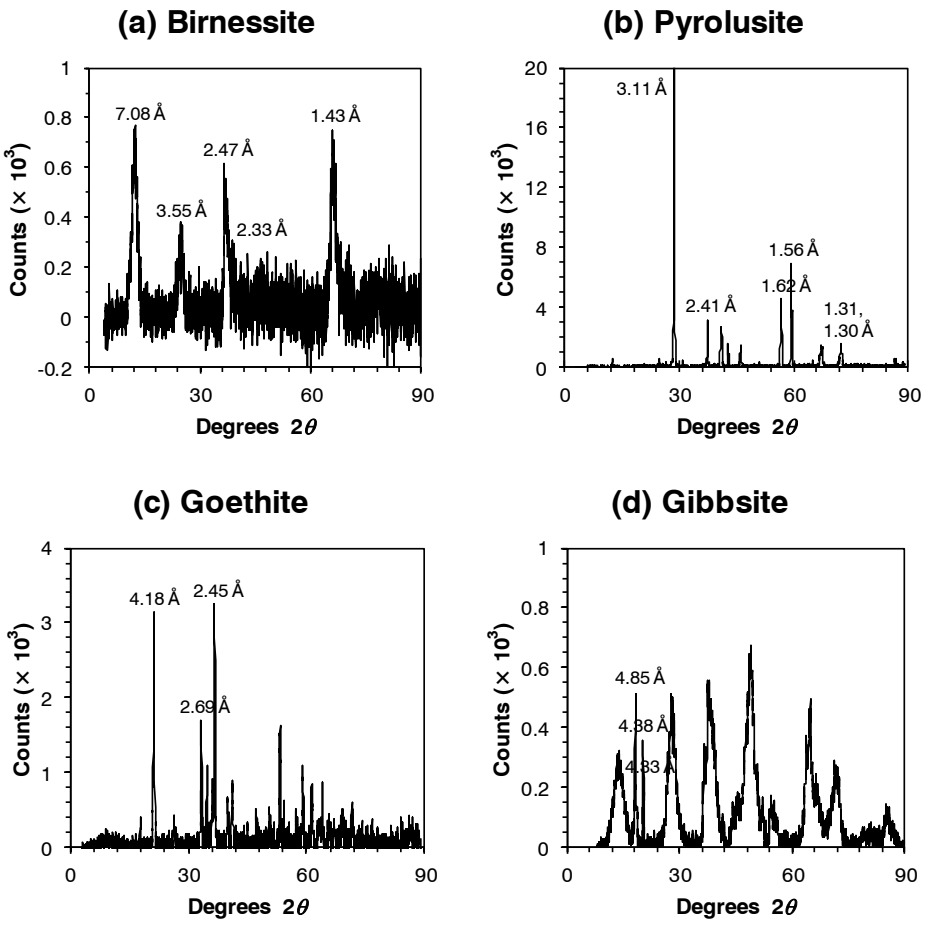

Fig. B.1 The powder XRD diffractograms of (a) birnessite, (b) pyrolusite, (c) goethite, (d) gibbsite, (e) quartz, (f) KGa-1b kaolinite and (g) STx-1b montmorillonite (with background subtracted).

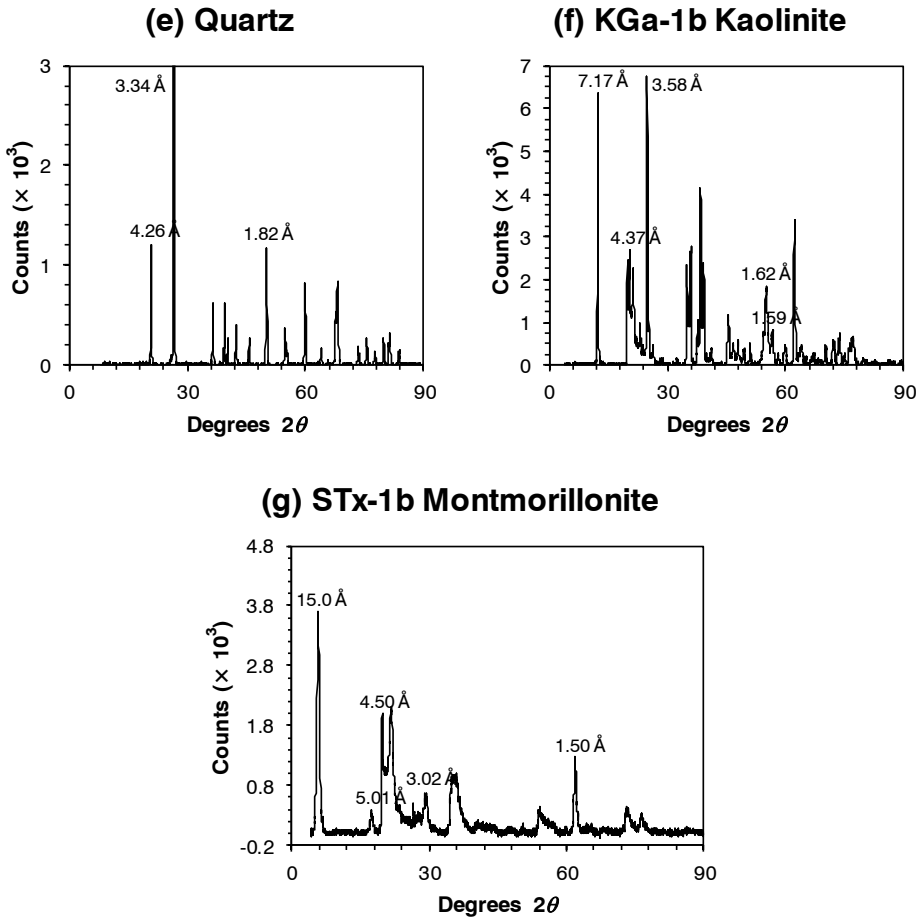

Fig. B.1 *Continued.*

Appendix C

ATR-FTIR spectra for the clays used in this study

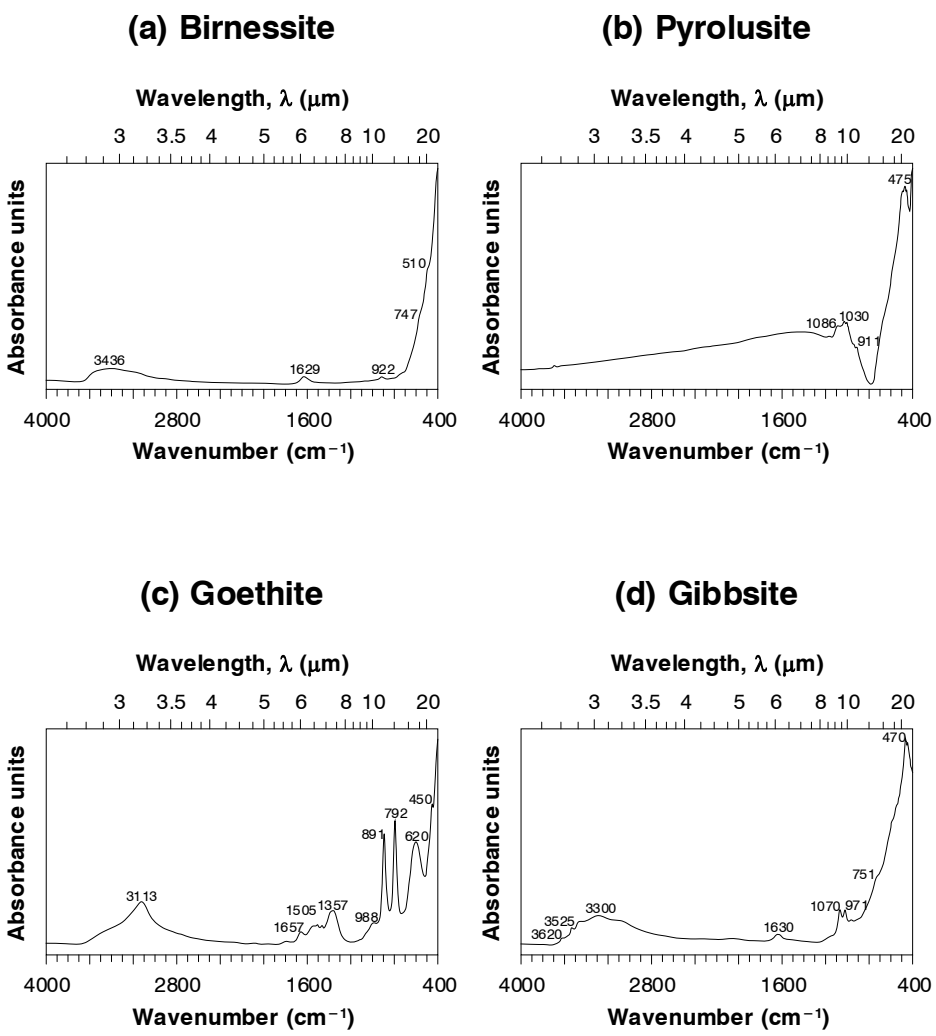

Fig. C.1 The ATR-FTIR spectra of (a) birnessite, (b) pyrolusite, (c) goethite, (d) gibbsite, (e) quartz, (f) KGa-1b kaolinite and (g) STx-1b montmorillonite.

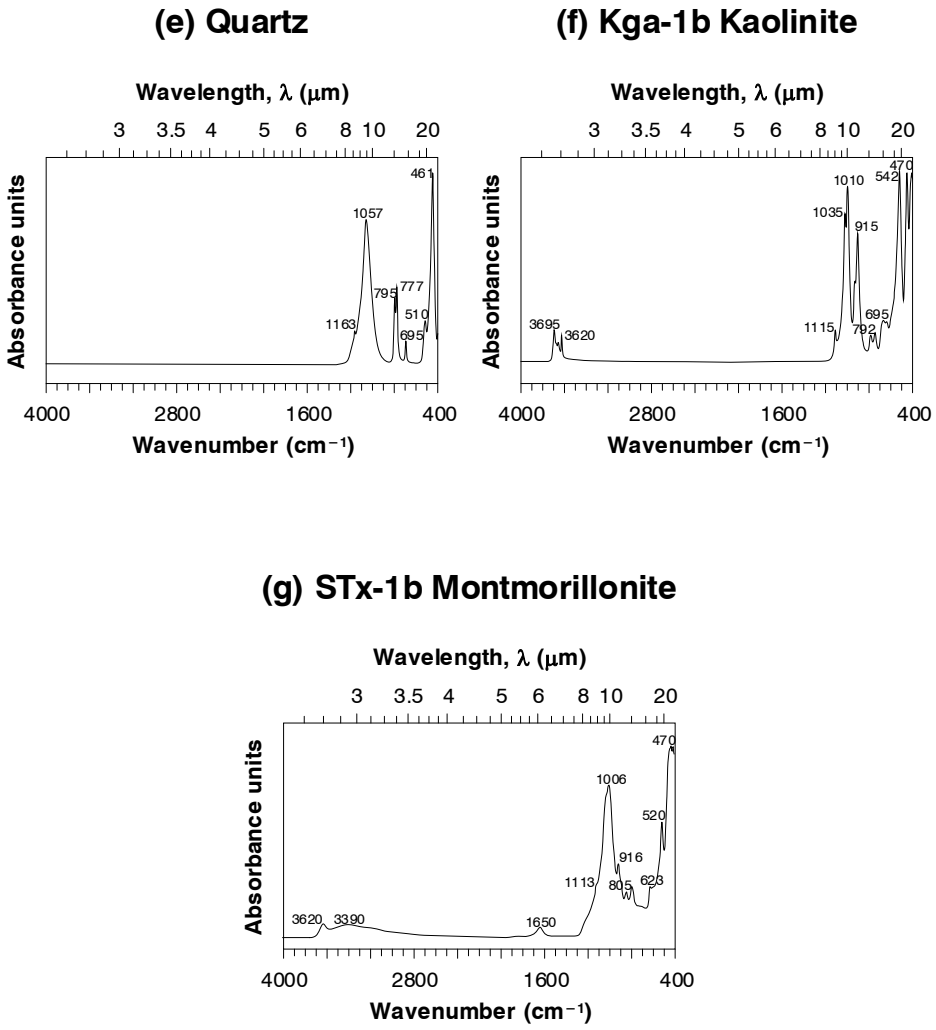

Fig. C.1 *Continued.*

Appendix D

Calibration of the Mn^{3+}-pyrophosphate extraction and UV-VIS quantification method

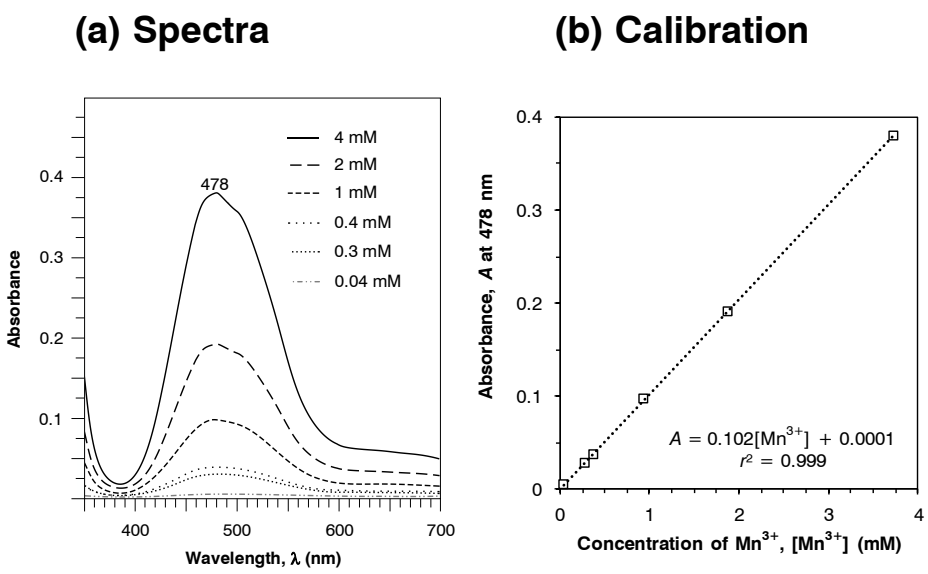

Fig. D.1 The (a) UV-VIS spectra of the Mn^{3+} calibration standards used and (b) the resulting calibration curve of Mn^{3+} concentration ($[Mn^{3+}]$) at 478 nm absorbance.

Appendix E

Autoxidation of oleic acid, linoleic acid and natural oils

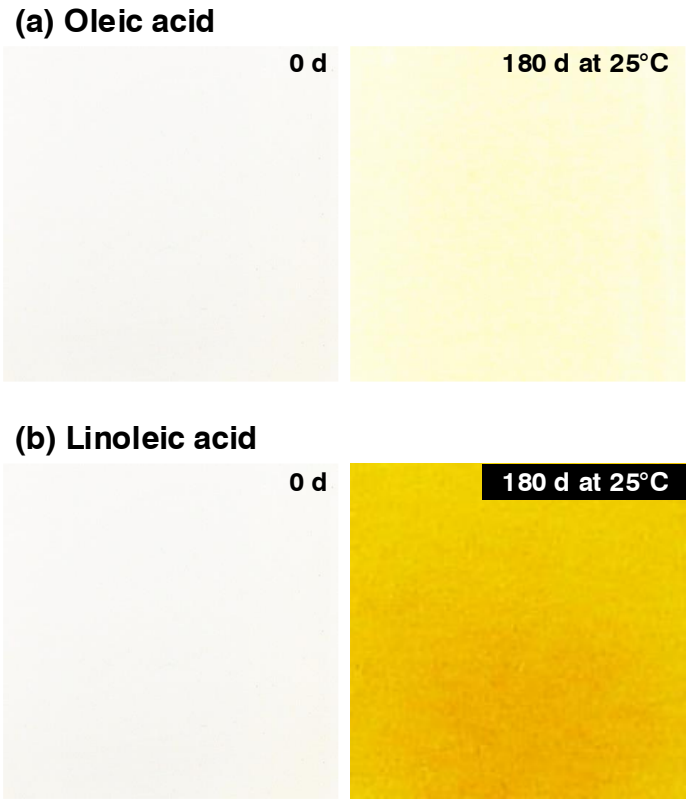

Fig. E.1 The autoxidation of (a) oleic acid, (b) linoleic acid, (c) raw linseed oil and (d) olive oil with no mineral present and under the same conditions as chapter 3—incubation for 6 months at 25°C in the dark.

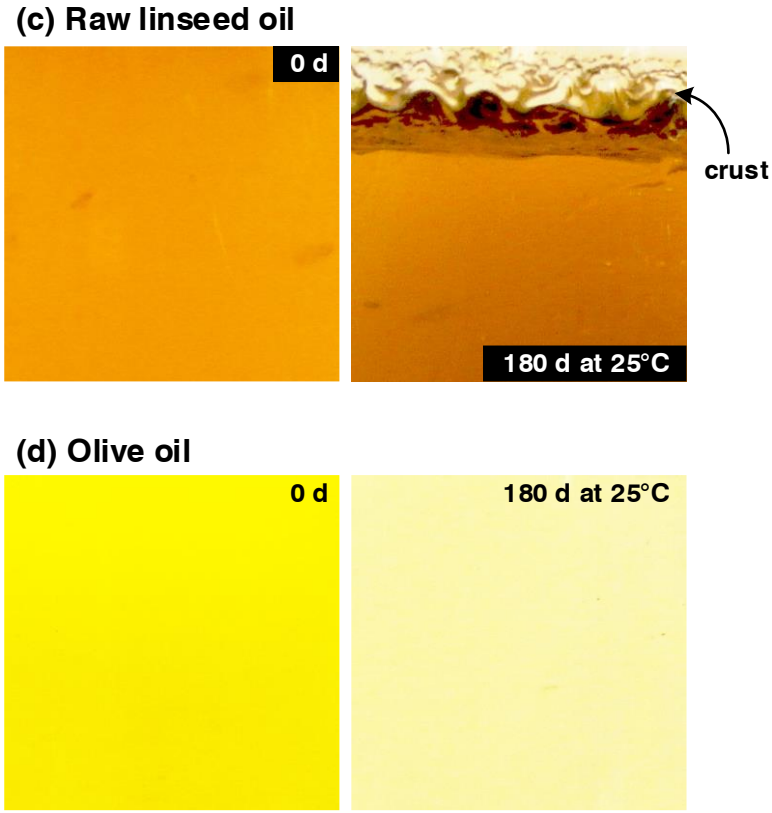

Fig. E.1 *Continued.*